



Thomas Kissinger

# **Range-Resolved Optical Interferometric Signal Processing**

Centre for Engineering Photonics  
School of Aerospace, Transport and Manufacturing

PhD Thesis

Academic Years : 2011 to 2015

Supervisors: Prof. Ralph P. Tatam  
Dr. Thomas O. H. Charrett

Submission: June 2015

This thesis is submitted in partial fulfilment of the  
requirements for the Degree of Doctor of Philosophy

# Abstract

The ability to identify the range of an interferometric signal is very useful in interferometry, allowing the suppression of parasitic signal components or permitting several signal sources to be multiplexed. Two novel range-resolved optical interferometric signal processing techniques, employing very different working principles, are theoretically described and experimentally demonstrated in this thesis. The first technique is based on code-division multiplexing (CDM), which is combined with single-sideband signal processing, resulting in a technique that, unlike prior work, only uses a single, regular electro-optic phase modulator to perform both range-based signal identification and interferometric phase evaluation. The second approach uses sinusoidal optical frequency modulation (SFM), induced by injection current modulation of a diode laser, to introduce range-dependent carriers to determine phase signals in interferometers of non-zero optical path difference. Here, a key innovation is the application of a smooth window function, which, when used together with a time-variant demodulation approach, allows optical path lengths of constituent interferometers to be continuously and independently variable, subject to a minimum separation, greatly increasing the practicality of the approach.

Both techniques are applied to fibre segment interferometry, where fibre segments that act as long-gauge length interferometric sensors are formed between pairs of partial in-fibre reflectors. Using a regular single-mode laser diode, six fibre segments of length 12.5 cm are multiplexed with a quadrature bandwidth of 43 kHz and a phase noise floor of  $0.19 \text{ mrad} \cdot \text{Hz}^{-0.5}$  using the SFM technique. In contrast, the 16.5 m spatial resolution achieved with the CDM technique points towards its applicability in medium-to-long range sensing. The SFM technique also allows high linearity, with cyclic errors as low as 1 mrad demonstrated, and with modelling indicating further room for improvement. Additionally, in an industrial measurement, the SFM technique is applied to single-beam, multi-surface vibrometry, allowing simultaneous differential measurements between two vibrating surfaces.

# Acknowledgements

I thank my family for all their encouragement and patience and my parents for supporting my education all through my life.

My thanks go to my supervisors, Tom Charrett and Ralph Tatam, for their guidance throughout this project and, in particular, to Ralph Tatam for providing me with the opportunity to carry out a blue-sky research project in the first place. Additionally, I am grateful to Steve James for his good advice, for initiating the vibrometry project and, together with Ricardo Correia, for inscribing the FBGs sensing fibre used in Chap. 6. I also appreciate the helpfulness of Steve Staines and I would like to thank the whole team at Engineering Photonics for the great working atmosphere.

Oxford Instruments plc kindly allowed me to publish vibration measurement data and I gratefully acknowledge funding during this PhD project from the Department of Engineering Photonics and from the Engineering and Physical Sciences Research Council (EPSRC) UK, via grant EP/G033900/1. Furthermore, follow-up funding from EPSRC, via grant EP/H02252X/1, via Institutional Impact Acceleration Account Early Stage Funding and future support under grant EP/M020401/1 has already allowed, and will continue to allow, this work to be carried forward.

# Contents

<b>Title</b>	<b>i</b>
<b>Abstract</b>	<b>ii</b>
<b>Acknowledgements</b>	<b>iii</b>
<b>Contents</b>	<b>vii</b>
<b>List of Figures</b>	<b>x</b>
<b>List of Tables</b>	<b>xi</b>
<b>List of Acronyms</b>	<b>xii</b>
<b>List of Symbols</b>	<b>xiv</b>
<b>1. Introduction</b>	<b>1</b>
1.1. Range-Resolved Optical Interferometric Signal Processing . . . . .	1
1.2. Fibre Segment Interferometry . . . . .	2
1.3. Contents of the Thesis . . . . .	2
<b>2. Review of Fibre Sensing Technology</b>	<b>4</b>
2.1. Basic Aspects of Fibre Sensing . . . . .	4
2.2. Distributed Sensing . . . . .	6
2.3. Fibre Grating Sensors . . . . .	8
2.4. Interferometric Sensors . . . . .	10
2.5. Summary Table . . . . .	14
<b>3. Review of Signal Processing for Single Optical Interferometers</b>	<b>15</b>
3.1. Basic Aspects of Optical Interferometric Signal Processing . . . . .	15
3.1.1. Interferometric Transfer Function . . . . .	15
3.1.2. Modulation Techniques . . . . .	17
3.1.3. Interferometric Configurations . . . . .	18
3.1.4. Quadrature Demodulation in Carrier-Based Processing . . . . .	21
3.2. Review of Non-Carrier-Based Processing . . . . .	24
3.2.1. Passive Homodyne Processing . . . . .	24
3.2.2. Phase Stepping Homodyne Processing . . . . .	25



3.2.3.	Active Homodyne Processing . . . . .	26
3.3.	Review of Single Carrier-Based Processing . . . . .	27
3.3.1.	Heterodyne Processing . . . . .	27
3.3.2.	Single Carrier Homodyne Processing . . . . .	28
3.4.	Review of Dual Carrier-Based Processing . . . . .	32
3.4.1.	Dual Carrier Homodyne Processing . . . . .	33
3.4.2.	Extended Dual Carrier Homodyne Processing . . . . .	34
3.5.	Summary Table . . . . .	35
<b>4.</b>	<b>Review of Configurations and Signal Processing Relevant to Fibre Segment Interferometry</b>	<b>36</b>
4.1.	Basic Aspects in Fibre Segment Interferometry . . . . .	37
4.2.	Fibre Segment Interferometry Based on Time-Division Multiplexing . . . . .	41
4.3.	Fibre Segment Interferometry Based on Code-Division Multiplexing . . . . .	42
4.4.	Fibre Segment Interferometry Based on Optical Illuminating Frequency Modulation . . . . .	45
4.5.	Summary Table . . . . .	49
<b>5.</b>	<b>Code-Division Multiplexing Technique for Fibre Segment Interferometry</b>	<b>50</b>
5.1.	Introduction . . . . .	50
5.2.	Theory . . . . .	51
5.2.1.	Single-Sideband Equations in Prior Work . . . . .	51
5.2.2.	Maximum Length Pseudo-Random Sequences for Code-Division Multiplexing . . . . .	52
5.2.3.	Extended Theory Combining Single-Sideband Processing and Code-Division Multiplexing . . . . .	53
5.3.	Modulation Waveform and Filter Design . . . . .	59
5.3.1.	Modulation Waveform Template Design . . . . .	59
5.3.2.	Filter Design . . . . .	61
5.3.3.	Complete Phase Modulation Waveform . . . . .	65
5.3.4.	Design Parameter Summary . . . . .	68
5.4.	Implementation . . . . .	69
5.4.1.	Optical Setup . . . . .	69
5.4.2.	Signal Generation . . . . .	71
5.4.3.	Measurement Arm Configuration . . . . .	72
5.4.4.	Signal Processing . . . . .	73
5.4.5.	Implementation Parameter Summary . . . . .	75
5.5.	Experiments . . . . .	75
5.5.1.	Single Reflector Measurements . . . . .	76
5.5.2.	Multiple Reflector Measurements . . . . .	87
5.5.3.	FSI Strain Measurements . . . . .	95
5.6.	Discussion and Future Work . . . . .	98
5.6.1.	Discussion and Improvements to Current Work . . . . .	98
5.6.2.	Future Research Directions . . . . .	104
5.7.	Summary . . . . .	107

<b>6. Sinusoidal Frequency Modulation Technique for Fibre Segment Interferometry</b>	<b>108</b>
6.1. Introduction . . . . .	108
6.2. Theory . . . . .	110
6.2.1. Basic Equations . . . . .	110
6.2.2. Demodulation Process . . . . .	115
6.2.3. Spatial Resolution . . . . .	119
6.2.4. Non-Linearity and Crosstalk due to Quantisation Errors . . . . .	120
6.2.5. Correction of Non-Ideal Modulation Characteristics . . . . .	123
6.3. Nested Mach-Zehnder Experiment . . . . .	125
6.3.1. Implementation . . . . .	125
6.3.2. Results for Nested Mach-Zehnder Experiment . . . . .	131
6.4. Single Interferometer Noise Investigation . . . . .	139
6.5. Fibre Segment Interferometry Experiment . . . . .	142
6.5.1. Implementation . . . . .	142
6.5.2. Linearity and Noise Measurements . . . . .	146
6.5.3. Speed-of-Sound Measurements . . . . .	150
6.6. Discussion and Future Work . . . . .	153
6.6.1. Discussion and Improvements to Current Work . . . . .	153
6.6.2. Future Research Directions . . . . .	159
6.7. Summary . . . . .	161
<b>7. Application of the Sinusoidal Frequency Modulation Technique to Multi-Surface Vibrometry</b>	<b>162</b>
7.1. Introduction . . . . .	162
7.2. Setup and Implementation . . . . .	164
7.3. Experimental Results . . . . .	168
7.4. Discussion . . . . .	170
7.5. Summary . . . . .	171
<b>8. Conclusion and Outlook</b>	<b>172</b>
8.1. Conclusion . . . . .	172
8.2. Outlook . . . . .	175
<b>List of Publications and Outcomes</b>	<b>178</b>
<b>Appendix A. Derivation of the Single Sideband Equations</b>	<b>180</b>
A.1. Derivation of Single Sideband Equations in Prior Work . . . . .	180
A.2. Derivation of Extended Single Sideband Equations for Stationary Phase Signals . . . . .	182
<b>Appendix B. Laser Diode Characterisation</b>	<b>184</b>
B.1. Current and Temperature Characteristics . . . . .	184
B.2. Linewidth Measurement . . . . .	186
B.3. Frequency Modulation Characteristics . . . . .	187
B.3.1. Characterisation Methods . . . . .	188
B.3.2. Characterisation Results . . . . .	190

<b>Appendix C. FPGA Based Processing</b>	<b>194</b>
<b>Appendix D. Noise and Crosstalk in the Complex Quadrature Signals</b>	<b>196</b>
D.1. Quadrature Noise . . . . .	196
D.2. Spurious Unwrappings due to Quadrature Noise . . . . .	197
D.3. Crosstalk in the Phase Signals . . . . .	199
<b>Appendix E. Derivation of Equations for Sinusoidal Optical Frequency Modulation</b>	<b>201</b>
<b>Appendix F. Power Calibration for Sinusoidal Optical Frequency Modulation</b>	<b>203</b>
<b>References</b>	<b>222</b>

# List of Figures

1.1. FSI sensing fibre configuration . . . . .	2
2.1. Spatial distribution of fibre sensing regions . . . . .	6
2.2. Distributed fibre sensing techniques . . . . .	7
2.3. Working principle of fibre grating sensors . . . . .	9
2.4. Fabry-Perot sensor concepts . . . . .	11
2.5. Long-gauge length interferometric fibre sensing concepts . . . . .	12
2.6. FSI sensing fibre configuration . . . . .	13
3.1. Transfer function of two-path interferometer . . . . .	16
3.2. Basic interferometric configurations . . . . .	19
3.3. Remote interrogation configurations . . . . .	20
3.4. Single carrier quadrature demodulation process . . . . .	21
3.5. Quadrature signal bandwidth requirements . . . . .	23
3.6. Complex quadrature circle/ellipse . . . . .	24
3.7. Passive homodyne processing . . . . .	25
3.8. Phase stepping homodyne processing . . . . .	26
3.9. Active homodyne processing . . . . .	27
3.10. Free-space heterodyne vibrometer . . . . .	28
3.11. Single-sideband processing . . . . .	29
3.12. Pseudo-heterodyne processing . . . . .	30
3.13. Gated sinusoidal processing . . . . .	31
3.14. Bessel dual carrier processing . . . . .	33
4.1. Basic FSI configurations . . . . .	38
4.2. In-fibre partial reflector concepts . . . . .	40
4.3. Two-pulse TDM FSI technique . . . . .	41
4.4. Digitally enhanced heterodyne technique . . . . .	43
4.5. Digitally enhanced homodyne technique . . . . .	44
4.6. Linear optical frequency modulation multiplexing . . . . .	46
4.7. Gated sinusoidal optical frequency modulation multiplexing . . . . .	48
5.1. Typical signal shapes for the CDM technique . . . . .	54
5.2. Exact Blackman window function . . . . .	60
5.3. Phase modulation waveform template . . . . .	60
5.4. SSB coefficient scaling for phase modulation waveform template . . . . .	61
5.5. Harmonic content expected at digitisation . . . . .	62

5.6.	Digital filter response . . . . .	63
5.7.	Anti-aliasing filter spectrum . . . . .	64
5.8.	Anti-aliasing filter impulse response . . . . .	65
5.9.	SSB coefficient scaling for complete phase modulation function . . . . .	66
5.10.	Spatial dependence of SSB coefficients . . . . .	67
5.11.	Setup for CDM technique . . . . .	69
5.12.	Improvement of signal generation chain output . . . . .	72
5.13.	Signal processing implementation for CDM technique . . . . .	74
5.14.	Measurement arm configuration for single reflector experiment . . . . .	76
5.15.	Quadrature signals for single reflector experiment . . . . .	77
5.16.	Quadrature signal ellipse coefficient ratios . . . . .	78
5.17.	Comparison of measured quadrature signal properties with theory . . . . .	79
5.18.	OPD dependence for single reflector experiment . . . . .	81
5.19.	Power dependence for single reflector experiment . . . . .	83
5.20.	Measurement arm configuration for crosstalk experiment . . . . .	85
5.21.	Fourier spectra of quadrature signal crosstalk . . . . .	86
5.22.	Quadrature signal crosstalk suppression . . . . .	86
5.23.	Measurement arm configuration for multiple reflector experiment . . . . .	88
5.24.	Quadrature signals for multiple reflector experiment . . . . .	89
5.25.	Noise in multiple reflector experiment . . . . .	90
5.26.	Reflector phase signals for multiple reflector experiment . . . . .	92
5.27.	Quadrature signal spectra for multiple reflector experiment . . . . .	93
5.28.	Segment phase signals for multiple reflector experiment . . . . .	94
5.29.	Low-frequency noise suppression in segment phase signals . . . . .	95
5.30.	Measurement arm configuration for FSI strain sensing experiment . . . . .	96
5.31.	FSI strain measurement . . . . .	97
5.32.	FSI tip displacement measurement . . . . .	98
5.33.	Future FSI configurations for CDM technique . . . . .	105
6.1.	Typical signal shapes for the SFM technique . . . . .	111
6.2.	Effect of smooth window function . . . . .	116
6.3.	Baseband suppression plot . . . . .	116
6.4.	Complete demodulation process . . . . .	118
6.5.	Signal suppression for quantised processing . . . . .	121
6.6.	Quantisation model results for two-cycle errors . . . . .	122
6.7.	Setup for nested MZ experiment . . . . .	125
6.8.	Signal processing implementation for SFM technique . . . . .	126
6.9.	Photo detector signal shape and spectrum . . . . .	128
6.10.	Demodulation parameter maps . . . . .	130
6.11.	Quadrature signals for nested MZ experiment . . . . .	132
6.12.	Phase signal time traces for nested MZ experiment . . . . .	134
6.13.	Phase signal spectra for nested MZ experiment . . . . .	134
6.14.	Quadrature and phase signal spectra for nested MZ experiment . . . . .	135
6.15.	Linearity dependence on window width parameter . . . . .	137
6.16.	Detuning test results . . . . .	138
6.17.	Setup for single interferometer noise experiment . . . . .	139

6.18. Power and OPD dependence of noise for a single interferometer . . .	140
6.19. Setup for FSI experiment . . . . .	143
6.20. Photo detector signal for FSI experiment . . . . .	144
6.21. FBG in-fibre partial reflector spectra in FSI experiment . . . . .	145
6.22. Quadrature signals for FSI experiment . . . . .	146
6.23. Wavelength dependence of power and phase noise for FSI experiment	147
6.24. OPD dependence of noise for FSI experiment . . . . .	148
6.25. Power dependence of reflector and segment noise for FSI experiment .	150
6.26. Speed-of-sound measurement results . . . . .	151
6.27. FSI phase signals for fundamental vibration mode . . . . .	152
7.1. Multi-surface vibrometry setup . . . . .	164
7.2. Photo detector signal and range dependency . . . . .	165
7.3. Multi-surface vibrometry dual bounce alignment . . . . .	166
7.4. Picture of experimental arrangement . . . . .	167
7.5. Vibration signatures for three measurement directions . . . . .	169
7.6. Enlarged vibration signatures . . . . .	170
8.1. Illustration of robotic end-effector sensing concept . . . . .	176
8.2. Illustration of future fibre optic shape sensing project . . . . .	177
B.1. Static laser power dependence . . . . .	185
B.2. Static laser emission wavelength dependence . . . . .	185
B.3. Setup for laser linewidth measurement . . . . .	186
B.4. Laser linewidth measurement . . . . .	187
B.5. Setup for frequency modulation parameter measurement . . . . .	188
B.6. Illustration of intensity modulation delay measurement . . . . .	189
B.7. Frequency dependence of frequency modulation parameters . . . . .	190
B.8. Optical spectrum analyser trace . . . . .	191
B.9. Harmonic content of frequency modulation parameters . . . . .	192
B.10. Bias dependency of frequency modulation parameters . . . . .	193
C.1. Illustration of FPGA working principle . . . . .	194
C.2. Picture of FPGA system used . . . . .	195
D.1. Quadrature noise phasor model . . . . .	196
D.2. Spurious phase unwrappings phasor model . . . . .	198
D.3. Crosstalk phasor model . . . . .	199
D.4. Phase signal crosstalk simulation results . . . . .	200
F.1. Setup for effective power calibration measurement . . . . .	203
F.2. Effective power calibration measurement . . . . .	204

# List of Tables

2.1. Comparison of widely-used optical fibre sensing techniques . . . . .	14
3.1. Comparison of single interferometer signal processing techniques . . .	35
4.1. Characteristics of the three FSI configurations of Fig. 4.1 . . . . .	39
4.2. Comparison of range-resolved processing techniques for FSI . . . . .	49
5.1. Design parameters for complete CDM phase modulation function . .	68
5.2. Signal processing parameters for CDM implementation . . . . .	75
6.1. Complex exponential terms occurring in Fig. 6.4 . . . . .	119
8.1. Comparison of key performance parameters . . . . .	173

# List of Acronyms

AC	Alternating current
ADC	Analogue-to-digital converter
AOM	Acousto-optic modulator
BS	Non-polarising beam splitter
CDM	Code-division multiplexing
CDMA	Code-division multiple access
CNR	Carrier-to-noise ratio
CPU	Central processing unit
DAC	Digital-to-analogue converter
DC	Direct current
DCM	Differentiate and cross-multiply algorithm
DFB	Distributed feedback
DPMZ	Dual parallel Mach-Zehnder phase modulator
ECL	External cavity laser
EOM	Electro-optic modulator
FBG	Fibre Bragg grating
FDM	Frequency-division multiplexing
FMCW	Frequency modulated continuous-wave
FPGA	Field programmable gate array
FSI	Fibre segment interferometry
FWHM	Full-width half maximum
LDV	Laser Doppler vibrometry
LIDAR	Light detection and ranging
LO	Local oscillator
LP	Low-pass filter
LPG	Long period grating
LPOL	Linear polariser
MCF	Multi-core fibre
MEMS	Micro-electromechanical system



MLS	Maximum length sequence
MZ	Mach-Zehnder
OCT	Optical coherence tomography
OFDR	Optical frequency domain reflectometry
OIFM	Optical illuminating frequency modulation
OPD	Optical path difference
OTDR	Optical time domain reflectometry
OVC	Outer vacuum chamber
PBS	Polarising beam splitter
PC	Personal computer
PGC	Phase-generated carrier technique
PMDI	Path-matched differential interferometry
PZT	Piezo-electric transducer
RADAR	Radio detection and ranging
RMS	Root mean square
SFM	Sinusoidal optical frequency modulation
SOFO	Surveillance d'ouvrages par fibres optiques (Sec. 2.4)
SSB	Single-sideband signal processing
TDM	Time-division multiplexing
WDM	Wavelength-division multiplexing

# List of Symbols

$A$	Generic sinusoidal amplitude	32, 114
$A_d$	Sinusoidal demodulation carrier amplitude	113
$A_k$	Sinusoidal phase modulation amplitude for $k$ th interferometer	110
$A_{\min}$	Minimum value of sinusoidal amplitude $A$	119
$A_{\text{sig}}$	Sinusoidal phase signal amplitude	22
$a_{1\dots 3}$	Amplitudes of exponential terms in Eq. (3.8)	23
$\alpha_{1\dots 3}$	Phases of exponential terms 1...3 in Eq. (3.8)	23
$b$	Processing bitwidth	120
$B_Q$	Quadrature bandwidth requirement	22, 92, 154
$\beta_n$	Fractional harmonic amplitude of index $n$	124
$c$	Complex SSB carrier coefficient	52, 58
$c_0$	Vacuum speed of light	4
$C$	Complex demodulation carrier function	57, 113
$C_{\text{corr}}$	Corrected complex demodulation carrier function	124
$D$	Duty cycle	41
$d$	CDM decoding function	56
$d_{\text{core}}$	Distance between fibre cores	97
$D_h$	Number of samples in filter impulse response	62
$D_{\text{wf}}$	Number of samples per waveform template	59
$\delta_n$	Phase shift of the $n$ th non-linear frequency modulation harmonic	124
$\Delta\epsilon$	Longitudinal strain change relative to the measurement start time $t_0$	96
$\Delta\varphi$	Interferometric phase change relative to the measurement start time $t_0$	96, 167
$\Delta\eta_{\min}$	Minimum permissible OPD difference	120
$\Delta f_{\text{opt}}$	Optical frequency modulation amplitude	110
$\Delta I_{\text{LD}}$	Laser diode injection current modulation amplitude	126
$\Delta l$	Generic length change or displacement	4, 167
$\Delta l_{\text{tip}}$	Tip displacement relative to the measurement start time $t_0$	97
$\Delta\Phi$	Phase difference between two interferometer arms	16

$E$	Generic complex exponential term	114
$\epsilon$	Longitudinal strain	4, 96
$\eta$	OPD	4, 15, 37
$\eta_k$	OPD of $k$ th interferometer	110
$f_c$	Heterodyne carrier frequency	17, 27
$f_{\text{code}}$	Repetition frequency of whole CDM code	55
$f_{i,\text{pk}}$	Peak instantaneous frequency	22
$f_m$	Modulation frequency	29, 51, 110
$f_{\text{opt}}$	Optical frequency	41, 110
$f_{\text{opt},c}$	Optical centre frequency	110
$f_{Q,\text{co}}$	Quadrature signal cut-off frequency	21, 52, 58, 114
$f_{Q,\text{co},\text{max}}$	Maximally permitted value for $f_{Q,\text{co}}$	58, 114
$f_s$	Digital sample frequency	64, 71, 99, 126
$f_{\text{sig}}$	Sinusoidal phase signal frequency	22
$f_{\text{wf}}$	Repetition frequency of waveform template	55
$G_h$	Filter impulse response normalisation factor	63
$G_{\text{wf}}$	Waveform template normalisation factor	60
$ \gamma(\tau) $	Absolute value of degree of coherence	16
$h_{\text{anag}}$	Impulse response of analogue filter	56
$h_{\text{comb}}$	Impulse response of combined filter	56
$h_{\text{dig}}$	Impulse response of digital filter	56, 63
$h_{\text{sg}}$	Impulse response of signal generation chain	71
$H_{\text{sg}}$	Fourier transform of $h_{\text{sg}}$	72
$I$	Intensity modulation function	124
$i$	Generic positive integer index	52, 59, 62
$I_{\text{LD}}$	Laser diode bias injection current	126
$J_n$	Bessel function of first kind of index $n$	32
$k$	Index of constituent interferometer	55, 110
$k_{\text{max}}$	Total number of constituent interferometers	55, 110
$\kappa$	Fibre strain sensitivity factor	96
$l_b$	Base length unit	46
$l_g$	Sensor gauge length	4
$l_{\text{off}}$	Offset length in Fig. 4.1	38
$l_s$	Fibre segment length	73, 99, 120
$\lambda_0$	Vacuum wavelength of light	4
$m$	Generic integer index	16, 59

$N$	Maximally possible number of sensors	41
$n$	Integer harmonic index	29, 52, 57, 124
$n_g$	Group index of refraction	4
$o$	Multiple reflection order	39
$P_1$	Power of first interferometric arm	16
$P_2$	Power of second interferometric arm	16
$P_{\text{eff}}$	Effective interferometric power	17, 39
$P_{\text{eff},k}$	Effective interferometric power of $k$ th interferometer	55, 112
$P_{\text{in}}$	Input power	39
$P_{\text{max}}$	Maximum observable power	16
$P_{\text{min}}$	Minimum observable power	16
$P_{\text{off}}$	Stationary offset power	17
$\varphi$	Interferometric phase signal	17
$\varphi_k$	Interferometric phase signal for $k$ th interferometer	57, 112
$\varphi_r$	Residual phase signal	133
$\Phi_1$	Phase of first interferometric arm	16
$\Phi_2$	Phase of second interferometric arm	16
$q_{1...3}$	Coefficients of exact Blackman window	59
$R$	Photo detector responsivity	16
$r$	Reflectivity	39, 145
$\square$	Rectangular gating/window function	115
$\rho$	Generic scale factor	99, 102
$s$	Phase modulation waveform scale factor	29, 51, 55
$S_{\text{bb}}$	Baseband suppression ratio	115
$S_{\text{bb,accept}}$	Maximum acceptable baseband suppression ratio	119
$S_{\text{cr}}$	Crosstalk suppression ratio	58, 119
$S_{\text{cr,bp-bp}}$	$S_{\text{cr}}$ for bipolar-bipolar MLS coding	53, 87
$S_{\text{cr,up-bp}}$	$S_{\text{cr}}$ for unipolar-bipolar MLS coding	53, 87
$S_{\text{sb}}$	Sideband suppression ratio	52, 58, 122
$\sigma$	Gaussian window width parameter	113
$\sigma_{\text{amp}}$	Standard deviation of amplitude noise	89
$\sigma_{\text{amp,norm}}$	$\sigma_{\text{amp}}$ normalised by mean quadrature amplitude	82
$\sigma_{\text{phase}}$	Standard deviation of apparent phase noise	82
$\sigma_{\text{phase,direct}}$	Standard deviation of direct phase noise corrected for quadrature noise	82
$T$	Temperature	4
$T_{\text{LD}}$	Laser Diode Temperature	147
$t_0$	Measurement start time	96
$t'$	Time variable compensated for $\tau_{\text{sp}}$	112
$T_{\text{code}}$	Duration of whole CDM code	55, 71

$T_g$	Gating duration	48
$T_{\text{grace}}$	CDM code symbol transition grace period	57
$T_h$	Anti-aliasing filter impulse response duration	56
$T_m$	Modulation period	52, 113
$T_s$	Sampling period	71
$T_{\text{symb}}$	CDM code symbol duration	55
$T_{\text{wf}}$	Waveform template duration	55
$\tau$	Generic delay	4, 15
$\tau_{\text{comp}}$	Compensating interferometer delay	104
$\tau_d$	Decoding/demodulation delay	56, 113
$\tau_I$	Intensity to optical frequency modulation delay	124
$\tau_k$	Time-of-flight delay of $k$ th interferometer	55, 110
$\tau_{\text{sp}}$	Signal processing delay	112, 129
$\theta$	Phase modulation function	17
$\theta_k$	Phase modulation function of $k$ th interferometer	110
$\theta_{k,\text{ext}}$	Non-linear extension of $\theta_k$	124
$\hat{\theta}$	Normalised phase modulation function	29, 51, 55
$\tilde{\theta}_{\text{wf}}$	Normalised phase modulation waveform template	60
$U_{\text{aa}}$	Anti-aliased filtered signal	56
$U_{\text{dec}}$	Signal following CDM decoding	57
$U_{\text{dem}}$	Demodulated signal	114
$U_{\text{dem,corr}}$	Corrected demodulated signal	125
$U_{\text{pd}}$	Photo detector signal	15, 17, 51, 55, 112, 124
$U_Q$	Complex quadrature signal	22, 52, 58, 114
$U_{Q,\text{corr}}$	Corrected complex quadrature signal	125
$V$	Interferometric visibility	16
$v_s$	Speed-of-sound	150
$W$	Dual Gaussian window function	113
$W_{\text{B,h}}$	Exact Blackman window function for filter	62
$W_{\text{B,wf}}$	Exact Blackman window function for waveform template	59
$X$	Generic measurand in Eq. (2.1)	4
$x$	Waveform templates per CDM code symbol	55, 65
$\xi$	Relative amplitude of intensity modulation	124
$Y$	Generic variable for least square fit	81
$Y_{0\dots 2}$	Coefficient for least square fit	82
$y$	MLS code sequence length	52, 65

# 1. Introduction

## 1.1. Range-Resolved Optical Interferometric Signal Processing

In many applications of optical interferometry, range-resolved signal processing is very desirable [1] as it allows the influence of spurious reflections to be suppressed, if these occur at different ranges to the desired signals, or permits multiple interferometers at different ranges to be multiplexed. Range-resolved optical interferometric signal processing techniques can identify and evaluate otherwise identical signal sources solely based on their range, using only a single laser source and a single photo detector. For range-resolved optical interferometric signal processing, two functions have to be performed simultaneously: interferometric signal processing to determine the interferometric phase signals and range-based demodulation to allow multiple interferometric signals to be separated. For the former, a wide variety of techniques have been developed over the long history of interferometry, with the most relevant techniques reviewed in Chap. 3. The physical principle exploited for the second function, range-based signal identification, is the time-of-flight of the interrogating light, with relevant techniques reviewed in Chap. 4.

The conceptually simplest and most widely used range-based signal identification technique is time-division multiplexing (TDM), where the different arrival times following pulsed interrogation are evaluated to allow the range of the signal sources to be identified. A further technique to separate signal sources based on their time-of-flight involves code-division multiplexing (CDM), where continuous-wave laser light is modulated by a code that helps to uniquely identify the delay of the signals. In this thesis, a novel technique using a CDM approach is proposed in Chap. 5. Here, in contrast to prior work, a single, regular electro-optic phase modulator is employed to both perform interferometric signal processing as well as to introduce the code for range-based signal separation. Another possibility for range-resolved signal processing is the evaluation of the induced phase modulation waveform that results from optical frequency modulation of the light illuminating an interferometer of non-zero optical path difference (OPD). Here, the different phase modulation waveforms in interferometers with differing OPDs can be used as range-dependent carriers to both allow interferometric phase evaluation and range-based signal identification. A novel technique based on this approach is presented in Chap. 6, which, using only the sinusoidal optical frequency modulation (SFM) available from injection current modulation of a regular diode laser, allows highly linear interferometric phase measurements of multiple, comparatively closely spaced signal sources.

## 1.2. Fibre Segment Interferometry

This PhD project initially set out to explore range-resolved signal processing techniques for range-based signal separation in Doppler lidar anemometry [2–9]. However, in the early stages of this project, in order to avoid the difficulty of the low return signal powers typical for anemometry, the developed techniques were tested in an optical fibre-based setup. Taking up an idea first proposed by Dakin *et al.* [10], the PhD project then developed into an application of these techniques to fibre segment interferometry (FSI), now forming the main theme of the thesis.

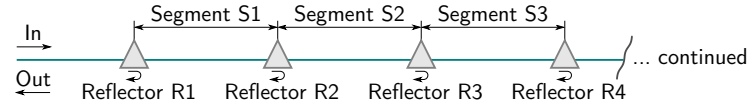


**Figure 1.1.:** Illustration of the basic principle of FSI.

In FSI, as illustrated in Fig. 1.1, optical fibre segments are formed between in-fibre partial reflectors and are interrogated in a low-finesse Fabry-Perot setup, where two-path interference is assumed. Phase measurements from each segment are then obtained by subtraction of the reflector signals, resulting in an array of long-gauge length interferometric sensors that integrate any OPD-induced phase changes due to strain, temperature, etc. over their gauge length. While, in prior work, this approach was mainly aimed at high-fidelity optical hydrophone applications [10–12] using low-noise solid state lasers, the FSI techniques proposed in this thesis are targeted at strain sensing in areas such as structural health monitoring [13–15]. Therefore, noise performance expectations are reduced in order to enable a simpler, more cost-effective and robust system implementation. In particular, all the work in this thesis has been performed using the same £1k single-mode laser diode and one objective of this work is to demonstrate the levels of performance achievable using such a device. In general, compared to widely used fibre-based sensors in structural health monitoring, such as fibre Bragg gratings (FBG), in FSI the measurand is integrated over the whole segment length. It was recognised before [16] that the inherent averaging of strain data in long-gauge length sensing can also be beneficial to make measurement interpretation for large engineering structures more robust, reducing the effect of local inhomogeneities. Also, compared to localised sensors such as FBGs, the FSI approach allows spatially continuous sensing of the measurand without sensing gaps and thus guarantees that no disturbance is missed. Therefore, the FSI approach also offers complementary information that is not easily available with other fibre sensing techniques.

## 1.3. Contents of the Thesis

This thesis starts with a detailed review of the concepts and prior work in the relevant areas because a thorough understanding of this is considered a prerequisite for the later work in the thesis. This is split into three chapters, Chaps. 2, 3 and 4, where the first section in each chapter introduces the basic concepts that are relevant for the subject area. These initial sections are written in a text-book style with fewer references, whilst a detailed review of published prior work is then presented in the subsequent sections of each chapter. This stylistic choice to first treat the key

concepts in an abstract way was made to avoid duplication in the explanation of these concepts, also with regard to the later experimental chapters, which show much commonality in their fundamental aspects and often reference back to these initial sections of the review chapters.

Following the three review chapters, there are the two main experimental chapters, Chaps. 5 and 6, which each discuss one of the two signal processing techniques proposed in this work, both theoretically and experimentally. It was aimed to keep the theoretical description, the characterisation measurements and evaluation criteria of the two techniques as uniform as possible in order to allow their direct comparison. A thorough discussion of ideas to improve the current implementation and of future research directions, along with a brief chapter summary, then concludes each main experimental chapter. In addition to the two main experimental chapters that ultimately demonstrate the application of the proposed techniques to FSI, Chap. 7 is an additional, brief experimental chapter that showcases the application of the range-resolved signal processing technique proposed in Chap. 6 to multi-surface free-space vibration measurements. Finally, a conclusion of the work in this thesis and a general outlook involving both proposed techniques is given in Chap. 8. Additionally, appendix sections are used to expand the theoretical derivations, introduce the signal processing hardware, develop a noise and crosstalk model and detail the characterisation measurements for the laser diode used.

In this thesis the individual chapters cover the following areas:

Chapter 2 reviews optical fibre sensing technology, with a particular view to providing context for the FSI sensing approach that forms the main theme of this thesis.

Chapter 3 details the relevant interferometric theory, basic interferometric configurations and concepts before reviewing the wide field of interferometric signal processing techniques that can be used to extract phase information in a single, two-path interferometer using quasi-monochromatic light.

Chapter 4 discusses basic FSI configurations and design aspects before reviewing prior work in range-resolved signal processing techniques that either have already been applied to FSI or that are in principle capable of being applied to FSI.

Chapter 5 presents the CDM signal processing technique that is the first novel approach proposed in this thesis. Here, the detailed theory is developed, the signal processing implementation is described and a variety of characterisation experiments as well as an application to FSI are shown and discussed.

Chapter 6 then presents the SFM technique that is the second novel approach proposed. Again, a detailed theoretical description is developed, the signal processing implementation is explained and a variety of characterisation experiments as well as an application to FSI are shown and discussed.

Chapter 7 additionally highlights the potential of the SFM technique of Chap. 6 outside FSI. Here, the approach is applied to multi-surface vibrometry as part of an industrial measurement on a commercial cryostat system.

Chapter 8 concludes this thesis by summarising the results and providing an outlook into the most promising future applications for the proposed techniques.



## 2. Review of Fibre Sensing Technology

This chapter gives a short introduction to the most widely-used optical fibre sensing technologies, mainly in regard to longitudinal strain measurements, in order to relate their capabilities to the fibre segment interferometry (FSI) approach investigated in this thesis. Further detailed reviews of optical interferometric signal processing in general, and range-resolved optical interferometric signal processing techniques relevant to FSI in particular, are then presented in Chaps. 3 and 4, respectively.

### 2.1. Basic Aspects of Fibre Sensing

**Measurands:** Both temperature,  $T$ , and longitudinal strain,  $\epsilon = \Delta l/l_g$ , i.e. length change  $\Delta l$  over the gauge length  $l_g$ , are intrinsic measurands that directly affect an optical fibre [17, 18]. For sensors that are based on interference effects within the core of single-mode fibres such as fibre Bragg gratings (FBGs) (further discussed in Sec. 2.3) or interferometric sensors (further discussed in Sec. 2.4), the sensitivity to any of these stimuli is proportional to the change in  $\eta$ , the optical path difference (OPD).  $\eta$  is given by  $\eta = \tau c_0$ , where  $\tau$  is the time-of-flight delay and  $c_0$  is the vacuum speed of light. Over the sensing region, the time-of-flight  $\tau$  and therefore the OPD  $\eta$  is proportional to both the sensor gauge length  $l_g$  and the local group refractive index  $n_g$  of the fibre core. Thus changes in OPD can occur due to two independent effects: the change in  $l_g$  of the fibre itself and any change in  $n_g$  due to the measurand. Neglecting polarisation dependence, this is given by Jackson *et al.* [19] for measurands  $X$ , such as  $T$  or  $\epsilon$ , with the vacuum light wavelength  $\lambda_0$ , as:

$$\frac{\partial \eta}{\partial X} = \frac{2\pi}{\lambda_0} \left( n_g \frac{\partial l_g}{\partial X} + l_g \frac{\partial n_g}{\partial X} \right) \quad \text{with } X = T, \epsilon, \text{ etc.} \quad (2.1)$$

When several stimuli change simultaneously, changes in the OPD add independently in the first order approximation, but may contain cross-sensitivities at higher orders [20]. Because changes in the OPD originating from temperature or longitudinal strain are cumulative, these cannot be easily distinguished when they occur together, which is often the case. There have been manifold approaches, reviewed by Jones [21], aimed at discriminating temperature and longitudinal strain measurements. This discrimination is of prime importance [22] in many practical applications for strain sensing because the temperature sensitivity is comparatively large relative to typical

longitudinal strain sensitivity requirements. Common approaches, applicable to both FBGs and interferometric sensors, include using two sensors with one sensor isolated from strain [23] or the use of different types of fibres [24]. Also, two interrogation wavelengths [25] on one sensor can be used, exploiting small wavelength-dependent differences in the thermo-optic component of the index of refraction. Another intrinsic direct fibre measurand is bend (curvature) sensing. Most bend sensing techniques evaluate differential longitudinal strain between different fibres in a laterally offset fibre arrangement or a multi-core fibre (MCF) using interferometric [26] or FBG sensors [27], or between the core and the cladding of an optical fibre itself using long-period gratings (LPG) [28, 29] (see also Sec. 2.3).

The reaction of the fibre to the measurand can also be increased using an external transducer. The transduction mechanism is ideally highly sensitive to the desired measurand and converts an external stimulus into an intermediate quantity, usually longitudinal strain, which can then be detected by the optical fibre with high sensitivity. A typical intrinsic transduction mechanism, where the light does not leave the fibre, could simply be a compliant mandrel with fibre wrapped around a coil. Pressure transducers of this kind are extensively used for fibre optic hydrophones and are reviewed by Kirkendall *et al.* [30]. Further measurands where external transducers can be used beneficially include magnetostrictive transducers [31] in magnetic field measurements or piezoelectric transducers [31] for electric field measurements. Additionally, many different kinds of extrinsic sensing transducers, where the light exits the fibre over a, usually short, distance are in use, often in Fabry-Perot interferometric configurations, further reviewed in Sec. 2.4. In general, because any transduction mechanism introduces its own characteristics, additional uncertainties that require calibration and cross-sensitivities to other measurands may occur. In some cases, fibre-coupled measurement configurations in areas such as anemometry [2, 5, 8, 9] or vibrometry [32–37] are also regarded as extrinsic fibre sensing techniques.

**Optical Fibre Types:** The bulk of optical fibre sensing technology, including this thesis, makes use of the superior qualities offered by silica-based single-mode optical fibres. The fact that, neglecting degeneracy due to birefringence, only a single mode can propagate within the fibre is a prerequisite for many types of sensors that rely on interference effects, including most grating (see Sec. 2.3) or interferometric sensors (see Sec. 2.4). Further advantages of these fibres include low-loss guiding, with typical losses in their optimal transmission wavelength as low as  $0.2 \text{ dB} \cdot \text{km}^{-1}$  [38], well-characterized material properties and the availability of cost-effective fibre and components, particularly when sensing is performed in wavelength regions also used by the telecoms industry. In some specific applications, however, silica-based multimode optical fibres can also be used advantageously for sensing. These include some distributed sensing techniques or certain kinds of interferometric sensors that make use of the interference between the different modes within a multimode fibre [39]. Furthermore, silica-based, multi-core, single-mode fibres can be used for differential measurements [26], such as for fibre optic bend sensing as discussed above.

Polymer optical fibres, also reviewed by Peters [38], have also recently become a widely researched topic. While most polymer optical fibres are multimode, single-mode fibres and even grating sensors such as FBGs [40, 41] have all been demonstrated

using polymer fibres. The main advantages of polymer optical fibre sensors are their biocompatibility and their much increased values for the maximum breaking strain when compared to silica fibres, allowing them to be embedded in applications such as soil monitoring [42], where silica-based fibres risk breakage. Their main disadvantages compared to silica-based fibres include lower operating temperatures, incompatibility with established fibre handling technology and much increased optical losses, with losses typically well above  $30 \text{ dB} \cdot \text{km}^{-1}$  [38].

**Spatial Distribution of Multiple Measurements:** In optical fibre sensing with multiple sensors, the spatial distribution of sensing regions can be distinguished between multiplexed point sensors, quasi-distributed point sensors, quasi-distributed long-gauge length sensors and fully distributed sensing as illustrated in Fig. 2.1.

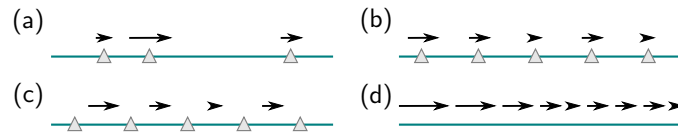


**Figure 2.1.:** The spatial distribution of the active sensing regions for (a) point sensing, (b) quasi-distributed point sensing, (c) quasi-distributed long-gauge length sensing and (d) distributed sensing, with the measurand magnitude indicated by arrows and triangles marking reflective nodes.

In Fig. 2.1(a), for measurements using point sensors, the measurand field is interrogated using discrete point sensors, such as grating-based FBG sensors or interferometric Fabry-Perot sensors, further discussed in Sec. 2.3 and Sec. 2.4, respectively. In this case, it is assumed that the measurand field is of interest only at the point sensor locations. In contrast, in quasi-distributed point sensing, further discussed in Sec. 2.3, the whole measurand field is of interest and this field is sampled using an array of regularly placed point sensors, typically FBG sensors, which is depicted in Fig. 2.1(b). Analogous to the Nyquist sampling theorem, in order to give a complete representation of the measurand field, the spacing of the point sensors has to be sufficiently close. Quasi-distributed long-gauge length sensing, illustrated in Fig. 2.1 (c), also attempts to measure the complete measurand field. However, unlike quasi-distributed point sensing, the integrated measurand field between the regularly distributed nodes is measured using, for example, long-gauge length interferometric sensors, further discussed in Sec. 2.4. The discrete nodes thus only serve to define the sensing region and are not used for sensing the measurand themselves. In distributed sensing, further discussed in Sec. 2.2 and depicted in Fig. 2.1(d), the interrogation system allows this measurand field to be determined continuously at a given spatial resolution over the whole length of an unmodified optical fibre.

## 2.2. Distributed Sensing

In distributed sensing the measurand field is mapped continuously over the whole length of an unmodified optical fibre section. The interrogation unit thus has to perform two functions simultaneously: the actual measurements of the quantity of interest and the range-resolved recording of these measurements based on the

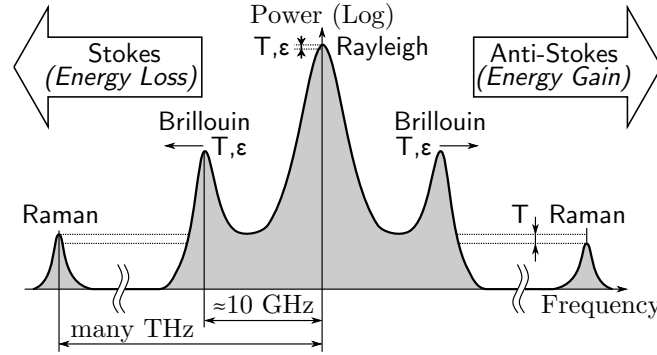


**Figure 2.2.:** Illustration of typical peak powers and frequency shifts for Rayleigh, Brillouin and Raman scattering peaks in silica fibre and their dependence on temperature  $T$  and longitudinal strain  $\epsilon$  (adapted from Güemes *et al.* [45]).

time-of-flight of the return signal. Most distributed systems obtain their range information using pulsed optical time domain reflectometry (OTDR) [43], although in some applications optical frequency domain reflectometry (OFDR) [44], with its higher spatial resolution can be of advantage. The physical origins of the return signal are typically scattering phenomena, such as Rayleigh, Raman or Brillouin scattering. Fig. 2.2 illustrates typical peaks originating from the different scattering phenomena, which will be discussed in more detail in the following.

**Rayleigh Scattering:** The origin of Rayleigh scattering are microscopic irregularities in the refractive index of the fibre core and, as can be seen in Fig. 2.2, it has zero offset frequency shift and a comparatively high scattering cross-section, making it the easiest scattering process to detect. The first distributed fibre sensing technique that utilised Rayleigh scattering has been polarisation-resolved OTDR [46], exploiting the changes in fibre birefringence evident in the Rayleigh backscatter trace to determine a multitude of measurands such as temperature, strain, pressure, etc. More recently, using polarisation-resolved OFDR, spatial resolutions in the tens of  $\mu\text{m}$  can be reached [47]. The changes in Rayleigh scattering cross-section caused by temperature have also been used for distributed temperature change measurements, however, with the effect being relatively small in regular glass fibres, liquid core [48] or rare-earth doped [49] fibres needed to be used. Because polymer optical fibres show a dependence of the Rayleigh scattering cross-section on longitudinal strain, the distributed backscattering loss can also be exploited for strain sensing [42] there.

Recently, distributed acoustic sensing [50] has gained popularity [51] for the cost-effective sensing of sound along the fibre for seismic, flow measurement or security monitoring purposes. State-of-the-art systems allow vibration measurements over up to 50 km of fibre at a sub-metre spatial resolution [51]. Also, fibre learning techniques, where changes in the Rayleigh backscatter trace, obtained by high-spatial resolution reflectometry in before/after measurements, are used for strain and temperature measurements, have been demonstrated [52]. In summary, as evident from the works previously cited, Rayleigh scattering measurements are mostly useful for determining changes of measurands over spatial resolutions on the order of metres.

**Raman Scattering:** Spontaneous Raman scattering is the interaction of the illuminating light with molecular vibration modes in the silica core of the fibre. The

interaction can cause the scattered photon to lose energy (Stokes process) or gain energy (Anti-Stokes process), where especially the latter process is highly dependent on the temperature. Extracting the ratio of these peaks allows absolute temperature measurements to be computed, as illustrated in Fig. 2.2. Distributed temperature sensing based on spontaneous Raman scattering was first proposed by Dakin *et al.* [53] and has since enjoyed large popularity [54, 55].

A key advantage of Raman based distributed sensing is its exclusive sensitivity to temperature, avoiding all cross-sensitivity issues with other measurands. Because the Raman signal is very weak, multi-mode fibres are often used due to their higher backscatter cross-section, although single-mode fibres have advantages for long ranges due to their lower attenuation. A typical Raman distributed temperature system obtains its range resolution using pulsed OTDR and acquisition times of recent devices are on the order of 10 s for a sub-metre spatial and a 0.1 K temperature resolution over a range of 1 km [55]. Because of this performance Raman distributed sensing is widely-used in the oil and gas industries for downhole applications, but also in the electrical transmission industry for power line monitoring [55].

**Brillouin Scattering:** Distributed sensing using Brillouin scattering [56, 57], recently reviewed by Thévenaz [58] and Bao *et al.* [59], exploits acoustic interactions within the fibre. Unlike Rayleigh and Raman techniques, Brillouin scattering methods are not intensity-based but instead measure frequency shifts, giving immunity to uncontrollable changes in the loss profile of the fibre. As illustrated in Fig. 2.2, the Brillouin frequency shift is dependent on both temperature and longitudinal strain, preventing straightforward independent measurement of either quantity.

The acoustic interaction can be actively induced through a pump pulse in stimulated Brillouin scattering [56, 57], requiring access to both sides of the fibre but yielding stronger signal levels, or it can be passively read out by registering the backscatter trace due to spontaneous Brillouin sensing [60] from a single pulse, requiring access to only one fibre end but resulting in lower signal levels. Most Brillouin scattering systems employ one or more fibre amplifiers for high pulse energies and require high-performance signal processing hardware [58]. Sophisticated stimulated Brillouin systems can obtain performance parameters [59] of 100 km sensing length with 2 m spatial resolution, temperature resolutions of 1.5 °C and/or a longitudinal strain resolutions of 30  $\mu\epsilon$  [59, 61] and typical acquisition times of seconds [62].

## 2.3. Fibre Grating Sensors

**Fibre Bragg Grating (FBG) Sensors:** The origin of fibre grating sensors development lies in the discovery of the photosensitivity [63] of germanium-doped optical fibre and the subsequent exploitation of this phenomenon to write FBGs [64] for telecommunication and sensing applications, where FBGs have since gained large popularity [65]. The working principle of FBGs is illustrated in Fig. 2.3(a), where a resonance condition exists when wavefronts back-reflected from each consecutive index modulation node within the fibre core overlap coherently. This occurs when the spatial period of the back-reflecting nodes is half that of the optical wavelength

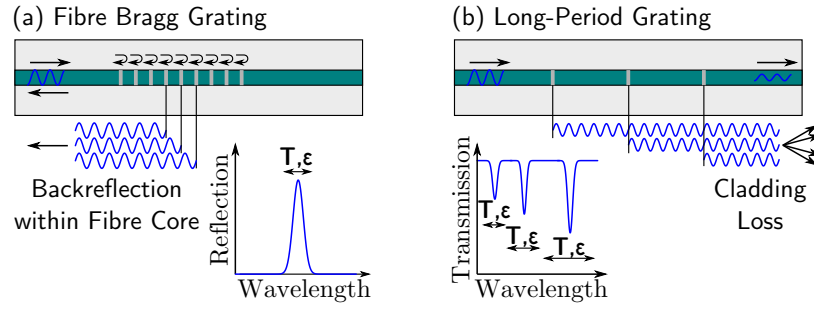


**Figure 2.3.:** Illustration of the resonance conditions of fibre Bragg gratings (a) and long-period gratings (b) as well as the typical shape of a corresponding reflection (a) or transmission (b) spectrum with dependence on temperature  $T$  and longitudinal strain  $\epsilon$ .

in the fibre core medium. The resulting peak in the reflection spectrum of an FBG is then subject to changes in its spectral position in response to the OPD change induced by measurands such as temperature or longitudinal strain (see also Sec. 2.1), and where typical FBG sensor gauge lengths are on the order of 5 to 10 mm [66].

In most cases, FBGs are interrogated using wavelength-based interrogation, measuring the spectral position of the FBG peak using a wavelength-tunable laser or a broadband source in conjunction with a wavelength-tunable filter or spectrometer. An advantage of using wavelength-based interrogation is the polarisation insensitivity, and, because only the position of the peak is the registered quantity, immunity to power variations [65]. Intrinsic wavelength sensitivities of FBGs are on the order of  $1 \text{ pm}/\mu\epsilon$  for longitudinal strain and  $10 \text{ pm}/\text{K}$  for temperature (at  $\lambda_0 = 1.3 \mu\text{m}$ ) [67]. Using typical wavelength-based interrogation systems, absolute static strain resolutions on the order of  $1 \mu\epsilon$  or, equivalently, temperature resolutions  $0.1^\circ\text{C}$  can be achieved with dynamic strain resolutions down to  $5 \text{ n}\epsilon \cdot \text{Hz}^{-0.5}$  and update rates in the kHz range [15, 65]. Alternatively, interferometric interrogation of FBGs can be employed to obtain higher dynamic resolutions [68], however, in this case only relative signal changes can be measured and polarisation sensitivity exists.

A major advantage of FBG-based sensing is the ability to serially multiplex FBG point sensors (see also Fig. 2.1(a)) along one fibre in a simple fashion using wavelength-division multiplexing (WDM) [67], with each FBG written at a different centre wavelength, allowing typically up to 30 FBGs to be multiplexed, depending on the required dynamic range [69]. As previously discussed in Sec. 2.1, FBGs are sensitive to both temperature and longitudinal strain and temperature-strain discrimination techniques may need to be employed. Furthermore the use of FBGs to measure other measurands, such as pressure sensing [70] using appropriate external transduction mechanisms (see also Sec. 2.1), has also been explored.

**Quasi-Distributed Point Sensing using Fibre Bragg Gratings:** As described above, the number of FBGs that can be multiplexed using WDM is limited. Thus, in order to implement large quasi-distributed point sensing arrays, as illustrated in Fig. 2.1(b), low-reflectivity, equidistantly-placed FBGs have to be evaluated at the same nominal wavelength using range-resolved interrogation techniques. Such systems have been implemented using OTDR [71] and OFDR [72], where the latter approach offers higher spatial resolution and faster scanning speeds [73]. Up to 3000 FBGs placed 1 cm apart, over an acquisition time of 15 s, have been multiplexed

using an OFDR technique [74] and efficient mass-production of FBGs using draw tower gratings [75] with the same illumination phase mask is possible.

An area where quasi-distributed point sensing using FBGs can be used beneficially is fibre optic bend sensing (see also Sec. 2.1) in a multi-core fibre [76, 77]. Here, the interrogation of a large number of sensors, with sensor spacing in the cm range, permitted by OFDR techniques [72, 74], as mentioned above, allows the shape of an optical fibre to be followed through space with high spatial resolution. However, problems with the use of a large number of FBGs at the same nominal wavelength include spectral shadowing and multi-path interference effects as investigated in detail by Yüksel *et al.* [73].

**Long Period Gratings:** Originally developed for telecommunication applications, LPGs have also been widely used for sensing purposes [78, 79]. LPGs have periodic index perturbations at a spatial period much wider than the optical wavelength, typically 0.1 to 1 mm at typical gauge lengths of  $l_g \approx 30$  mm [79]. Unlike FBGs, where back-reflected light is in resonance, the resonance condition in LPGs is between forward-propagating modes in the fibre core and those coupled into the cladding by the regular index perturbations of the LPG, as illustrated in Fig. 2.3(b). Due to the lossy nature of cladding modes, a dip in the transmission spectrum will occur for each of the several cladding modes that can be resonant, each with distinct sensitivities, as shown in the spectrum in Fig. 2.3(b). Intrinsic wavelength sensitivities of LPGs can reach up to 100 pm/K and 2 pm/ $\mu\epsilon$ , which is higher than those of FBGs [79].

A considerable advantage of LPGs is that their properties and sensitivities can be very well tailored to specific requirements [80]. Also, compared to most other types of fibre sensors, in LPGs the presence of multiple attenuation bands can be used for single parameter sensing, i.e. exclusively sensing temperature or longitudinal strain, with a single sensor [80]. Further applications of LPGs include bend sensing, where LPGs can show very high curvature sensitivities and allow directional curvature measurements when written in non-radially symmetric fibres [81, 82]. Another wide application field for LPGs is refractive index sensing, exploiting the sensitivity of LPGs to the refractive index of the medium surrounding the cladding. With appropriate coatings, this allows many kinds of chemical and environmental sensing applications to be performed [83]. Disadvantages of LPGs are the need for them to be desensitised in some applications to reduce the impact of the surrounding medium on the measurement [79] and their limited multiplexing capability [84].

## 2.4. Interferometric Sensors

**Short-Gauge Length Interferometric Sensors:** Short-gauge length interferometric sensors are also widely referred to as Fabry-Perot sensors. Here the interference between the signals from two reflective surfaces is evaluated to measure the OPD between the surfaces. The corresponding sensor gauge length is typically very small, well below 1 mm in most cases cited here, making Fabry-Perot sensors a close approximation to true point sensors. For low reflectivities of the constituent surfaces, a two-path interference transfer function (further discussed in Sec. 3.1.1) can be

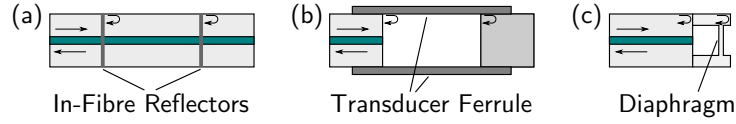


**Figure 2.4.:** Illustration of (a) intrinsic Fabry-Perot sensor, (b) extrinsic transducer Fabry-Perot sensor (both (a) and (b) adapted from Grattan *et al.* [54]) and (c) extrinsic Fabry-Perot diaphragm pressure sensor by Cibula *et al.* [90].

assumed, otherwise multi-path interference effects occur [85] that alter the transfer function. Fabry-Perot sensors can be interrogated at one wavelength using simple fringe-counting for relative measurements without information about the sign of the phase changes. Often, however, they are interrogated spectrally over a wide wavelength range to obtain absolute measurements of the OPD in the sensor [54, 86]. Also, time-domain low-coherence interrogation with a moveable reference arm can be used [87] for absolute measurements. Using spectral interrogation and statistical estimation techniques [88, 89], resolutions below 1 ppm can be achieved, equalling a displacement resolution of 100 pm over a typical dynamic range of 100  $\mu\text{m}$ .

Fig. 2.4 shows typical examples of Fabry-Perot sensors [54], where in Fig. 2.4(a) a generic intrinsic Fabry-Perot sensor [91] is drawn that consists of two semi-transparent in-fibre reflectors. In an extrinsic Fabry-Perot sensor [92], such as the one shown in Fig. 2.4(b), the air-to-glass end-face reflections of the interrogation fibre and a further place-holder fibre on the right define the air-filled sensing cavity. Here, the ferrule acts as a transducer determining the sensitivity to the desired measurand. Fig. 2.4(c) shows a recent design for an extrinsic Fabry-Perot diaphragm pressure sensor [90], with the reflective diaphragm produced from the optical fibre tip by an etching process. A drawback of Fabry-Perot sensors is the difficulty in multiplexing sensors [93]. In the approach by Wang *et al.* [94] several intrinsic Fabry-Perot sensors have been multiplexed using low-reflectivity broadband FBGs acting as in-fibre partial reflectors, which, however, results in different gauge lengths for each sensor.

**Long-Gauge Length Interferometric Sensors:** The principle difference between long-gauge length interferometric sensors, with gauge lengths well above 1 mm, sometimes up to hundreds of meters, and Fabry-Perot sensors discussed above lies in the interferometric signal processing techniques that can be used. Here, signal processing techniques appropriate for long-gauge length interferometric fibre sensors are also discussed in detail in Chap. 3. Some of the earliest long-gauge length interferometric fibre sensors were used as fibre-optic hydrophones [95] or for longitudinal strain or temperature sensing [17, 18] (see also Sec. 2.1). These were basically fibre-based implementations of well-known interferometric configurations. An example of a fibre-based Mach-Zehnder hydrophone or longitudinal strain sensor is shown in Fig. 2.5(a). Using high-performance interferometric signal processing (see Chap. 3) very high phase sensitivities below  $1 \mu\text{rad} \cdot \text{Hz}^{-0.5}$  [96] can be achieved with long-gauge length interferometric sensors, where  $1 \mu\text{rad} \cdot \text{Hz}^{-0.5}$  equates to a longitudinal strain resolution of  $100 \text{ f}\epsilon \cdot \text{Hz}^{-0.5}$  for a gauge length of  $l_g = 1 \text{ m}$  and  $10 \text{ f}\epsilon \cdot \text{Hz}^{-0.5}$  for  $l_g = 10 \text{ m}$  [30, 97] (at  $\lambda_0 = 1.55 \mu\text{m}$ ). A major drawback of long-gauge length interferometric sensing, absent in FBGs and short-gauge length interferometric sensing, however, is their inherent polarisation sensitivity due to the



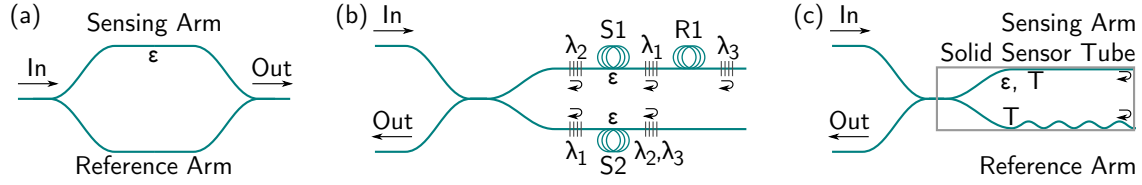


**Figure 2.5.:** Illustration of a basic fibre optic longitudinal strain sensor or hydrophone in a Mach-Zehnder configuration (adapted from Butter *et al.* [17]) in (a). A nested Michelson interferometer, based on FBGs at different wavelengths, as proposed by Kersey *et al.* [105], is shown in (b), while (c) sketches the working principle of the SOFO sensor by Inaudi *et al.* [106].

uncontrolled polarisation state evolution in a regular optical fibre. This can lead to a phenomenon known as polarisation-induced signal fading [98,99] that can cause total signal loss, but can be mitigated using polarisation-maintaining fibre, polarisation controllers [100] or polarisation-diversity detection [101].

The need for optical hydrophones drove research into long-gauge length interferometric fibre sensor arrays in a multitude of interferometric configurations and, as the ability to multiplex sensors is the key to economic use of fibre hydrophones, it received particular attention. The most widely-used multiplexing techniques are based on time-division multiplexing (TDM), wavelength-division multiplexing (WDM), frequency-division multiplexing (FDM), code-division multiplexing (CDM) and coherence-division multiplexing. Common practical issues distinguishing these techniques involve design simplicity, number of lasers and photo detectors needed or achievable power budgets. Multiplexing techniques for long-gauge length fibre sensors are reviewed by Sakai *et al.* [102], Kersey *et al.* [103], Nash [104] and Dandridge *et al.* [30]. Those multiplexing techniques that are relevant to FSI are reviewed in detail in Chap. 4.

A separate area of long-gauge length interferometric sensing is nested interferometers, where some parts of the sensitive regions are shared between several sensors. Fig. 2.5(b) shows an example of a nested interferometer in a Michelson configuration proposed by Kersey *et al.* [105] using FBGs at different wavelengths as reflectors. Here interrogation at wavelength  $\lambda_1$  yields the signal of sensor coil S1, while  $\lambda_2$  yields the signal from sensor coil S2. Interrogation at  $\lambda_3$  then results in the differential signal between S1 and S2, using an additional stationary reference coil R1, inserted to provide the required non-zero OPD for interferometric signal processing.

Further uses of long-gauge length interferometric sensing can be found in structural health monitoring in civil engineering. Here SOFO (Surveillance d'Ouvrages par Fibres Optiques) sensors [106] are used to measure longitudinal strain over gauge lengths of up to several metres [16]. The principle is explained by Fig. 2.5(c), where two arms of a fibre Michelson interferometer are placed in a metal tube with one of them attached to the tube, experiencing both longitudinal strain and temperature, while the other fibre is only loosely inserted and acts as a temperature reference. Interrogation is performed using low-coherence interferometry, yielding absolute OPD measurements. Key to the success of this sensor concept is its stability, with typical long-term OPD uncertainties of  $2\mu\text{m}$ , and that it can be used off-line requiring only an occasional site visit with the interrogation unit [13].

**Fibre Segment Interferometry:** In FSI<sup>1</sup>, multiple, non-overlapping fibre segments that individually act as long-gauge length interferometric sensors are formed by pairs of identical in-fibre partial reflectors. Also, a single, continuous sensing fibre, using the same fibre end for light input and return, is employed, allowing easy deployment. The interferometric configuration can be classified as a low-reflectance reflectometric Fabry-Perot or Fizeau array [107], based on the assumption that the in-fibre reflections are sufficiently weak that the interferometric transfer function can be approximated by two-path interference (further discussed in Sec. 3.1.1). Because of the reflectometric arrangement of the sensors in FSI, there is the possibility of crosstalk due to interference signals from unwanted reflector combinations or multiple reflections [103]. In most potential applications of FSI, the sensors are equal-length and concatenated, thus reflectors are shared between two neighbouring segments except at the ends of the array. Concatenated FSI then constitutes a quasi-distributed long-gauge length sensing system as shown in Fig. 2.1(c). In this case, a particular advantage of FSI is that the measurand is sensed continuously along the fibre and thus phase changes are integrated over the segment length, leaving no sensing gaps.

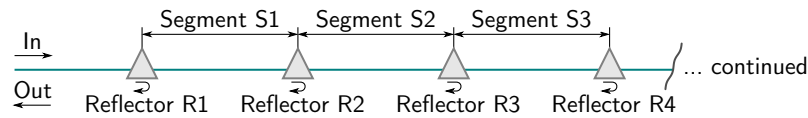


**Figure 2.6.:** Illustration of the basic principle of concatenated FSI, where four in-fibre reflectors form three segments, each constituting a long-gauge length interferometric sensor.

In most FSI techniques, range-based signal separation is performed using the physical time-of-flight of the light to the reflectors using range-resolved optical interferometric signal processing techniques. Historically, the first FSI technique was proposed by Dakin *et al.* [10] in 1984 for optical hydrophone applications with many subsequent implementations also in this area [11, 12]. The different range-resolved processing techniques that can be used to implement FSI are reviewed in detail in Chap. 4, with the basic concatenated FSI configuration also illustrated in Fig. 2.6.

Apart from signal processing, practical aspects of FSI involve the choice of in-fibre partial reflector, which will be further discussed in Sec. 4.1. A considerable practical advantage of FSI compared to, for example, WDM-based FBG sensing, is that reflectors can be identical, thus easing production. Challenges in FSI include the previously discussed possibility of polarisation-induced signal fading common to all long-gauge length interferometric sensors. For the measurement of static quantities, a major drawback of using FSI compared to, for example, FBG-based sensing is that absolute measurements of the OPD cannot be performed due to the interferometric  $2\pi$  phase ambiguity, further discussed in Chap. 3. Thus only relative measurements from a given starting point by fringe counting can be performed. There are, however, several possibilities to implement an absolute sensing capability for long-gauge length interferometric sensors such as a two-wavelength approach [108, 109] or using optical frequency modulation [110].

<sup>1</sup>The term fibre segment interferometry (FSI) is first used in this thesis as no appropriate term was found in prior work to describe this group of techniques.

## 2.5. Summary Table

A brief summary of the main distinguishing features of the most widely-used fibre sensing technologies reviewed in Secs. 2.2, 2.3 and 2.4 is given in Table 2.1.

**Table 2.1.:** Comparison of widely-used optical fibre sensing techniques.

Abbreviations used: Advantage (+), Disadvantage (–)

Technique	Notes
<i>Distributed Rayleigh</i> [42, 46, 48–52]	Range-resolved recording of Rayleigh scattering power (+) Widely used for measurement of dynamic acoustic changes (–) Other measurands possible but not widely used
<i>Distributed Raman</i> [53–55]	Range-resolved recording of Raman scattering peak ratio (+) Widely used due to exclusive sensitivity to temperature (–) Weak signals require long acquisition ( $\approx 10$ s)
<i>Distributed Brillouin</i> [56–62]	Range-resolved recording of Brillouin scattering frequency shift (+) Interrogation of very long fibre lengths possible (–) Complex interrogation units and long acquisition ( $\approx 1$ s)
<i>FBGs</i> [15, 63–70]	Measurement of spectral position of resonance peak from grating (+) Frequency shift instead of intensity is evaluated $\Rightarrow$ stability (+) Simple WDM multiplexing for FBGs at different wavelengths (–) Only a limited number of FBGs can be easily multiplexed
<i>Quasi-Distr. Point Sensing</i> [71–77]	Range-resolved measurements using a large number of FBGs (+) Identical draw-tower gratings can be used (–) Only for quasi-static measurements ( $\approx 10$ s)
<i>LPGs</i> [78–84]	Measurement of spectral position of grating-cladding resonances (+) Multiple peaks can be used for multi-parameter sensing (+) Sensitivity to surrounding medium allows chemical sensing (–) Difficult to multiplex
<i>Interferometric Fabry-Perots</i> [54, 85–94]	Interference between two closely-spaced ( $< 1$ mm) reflectors (+) Absolute data using spectral or low-coherence interrogation (+) Short gauge length allows true point measurements (–) Difficult to multiplex
<i>Interferometric Long-Gauge</i> [16–18, 30] [95–106]	Interference between two widely-spaced ( $\gg 1$ mm) reflectors (+) Widely used for optical hydrophones (+) Very large sensitivities over long gauge lengths (–) Possibility of polarisation-induced signal fading
<i>Interferometric FSI</i> [10–12]	Interference over multiple segments formed by weak reflectors (+) Quasi-distributed monitoring without sensing gaps (+) Identical reflectors can be used for every segment (–) No straightforward absolute measurements (–) Possibility of polarisation-induced signal fading

## 3. Review of Signal Processing for Single Optical Interferometers

This chapter reviews optical interferometric signal processing techniques that can be used for interferometric phase measurements in a single, two-path interferometer. Interferometric signal processing is a very wide area, hence this review is limited to techniques where the interferometer is illuminated with quasi-monochromatic light [111] and that do not use wavelength-based evaluation, as only these are relevant to the fibre segment interferometry (FSI) approach investigated in this thesis.

### 3.1. Basic Aspects of Optical Interferometric Signal Processing

#### 3.1.1. Interferometric Transfer Function

Evaluation of the phase information carried by electromagnetic waves has many useful applications such as information encoding for communication purposes or the measurement of phase delays due to a change in a physical quantity. However, in the optical frequency region of the electromagnetic spectrum, unlike for low-frequency radio frequencies, the phase information contained in the waves cannot be directly measured as the frequencies involved are too high for direct detection and processing. Instead, a technique known as interferometry can be used to measure phase differences between two electromagnetic waves. In an optical interferometer, such as the Mach-Zehnder interferometer previously depicted in Fig. 2.5(a), light passes through two separate paths or interferometer arms and is then recombined, where, in general, there exists an optical path difference (OPD)  $\eta = c_0\tau$  between the paths, where  $c_0$  is the vacuum speed of light and  $\tau$  is the time-of-flight delay between the two arms of the interferometer. A non-zero OPD results in a phase difference for the radiation corresponding to the separate paths and, after recombination, a measurable signal containing information about this phase difference may be obtained when the light is detected by a square-law detector such as a photo diode. For two-path interference of quasi-monochromatic light with complete polarisation overlap, the signal  $U_{\text{pd}}(t)$  at the output of a photo detector can be written as [111]:

$$U_{\text{pd}}(t) = R(P_1 + P_2 + 2|\gamma(\tau)|\sqrt{P_1 P_2} \cos[\Delta\Phi(t)]) \quad \text{with } \Delta\Phi(t) = \Phi_1(t) - \Phi_2(t) \quad (3.1)$$

Here,  $P_1$  and  $P_2$  are the powers of the light returning from the two interferometric arms and  $R$  is the responsivity of the photo detector, relating input power to the signal output. Here, the absolute value of the complex degree of coherence  $|\gamma(\tau)|$  is used to incorporate temporal coherence as a function of the time-of-flight delay  $\tau$ , and which is related to the measurable visibility  $V$  by [111]:

$$V = \frac{P_{\max} - P_{\min}}{P_{\max} + P_{\min}} := \frac{2\sqrt{P_1 P_2}}{P_1 + P_2} \cdot |\gamma(\tau)| \quad (3.2)$$

The measurable visibility  $V$ , with values between 0 and 1, is obtained from the fringe contrast using the maximum and minimum observable power,  $P_{\min}$  and  $P_{\max}$ , respectively. In this thesis, the use of  $|\gamma(\tau)|$  allows the separation of reductions in visibility that are expected due to unequal power ratios between  $P_1$  and  $P_2$  from those reductions that are due to a lack of coherence, which are now incorporated solely in  $|\gamma(\tau)|$ , with values between 0 and 1. In Eq. (3.1)  $\Phi_1(t)$  and  $\Phi_2(t)$  are the respective phases of the electromagnetic radiation for the two arms and it can be seen that, in principle, interferometry only allows the phase difference  $\Delta\Phi(t)$ , not the individual phases  $\Phi_1(t)$  and  $\Phi_2(t)$ , to be measured. In many cases the sensing quantity affects only one of the arms of the interferometer and in this case the arm that is not affected by the sensing quantity is called the reference arm or local oscillator (LO). Furthermore, the term  $\sqrt{P_1 P_2}$  in Eq. (3.1) can result in the phenomenon of heterodyne gain, where, for a strong LO, very weak signals from the sensing arm of the interferometer can be effectively amplified.

Eq. (3.1) can also be described as the transfer function of the interferometer, relating the phase difference input signal to the output signal at the photo detector, which in the case of a two-path interferometer is cosine-shaped and is further illustrated in Fig. 3.1. Because the cosine-shaped transfer function of the interferometer, given by Eq. (3.1), is highly non-linear outside the quadrature points with bias phase differences  $\Delta\Phi = \frac{\pi}{2} + m\pi$ , where  $m$  is any integer, no straightforward determination of the interferometric phase difference  $\Delta\Phi(t)$  is possible. Also, because the transfer function is periodic with  $2\pi$ , there is a projection of the absolute phase difference  $\Delta\Phi(t)$  for values outside the  $[0, 2\pi]$  interval onto this interval, a phenomenon that

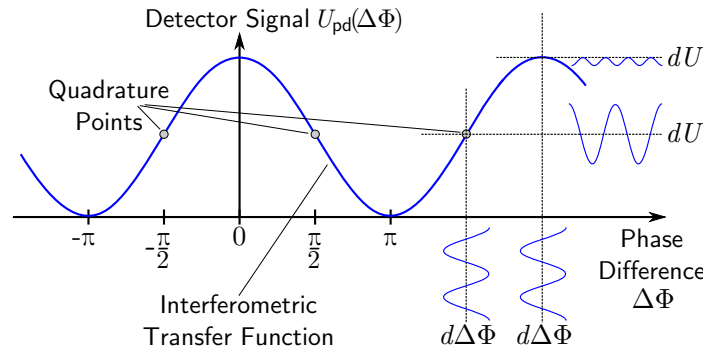


**Figure 3.1.:** Illustration (adapted from Kirkendall *et al.* [30]) of the cosine shaped transfer function of a two-path interferometer, given by Eq. (3.1), with full visibility  $V = 1$  and an equal power ratio  $P_1 = P_2$ . As illustrated, an approximately linear transfer of the phase difference information  $d\Delta\Phi$  is possible where the bias phase difference  $\Delta\Phi$  of the interferometer is on the quadrature points.

is referred to as interferometric  $2\pi$ -ambiguity and which prevents determination of the absolute value of  $\Delta\Phi(t)$  without further knowledge. To obtain continuous phase signals, phase unwrapping [112] is usually employed, allowing reconstruction of the phase signals by inferring any  $2\pi$ -interval change from consecutive phase changes.

In order to obtain linear information about the interferometric phase difference  $\Delta\Phi(t)$  from the physically measurable signal of Eq. (3.1) regardless of the bias phase difference, optical interferometric signal processing techniques have to be employed. Interferometric signal processing techniques allow the linear determination of  $\Delta\Phi(t)$  with the help of a phase modulation function that has been separately introduced into the interferometer. In this context it is advantageous to split the description of the interferometric phase difference  $\Delta\Phi(t)$  into  $\Delta\Phi(t) = \varphi(t) + \theta(t)$ . Here  $\varphi(t)$  is the signal that carries the desired information about the OPD of the interferometer and  $\theta(t)$  is the described phase modulation function. In line with common usage, the correct designation “difference” is dropped in this thesis, hence  $\varphi(t)$  is referred to simply as interferometric phase signal and  $\theta(t)$  simply as the phase modulation function. Therefore Eq. (3.1) can be restated as:

$$U_{\text{pd}}(t) = R(P_{\text{off}} + P_{\text{eff}} \cos[\varphi(t) + \theta(t)]) \quad (3.3)$$

Here,  $P_{\text{off}} = P_1 + P_2$  is the stationary offset power and  $P_{\text{eff}} = 2|\gamma(\tau)|\sqrt{P_1 P_2}$  is the effective interferometric power that is relevant to interferometric signal processing, with  $|\gamma(\tau)|$  defined by Eq. (3.2). In order to perform signal processing, a stationary or time-variable phase modulation function  $\theta(t)$  has to be introduced into the interferometer. The different ways in which  $\theta(t)$  can be used to recover the desired phase signal  $\varphi(t)$  will be reviewed in detail in the following sections.

### 3.1.2. Modulation Techniques

Optical interferometric signal processing techniques can be classified as homodyne or heterodyne according to the type of phase modulation function  $\theta(t)$  of Eq. (3.3) employed. In heterodyne schemes, a constant optical frequency shift or carrier of magnitude  $f_c$  is introduced into the interferometer, thus  $\theta(t)$  is of the general shape  $\theta(t) = 2\pi f_c t$ . Therefore, in heterodyne schemes, all possible phase values of the interferometer are swept through continuously, while in homodyne techniques there is no sweep and the average phase modulation function  $\theta(t)$  is always zero.

While some homodyne optical interferometric signal processing techniques use stationary phase offsets  $\theta$ , most homodyne and all heterodyne schemes use a time-dependent phase modulation function  $\theta(t)$  and thus require some kind of active modulation. The different types of modulation can be classified as direct phase modulation (homodyne) and direct frequency modulation (heterodyne), both within the interferometer, and optical frequency modulation of the illuminating light induced from outside the interferometer (homodyne).

**Direct Phase Modulation:** Direct phase modulation within the interferometer in free-space optics can be applied using tilted transparent plates, diffraction gratings,

rotating half-wave plates or moving mirrors [113]. Electro-optic crystal phase modulators, such as those based on lithium niobate ( $\text{LiNbO}_3$ ) [114], can be built in both free-space and fibre-coupled versions. Using modulators such as Piezo-electric transducers (PZT) [115, 116], where fibre wrapped around the cylinder can be stretched by an applied voltage, is a simple way to achieve phase modulation in fibre optics without the light having to leave the fibre.

**Direct Frequency Modulation:** For direct frequency modulation within the interferometer, the most widely used device is an acousto-optic modulator (AOM) [117], also known as Bragg cell, that uses high frequency acoustic waves to induce a static Doppler shift on the transmitted light. Because AOMs are essentially free-space devices, they require coupling optics that can be lossy when used in fibre-coupled configurations and coupling efficiency can also be susceptible to temperature drifts and vibration. Further approaches for direct frequency modulation that are inherently compatible with fibre optics are the use of stimulated Brillouin scattering inside long pieces of birefringent fibres [118] or using a fibre ring resonator [119]. Another possibility for maintaining a frequency difference in an interferometer is to use two separate lasers that are coherently locked with an absolute frequency offset and that illuminate the two arms of the interferometer separately [120].

**Optical Frequency Modulation of the Illuminating Light:** A fundamental property of optical interferometry is that when a non-zero OPD exists between the two arms of an interferometer, an induced optical frequency shift of the illuminating light results in an interferometric phase shift that is proportional to the OPD for near-static conditions. For transient optical frequency shifts this correspondence can become more complicated [121], however, a nearly proportional behaviour between OPD and resultant interferometric phase shift from optical frequency modulation can often be assumed in practice and for the cases treated in this thesis. Thus changing the illuminating optical frequency of an interferometer by using, amongst others, injection current modulation for laser diodes [122–124], diffractive feedback tuning for external cavity lasers [125, 126], thermo-optic tuning [127] or using rapid direct phase modulation before the light enters the interferometer [128, 129] allows the introduction of a phase modulation waveform that can be used as a carrier for interferometric demodulation. Because the optical frequency modulation is applied externally, it is fundamentally different to direct frequency modulation using, for example, a Bragg cell within the interferometer. Mathematically, the phase modulation waveform induced using optical illuminating frequency modulation is equivalent to the same waveform introduced by an appropriate direct phase modulator inside the interferometer and several of the interferometric signal processing schemes reviewed later can be equally realized by either using external optical frequency modulation of the illuminating light or by using a direct phase modulator within the interferometer.

### 3.1.3. Interferometric Configurations

**Common Interferometric Configurations:** Four widely-used interferometric two-path configurations are shown in their fibre-coupled versions [85] in Fig. 3.2. The

Mach-Zehnder interferometer of Fig. 3.2(a) can be described as a transmission interferometer since light in the sensitive region only travels in one direction, whereas in the other interferometer types, Figs. 3.2(b) to (d), light in the active regions travels in both directions. The Michelson interferometer of Fig. 3.2(b) and the low-finesse Fabry-Perot interferometer of Fig. 3.2(c) rely on reflections from partial or full reflectors. The Fabry-Perot configuration can only be considered a two-path interferometer in the limit of low reflectivity (low-finesse) of its constituent reflectors, otherwise multi-path interference effects [130] that alter the transfer function from its two-path version given by Eq. (3.3) or transient effects [131] might come into play. For these reasons low-finesse Fabry-Perot interferometers are sometimes also referred to as Fizeau interferometers [85].

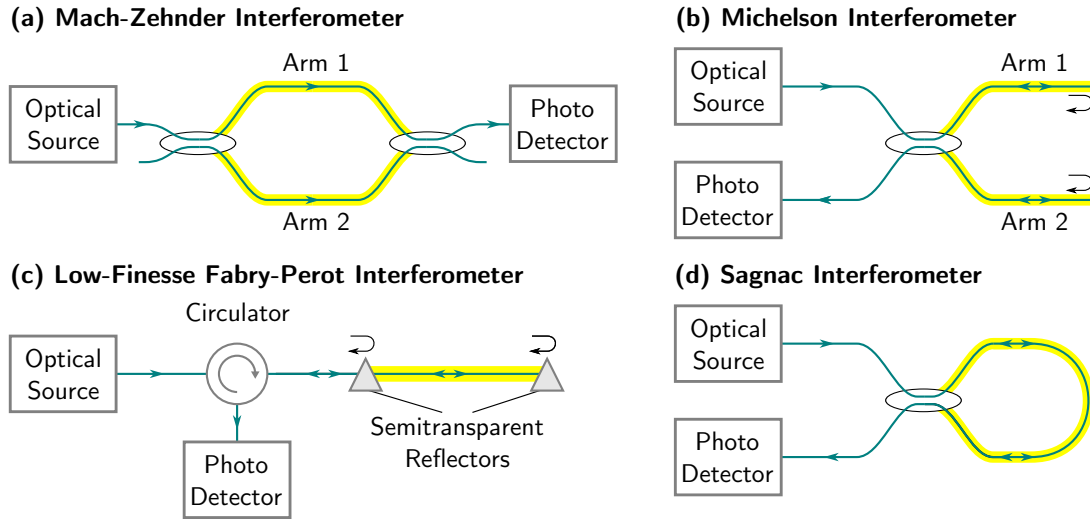


**Figure 3.2.:** Illustration of four widely used interferometric configurations in their fibre-coupled versions. The arrows indicate the intended direction of light travel and the sensitive regions of each interferometer is highlighted.

The interferometric configurations of Figs. 3.2(a) to (c) can be described as dual-path configurations, where in the case of the low-finesse Fabry-Perot interferometer one of the two paths has zero length. In contrast, the Sagnac interferometer [132] of Fig. 3.2(d) is a common-path interferometer as the light of both arms travels exactly the same path, however in opposing directions. Thus the Sagnac interferometer is automatically OPD-balanced and only non-reciprocal or transient effects occurring asymmetrically in the loop give rise to changes of the phase signal  $\varphi(t)$ .

**Remote Interrogation:** In many applications for interferometric measurements, it is required or beneficial to physically separate (isolate) the sensing region of the interferometer from the interrogation unit for reasons including reductions in physical size, lowering costs when multiplexed, mitigating influences on the measurand due to the modulator or vibrations, or to achieve electrical passiveness. This requires light corresponding to both interferometric arms to travel together to and from the remote interferometer along a common free-space path or fibre lead, where the interferometer should ideally be totally insensitive to any kind of perturbation on the common path/lead. The various ways to achieve this are illustrated in Fig. 3.3, in this case



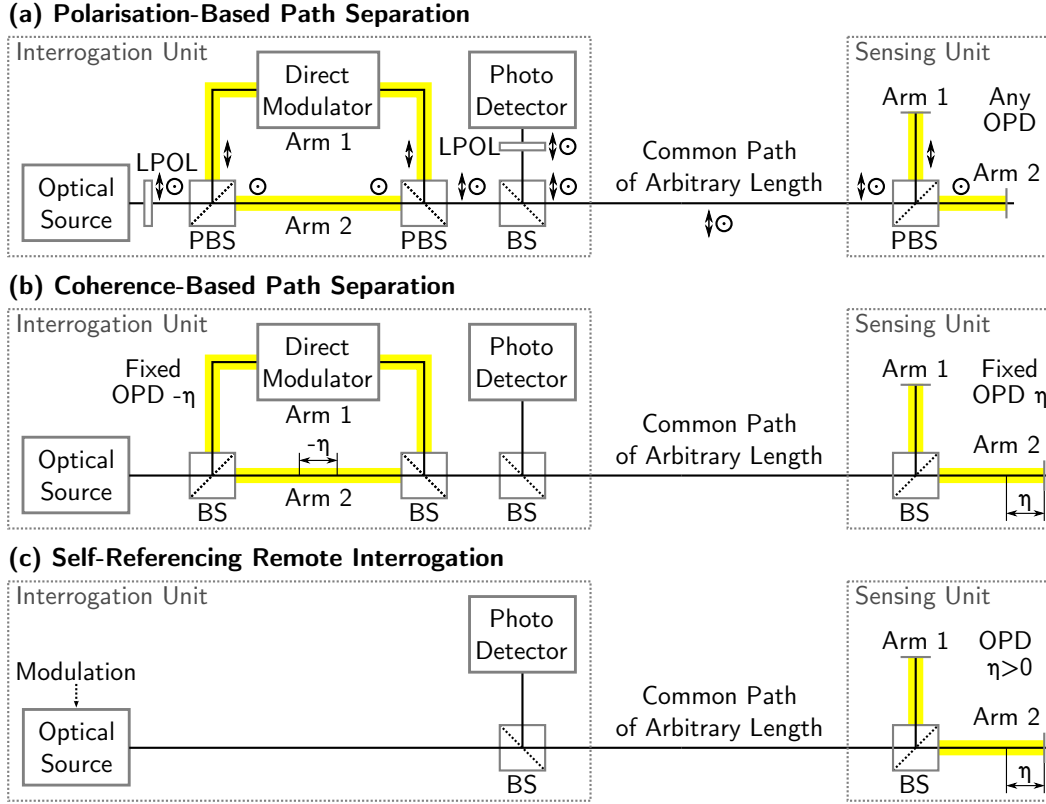


**Figure 3.3.:** Illustration, using a free-space setup, of three configurations for remote or down-lead insensitive interrogation, where physical separation between the interrogation and sensing unit though a common path or lead is given and with the sensitive regions in each interferometer highlighted. In (a), polarisation-sensitive path guidance equipment, such as linear polarisers (LPOL) and polarising beam splitters (PBS), are used and the polarisation states are indicated by appropriate symbols. In contrast, (b) and (c) rely on a non-zero OPD  $\eta$  of the sensing unit and non-polarising guiding equipment, such as a non-polarising beam splitter (BS), is used.

for a free-space Michelson-type interferometer, where, for illustrative purposes, the free-space version is shown instead of the equivalent fibre-coupled setup.

In *polarisation-based path separation* [113], illustrated in Fig. 3.3(a), light travelling to and from the modulated and unmodulated interferometric arms is guided and separated according to the unique polarisation state of each arm. Thus a direct phase/frequency modulator can be included in the interrogation unit instead of the sensing unit, however, passive polarisation manipulation and splitting elements still need to be used there. A particular advantage of polarisation-based path separation is that it can be used to interrogate OPD-balanced interferometers.

In *coherence-based path separation* [133,134], illustrated in Fig. 3.3(b), a non-zero OPD in the sensing unit is compensated in the interrogation unit by a second interferometer of approximately inverse OPD and the low coherence of the illuminating light ensures that only the intended path combination of near-zero effective OPD after compensation gives rise to an interferometric signal. A direct phase/frequency modulator may be included in the compensating interferometer to perform interferometric signal processing. The low coherence can be a natural property of the source or

which reduces phase noise because highly coherent optical sources can be used.

In *self-referencing remote interrogation*, a non-zero OPD between the two interferometric arms in the sensing unit allows the identification of the interferometric signals based on its time-of-flight. This can be achieved through time-gating, but also by using optical frequency modulation of the light illuminating the sensing interferometer, with both approaches further reviewed in Chap. 4. The principle of self-referencing remote interrogation is illustrated in Fig. 3.3(c), highlighting the simple setup required to achieve down-lead insensitivity, however, self-referencing techniques require a minimum OPD and do not work in OPD-balanced interferometers.

### 3.1.4. Quadrature Demodulation in Carrier-Based Processing

The final stages of most single carrier-based optical interferometric signal processing techniques reviewed later in this chapter are very similar and require the demodulation of the desired phase signal  $\varphi(t)$  from a carrier signal, with the demodulation process for dual carrier homodyne techniques also related. The demodulation techniques used in these cases originate from communication techniques [136]. While traditionally a variety of approaches, such as phase-locked loops [137], were used in optical interferometric signal processing, in recent times, quadrature demodulation is favoured in most cases due to its superior properties, such as simplicity, stability and accuracy, when implemented digitally [138]. In general, carrier-based interferometric processing techniques are subject to similar limitations of the quadrature signal bandwidth as well as being prone to cyclic errors that limit accuracy. Therefore these common attributes are discussed here before the schemes are reviewed individually later.

**Demodulation Process:** The principle of single carrier quadrature demodulation [138] is illustrated in Fig. 3.4. Here, the incoming signal from the photo detector,  $U_{pd}(t)$ , where the desired phase signal  $\varphi(t)$  is phase modulated onto a carrier of frequency  $f_c$ , is multiplied (mixed) with the sine and cosine versions of the carrier signal at frequency  $f_c$ . The sum and difference frequencies arising from these multiplications thus shift the offset frequencies to  $2f_c$  and 0, respectively. Also, any remaining DC offset in the photo detector signal  $U_{pd}(t)$  will now be shifted to a frequency offset of  $f_c$ . The signals from the sine and cosine channels are subsequently low-pass filtered with quadrature cut-off frequency  $f_{Q,co} \leq 0.5f_c$  to exclude the sum frequency components centred at  $2f_c$  and any former DC component at  $f_c$ , resulting

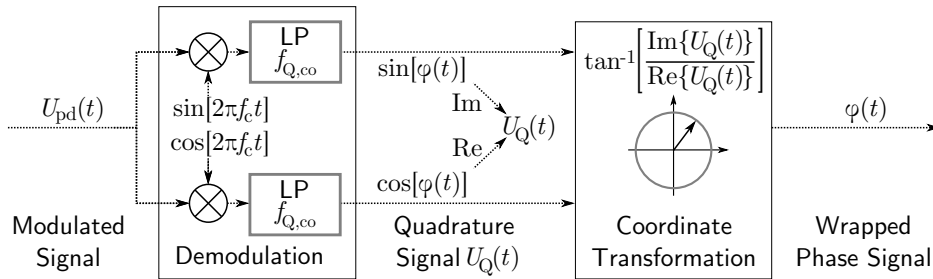


**Figure 3.4.:** Illustration of the single carrier quadrature demodulation process (adapted from Bauer *et al.* [138]), showing the demodulation stage, including multiplication and low-pass (LP) filtering with quadrature cut-off frequency  $f_{Q,co}$ , resulting in the complex quadrature signal  $U_Q(t)$ . Following this the coordinate transformation stage then yields the wrapped phase signal  $\varphi(t)$ .

in the complex quadrature signal  $U_Q(t)$ . The real and imaginary parts of  $U_Q(t)$  are then subjected to an arctangent operation in the coordinate transformation stage to obtain the phase signal  $\varphi(t)$ , which, due to the interferometric  $2\pi$ -ambiguity, is wrapped (projected) onto the interval  $[-\pi, \pi]$ . As discussed previously, the phase signal then needs to be unwrapped [112] to extend its value range beyond  $\pm\pi$ .

**Quadrature Signal Bandwidth Requirements:** In every interferometric signal processing system according to Fig. 3.4, the bandwidth of the complex quadrature signal  $U_Q(t)$  is limited by the cut-off frequency  $f_{Q,co}$  of the low-pass filter (LP) shown. The bandwidth requirements of a given phase signal are conveniently expressed by the quadrature bandwidth<sup>1</sup>  $B_Q$ , where  $B_Q \leq f_{Q,co}$  is necessary for proper operation of the interferometric signal processing. Due to the cosine-shaped transfer function of Eq. (3.3), it is a general property of interferometric systems that phase signals at frequency  $f_{sig}$  may have quadrature bandwidths of many multiples of  $f_{sig}$  in order for them to be resolved [30]. This is a well-known fact in frequency modulated communications and radio engineering, and is normally approximated by Carson's rule [11, 139, 140], which defines the bandwidth at which 98% of the power of a sinusoidal signal is transmitted and which is given by [140]:

$$B_Q \approx (|f_{i,pk}| + |f_{sig}|) \quad (3.4)$$

For the simplified case of a sinusoidal test signal, with phase signal amplitude  $A_{sig}$  and frequency  $f_{sig}$ ,  $\varphi(t)$  is given by:

$$\varphi(t) = A_{sig} \cdot \sin[2\pi f_{sig}t] \quad (3.5)$$

The peak instantaneous frequency  $f_{i,pk}$  can then be stated as:

$$f_{i,pk} = A_{sig} \cdot f_{sig} \quad (3.6)$$

Using Eq. (3.4), this results in the following approximate relation between the absolute values of the maximum permissible amplitude  $|A_{sig}|$  and frequency  $|f_{sig}|$  for a sinusoidal phase signal at any given absolute value of  $|B_Q|$ :

$$|A_{sig}| \approx \frac{|B_Q|}{|f_{sig}|} - 1 \quad (3.7)$$

The lines defined by Eq. (3.7) are plotted in Fig. 3.5 for four cases of  $B_Q = [17, 37, 153, 177]$  kHz, which, including an additional safety factor of 15% as discussed later in Sec. 5.5.2, are the maximally resolvable bandwidths corresponding to the quadrature cut-off frequencies  $f_{Q,co} = [20, 43, 180, 208]$  kHz that are relevant in the later experiments in Chaps. 5, 6 and 7. Sinusoidal phase signals with parameters located to the left and below these lines can be readily resolved, while those located to the right and above these lines will give spurious readings. Phase signals in real

---

<sup>1</sup>In this work, in line with common usage, all bandwidth specifications for low-pass filters specify the single-sided bandwidth starting from zero frequency onwards, implicitly implying that this bandwidth is mirrored in the negative frequency sideband.

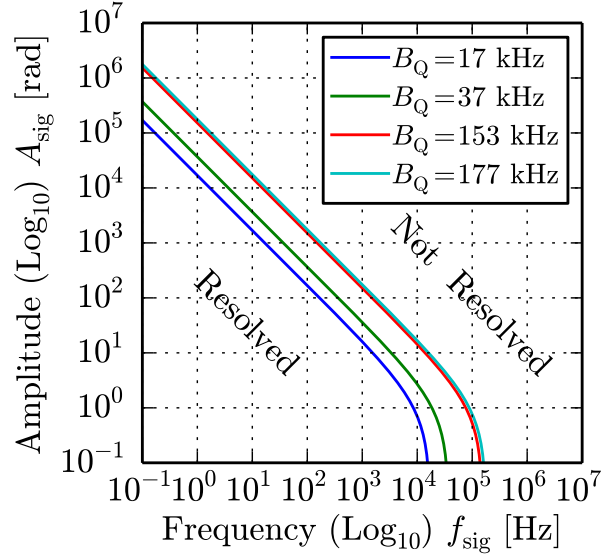


**Figure 3.5.:** Quadrature signal bandwidth requirements of a sinusoidal phase signal of frequency  $f_{\text{sig}}$  and amplitude  $A_{\text{sig}}$  for example quadrature bandwidth values  $B_Q$  that are relevant to later chapters, where the lines drawn are the borders of the resolvable signal parameter regions.

applications that are more complicated than a simple sine function may need further investigation [30] but the general behaviour evident in Fig. 3.5, regarding the inverse relation between phase signal amplitude and frequency, remains valid.

**Cyclic Errors:** Cyclic errors, sometimes also described as periodic non-linearity errors, are  $2\pi$ -periodic inaccuracies in the demodulation process common to most carrier-based interferometric signal processing techniques [141, 142]. This is because in order to perform correct demodulation in a carrier-based demodulation scheme, the carrier is only permitted to occupy a single sideband in the complex frequency spectrum. When this is not given and spectral components at the chosen carrier frequency do not vanish in the undesired sideband of the complex frequency spectrum, cyclic errors will ensue. The magnitude of the cyclic errors is dependent on the carrier amplitudes ratio between the desired and undesired sidebands of the complex frequency spectrum. Additionally, cyclic errors can also occur when the signal power corresponding to a complex exponential term that is not dependent on the phase signal  $\varphi(t)$  infiltrates into the quadrature signal  $U_Q(t)$  due to, for example, crosstalk between signal sources or non-idealities in the demodulation process.

In order to model the dominant cyclic error types, the complex quadrature signal  $U_Q(t)$  can be expressed in terms of two  $\varphi(t)$ -dependent complex exponential terms of amplitudes  $a_1$  and  $a_2$  as well a stationary complex exponential term of amplitude  $a_3$ , with phases  $\alpha_1$ ,  $\alpha_2$  and  $\alpha_3$ , respectively<sup>2</sup>, as:

$$U_Q(t) = a_1 \exp \left[ j \cdot (\varphi(t) + \alpha_1) \right] + a_2 \exp \left[ -j \cdot (\varphi(t) + \alpha_2) \right] + a_3 \exp \left[ j \cdot \alpha_3 \right] \quad (3.8)$$

In the ideal case without cyclic errors, only the first exponential term in Eq. (3.8)

<sup>2</sup>Eq. (3.8), has been obtained by re-expressing the analysis of Wu *et al.* [141] using complex exponential terms.

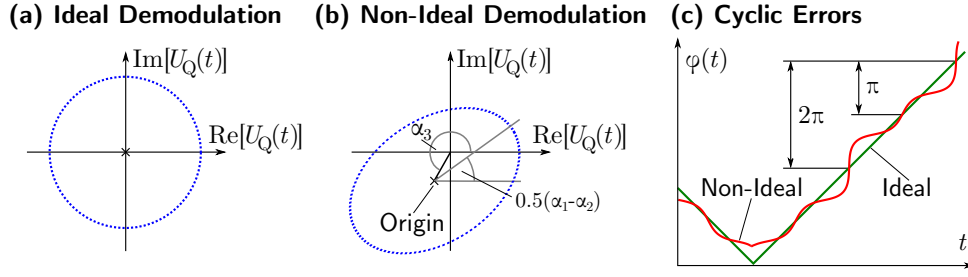


**Figure 3.6.:** The quadrature signal  $U_Q(t)$  plotted in the complex plane will resemble a circle (a) for an ideal demodulation and an offset ellipse (b) when neither  $a_2$  or  $a_3$  vanishes in Eq. (3.8). This results in cyclic errors, illustrated in (c) for a section of a triangular phase signal.

will contribute to the quadrature signal and both amplitudes  $a_2$  and  $a_3$  as well as  $\alpha_1$  will reduce to zero. In this case the desired phase signal  $\varphi(t)$  can be obtained without cyclic errors using an arctangent operation, as previously shown in Fig. 3.4. When plotted in the complex plane, the ideal quadrature signal for  $a_1 \neq 0$  and  $a_2 = a_3 = 0$  will be perfectly circular and centred on the origin, as shown in Fig. 3.6(a). For  $a_2 \neq 0$  the plot of the quadrature signal will turn elliptic and  $a_3 \neq 0$  will offset the origin of the plot. This is illustrated in Fig. 3.6(b), which also shows the effect that the angles  $\alpha_1$  and  $\alpha_2$  have in respect to the orientation of the semi-major axis of the ellipse and  $\alpha_3$  in respect to the position of the ellipse origin. With  $a_2 \neq 0$  and/or  $a_3 \neq 0$  cyclic errors will result, which lead to phase-dependent periodic deviations of the measured phase value from the true phase value  $\varphi(t)$ . For error amplitudes that are not too large, offset errors due to  $a_3 \neq 0$ , originating from crosstalk, will result in one-cycle non-linearities with periodicity  $2\pi$ , while errors due to  $a_2 \neq 0$ , originating from imperfect sideband suppression, result in two-cycle non-linearities with periodicity  $\pi$  [141], where the combined effect of both types of errors is illustrated in Fig. 3.6(c).

## 3.2. Review of Non-Carrier-Based Processing

### 3.2.1. Passive Homodyne Processing

In passive homodyne processing  $n$  photo detectors are used and stationary phase offsets,  $\theta_n$ , are maintained between the interference signals incident on the individual detectors. The interferometric phase signal  $\varphi(t)$  can then be recovered by appropriately combining the signals from the  $n$  detectors using basic trigonometric identities. A common requirement of most passive homodyne processing techniques is the need to calibrate the offset signal and gain factors from the detectors [143, 144] to avoid cyclic errors (see Sec. 3.1.1) or otherwise employ a “differentiate and cross-multiply” (DCM) algorithm [145]. Here, the phase signal obtained by a DCM algorithm is inherently free from cyclic errors, however, the phase signal is multiplied by an unknown constant whose value is furthermore subject to power and visibility drifts.

A 3x3 fibre coupler [145] has been used to implement passive homodyne processing in a fibre-based setup as shown in Fig. 3.7. Here, the  $n = 3$  outputs of the coupler correspond to stationary phase offsets  $\theta_n = [+120^\circ, 0, -120^\circ]$  respectively for a

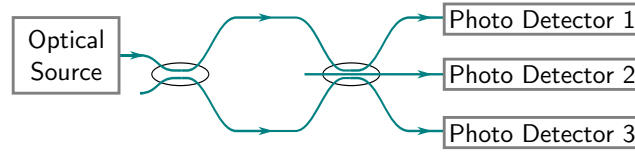


**Figure 3.7.:** A typical fibre-coupled passive homodyne setup [145] with a 3x3 coupler in a Mach-Zehnder configuration is shown.

symmetric coupler. The widespread use of passive homodyne processing in fibre sensing technology appears to be hampered by the fact that 3x3 couplers are complex to produce and imperfections in coupling constants need to be individually calibrated and might also be subject to uncontrollable temperature or polarisation drifts. Also, three photo detectors are needed for each interferometer. Nevertheless, advantages include the absence of an active modulated element, its capability of working in an OPD-balanced setup, thus mitigating laser phase noise, and its, in theory, unlimited quadrature signal bandwidth. In other areas, such as precision free-space displacement measuring interferometry, a passive homodyne technique known as polarisation-based quadrature homodyne interferometry [141, 146] is widely employed, making use of the  $90^\circ$  phase offset inherent in circularly polarised light.

### 3.2.2. Phase Stepping Homodyne Processing

Phase stepping, also known as phase shifting interferometry, is a group of homodyne techniques where discrete phase steps are applied in a fixed temporal sequence to an interferometer. Unlike carrier-based techniques reviewed later in this chapter, the signal processing is not continuous. Thus, whereas in carrier-based techniques phase signals  $\varphi(t)$  can be resolved up to a given signal bandwidth, phase stepping processing assumes fully static phase signals. Therefore, phase stepping techniques are primarily designed to obtain measurements of static phase values,  $\varphi$ , employing a minimum amount of steps and are mostly used in imaging interferometry [147]. It has, however, also been employed in fibre interferometers by Kersey *et al.* [148] using optical illuminating frequency modulation and by Milnes *et al.* [149] using direct phase modulation, with the former using a minimalist two phase step approach.

The principle used in phase stepping processing is that the modulation phase  $\theta(t)$  of Eq. (3.3) is altered using a direct phase modulator or by optical frequency modulation of the illuminating light (see Sec. 3.1.2) in a number of discrete phase steps, often four steps of magnitude  $0.5\pi$ . This is illustrated in Fig. 3.8, where Fig. 3.8(a) shows a four phase steps sequence with steps  $\theta_1$  to  $\theta_4$ , while Fig. 3.8(b) shows a typical resultant signal for a single pixel or photo detector. The desired interferometric phase value  $\varphi$  can then be found using a multitude of possible algorithms [150, 151].

The disadvantages of phase stepping techniques are that any error in phase step amplitude or transient changes through vibration or in illumination power can affect the measurement accuracy, however, some algorithms are specifically designed to mitigate such problems [150, 151]. While many phase stepping techniques rely on discrete phase steps, there are some related techniques, also mainly used in imaging

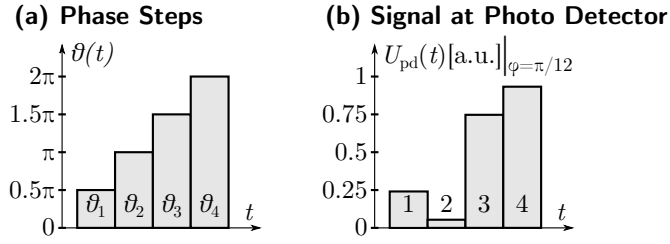


**Figure 3.8.:** Illustration in (a) of the phase steps applied and in (b) of resultant signals at a single photo detector or camera pixel for an example phase value of  $\varphi = \pi/12$  (adapted from Creath [113]).

interferometry, that use continuous sinusoidal [152, 153] or triangular modulation waveforms [154], which both have advantages in easing the requirements on the phase modulator. Since the modulation waveform is continuous in these cases, if a camera detector is used, the integration over the exposure time has to be taken into account in the algorithm. However, even though the modulation waveform is continuous, the phase extraction algorithms still assume static phase values  $\varphi$ , similar to the regular phase stepping techniques described above. A further variant of phase stepping signal processing is often used for interferometric fibre-optic gyroscopes [155, 156] based on the Sagnac interferometer (see Fig. 3.2). Here, a phase modulator rapidly varies the phase periodically between the positive and negative quadrature points at phase offsets of  $\pm \frac{\pi}{2}$ . If the interferometric phase  $\varphi(t)$  is exactly 0 this will result in a DC-only signal. Any departure from  $\varphi(t) = 0$  will result in an AC signal at the changeover frequency with an amplitude that is initially proportional to  $\varphi(t)$  and which can be used as a measurement signal.

### 3.2.3. Active Homodyne Processing

In active homodyne detection [116], a control loop is employed to maintain the interferometer biased at the quadrature point, where, as described in Sec. 3.1.1, the interferometer has a nearly linear response with respect to small changes in the desired phase signal  $\varphi(t)$  of Eq. (3.3). When the interferometer is maintained on the quadrature point, large-scale phase changes will be manifested in the output of the control loop, providing an additional phase measurement with high dynamic range, albeit, only at a bandwidth well below the control loop bandwidth. A typical setup for actively controlled homodyne processing is shown in Fig. 3.9.

To keep the interferometer on the chosen quadrature point, the phase within the interferometer has to be changed in response to the control loop (see also Sec. 3.1.2), either by direct phase modulation [116] or by optical frequency modulation of the illuminating light in a setup with non-zero OPD [157]. In general, when direct phase modulation is used, the phase modulator can be placed inside the interferometer as shown in Fig. 3.9 or in a remote interrogation configuration [158] (see also Sec. 3.1.3) where the phase modulator is separated from the sensing interferometer. Drawbacks of active homodyne processing are that resets of the control loop might be necessary if the phase modulator driving signal reaches its limit. Also, multiplexing of sensors requires an individual phase modulator for each interferometer. However, because

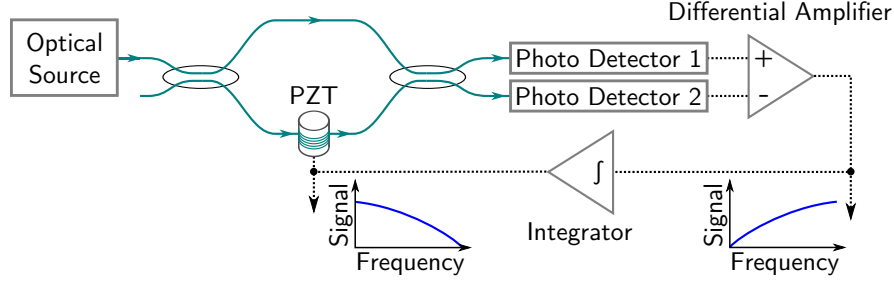


**Figure 3.9.:** Illustration (adapted from Kirkendall *et al.* [30]) of a typical active homodyne setup. A low-pass filtered phase signal with large dynamic range can be obtained from the driving signal of the PZT phase modulator. Conversely, a high-pass filtered version of the phase signal is available at the output of the differential amplifier.

it is a convenient way to balance an interferometer to eliminate laser phase noise, active homodyne processing appears to be the technology of choice when very high interferometric sensitivities are required [30], with phase noise levels lower than  $1 \mu\text{rad} \cdot \text{Hz}^{-0.5}$  reported [96] using this technique. Further variants of active homodyne processing, known as  $J_1(\text{max})$ ,  $J_1(\text{null})$ ,  $J_1/J_2$  or  $J_2/J_3$ -methods [159, 160] that employ small scale sinusoidal phase modulation around the quadrature points have also been developed in the area of precision displacement measuring interferometry.

## 3.3. Review of Single Carrier-Based Processing

### 3.3.1. Heterodyne Processing

In heterodyne optical interferometric signal processing [161], a single carrier at frequency  $f_c$  is maintained between the two arms of the interferometer by a suitable direct frequency modulation technique (see also Sec. 3.1.2). Mathematically this corresponds to a continuous phase modulation function  $\theta(t) = 2\pi f_c t$  in Eq. (3.3) where the modulation frequency of the AOM equals the carrier frequency  $f_c$  used for demodulation and the desired phase signal  $\varphi(t)$  can be demodulated as illustrated in Fig. 3.4. A typical free-space heterodyne Mach-Zehnder interferometric configuration that is widely used in laser vibrometry [138] is shown in Fig. 3.10, also employing polarisation-sensitive equipment to reduce power losses due to light guiding. In order to implement heterodyne signal processing, an AOM induces a direct frequency modulation at  $f_c$  and the movement of the target can be retrieved from the phase signal  $\varphi(t)$  after demodulation.

A key advantage of heterodyne interferometry is that it is practically free from cyclic errors (see Sec. 3.1.1) because direct frequency modulation ideally only contains frequency components in a single sideband. This appears to hold well in practice as publications investigating cyclic errors in precision displacement measuring heterodyne interferometry, such as McRae *et al.* [142], do not discuss problems due to the frequency modulator but rather find cyclic errors originating from the polarisation-based path separation required for the remote interrogation configura-



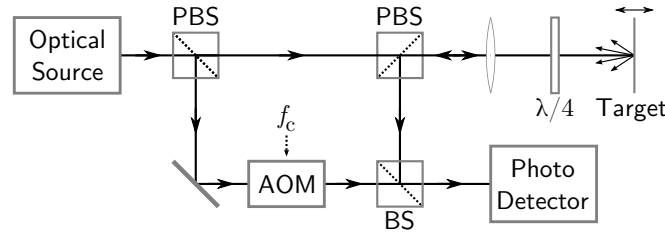


**Figure 3.10.:** Typical free-space Mach-Zehnder interferometer with heterodyne signal processing used for vibrometry applications [138]. Here polarising beam splitters (PBS), non-polarising beam splitters (BS), quarter-wavelength plates ( $\lambda/4$ ), lenses and mirrors are used to guide the light to and from the target and through the acousto-optic modulator (AOM).

tion (see Sec. 3.1.3) used. Also Bragg cells typically offer high frequency shifts of many tens of MHz [138], allowing very high quadrature bandwidths. The practical difficulties of using direct frequency modulators, described in Sec. 3.1.2, can be considered a drawback of heterodyne interferometry, especially for fibre-coupled sensing. However, heterodyne processing is very widely used in a diverse range of areas such as precision displacement measurements [142, 162], vibrometry [138, 161, 163] and Doppler lidar anemometry [3–9].

### 3.3.2. Single Carrier Homodyne Processing

Single carrier homodyne processing encompasses all homodyne techniques where the interferometric phase signal  $\varphi(t)$  can be recovered from a single carrier frequency and demodulated as illustrated in Fig. 3.4. In homodyne single-carrier techniques, the carrier is introduced by periodic phase modulation, which results in multiple harmonic frequency components, and not by direct frequency modulation as in heterodyne processing. Thus, apart from the chosen carrier frequency, other harmonic frequency components of the phase modulation waveform that also act as carriers, may be present in the resultant photo detector signal  $U_{pd}(t)$  of Eq. (3.3). Hence suitable filtering is required to limit the demodulation to the chosen carrier.

Common phase modulation waveforms used in single carrier homodyne processing are of serrodyne (sawtooth) or sinusoidal shape and these waveforms can be introduced by both direct phase modulation or optical illuminating frequency modulation in interferometers with a non-zero OPD (see also Sec. 3.1.2). Historically, techniques based on direct phase modulation with a serrodyne waveform are referred to as single-sideband (SSB) homodyne, whilst those techniques based on serrodyne optical illuminating frequency modulation are termed pseudo-heterodyne, even though mathematically there is no difference. When a sinusoidal waveform is used, single carrier demodulation is only possible using an additional window function, otherwise dual carrier demodulation techniques, discussed in Sec. 3.4, need to be used.

In the context of the SSB technique, a set of equations that is based on the series expansion of the cosine shaped interferometric transfer function of Eq. (3.3) for a given periodic phase and optional intensity modulation function has been developed by Ostwald *et al.* [164] and Voges *et al.* [165]. This theory would be sufficiently generic

to allow the unified description of all single carrier homodyne processing techniques, including those that use windowing, in a simple way. However, this possibility is not widely realized and most schemes use independent theoretical approaches. The details of the different approaches for single-sideband homodyne, pseudo-heterodyne and windowed sinusoidal homodyne processing are reviewed in the following sections:

**Single-Sideband Homodyne Processing:** SSB signal processing is a technique that originally evolved from radio engineering [164, 166]. In the optical domain, several approaches using stepped direct phase modulation [167, 168] or continuous direct phase modulation [165] have subsequently been developed for both communication and sensing applications. In SSB, the periodic phase modulation waveform  $\theta(t)$  is usually introduced by direct phase modulation (see Sec. 3.1.2). The SSB approach using direct phase modulation has found some applications, mainly for fibre optic gyroscopes [169, 170], but it does not appear to be widely used in recent work.

The corresponding SSB theory developed by Ostwald *et al.* [164] for radio engineering applications and first applied to the optical domain by Voges *et al.* [165] is a generic approach specifying the shape and scale that a periodic phase-modulated and possibly intensity-modulated waveform must possess for it to contain only positive or negative frequency components (termed sidebands) at the chosen carrier frequency. This permits the desired phase signal  $\varphi(t)$  to be demodulated as described in Sec. 3.1.4 without cyclic errors. The periodic phase modulation  $\theta(t)$  needs to fulfil certain symmetry conditions [164], but is not limited to serrodyne waveforms. It appears that this thesis is the first work that explores phase modulation waveforms that differ in shape from serrodyne waveforms and this will be further discussed in Chap. 5, along with a statement of the relevant SSB equations. In SSB processing the chosen carrier frequency has to be a harmonic multiple of integer harmonic index  $n$  of the modulation frequency  $f_m$ . Due to the possible presence of other harmonic frequency components, the output signal from the photo detector has to be band-limited to  $\pm 0.5f_m$  around the chosen carrier frequency  $f_c = n \cdot f_m$ .

The working principle of single-sideband homodyne signal processing is also illustrated in Fig. 3.11, where (a) shows a free-space Mach-Zehnder setup that is used in Voges *et al.* [165], employing a direct phase modulator, while Fig. 3.11(b) plots the serrodyne phase modulation waveform  $\theta(t)$  used there. The normalised waveform  $\tilde{\theta}(t)$  is scaled with a scale factor,  $s$ , which is tuned until the correct phase excursion

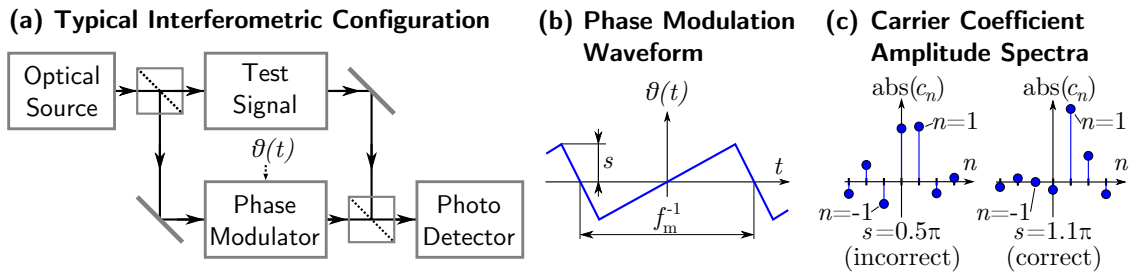


**Figure 3.11.:** Illustration (adapted from Voges *et al.* [165]) of single-sideband signal processing, where (a) shows an example setup using direct phase modulation, (b) plots an example serrodyne periodic phase modulation waveform, while (c) compares the complex carrier coefficient amplitude spectra for correct and incorrect phase scaling factors.

is reached and single-sideband operation is achieved. Fig. 3.11(c) shows the effect of this tuning by plotting the amplitude spectra of the complex carrier coefficients  $c_n$ . It can be seen that for the correct phase scale, i.e.  $s = 1.1\pi$ , the carrier coefficient of the unwanted sideband, here at  $n = -1$ , vanishes and single-sideband operation is thus achieved for the carrier at  $n = +1$ , in contrast to the plot for  $s = 0.5\pi$ , where the amplitudes of both carriers at  $n = \pm 1$  remain non-zero.

**Pseudo-Heterodyne Processing:** Pseudo-heterodyne signal processing is most often used with serrodyne optical frequency modulation of the light illuminating an interferometer with non-zero OPD. This is sometimes also referred to as a frequency modulated continuous-wave (FMCW) technique [171]. Its main attraction lies in the fact that due to the use of optical illuminating frequency modulation, self-referencing interferometric configurations can be used that prove highly stable, especially for remote interrogation configurations (see Sec. 3.1.3).

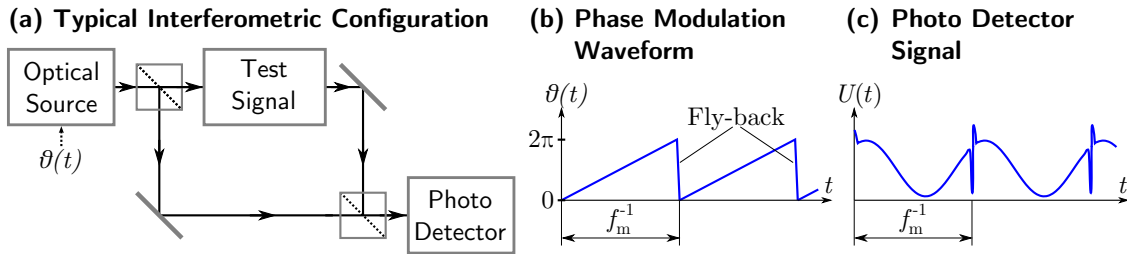


**Figure 3.12.:** Illustration (adapted from Jackson *et al.* [172]) of pseudo-heterodyne interferometric signal processing, where (a) shows an example setup using optical illuminating frequency modulation by the optical source, (b) shows a typical periodic phase modulation waveform, while (c) plots the shape of the signal at the output of a photo detector that can then be low-pass filtered to obtain a single-frequency sinusoidal carrier signal.

The working principle of pseudo-heterodyne signal processing is illustrated in Fig. 3.12, where Fig. 3.12(a) shows a free-space Mach-Zehnder setup that is used in Jackson *et al.* [172], employing optical frequency modulation of the optical source, while Fig. 3.12(b) shows the serrodyne phase modulation waveform of modulation frequency  $f_m$  and phase scale  $2\pi$  that is used there. Fig. 3.12(c) shows the resultant signal  $U_{pd}(t)$  from the photo detector in this case, where the effect of the fly-back of the serrodyne waveform can also be observed. Most implementations of pseudo-heterodyne processing make use of the assumption that the fly-back of the serrodyne waveform can be neglected if the fly-back is sufficiently short and the filtering is sufficiently good. In this case no cyclic errors are observed if, additionally, the tuning of the scale of the serrodyne waveform is maintained at  $2\pi$ , as verified by Onodera *et al.* [173]. However, using the theoretical approach developed for SSB processing discussed previously, the effect of the fly-back could be precisely quantified to adjust the tuning of the serrodyne phase excursion. Alternative implementations of pseudo-heterodyne signal processing use triangular phase modulation waveforms and employ rectangular windowing (gating) to help mitigate fly-back disturbances [174].

**Windowed Sinusoidal Homodyne Processing:** In windowed sinusoidal modulation techniques, the application of a window function through multiplication in the time-domain results in a mixing of frequency components in the frequency domain.

In the frequency domain this process can also be viewed as a convolution of the spectra of the incoming signal and the window function. If the correct values for the phase excursion of the sinusoidal phase modulation, the window width and its symmetry centre are set, then one of the frequency sidebands will disappear in a similar fashion to SSB processing discussed earlier. The interferometric phase signal  $\varphi(t)$  can then be demodulated without cyclic errors. Again, these effects could be described by the single-sideband theory using the optional periodic intensity modulation, however, this description appears to have not yet been attempted in the literature. In general, the main advantage of using a sinusoidal modulation waveform, compared to the serrodyne waveforms discussed previously, is the ease of modulation, since the modulation drive signal only contains one frequency component [174]. In contrast to the sinusoidal optical frequency modulation technique presented in this thesis in Chap. 6 using a smooth window function, published work so far has only used rectangular window functions (also termed gating).

Two approaches by Kersey *et al.* [175] and by Sakai *et al.* [128] can be found in the literature. The interferometric configuration used by Kersey *et al.* [175] is similar to the one shown in Fig. 3.11(a) using direct phase modulation, while the configuration by Sakai *et al.* [128] using optical illuminating frequency modulation is comparable to the one shown in Fig. 3.12(a), although either scheme could be made to work with both types of modulation. Typical intermediate signal waveforms are shown in Fig. 3.13 in arbitrary units with scales that are, however, at each stage (i) to (iv), comparable for both approaches in Figs. 3.13(a) and (b). Here, stage (i) shows the phase modulation waveform that is applied to the interferometer. While for Kersey *et al.* [175] in Fig. 3.13(a), the phase modulation amplitude is exactly 2.82 rad, Sakai *et al.* [128] allows several possible phase modulation amplitude values with appropriate adjustment of the rectangular window width and, in general, uses much higher phase modulation amplitudes than Kersey *et al.* [175]. Stage (ii) shows a

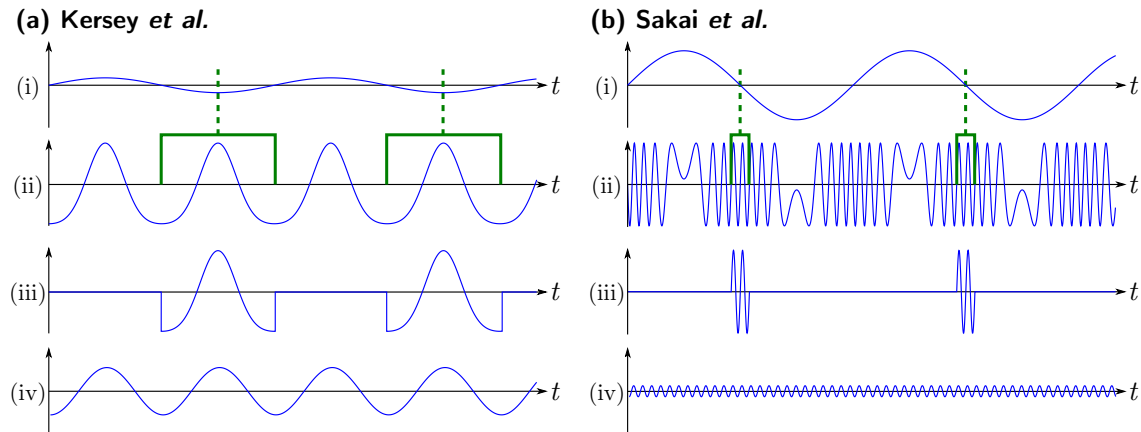


**Figure 3.13.:** Typical waveforms for the windowed sinusoidal processing schemes by Kersey *et al.* [175] in (a) and Sakai *et al.* [128] in (b). In both (a) and (b), at each stage (i) to (iv), arbitrary units with approximately comparable scaling between (a) and (b) are used. Stage (i) shows a representation of the applied phase modulation. Stage (ii) shows the resultant photo detector signal together with the applied rectangular window drawn in green and its symmetry in respect to the phase modulation waveform indicated. Stage (iii) plots the resultant signal after windowing and stage (iv) is the bandpass filtered version of stage (iii) used for demodulation of the phase signal.

typical representation of the photo detector signal  $U_{\text{pd}}(t)$  as well as the gating window used, drawn using green boxes, where it can also be seen that the symmetry centres of the window functions are offset by  $90^\circ$  for the two approaches. Stage (iii) shows the resultant windowed signal, while in stage (iv) this signal is bandpass filtered and allows subsequent demodulation of the phase signal  $\varphi(t)$  similar to Fig. 3.4. Due to energy conservation and the shorter window length in Sakai *et al.* [128], the signal amplitude is much reduced in Fig. 3.13(a)(iv) compared to Fig. 3.13(b)(iv).

There has been some use of windowed sinusoidal modulation processing in applications outside fibre gyroscopes and hydrophones for which the schemes by Kersey *et al.* [175] and Sakai *et al.* [128] were originally developed, including vibrometry [176] and magnetometry [177]. Also, a technique related to Sakai *et al.* [128] was independently developed several years later by Chien *et al.* [178] for fibre gyroscopes, however, there is little recent use reported. In general, it can be said that the approach by Kersey *et al.* [175] permits signal processing at a very low sinusoidal phase modulation amplitude, easing modulation requirements, however, the approach by Sakai *et al.* [128] is capable of addressing multiple sensors and its use in multiplexing will be further reviewed in Chap. 4.

### 3.4. Review of Dual Carrier-Based Processing

Dual or extended dual carrier modulated homodyne processing encompasses all techniques where the interferometric phase signal  $\varphi(t)$  is recovered by evaluating two or more carrier frequencies. In all schemes reviewed here, the multiple carrier frequencies are the result of sinusoidal phase modulation. The sinusoidal phase modulation waveform can be introduced by both direct phase modulation or optical illuminating frequency modulation for an interferometer with a non-zero OPD and both techniques are mathematically equivalent. In general, when a periodic sinusoidal phase modulation waveform  $\theta(t) = A \cos(2\pi f_m t)$  of sinusoidal phase modulation amplitude,  $A$ , and modulation frequency,  $f_m$ , is applied to the interferometer, Eq. (3.3) can be rewritten, using a Bessel series expansion [179, 180], as:

$$U_{\text{pd}}(t) = RP_{\text{off}} + RP_{\text{eff}} \cdot \left( \begin{aligned} &\cos[\varphi(t)] \cdot \left( J_0(A) + 2 \sum_{m=1}^{\infty} (-1)^m J_{2m}(A) \cos[(2m)2\pi f_m t] \right) \\ &- \sin[\varphi(t)] \cdot \left( 2 \sum_{m=0}^{\infty} (-1)^m J_{2m+1}(A) \cos[(2m+1)2\pi f_m t] \right) \end{aligned} \right) \quad (3.9)$$

Here  $J_n(A)$  are the Bessel functions of the first kind for integer harmonic index  $n$ . It can be seen in Eq. (3.9) that in the Bessel function expansion, carriers at even harmonics are amplitude modulated with the cosine of  $\varphi(t)$ , while carriers at odd harmonics are amplitude modulated with the sine of  $\varphi(t)$ . The signals encoded onto odd and even harmonic carriers can then be individually demodulated and appropriately combined to obtain the desired interferometric phase signal  $\varphi(t)$ . This can be achieved in a variety of ways, with widely used techniques reviewed here.

### 3.4.1. Dual Carrier Homodyne Processing

The phasegenerated carrier method (PGC), introduced by Dandridge *et al.* [180], has become a very popular dual carrier method, especially in the area of fibre optic sensing. Though implementation of PGC is also possible using direct phase modulation, the term PGC is often used synonymously for dual carrier interferometric signal processing techniques based on sinusoidal optical illuminating frequency modulation. Initially, prior to the availability of cost-effective digital electronic signal processing hardware, the original PGC method [180] was based on the “Differentiate and Cross-Multiply”-algorithm (DCM), also discussed in Sec. 3.2.1, however more recent implementations favour phase recovery using the arctangent method [30] discussed below. Example interferometric configurations that are compatible with PGC have previously been shown in Fig. 3.11(a) for direct phase modulation and in Fig. 3.12(a) for sinusoidal optical illuminating frequency modulation.

The arctangent method is the simplest possible dual carrier demodulation method. Here the phase modulation amplitude  $A$  in Eq. (3.9) is tuned until the Bessel coefficients for one even and one odd harmonic have the same value. The Bessel functions for the first four harmonics  $J_1$  to  $J_4$  are also plotted in Fig. 3.14(a), where for example, the first and second Bessel harmonic  $J_1$  and  $J_2$  are found to be of equal value at  $A = 2.63$  rad. The demodulation process for this choice of  $J_1$  and  $J_2$  is illustrated in Fig. 3.14(b), where it can be seen that the demodulation process is very similar to the single carrier demodulation process shown in Fig. 3.4, with the exception of the use of two cosine-shaped carriers at frequencies  $f_{c,1}$  and  $f_{c,2}$ , which in this example equal  $f_m$  and  $2f_m$ , respectively.

PGC techniques have become very popular due to their conceptual simplicity, their ease of modulation using sinusoidal waveforms and the possibility of using optical illuminating frequency modulation, allowing passive, remotely interrogated interferometric sensors due to their self-referencing capability (see also Sec. 3.1.3). Also, the compatibility with frequency-division multiplexing techniques, further reviewed in Kersey *et al.* [181], where several optical sources with different modulation frequencies  $f_m$  are used, makes them attractive for multiplexing fibre sensor arrays. Outside its original use in fibre hydrophones [180], PGC has also found applications in areas such as seismology [182], fibre-optic impact measurement [183], fibre magnetometers [184] or fibre-optic accelerometers [185]. Hybrid PGC methods

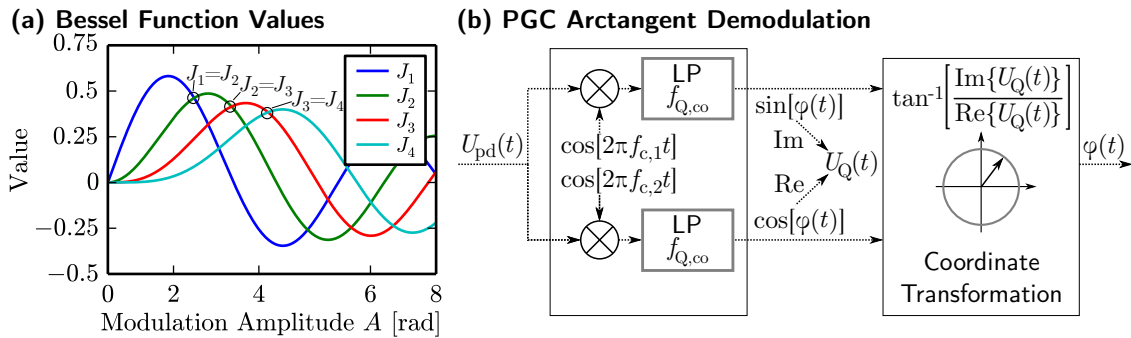


**Figure 3.14.:** Illustration of the working points in the Bessel function plot (a) and the demodulation process (b) used in arctangent PGC phase recovery using dual carriers  $f_{c,1}$  and  $f_{c,2}$ .

that use a technique related to the original DCM algorithm to determine the current sinusoidal phase modulation amplitude  $A$  and use this knowledge to then correct the arctangent method that is used to demodulate the phase signal  $\varphi(t)$  have also been proposed in recent years [186]. This approach combines the main advantage of the DCM algorithm, i.e. demodulation without cyclic errors (see also Sec. 3.1.4), with the immunity against power and visibility changes and the correct phase scaling that arctangent demodulation offers.

In addition to what is generally termed PGC, several other dual carrier modulated homodyne techniques using sinusoidal phase modulation waveforms have been proposed, such as the sinusoidal phase modulating interferometry technique [187] in the area of imaging interferometers, or, in the area of fibre-optics, the quadrature recombination [188] or synthetic heterodyne [189] approaches. For instance, in the synthetic heterodyne technique, signals from the first and second Bessel harmonic carriers in Eq. (3.9) are multiplied by carriers at frequencies  $2f_m$  and  $f_m$  respectively. In both cases the sum frequencies lie at  $3f_m$  and, for the correct sinusoidal phase modulation amplitude  $A$ , the appropriately filtered signals from these carriers can be added to obtain a synthetic heterodyne carrier that can be demodulated in the same way as a heterodyne carrier (see also Fig. 3.4).

### 3.4.2. Extended Dual Carrier Homodyne Processing

Extended dual carrier methods make use of more than two Bessel harmonic carriers in Eq. (3.9) to obtain all the parameters required for the measurement of the interferometric phase  $\varphi(t)$  without the need for any calibration or feedback control. In particular, the sinusoidal phase modulation amplitude  $A$  of Eq. (3.9) can be, within limits, obtained directly in real time from the measurements and thus  $\varphi(t)$  can theoretically be measured without cyclic errors (see also Sec. 3.1.1) even for changeable environmental conditions. Techniques such as the J1..J4 approach [190, 191] are based on four Bessel harmonic carriers and analytically solve the parameters  $\varphi(t)$  and  $A$ . However, the valid range of the phase modulation amplitude  $A$  in J1..J4 techniques is still limited, typically to below  $A \leq 5$  rad [192]. Recently, in 2010, the deep phase modulation approach evaluating up to 20 carrier harmonics has been presented by Heinzl *et al.* [192] using direct phase modulation. Very recently, in 2015, a similar approach using optical frequency modulation of external cavity lasers at kHz modulation frequencies has been proposed by Gerberding [193]. In all these works, the Bessel equations are not analytically solved but numerical least-square algorithms are used. Compared to phase extraction using the J1..J4 approach, the deep phase modulation approach increases the valid range of  $A$ . Additionally, the increase in measurement observables allows improvements in the signal-to-noise ratios and permits the introduction of consistency checks [192].

### 3.5. Summary Table

A brief summary of the main distinguishing features of the signal processing techniques reviewed in Secs. 3.2, 3.3 and 3.4 for single interferometers is given in Table 3.1.

**Table 3.1.:** Comparison of optical interferometric signal processing techniques. Abbreviations used: Advantage (+), Disadvantage (−), Direct Phase Modulation (DPM), Direct Frequency Modulation (DFM), Optical Illuminating Frequency Modulation (OIFM)

Technique	Notes
<i>Passive</i>	Individual static phase offsets for multiple photo detectors
<i>Homodyne</i> [141, 143–146]	(+) No active element & unlimited bandwidth (−) Requires special hardware
<i>Phase Stepping</i> [113, 147–154]	Multiple phase steps in a fixed temporal sequence Phase steps applied using DPM or OIFM (+) Simple algorithms, minimized acquisition time (−) Assumes static phase signals, errors from signal fluctuations
<i>Active</i>	Interferometer held at quadrature point using control loop
<i>Homodyne</i> [30, 96, 116] [155–160]	Quadrature point maintained using DPM or OIFM (+) Very low-noise operation below $1 \mu\text{rad} \cdot \text{Hz}^{-0.5}$ possible (−) One complete control loop required per interferometer (−) Control loop can overload, limiting dynamic range
<i>Single Carrier</i>	Frequency offset introduced between two arms using DFM
<i>Heterodyne</i> [3–9, 138, 142] [161–163]	(+) Stable demodulation without cyclic errors (+) High quadrature bandwidths of many MHz possible (−) No self-referencing configurations because DFM is used
<i>Single Carrier</i>	Serrodyne modulation waveform applied using DPM or OIFM
<i>Serrodyne</i>	Modulation scale tuned until unwanted sideband disappears
<i>Homodyne</i> [164–166] [169–174]	(+) Self-referencing configurations using OIFM (−) Reproduction of serrodyne waveform difficult (−) Cyclic errors result for wrong scale factor
<i>Single Carrier</i>	Sinusoidal modulation waveform applied using DPM or OIFM
<i>Windowed</i>	Appropriate window function suppresses unwanted sideband
<i>Sinusoidal</i>	(+) Self-referencing configurations using OIFM
<i>Homodyne</i> [128, 175–178]	(+) Simple sinusoidal modulation waveform (−) Cyclic errors result for wrong scale or window width
<i>Dual Carrier</i>	Sinusoidal modulation waveform applied using DPM or OIFM
<i>Homodyne</i> [30, 179–193]	Two or more carrier harmonics are evaluated Based on Bessel expansion for sinusoidal phase modulation (+) Self-referencing configurations using OIFM (+) Modulation scale can be self-calibrated using $\geq 4$ carriers (−) Multiple carrier frequencies have to be evaluated



## 4. Review of Configurations and Signal Processing Relevant to Fibre Segment Interferometry

This chapter aims to review basic configurations and range-resolved interferometric signal processing techniques that have been used previously, or can, in principle, be used to implement the fibre segment interferometry (FSI) approach that forms the main theme of this thesis. In contrast to the previous chapters, the main focus here lies on signal processing aspects arising from the interrogation of multiple interferometers and on practicalities of interferometric measurements in FSI configurations. To limit the scope of this chapter, some multiplexing techniques, such as coherence-division multiplexing [134] are not reviewed, as, in an FSI setup, this approach would require individual compensating interferometers for every reflective node present and hence is not considered practical. Furthermore, wavelength-division multiplexing (WDM), where interferometric sensors are separated in wavelength, could, in principle, be used to multiplex several sensors in an FSI configuration (see also Kersey *et al.* [67]). However, this requires a dedicated laser source for each interferometric sensor, which is also not considered practical, except in combination with time-division multiplexing (TDM), as discussed in Sec. 4.2. Comprehensive review articles covering the wider field of interferometric sensor multiplexing (for both discrete and distributed sensing) have also been compiled by Kersey *et al.* [103], Dakin [194], Kersey *et al.* [107], Kersey [195], Rogers [69] and Kirkendall *et al.* [30].

In addition to techniques evaluating interferometric phase information, there are several incoherent reflectometry techniques, such as subcarrier-based reflectometry [196, 197] or incoherent optical frequency-domain reflectometry [198] that are related to FSI sensing. In common with FSI, these techniques may be used to interrogate equidistantly spaced in-fibre partial reflectors forming fibre segments that act as long-gauge length sensors, but because they do not use interferometric phase evaluation these techniques generally operate at much lower measurement resolutions. However, unlike interferometric phase evaluation techniques, these schemes directly measure absolute optical path length values and are not polarisation sensitive and therefore their use may be beneficial in certain applications.

In this chapter, some basic aspects of FSI, including typical configurations and the choice of in-fibre partial reflectors, are first discussed in a general way in Sec. 4.1. This is followed by more detailed reviews of prior work in TDM-based FSI in Sec. 4.2,

FSI based on code-division multiplexing (CDM) in Sec. 4.3 and finally FSI based on frequency modulation of the illuminating light before concluding with a summary table of the reviewed FSI signal processing approaches.

## 4.1. Basic Aspects in Fibre Segment Interferometry

**Fibre Segment Interferometry Configurations:** In FSI, where a serial array of low-finesse Fabry-Perot interferometers are interrogated, the occurrence of interference signals from undesired reflector combinations or multiple reflections may lead to considerable noise and crosstalk [103]. This is in contrast to other types of fibre sensor array configurations, such as the forward-ladder topology [195], where different terminals for input and return signals are used. Because sensors are interrogated in a transmissive Mach-Zehnder configuration, these configurations are virtually immune to the negative effects of undesired path combinations or multiple reflections. However, unlike FSI, these configurations do not offer the simplicity and deployment advantages of a single, continuous sensing fibre with light entering and exiting at the same fibre end [199]. In FSI techniques, crosstalk can be reduced through signal processing as well as by optimising the physical FSI configuration and both aspects will be reviewed in detail in the remainder of this chapter.

Several interferometric configurations that can be used in FSI are illustrated in Fig. 4.1. Here, all configurations are shown in a fibre-optic circulator-based setup, however, at the penalty of increased losses, a simple fibre coupler could also be used. In the direct configuration [10, 11] shown in Fig. 4.1(a), light from neighbouring reflectors interferes directly, yielding an interferometric phase signal,  $\varphi(t)$ , which directly corresponds to the optical path difference (OPD) of the fibre segment that is spanned between two neighbouring reflectors. For each segment, the nominal OPD is  $\eta = 2n_g l_s$ , where  $l_s$  is the physical length of the segment and  $n_g$  is the group refractive index of the optical fibre. In contrast, in the compensating configuration [199, 200] shown in Fig. 4.1(b), a compensating interferometer of OPD  $\eta = 2n_g l_s$  reduces the effective OPD of every segment interference to near zero, an approach related to coherence-based path separation shown in Fig. 3.3(b). This OPD balancing can be useful to reduce laser phase noise or to permit the use of low-coherence sources to eliminate signals from undesired reflector combinations with non-zero OPD. In some techniques, the compensating interferometer in Fig. 4.1(b) could alternatively also be placed in front of the photo detector with equal performance.

Contrary to the direct and compensating configurations of Figs. 4.1(a) and (b), which yield one interferometric phase signal per fibre segment, the common local oscillator (LO) configuration [1, 201–204] of Fig. 4.1(c) results in a separate interferometric signal for each individual reflector. Segment data can then be obtained by numerical subtraction of the phase signals from two neighbouring reflectors. Furthermore, in the common LO configuration, through altering the common LO length, the position of the LO OPD balancing point can be placed anywhere along the sensing fibre. In general, the direct and compensating configurations of Figs. 4.1(a) and (b) are physically down-leak insensitive (see also Sec. 3.1.3), while the common

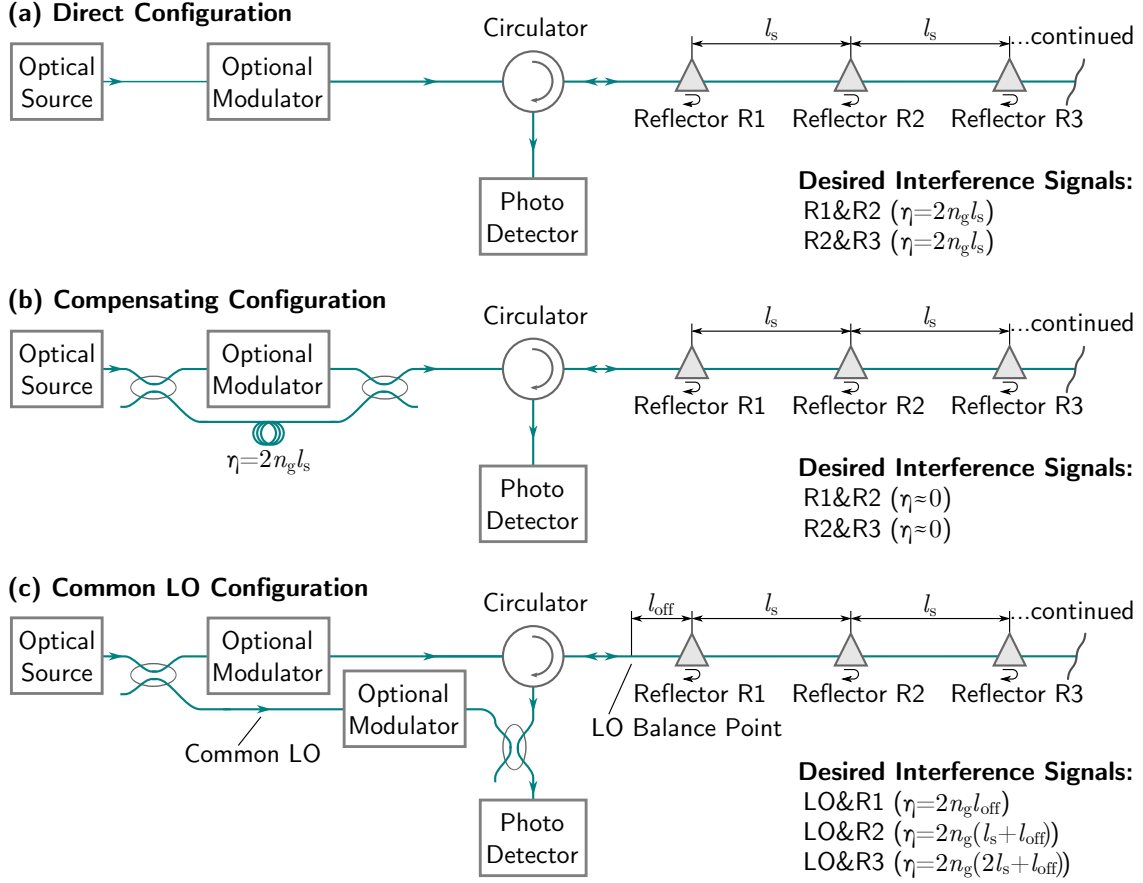


**Figure 4.1.:** Illustration of three basic FSI configurations. In (a), the interference occurs directly between signals from neighbouring reflectors at segment distance  $l_s$  at non-zero OPD  $\eta = 2n_g l_s$ , where  $n_g$  is the group refractive index of the optical fibre. In (b), a compensating interferometer of OPD  $\eta = 2n_g l_s$  is used to reduce the OPD of the desired interference signals to near zero. In (c), a common local oscillator (LO) is used to interrogate signals from each reflector individually, leading to unique OPDs for each reflector. Here, the LO offset length  $l_{\text{off}}$ , measured from the LO balance point, is additionally required to calculate the OPD  $\eta$ , as shown in the bottom right corner.

LO configuration of Fig. 4.1(c) only achieves down-lead insensitivity after numerical subtraction of the reflector data when segment data is calculated.

In all three configurations shown in Fig. 4.1, an optional direct frequency or phase modulator can be inserted for techniques that require such a modulator. In the direct configuration of Fig. 4.1(a), the modulator inherently acts on both arms of any segment interferometer, while in the compensating and common LO configurations, the modulation within the two arms is different. Out of the three configurations shown in Fig. 4.1, only the common LO configuration of Fig. 4.1(c) can be used for techniques based on optical illuminating frequency modulation (discussed further in Sec. 4.4), because there each reflector signal needs to be addressed by a unique nominal OPD. In the common LO configuration, through the placement of the LO balance point, signals from any unintended direct segment interference can be arbitrarily offset in OPD from the desired reflector signals interfering with the common LO, thus allowing range-based rejection of undesired signals, which will be used beneficially in the experiments in Chap. 6. However, because the light,

especially for the further away reflectors, has to travel long distances through the fibre before interference, there is greater susceptibility to polarisation-induced signal fading [98, 99] (see also Sec. 2.4) in the common LO configuration of Fig. 4.1(c), compared to the other configurations of Figs. 4.1(a) and (b). Key aspects of the three FSI configurations of Fig. 4.1 are also summarised in Table 4.1.

The properties of the in-fibre partial reflectors used also influence the choice of FSI configuration. For a given reflective power  $rP_{\text{in}}$ , with reflectivity  $r$  of the in-fibre partial reflectors and input power  $P_{\text{in}}$ , the direct and compensation configuration of Figs. 4.1(a) and (b) lead to an effective interferometric power  $P_{\text{eff}}$ , according to Eq. (3.3), of  $P_{\text{eff}} \propto \sqrt{r^2 P_{\text{in}}^2} = rP_{\text{in}}$ . This means that the interference signals of undesired, non-neighbouring reflector combinations are principally on the same power level as the desired interference signals between neighbouring reflectors, while multiple reflections are at power levels  $\propto r^o P_{\text{in}}$ , where  $o$  is the multiple reflection order. In contrast, for the common LO configuration of Fig. 4.1(c) with LO power  $P_{\text{LO}}$ ,  $P_{\text{eff}}$  is proportional to  $\sqrt{r} \sqrt{P_{\text{LO}} P_{\text{in}}}$ , using the phenomenon of heterodyne gain that has been previously described in Sec. 3.1.1. Therefore, by increasing  $P_{\text{LO}}$  or lowering  $r$ , the power ratios between desired interference signals, where light from the reflectors interferes with the LO, and undesired interferometric signals from direct interference between reflectors as well as multiple reflections, with power levels as described above, can be changed, allowing suppression of direct reflector interference. Furthermore, in the common LO configuration of Fig. 4.1(c), a strong LO also lowers the reflectivity requirements and therefore eases reflector production effort, which will be used beneficially in the later experiments in Chap. 6. In general, a lower limit on the reflectivity of the partial in-fibre reflectors in FSI, apart from carrier-to-noise concerns, is also set by the natural occurrence of Rayleigh scattering (see also Sec. 2.2), where the signal from the reflectors needs to be significantly stronger than the Rayleigh back-scatter returned from the fibre. The effects of reflector power in fibre sensor arrays are also further discussed in Kersey *et al.* [107].

**Table 4.1.:** Comparison of the three FSI configurations of Fig. 4.1.

Abbreviations used: Advantage (+), Disadvantage (−)

Configuration	Notes
<i>Direct</i>	Direct interference between segment signals. (+) Simple configuration which yields segment signals (−) Multiple reflections and path combinations may present (−) Phase noise due to OPD-imbalanced operation
<i>Compensating</i>	Compensating interferometer reduces segment OPDs to $\approx 0$ . (+) Allows OPD-balanced operation and yields segment signals (+) Low-coherence sources allow suppression of unwanted paths (−) More complex interferometric configuration
<i>Common LO</i>	Interference of individual reflector signals with common LO. (+) Reflectivity requirements are relaxed (+) Unwanted path combinations are suppressed (−) Phase noise due to non-zero OPD

**Choice of In-Fibre Partial Reflectors:** The choice of partial reflector is very important for the practical implementation of FSI. Historically, the first FSI implementations [10] used mechanical fibre splices, as illustrated in Fig. 4.2(a), where a small gap between adjacent fibre ends is maintained by a mechanical fixture and the glass-to-air Fresnel reflections are used to provide a return signal. Apart from bulkiness and possible mechanical instability, this solution may also cause light losses and consistent reflectivities are difficult to achieve. However, this approach is low-cost and simple to set up and is used during parts of this thesis. Later works on FSI for fibre optical hydrophone arrays, such as Cranch *et al.* [11, 12], often use coupler-based reflectors. Here, a fibre coupler is used to guide parts of the incoming light towards a fibre-end mirror, as shown in Fig. 4.2(b), or towards a fibre loop [200]. The reflectivity of this assembly can be tailored by adjusting the coupler split ratio. While still being bulky, this all-fibre solution offers increased stability compared to the use of mechanical splices.

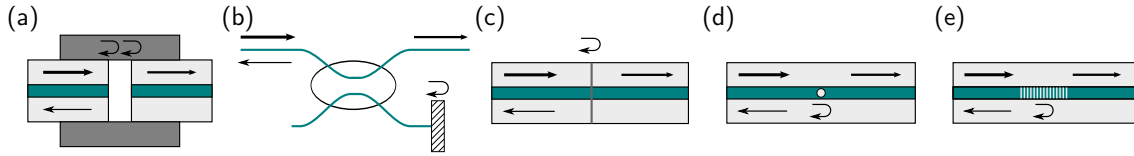


**Figure 4.2.:** Partial reflectors for FSI: (a) Mechanical splice reflector (b) Coupler-based reflector (c) Fusion splice reflector (d) Cavity-based reflector (e) FBG-based reflector

Further possibilities for in-fibre reflectors include the use of fusion-spliced, cavity-based or FBG-based partial in-fibre reflectors. Fusion-splice reflectors [205], illustrated in Fig. 4.2(c), can be formed by coating one fibre end with a thin layer of a reflective substance, such as  $\text{TiO}_2$ , before fusion splicing. The reflectivity of the splices can then be adjusted by altering the coating thickness and splice parameters. In cavity-based reflectors, illustrated in Fig. 4.2(d), a cavity, with dimensions on the order of  $\mu\text{m}$ , is formed within the core of an optical fibre and acts as a partial in-fibre reflector. A cavity can be fabricated using techniques such as selective etching of the core [206] or femtosecond laser-induced micro-void inscription [207]. When FBGs are used as in-fibre partial reflectors in FSI, as first proposed by Morey [208], and demonstrated by Okawara *et al.* [199] and illustrated in Fig. 4.2(e), the FBGs need to be sufficiently broadband to return signals in all conceivable strain and temperature conditions. Very short and therefore very broadband FBGs have also been successfully used as in-fibre partial reflectors [94] in techniques related to FSI. In general, for both cavity and FBG-based reflectors, the use of infrared femtosecond lasers [209] would allow the inscription of the reflectors without removing the fibre coating, which would offer many practical advantages, such as increased mechanical strength and ease of production. As previously mentioned in Sec. 2.3, for FBG-based reflectors similar practical advantages could also be expected from the use of draw-tower gratings [75].

## 4.2. Fibre Segment Interferometry Based on Time-Division Multiplexing

In time-division multiplexing (TDM), which originates from light/radio detection and ranging (lidar/radar) technologies [210], a pulsed signal is used to address multiple constituent interferometers and time-dependent gating is used to separate the return signals into individual range channels according to their time-of-flight. The spatial resolution in TDM is proportional to the resolvable pulse duration and is thus inversely related to the modulation hardware bandwidth. In the context of fibre sensing, TDM is also frequently used as optical time domain reflectometry [43] for the incoherent multiplexing of intensity-based sensors such as FBGs (see Sec. 2.3) or in distributed sensing (see Sec. 2.2). A general feature of TDM multiplexing in both coherent and incoherent cases is the dependence, due to the potential overlap of pulses, of the duty cycle  $D$  on the maximum number of sensors  $N$  that can be multiplexed, with  $D = N^{-1}$  being the maximum duty cycle possible. Low duty cycles limit the achievable carrier-to-noise ratios (CNR), where for the case of a direct FSI configuration of Fig. 4.1(a), the CNR was found to be proportional to  $D^2$  [11].

As previously discussed in Sec. 2.4, historically the first FSI technique has been proposed by Dakin *et al.* [10] using a two-pulse, or differential delay, TDM approach employing the direct interference configuration of Fig. 4.1(a). This is also illustrated in Fig. 4.3, with further implementations demonstrated by Cranch *et al.* [11, 12] and Liao *et al.* [211, 212]. Here two sequential light pulses of different optical frequencies  $f_{\text{opt},1}$  and  $f_{\text{opt},2}$  exit the acousto-optic modulator (AOM), which are separated by a time difference equal to the time-of-flight required to traverse one fibre segment of length  $l_s$  and back. Upon returning from the sensor array, the light of the reflectors forming a segment interferes and the resulting photo detector signal can be range-gated. For each range channel, the signals can then be demodulated similar to regular heterodyne interferometry (see Sec. 3.3.1) at the difference frequency of  $f_{\text{opt},1}$  and  $f_{\text{opt},2}$  to extract the phase signals  $\varphi(t)$  for each segment. Fig. 4.3 also illustrates how a tail of multiple reflections as well as unwanted reflector combinations can be present in the photo detector signal, both within and after the intended gating periods for

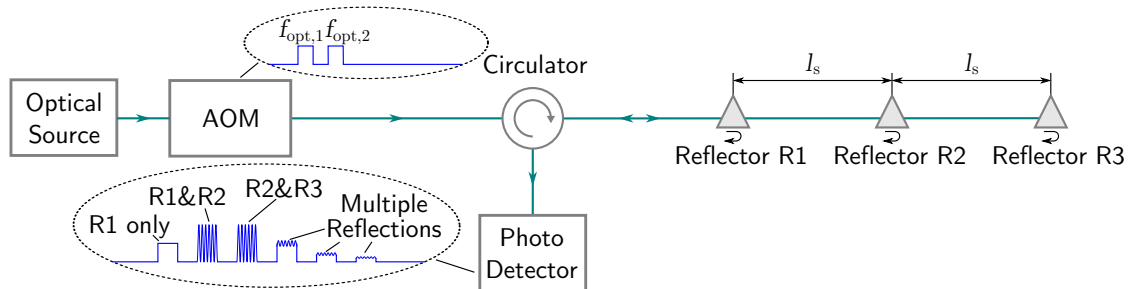


**Figure 4.3.:** Illustration of the two-pulse TDM FSI setup used by Dakin *et al.* [10] and Cranch *et al.* [11]. Here two sequential light pulses of different optical frequencies  $f_{\text{opt},1}$  and  $f_{\text{opt},2}$  exit the acousto-optic modulator (AOM) and the resulting signals at the photo detector are shown by the inset, marking the signals due to the desired segment interference as well as showing a tail of signals due to undesired path combinations.

the desired range channels. Here, in some cases, advanced algorithms based on a layer peeling inverse scattering approach [213] have also been used to separate undesired path combinations from the desired phase signals. A further group of FSI techniques, often referred to as path-matched differential interferometers (PMDI), originate from the work by Brooks *et al.* [214] for a non-FSI ladder configuration. FSI implementations of PMDI, using a compensating configuration of Fig. 4.1(b), have been proposed by Kersey *et al.* [200] using fibre loop reflectors and recently by Okawara *et al.* [199] using FBGs as in-fibre partial reflectors, where phase-generated carrier processing (see Sec. 3.4), employing a phase modulator within the compensating interferometer, was used for interferometric phase evaluation.

A general feature of the cited PMDI works that use homodyne processing [199, 200, 214] is that the pulse frequency is much greater than the signal processing carrier frequencies, effectively sampling the homodyne carrier signals. This is in contrast to dual-pulse heterodyne processing techniques [10–12], illustrated in Fig. 4.3, where the heterodyne carrier frequency is much faster than the inverse pulse duration and the interferometric phase signal can be independently evaluated for every pulse. Furthermore, TDM can also be combined with interferometric signal processing techniques that use optical illuminating frequency modulation, such as the phase-generated carrier technique (see Sec. 3.4), in a compensating configuration with non-zero OPD [215] or using serrodyne modulation in a non-FSI forward ladder configuration [216]. There has also been considerable recent work combining TDM with WDM for large scale hydrophone arrays [11, 12, 211, 212]. Here WDM is conveniently used to allow several banks of sensors to be addressed in parallel using an individual wavelength for each bank, where the two-pulse TDM FSI configuration, shown in Fig. 4.3, is then used to multiplex sensors within each bank. In one recent implementation in 2013 by Liao *et al.* [211], TDM FSI multiplexing of a total of 1024 sensors in four wavelength channels with phase noise levels of  $40 \mu\text{rad} \cdot \text{Hz}^{-0.5}$  was demonstrated for seismic reservoir exploration.

### 4.3. Fibre Segment Interferometry Based on Code-Division Multiplexing

CDM is a group of multiplexing techniques that are widely used in areas such as wireless communications and global positioning systems [136], where they are also known as code-division multiple access (CDMA) techniques, allowing several senders to transmit data simultaneously over one channel using coded modulation. Often pseudo-random sequences, such as the maximum length sequence (MLS) (further discussed in Sec. 5.2.2), are used due to their good auto-correlation properties, allowing signal energy to be dispersed evenly for out-of-range signals. A general feature of CDM techniques is that continuous-wave sources are used and therefore the duty cycle  $D$  can reach values of up to 50 % [217], allowing higher CNR levels to be achieved at lower peak powers, when compared to TDM approaches discussed in the previous section. Similar to TDM, the spatial resolution in CDM is proportional to the code symbol duration and thus inversely related to the modulation bandwidth.

CDM has also been applied to lidar [218–220], which has related requirements to FSI in some respects, however, there have only been few reported applications of CDM techniques in interferometric sensor multiplexing. These can be grouped into intensity-modulated interferometric and phase-modulated interferometric schemes, where a phase-modulated interferometric CDM scheme is also proposed and demonstrated in this thesis in Chap. 5. Phase-modulated interferometric CDM schemes inherently allow interferometric phase measurements, while intensity-modulated techniques only use CDM for range-based signal separation and rely on further interferometric signal processing techniques for interferometric phase evaluation. Here, the theoretical work by Street *et al.* [217], which is relevant to both intensity-modulated and phase-modulated CDM, recognised the importance of the anti-aliasing filter to crosstalk performance in CDM. Whilst this work did not receive much public attention, the investigation presented in this thesis in Chap. 5 also highlights the importance of anti-aliasing filtering in CDM.

Intensity-modulated interferometric CDM was first demonstrated in 1990 by Al-Raweshidy *et al.* [221] for multiplexing two Mach-Zehnder interferometric sensors. Advanced implementations of this concept have since been described by Kersey *et al.* [222] and Kullander *et al.* [223]. All of these publications demonstrate range-based signal separation in non-FSI interferometric configurations, but do not detail any interferometric signal processing techniques used for phase determination. Interestingly, Kersey *et al.* [222] also found that unipolar-bipolar MLS coding and decoding arrangements can result in theoretically zero crosstalk, a general result that is applicable to both intensity and phase-modulated interferometric CDM and that will be used in the work presented in Chap. 5.

The first phase-modulated interferometric CDM system that could, in principle, be applied to interferometric sensor multiplexing, was proposed by Rask *et al.* [4, 219] in the area of coherent Doppler lidar anemometry in the early 1990s. Here, in a common LO configuration related to Fig. 4.1(c), one AOM is included in the measurement arm and an additional AOM in the common LO arm. The AOMs can be driven to have a relative phase difference of  $0^\circ$  or  $180^\circ$  by reversing the AOM drive polarity, thus introducing a phase-modulated code. Additionally, a frequency offset between the

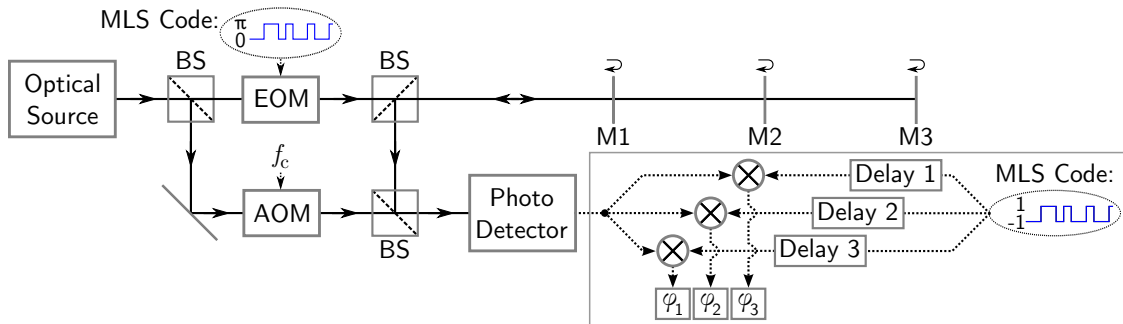


**Figure 4.4.:** Illustration of the original free-space digitally enhanced heterodyne implementation by Shaddock [1]. Here an AOM introduces the heterodyne carrier  $f_c$  into the common LO of the interferometer and a MLS code is applied by the EOM. Return signals originate from partial mirrors M1, M2 and M3 and the digital signal processing performs range-based signal separation using suitably delayed versions of the code.



two AOMs allows heterodyne interferometric signal processing (see also Sec. 3.3.1). However, because AOMs only allow slow reversal of polarities, the spatial resolution achievable was low, on the order of 150 m. More recently, in 2007, a related approach, using the common LO configuration of Fig. 4.1(c), where an AOM is included in the LO to introduce a heterodyne carrier and an electro-optic phase modulator (EOM) is inserted in the other interferometric arm to introduce  $0^\circ$  and  $180^\circ$  code symbols for CDM has been proposed by Shaddock [1]. This technique, named “digitally enhanced heterodyne processing”, has gained considerable popularity [201–203], mainly in the area of precision interferometry and this approach is illustrated in Fig. 4.4, however, it used two active modulators and cannot be used in a self-referencing configuration. Using high-speed digital signal processing, sub-metre spatial resolutions have been achieved in the very recent (2014) work by Isleif *et al.* [203], where also noise levels as low as  $9 \mu\text{rad} \cdot \text{Hz}^{-0.5}$  at 10 Hz have been demonstrated using a high-end laser system for the measurement of a single constituent interferometer.

Very recently, in 2012, a technique named “digitally enhanced heterodyne processing” has been proposed by Sutton and Shaddock *et al.* [204] that uses a monolithically integrated dual parallel Mach-Zehnder phase modulator (DPMZ) [224], also known as an optical quadrature modulator, which allows the introduction of four discrete code symbols with phase modulation [ $0^\circ, 90^\circ, 180^\circ, 270^\circ$ ] through a nested MZ configuration, as illustrated in Fig. 4.5. Here two digital bit streams for the real and complex component of the phase modulation are required and the amplitudes of the two bit stream signals as well as the bias voltage on the outer MZ interferometer need to be controlled precisely by the DPMZ controller. While the digital homodyne approach can be used in a common LO configuration according to Fig. 4.1(c), it can also be used in a self-referencing configuration, as illustrated in Fig. 4.5. This opens interesting new applications for this technique as a competitor to self-referencing techniques based on optical illuminating frequency modulation discussed later. A particular advantage of the digital homodyne approach compared to techniques based on optical illuminating frequency modulation in this context is that signals can be separated both by delay and OPD, once a minimum OPD is exceeded, in principle also allowing the use of digital homodyne schemes in the direct interference configurations shown in Fig. 4.1(a). However, the digital homodyne technique requires the use of a complex DPMZ modulator with two high-speed

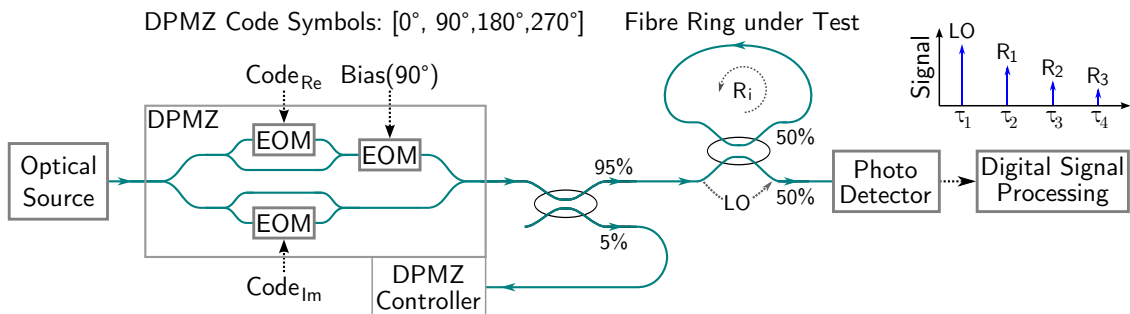


**Figure 4.5.:** Self-referencing implementation of the digitally enhanced homodyne technique proposed by Sutton *et al.* [204]. Here, a DPMZ can introduce four code symbols. This demonstration involves sequential passes through a fibre ring to produce test signals  $R_i$  that are each delayed by  $\tau_i$  and interfere with the LO formed by the direct pass through the fibre-ring coupler.

digital drive signals and associated control circuits and, in contrast to the optical illuminating frequency modulation approach discussed later, spatial resolution is proportional to the hardware bandwidth of the modulation equipment.

## 4.4. Fibre Segment Interferometry Based on Optical Illuminating Frequency Modulation

A general property of range-resolved interferometric signal processing techniques (see also Sec. 3.1.2) based on optical illuminating frequency modulation (OIFM) is that spatial resolution is a property of the optical frequency excursion achievable by the laser source. Therefore spatial resolution is decoupled from the modulation bandwidth in OIFM, contrary to both the TDM and CDM multiplexing approaches discussed earlier. This allows very high spatial resolutions to be achieved using OIFM, even for moderate signal processing hardware capabilities, as will also be experimentally demonstrated in Chap. 6. Since the 1980s, many continuous-wave ranging techniques based on OIFM, capable of absolute OPD measurements over large dynamic ranges, have been demonstrated, originating from earlier work in radar [225]. This includes linear (serrodyne or triangular) [226, 227] schemes, often referred to as frequency modulation continuous-wave (FMCW) techniques or wavelength scanning interferometry [228, 229] in the context of imaging interferometry, but also sometimes based on sinusoidal [230, 231] modulation approaches. Absolute OPD accuracies on the orders of parts-per-million have been achieved using linear OIFM systems based on widely-tunable lasers, equating to uncertainties on the orders of  $\mu\text{m}$  over a typical maximum range of 1 m [227]. However, there have only been few instances, as will be reviewed below, where interferometric phase evaluation was additionally attempted using these ranging techniques. In general, interferometric phase evaluation increases measurement resolution by many orders of magnitude, but raises the complexity, particularly due to the interferometric  $2\pi$  phase ambiguity (see also Sec. 3.1.1).

**Linear Range-Resolved Signal Processing Techniques:** In the literature, linear range-resolved signal processing techniques that allow interferometric phase determination are generally techniques that extend the previously discussed pseudo-heterodyne scheme (see Sec. 3.3.2) [172], which uses a serrodyne OIFM waveform, to multiplex interferometers. This is sometimes also referred to as FMCW multiplexing or frequency-division multiplexing (FDM)<sup>1</sup>. Following the first applications of OIFM-based ranging [232], it was recognized, as described by Sakai [102, 233, 234], that this could also be used for the phase-resolved interrogation of multiple interferometers. Furthermore, it was found that proper operation without crosstalk requires the nominal OPDs of every constituent interferometer to adhere to an integer grid. This is because the peak optical frequency excursion can, in principle, be then tuned so that each constituent interferometer experiences a peak phase excursion that is a multiple of  $2\pi$ . This is in addition to the previously described general requirement

<sup>1</sup>The term FDM is loosely defined and also refers to the multiplexing of interferometric sensors using several lasers [103], modulated at different frequencies using the phase-generated carrier method (see Sec. 3.4), which does not constitute a range-resolved signal processing technique.

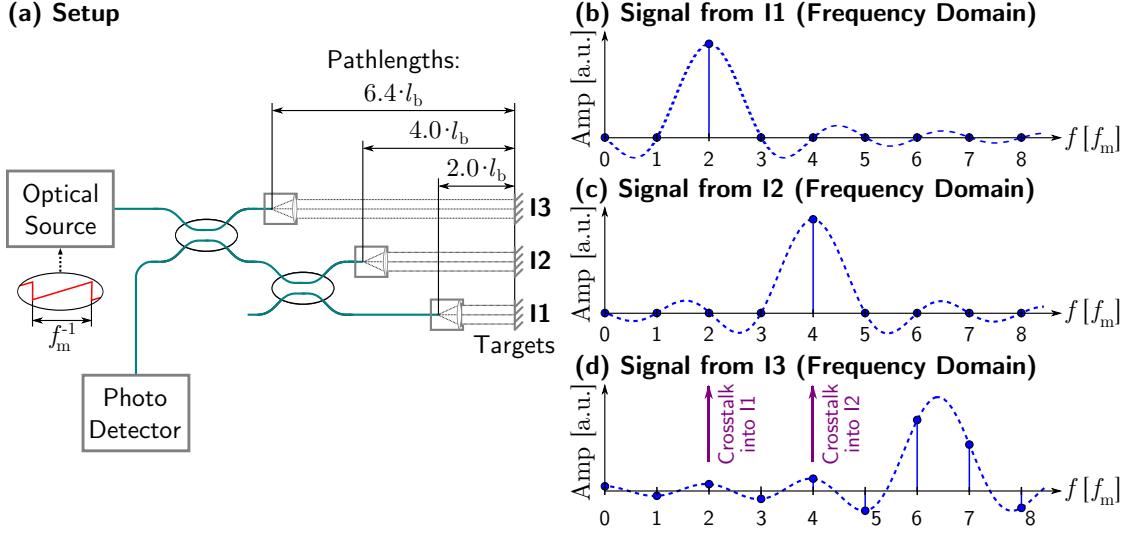


**Figure 4.6.:** Illustration of linear OIFM-based interferometric sensor multiplexing, adapted and extended from Zheng [235], using serrodyne OIFM at modulation frequency  $f_m$ . (a) shows the setup used, while (b), (c) and (d) plot the carrier amplitudes corresponding to each constituent interferometer (I1, I2 and I3) in the frequency domain, where the path length of I3 is not an integer multiple of the base length unit  $l_b$  for instructive purposes.

of the pseudo-heterodyne technique (see Sec. 3.3.2) for the peak phase excursion to be a multiple of  $2\pi$  in order to avoid cyclic errors [173].

This principle is also explained in Fig. 4.6, adapted and extended from Zheng [235]. Here Fig. 4.6(a) shows the setup for three free-space long gauge-length interferometric displacement sensors with differing nominal OPDs. These are multiplexed using serrodyne OIFM of modulation frequency  $f_m$ . In Fig. 4.6, for instructive purposes, only two (I1 and I2) constituent interferometers adhere to the integer OPD grid, derived from the base length unit  $l_b$ , while the third constituent interferometer (I3) is chosen to have a fractional OPD relation to I1 and I2. The peak frequency excursion of the serrodyne modulation waveform is tuned so that I1 and I2 have peak phase excursions that are integer multiples of  $2\pi$ . In this case, Figs. 4.6(b) to (d) show typical signals from each interferometer in the frequency domain, exhibiting frequency components at multiples of the modulation frequency  $f_m$ . These can then be used as carriers to demodulate (see Sec. 3.1.4) the desired phase signals.

In Figs. 4.6(b) to (d) a sinc-shaped envelope is drawn using dashed lines, which is a direct result of the serrodyne ramp. Here, it can be seen that when the OPDs of constituent interferometers are placed on the correct grid, as for I1 and I2 in Figs. 4.6(b) and (c), respectively, the signal is ideally concentrated in the main peak. Because the sinc-shaped envelope has zeros at multiples of the modulation frequency  $f_m$ , there is no signal amplitude at any other carrier frequency. Therefore, no crosstalk into other interferometers originates from I1 and I2. In contrast, for a constituent interferometer that is not placed on the integer OPD grid, as, for example I3 shown in Fig. 4.6(d), the carrier amplitudes spread over many frequencies with an amplitude distribution that is determined by the sinc-shaped envelope. This reduces the amplitude of the desired demodulation carrier, but more importantly, also causes crosstalk into other interferometers, where in Fig. 4.6(d) it can be seen

that carrier components of non-zero amplitude at the demodulation frequencies of the other constituent interferometers,  $2f_m$  for I1 and  $4f_m$  for I2, exist.

It is important to note that in the linear OIFM-based multiplexing approaches discussed, constituent interferometers that are not on the integer OPD grid and that can thus cause crosstalk can also originate from parasitic reflections or undesired path combinations. In some cases these are therefore unavoidable or place further restrictions on the choice of permissible OPDs of constituent interferometers [102,233]. In general, for realistic serrodyne modulation waveforms with a non-instantaneous fly-back period, frequency content corresponding to the fly-back will also be present in other parts of the carrier spectrum [232]. A further challenge is that ideal serrodyne optical frequency sweeps are often difficult to reproduce in practice due to the high frequency content of the serrodyne modulation signal [174,236], leading to broadened peaks in the frequency domain, which, in some cases, can be improved using triangular sweeps [121,174]. Linear OIFM-based multiplexing of interferometric sensors does not appear to be widely used [195], with papers mainly limited to the 1980s [102,216,233,237,238] and only two more recent papers in 2001 [239] and in 2007 by Zheng [235]. Although the application of linear OIFM-based multiplexing to FSI has been proposed previously by Morey [208], only one paper by Won *et al.* [239] uses a common LO FSI configuration of Fig. 4.1(c) and only demonstrates the multiplexing of two fibre segments.

**Sinusoidal Range-Resolved Signal Processing Techniques:** The only range-resolved interferometric signal processing technique based on sinusoidal optical illumination modulation that has been found in the literature is the windowed sinusoidal homodyne processing technique by Sakai *et al.* [128]. In this context, the well-known phase-generated carrier [180] method (see also Sec. 3.4) is also based on sinusoidal optical illumination modulation but does not, however, allow multiple interferometers to be interrogated using only a single laser source and a single photo detector. The technique by Sakai *et al.* [128] has previously been discussed for signal processing in single interferometers in Sec. 3.3.2, and Fig. 4.7(a) illustrates the setup used by Sakai *et al.* [128] to multiplex several interferometers with different OPDs, however, in a non-FSI configuration. In general, as discussed previously, the advantages of sinusoidal over linear waveforms lies in the ease of modulation, with a sinusoidal modulation waveform only consisting of a single spectral component without any harmonics. To be applied to FSI, the sinusoidal approach by Sakai *et al.* [128] would require the common LO configuration of Fig. 4.1(c).

The upper graph of Fig. 4.7(b) shows a typical photo detector signal resulting from the sole interrogation of interferometer 1 (I1) in Fig. 4.7(a), which has an OPD corresponding to 4 times the base length unit  $l_b$ . Also indicated is the rectangular gating period of duration  $T_g$ . The lower graph of Fig. 4.7(b) then shows the corresponding frequency content of the signal after gating. The working conditions of the technique as laid out by Sakai *et al.* [128] assume that the gating period is short enough that the part of the photo detector signal under the gating period can essentially be viewed as a single-frequency carrier and require that the sinusoidal optical frequency modulation amplitude is tuned so that an integer number of carrier periods fit within the gating period. For I1 this can be approximated by a

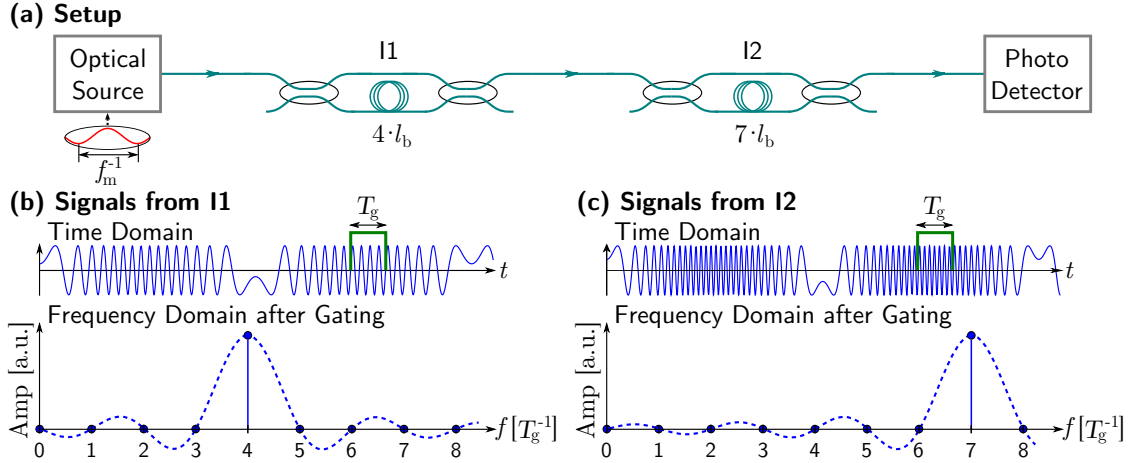


**Figure 4.7.:** Illustration of the setup (a) used by Sakai *et al.* [128] with forward-coupling MZ interferometers, where the OPDs correspond to integer multiples of the base length unit  $l_b$ . The upper graphs of (b) and (c) plot the photo detector signals attributed to interferometers (I1 and I2) in the time domain along with the rectangular gating function of duration  $T_g$ , while the lower graphs show the carrier amplitudes and the sinc-shaped envelope after gating.

sinc-shaped envelope centred at a frequency of  $4T_g^{-1}$  and with zeros at every other multiple of  $T_g^{-1}$  as shown in Fig. 4.7(b). Fig. 4.7(c) shows the analogous case for the signals originating from interferometer 2 (I2) at an OPD corresponding to  $7l_b$ . These spectra are related to the case of linear OIFM-based multiplexing shown in Figs. 4.6(b) to (d), with the key difference being that the frequency base unit in Sakai *et al.* [128] is determined by the inverse gating duration  $T_g^{-1}$  and not by the modulation frequency  $f_m$ . Just like in the previous case of serrodyne modulation, in order to avoid crosstalk, the OPDs of the constituent interferometers need to be on a grid derived from integer multiples of  $l_b$  so that the sinusoidal modulation amplitude can, in principle, be tuned for the maximum of the sinc-shaped envelope of each constituent interferometer to fall on the zeros in the sinc-shaped envelope of every other interferometer. The signals for each interferometer can then be uniquely separated by demodulation at the corresponding peak frequencies of the sinc-shaped envelope. Also, in comparison with linear OIFM-based multiplexing, the duty cycle in sinusoidal OIFM-based multiplexing is reduced by the requirement for gating, reducing the achievable CNR. For sinusoidal OIFM, crosstalk levels of  $-35$  dB were demonstrated experimentally [128] for the interrogation of two interferometers, with factors influencing crosstalk performance identified as the quality of the gating window implementation and the precision of the OPDs matching the OPD grid.

In general, for both linear and sinusoidal modulation approaches discussed here, it is obvious that the requirement of integer OPD ratios considerably reduces the flexibility and practicality of the techniques. Here, a key improvement will be the sinusoidal modulation approach presented in Chap. 6. There, a smooth window function is used instead of rectangular gating, which, together with a time-variable demodulation approach, permits continuously variable placement of the OPDs of the constituent interferometers once a minimum OPD separation is exceeded, removing any need to adhere to an integer OPD grid.

## 4.5. Summary Table

A brief summary of the main distinguishing features of the reviewed range-resolved signal processing techniques for FSI of Secs. 4.2, 4.3 and 4.4 is given in Table 4.2.

**Table 4.2.:** Comparison of range-resolved optical interferometric signal processing techniques in prior work that are, in principle, capable of FSI operation. Abbreviations used: Optical Illuminating Frequency Modulation (OIFM), Advantage (+), Disadvantage (–)

Technique	Notes
<i>Two-Pulse Time-Division</i> [10–12, 211–213]	Two pulses, offset in optical frequency, are reflected from either side of fibre segment and coincide at photo detector. (+) Uses simplest possible, direct FSI configuration (+) Large sensor arrays over 1000 sensors when used with WDM (–) Multiple reflections and path combinations may be present (–) Low duty cycle of source limits carrier-to-noise ratio
<i>Path-Matched Time-Division</i> [199, 200, 214]	One pulse is reflected from either side of fibre segment and compensating interferometer reduces OPD to near zero (+) Allows OPD-balanced operation with low phase noise (+) Low-coherence sources allow suppression of unwanted paths (–) Low duty cycle of source limits carrier-to-noise ratio
<i>Digitally Enhanced Heterodyne Code-Division</i> [1, 201–203]	Heterodyne interferometry is combined with phase modulation to perform phase-modulated code-division multiplexing (+) Good carrier-to-noise ratio from high duty cycle of source (+) Sub-metre spatial resolution (–) No self-referencing configurations possible (–) Requires two active modulators
<i>Digitally Enhanced Homodyne Code-Division</i> [204]	Quadrature phase modulator is used for both interferometric signal processing and code-division multiplexing (+) Self-referencing configuration possible (+) Good carrier-to-noise ratio from high duty cycle of source (–) Requires complex quadrature phase modulator
<i>Linear OIFM</i> [102, 216, 233] [235, 237–239]	Linear OIFM modulation allows OPD-dependent separation of interferometers by carrier frequency (+) Spatial resolution decoupled from processing bandwidth (–) Difficult modulation waveform with many harmonics (–) Crosstalk if OPDs do not adhere to integer grid
<i>Sinusoidal OIFM</i> [128]	Sinusoidal OIFM modulation allows OPD-dependent separation of interferometers by carrier frequency after rectangular gating (+) Spatial resolution decoupled from processing bandwidth (+) Simple modulation waveform with one frequency component (–) Reduced duty cycle due to requirement for gating (–) Crosstalk if OPDs do not adhere to integer grid

# 5. Code-Division Multiplexing Technique for Fibre Segment Interferometry

## 5.1. Introduction

In this chapter, a novel range-resolved interferometric signal processing technique, primarily intended for fibre segment interferometry (FSI) applications, is proposed. Here, phase-modulated code-division multiplexing (CDM) (see also Sec. 4.3), providing range-based signal separation, is combined with single-sideband [164, 165] (SSB) homodyne signal processing (see also Sec. 3.3.2), performing interferometric phase evaluation. This is novel because previous range-resolved optical interferometric signal processing techniques based on phase-modulated CDM, as reviewed in Sec. 4.3, required either two active modulators or a complex, dual parallel Mach-Zehnder phase modulator. By combining CDM with SSB homodyne signal processing as proposed in this thesis, both range-based signal separation and interferometric signal processing can be performed using only a single, regular electro-optic phase modulator with a single drive signal. This is applied to FSI applications in the common LO FSI configuration of Fig. 4.1(c).

In the first section of this chapter, the theory required for the combination of SSB with phase-modulated CDM is developed, extending the Fourier series expansion approach used to describe regular SSB processing [164, 165]. These extended equations allow the calculation of range-dependent crosstalk and sideband suppression values for an arbitrary phase modulation waveform. Additionally, the effects of inter-symbol interference caused by anti-aliasing filtering, necessary in any practical digital signal processing system, are considered. It should be noted that in prior phase-modulated CDM works [1, 4, 201, 202, 204] (see also Sec. 4.3), the influence of anti-aliasing filtering appears to be neglected or not specifically investigated. As discussed in Sec. 4.3, the only publication that researches the impact of anti-aliasing filtering is the work by Street *et al.* [217]. From the modelling performed there, it is concluded that, due to the influence of the anti-aliasing filter, the minimum sensor spacing needs to be increased in some cases and that strict rules describing these constraints are difficult to formulate. In this thesis, the influence of anti-aliasing filtering is included in the theoretical description, allowing both crosstalk and cyclic errors to be quantified in order to use this for system design decisions. Furthermore, the steps

necessary to design the modulation waveform are detailed and, using the theoretical description, it is shown how the impact of the anti-aliasing filter can be mitigated by the introduction of guard times at code symbol transitions, an approach that should, in principle, also be applicable to other CDM techniques. Following this theoretical treatment, the experimental setup and the electronic implementation are discussed. In the subsequent sections, results of quantitative measurements of cyclic errors, noise, crosstalk and dynamic response are presented. Also results from a strain measurement that is exemplary for the envisaged FSI applications, such as dynamic strain and curvature measurements on large engineering structures, are shown. At the end of the chapter, the general practicality of the scheme and improved concepts for future research are discussed, before concluding with a brief summary.

## 5.2. Theory

### 5.2.1. Single-Sideband Equations in Prior Work

SSB is a generic theory describing the shape and scale that a periodic phase modulation waveform must possess so that the desired phase signal  $\varphi(t)$  of Eq. (3.3) can be unambiguously demodulated at a single carrier frequency, as discussed previously in Sec. 3.3.2. This is possible when a suitable, periodic phase modulation waveform is scaled until one of the two carrier sidebands present in the complex Fourier spectrum, either at positive or negative frequencies, disappears. It is then said to be in single-sideband operation and SSB theory allows the prior calculation of the scale factor for the phase modulation waveform. In general, for a periodic phase modulation waveform of modulation frequency  $f_m$ , in addition to the desired carrier, there will also be a comb of carriers at other harmonics of the phase modulation waveform. Thus only interferometric signals  $\varphi(t)$  with quadrature bandwidths (see also Sec. 3.1.4)  $B_Q \leq 0.5f_m$  are in principle permitted, otherwise signals may be folded back into the original signal band by the other carriers of the comb.

In the following, the SSB equations derived by Ostwald *et al.* [164] and Voges *et al.* [165] are rewritten to fit the notation of this thesis and the demodulation of the phase signal  $\varphi(t)$  is also included. This derivation is thought to be instructive for the extended SSB equations discussed later. An additional periodic intensity modulation function, included in prior work, is not needed in this thesis and dropped.

Starting off with the equation for the signal at the photo detector  $U_{pd}(t)$ , originating from a single interferometer:

$$U_{pd}(t) = R(P_{\text{off}} + P_{\text{eff}} \cdot \cos[\varphi(t) + s\tilde{\theta}(t)]) \quad (5.1)$$

Here,  $R$ ,  $P_{\text{off}}$  and  $P_{\text{eff}}$  are the photo detector responsivity, stationary offset intensity and effective interferometric intensity, respectively, as previously used in the context of Eq. (3.3). However, the phase modulation function  $\theta(t)$  of Eq. (3.3) is replaced by  $s\tilde{\theta}(t)$ , where  $s$  is a dimensionless phase scale factor and  $\tilde{\theta}(t)$  is the normalised phase modulation waveform.  $\tilde{\theta}(t)$  is now required to be periodic with modulation period



$T_m^{-1} = f_m$ . As described by Ostwald *et al.* [164] and Voges *et al.* [165] and detailed in App. A.1, all periodic terms in Eq. (5.1) with  $s\tilde{\theta}(t)$  are separately expanded into a complex Fourier series, allowing Eq. (5.1) to be rewritten using complex Fourier coefficients. Then, as shown in App. A.1, after demodulation with a complex carrier function of integer harmonic index  $n$  and subsequent low-pass filtering with quadrature cut-off frequency  $f_{Q,co} \leq 0.5f_m$ , the resultant complex quadrature signal  $U_{Q,n}(t)$ , for the relevant cases with  $n \neq 0$ , is given by:

$$U_{Q,n}(t) = 0.5RP_{\text{eff}} \cdot (c_n \cdot \exp[j \cdot \varphi(t)] + c_{-n}^* \cdot \exp[-j \cdot \varphi(t)]) \quad (5.2)$$

The complex coefficients  $c_n$  can then be stated as:

$$c_n = \frac{1}{T_m} \int_{-\frac{T_m}{2}}^{+\frac{T_m}{2}} \exp[j \cdot (s\tilde{\theta}(t) - 2\pi n f_m t)] dt \quad (5.3)$$

It can be seen that the periodic phase modulation function  $s\tilde{\theta}(t)$  is missing in Eq. (5.2) and is completely incorporated into the coefficients  $c_n$  given by Eq. (5.3). To achieve single-sideband operation, the scale factor  $s$  will be tuned until one of the coefficients, or sidebands,  $c_{+n}$  or  $c_{-n}$  vanishes. The remaining sideband can then be used as a carrier and, for the case where the positive sideband is selected as carrier, the sideband suppression ratio  $S_{sb,n}$  [165] is given by:

$$S_{sb,n} = \frac{|c_{-n}^*|}{|c_n|} \quad (5.4)$$

When single-sideband operation is reached,  $S_{sb,n}$  theoretically approaches zero. It has been shown by Ostwald *et al.* [164] that single-sideband operation is, in principle, possible for every waveform  $\tilde{\theta}(t)$  with odd symmetry and any integer harmonic carrier with index  $n \neq 0$  can theoretically be chosen for the demodulation of the phase signal. The phase signal  $\varphi(t)$  can then easily be obtained by applying an arctangent function on the complex quadrature signal  $U_{Q,n}(t)$  of Eq. (5.2), where, when single-sideband operation is achieved, only one exponential term should remain.

### 5.2.2. Maximum Length Pseudo-Random Sequences for Code-Division Multiplexing

In CDM, the outgoing signal is encoded with a digital code, and the signal returning from a particular range is recovered using a time-delayed code version, represented by the decoding function  $d(t - \tau_d)$  with the decoding delay  $\tau_d$ , ideally equal to the expected time-of-flight of the desired signal. In this and in many other works [1, 204, 222] on CDM for optical sensing applications, a special class of pseudo-random sequences, known as maximal length sequences (MLS) [240, 241], are used for digital encoding. For a MLS of positive integer order  $i$ , the corresponding MLS code symbol length  $y$ , i.e. the number of bits in a MLS code sequence, is given by:

$$y = (2^i - 1) \quad (5.5)$$

In CDM, the autocorrelation function can be used to mathematically express the expected code overlap between the code at encoding and a delayed version at decoding. The special autocorrelation properties of MLS results in a constant autocorrelation value for any non-zero code delay. The resulting quadrature crosstalk suppression ratio  $S_{cr}$  is then given by the ratio between autocorrelation values at zero and non-zero code delays, i.e. between in-range and out-of-range signals. Also, a bipolar  $[-1, 1]$  MLS is derived from the original unipolar  $[0, 1]$  MLS by exchanging every 0 with a  $-1$ . Kersey *et al.* [222] first showed that decoding a signal with a unipolar MLS that was previously encoded with a bipolar MLS or vice versa will have an infinitely low amplitude suppression ratio resulting in theoretically zero crosstalk between range channels. This shall be referred to here as unipolar-bipolar coding with theoretical quadrature signal crosstalk suppression coefficient  $S_{cr,up-bp}$ . In contrast, other CDM schemes often use bipolar-bipolar coding with theoretical suppression ratio  $S_{cr,bp-bp}$ . Both  $S_{cr,bp-bp}$  and  $S_{cr,up-bp}$  in units of dBs for a MLS of length  $y$  are given by [222]:

$$\begin{aligned} S_{cr,bp-bp} &= -20 \log_{10}[y] \\ S_{cr,up-bp} &= -\infty \end{aligned} \tag{5.6}$$

### 5.2.3. Extended Theory Combining Single-Sideband Processing and Code-Division Multiplexing

In this work, the SSB equations that were given in prior work and presented in Sec. 5.2.1 are extended to incorporate multiple signal sources, phase-modulated CDM, the effects of anti-aliasing filtering as well as the complete interferometric demodulation process. As an overview of the signal processing steps discussed in detail later, four distinct phases can be identified and are summarised below:

Encoding and Photo Detection: Includes the phase modulation using the SSB-CDM code and the reception of the return signal by an ideal photo detector where no change in the frequency characteristic of the optical signal has occurred yet.

Anti-Aliasing Filtering: The filtering of the photo detector signal includes analogue and any additional digitally induced alterations in the frequency characteristic of the ideal photo detector signal prior to digital range decoding.

Range Decoding: The CDM decoding function is applied to the anti-aliasing filtered signal in the digital domain to separate the signals by range, resulting in an individual signal for each range channel.

Demodulation: By applying a complex carrier function at a chosen integer carrier harmonic and passing the signal through a low-pass filter, a complex quadrature signal can be obtained that directly contains the desired phase information.

Throughout this section, typical signal shapes at each intermediate signal processing step are illustrated in Fig. 5.1, while the actual experimental signal processing implementation is also illustrated later in Fig. 5.13. In this section, the theory is explained in detail, while the derivation steps required to obtain the discussed equations are performed in App. A.2.

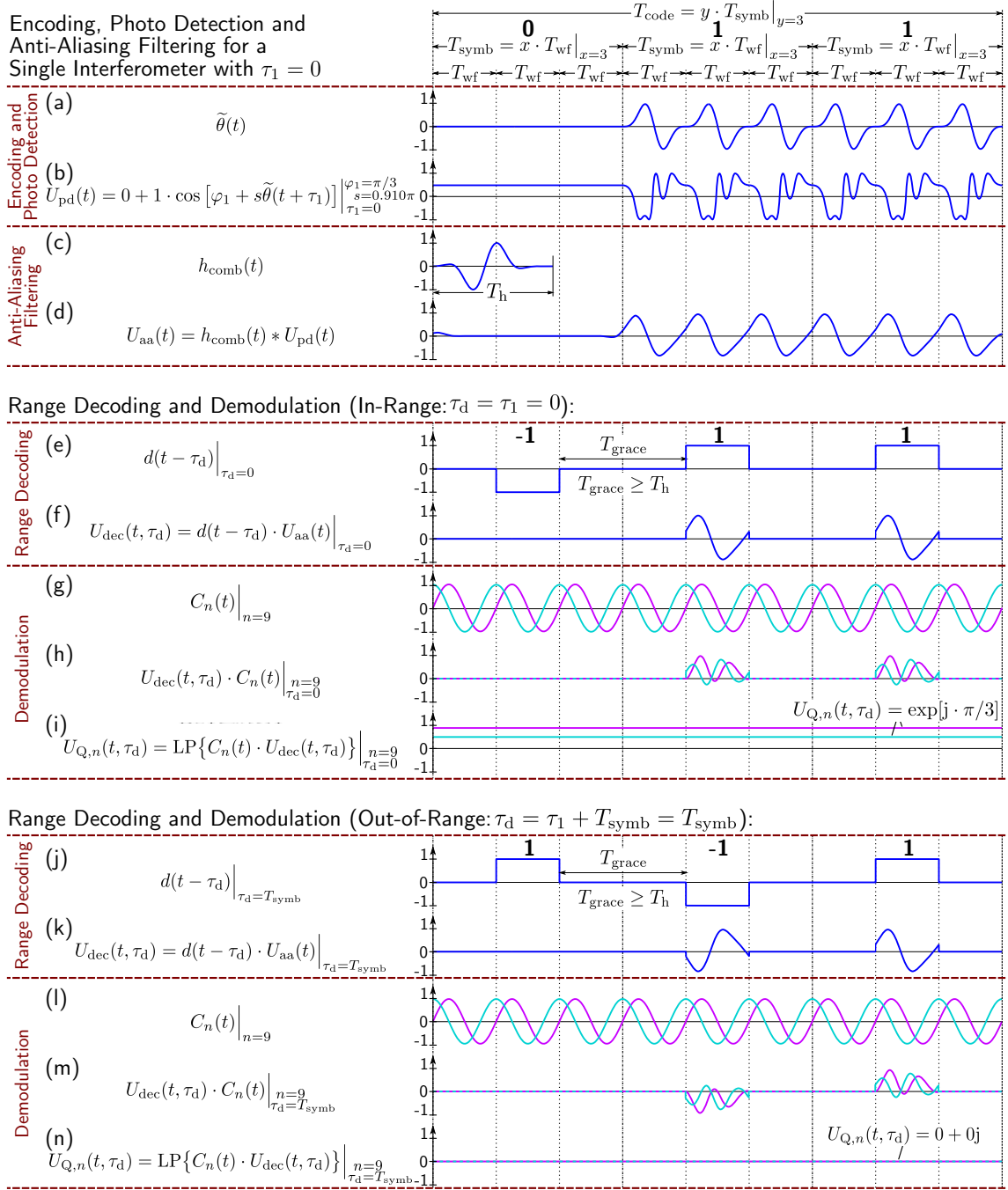


**Figure 5.1.:** Illustration of typical signals at intermediate stages of the signal processing with a detailed description of each stage given in the main text. For illustrative purposes, the plotted signals originate from a single interferometer  $k = 1$  with zero time-of-flight  $\tau_{k=1} = 0$  and are evaluated for a stationary phase value  $\varphi_1 = \pi/3$  in the simplified case of  $P_{off} = 0$  and  $RP_{eff,1} = 1$ . In this figure, real functions are drawn in blue, while for complex functions cyan (real) and magenta (imaginary) line colours are used and all signals are drawn normalised and unitless.

The depicted section shows how a unipolar code  $[0, 1, 1]$ , corresponding to an MLS with  $i = 2$  in Eq. (5.5) is modulated (a), photo detected (b), anti-alias filtered (d) using the filter with impulse response  $h_{comb}(t)$  shown in (c). The resultant signals are then decoded, demodulated and low-pass filtered using the corresponding bipolar MLS code  $[-1, 1, 1]$ , which is illustrated for both in-range signals (e)-(i) and out-of-range signals (j)-(n), resulting in the low-pass filtered complex quadrature signals shown in (i) and (n).

**Encoding and Photo Detection:** The interferometric phase of the outgoing light in the proposed CDM technique is encoded with a pseudo-random MLS code. This code is now incorporated within the phase modulation function  $s\tilde{\theta}(t)$ . Here, similar to the case of the basic SSB equations in Sec. 5.2.1, it is helpful to express  $s\tilde{\theta}(t)$  using the product of the dimensionless scale factor  $s$ , and  $\tilde{\theta}(t)$ , the normalised phase modulation function. In contrast to the earlier case,  $\tilde{\theta}(t)$  now contains the complete MLS code with  $y$  code symbols, as given by Eq. (5.5), where each code symbol of duration  $T_{\text{symb}}$  can contain  $x$  individual SSB waveform templates of length  $T_{\text{wf}}$  and corresponding repetition frequency  $f_{\text{wf}}$ . Thus  $s\tilde{\theta}(t)$  is periodic only with the repetition frequency of the whole code  $f_{\text{code}}$ , which is given by:

$$f_{\text{code}} = T_{\text{code}}^{-1} = (T_{\text{symb}} \cdot y)^{-1} = (xT_{\text{wf}} \cdot y)^{-1} = f_{\text{wf}} \cdot (x \cdot y)^{-1} \quad (5.7)$$

The reason for introducing multiple waveform templates per code symbol, as will become apparent later in this section, is to allow for code transition grace periods that are needed to avoid negative effects arising from anti-aliasing filtering.

To describe the return signal resulting from  $k_{\text{max}}$  constituent interferometers requires extending Eq. (5.1) to include multiple, time-delayed interferometric signals, leading to the signal  $U_{\text{pd}}(t)$  at the photo detector that is given by:

$$U_{\text{pd}}(t) = RP_{\text{off}} + \sum_{k=1}^{k_{\text{max}}} \left( RP_{\text{eff},k} \cdot \cos[\varphi_k(t + \tau_k) + s\tilde{\theta}(t + \tau_k)] \right) \quad (5.8)$$

Here, the responsivity  $R$  and the stationary offset power  $P_{\text{off}}$  were first introduced in the context of Eq. (3.3), while  $P_{\text{eff},k}$  is the effective interferometric power.  $P_{\text{eff},k}$  depends on the individual coherence and polarisation overlap between the two interferometer arms for each of the  $k_{\text{max}}$  constituent interferometers. Note that it is mathematically irrelevant whether the  $k_{\text{max}}$  constituent interferometers are formed by the interference of one local oscillator with  $k_{\text{max}}$  return signals or by more complicated interferometric configurations.  $\varphi_k(t + \tau_k)$  is the desired interferometric phase signal of the  $k$ th constituent interferometer and both  $\varphi_k(t + \tau_k)$  and the phase modulation function  $s\tilde{\theta}(t + \tau_k)$  are delayed with the propagation delay  $\tau_k$  corresponding to the time-of-flight between the two arms of the  $k$ th constituent interferometer plus any offset delay due to the signal processing. Note that the inclusion of an additional intensity modulation function, performed in prior work [164, 165], is not required in this thesis and has therefore been dropped. However, adding intensity modulation in future work should still be possible, but will require a more complicated notation to take care of transient effects.

The normalised phase modulation function,  $\tilde{\theta}(t)$ , similar in shape to the one used in later experiments, is shown in Fig. 5.1(a). Here, it can be seen to incorporate the code  $[0, 1, 1]$ , the simplest of all MLS (see Sec. 5.2.2) for  $i = 2$ , with Eq. (5.5) then yielding  $y = 3$  code symbols, theoretically allowing three range channels to be multiplexed. Each of these code symbols then consists of  $x = 3$  waveform templates, which is similar to the later experiments. For the plotted phase modulation waveform  $\tilde{\theta}(t)$ , the optimal phase scale factor for single-sideband operation is  $s = 0.910\pi$  and the determination of this value will be detailed later in Sec. 5.3.3. In Fig. 5.1(b), the resultant photo

detector signal  $U_{\text{pd}}(t)$  of Eq. (5.8) is shown for a single interferometer  $k = 1$  at zero time-of-flight delay  $\tau_1 = 0$ . The effect of the cosine-shaped transfer function of the interferometer for an arbitrarily chosen stationary phase value  $\varphi_1 = \pi/3$  can also be seen in Fig. 5.1(b), where for illustrative purposes, no intensity offset  $P_{\text{off}} = 0$  and full visibility  $RP_{\text{eff},1} = 1$  is also chosen.

**Anti-Aliasing Filtering:** After photo detection, the electronic signal is subjected to anti-aliasing filtering. In general, anti-aliasing filtering is necessary for the conversion from continuous-time to discrete-time signals to satisfy the Nyquist sampling theorem [242] and also to limit the noise bandwidth affecting the signal. However, even with ideal filters, there is a trade-off between anti-aliasing performance and the length of the impulse response, where a short impulse response without ringing is desirable to limit inter-symbol interference in CDM. In this work, the combined anti-aliasing filter impulse response  $h_{\text{comb}}(t)$ , incorporates the effects of both analogue anti-aliasing filtering, described by  $h_{\text{anag}}(t)$ , as well as any additional digital filtering, described by  $h_{\text{dig}}(t)$ , after digitisation. The combined impulse response  $h_{\text{comb}}(t) = h_{\text{anag}}(t) * h_{\text{dig}}(t)$  is then given by the convolution of both filtering operations and  $h_{\text{comb}}(t)$ , similar in shape to the later experimental implementation, is also plotted in Fig. 5.1(c). Ideally,  $h_{\text{comb}}(t)$  does not show any ringing and is thus zero-valued for any point in time outside the filter length  $T_h$ . The additional digital filtering described by  $h_{\text{dig}}(t)$  is inserted for several reasons:

- The digital filter can reduce ringing in the combined filter response  $h_{\text{comb}}(t)$ .
- The digital filter makes the combined filter impulse response more digitally controllable to avoid suffering from part variations in analogue components.
- As discussed in App. A.2, there is an additional requirement for the combined filter response  $h_{\text{comb}}(t)$  to have zero DC transmission, which can be easily implemented using a digital filter with a band-pass characteristic.

In general, because all individual filtering operations are now incorporated mathematically into  $h_{\text{comb}}(t)$ , filtering of the photo detector signal  $U_{\text{pd}}(t)$  of Eq. (5.8), shown in Fig. 5.1(b), in can now be fully described by a single convolution of  $U_{\text{pd}}(t)$  with  $h_{\text{comb}}(t)$ . For simplicity, this treatment remains in the analogue domain even after digitisation, assuming straightforward conversion to the digital domain as long as the Nyquist sampling theorem is satisfied. The resultant anti-aliasing filtered signal  $U_{\text{aa}}(t)$  is given by:

$$U_{\text{aa}}(t) = h_{\text{comb}}(t) * U_{\text{pd}}(t) \quad (5.9)$$

This signal is also plotted in Fig. 5.1(d), where it can be seen how signal energy can leak into neighbouring code symbols due to ringing by the anti-aliasing filter.

**Decoding:** Following the convolution with  $h_{\text{comb}}(t)$ , the resultant signal is multiplied with the CDM decoding function  $d(t - \tau_d)$ , which is also periodic in  $T_{\text{code}}$  and dependent on the decoding delay  $\tau_d$ . The decoding function  $d(t - \tau_d)$  is shown in Fig. 5.1 for two cases of the decoding delay  $\tau_d$ . Here, Figs. 5.1(e) to (i) shows the decoding of an in-range signal, where the decoding delay  $\tau_d$  is set equal to the physical time-of-flight  $\tau_k$  between the two arms of the  $k$ th constituent interferometer plus any offset signal processing delay. This ideally selects the desired interferometric

signal and suppresses signals from all other ranges. Conversely, Figs. 5.1(j) to (n) shows the case for out-of-range demodulation, where  $\tau_d \neq \tau_k$ , illustrating range-based signal suppression in CDM. Apart from the code information,  $d(t - \tau_d)$  additionally incorporates zero-valued grace periods of length  $T_{\text{grace}}$  between the code symbols as also illustrated in Figs. 5.1(e) and (j). As discussed before, this is intended to prevent code symbol transition effects due to ringing of the anti-aliasing filter from causing inter-symbol interference, which can lead to both crosstalk of signals between range channels and to cyclic errors due to non-ideal sideband suppression. In this work,  $T_{\text{grace}}$  is set equal to the anti-aliasing filter impulse response length  $T_h$ , theoretically ruling out any influence from one code symbol on the next. The anti-aliasing filtered and spatially decoded signal  $U_{\text{dec}}(t, \tau_d)$ , following from Eq. (5.9) and plotted in Figs. 5.1(f) or (k), can then be stated as:

$$U_{\text{dec}}(t, \tau_d) = d(t - \tau_d) \cdot U_{\text{aa}}(t) = d(t - \tau_d) \cdot (h_{\text{comb}}(t) * U_{\text{pd}}(t)) \quad (5.10)$$

Analogous to the derivation of the original SSB equations in Sec. 5.2.1, the extended SSB equations can be obtained by a Fourier series expansion, now incorporating  $d(t - \tau_d)$  and the convolution with  $h_{\text{comb}}(t)$ . For brevity, this expansion is detailed in App. A.2. A caveat of this derivation is, however, the requirement for stationary phase signals  $\varphi_k(t + \tau_k) := \varphi_k$ . This is mathematically necessary due to the convolution with  $h_{\text{comb}}(t)$ . The assumption of stationary phase signal appears to hold well in the later experiments, presumably because the phase signals in the experimental demonstration vary over time scales much longer than the duration  $T_h$  of  $h_{\text{comb}}(t)$ .

**Demodulation:** The final demodulation of the phase signals  $\varphi_k$  is analogous to the generic interferometric demodulation process described by Fig. 3.4. As detailed in App. A.2, this then involves digital multiplication of  $U_{\text{dec}}(t, \tau_d)$  of Eq. (5.10) with a complex carrier  $C_n(t)$  and subsequent low-pass filtering at cut-off frequency  $f_{\text{Q,co}}$  given below. The corresponding signals are illustrated in Figs. 5.1(f) to (i) for in-range demodulation and in Figs. 5.1(k) to (n) for out-of-range demodulation. The complex demodulation carrier function  $C_n(t)$  at the chosen carrier of integer harmonic index  $n$  is then given by:

$$C_n(t) = \exp[-j \cdot 2\pi n f_{\text{code}} t] \quad (5.11)$$

For proper SSB operation, the carrier frequency  $n \cdot f_{\text{code}}$  in  $C_n(t)$  that is used to demodulate  $U_{\text{dec}}(t, \tau_d)$  has to correspond to an integer multiple of the SSB waveform repetition frequency  $f_{\text{wf}}$ . Therefore  $n$  has to be an integer multiple of  $x \cdot y$ , according to Eq. (5.7), with the number of waveform templates per code symbol  $x$  and the MLS code length  $y$ . In the example shown in Fig. 5.1, where  $x = 3$  and  $y = 3$ , the carrier  $C_n(t)$  at the ninth harmonic  $n = 9$  of the code repetition frequency  $f_{\text{code}}$ , also given by Eq. (5.7), is chosen for demodulation. Theoretically, higher values for  $n$ , such as  $n = 18$  or  $n = 27$  are equally possible, however, these may require higher signal processing bandwidths and are therefore not the optimal choice in most cases.

After multiplication with  $C_n(t)$ , the resultant signals are low-pass filtered with a

quadrature cut-off frequency  $f_{Q,co}$  given by:

$$f_{Q,co} \leq f_{Q,co,max} = 0.5f_{code} = 0.5T_{code}^{-1} \quad (5.12)$$

This leads to the complex quadrature signal  $U_{Q,n}(t, \tau_d)$ , which, for the relevant cases with  $n \neq 0$ , is given by:

$$U_{Q,n}(t, \tau_d) = \sum_{k=1}^{k_{max}} 0.5RP_{eff,k} \cdot \left( c_{+n,k}(\tau_d) \cdot \exp[j \cdot \varphi_k] + c_{-n,k}^*(\tau_d) \cdot \exp[-j \cdot \varphi_k] \right) \quad (5.13)$$

The complex coefficients  $c_{\pm n,k}(\tau_d)$ , describing the amplitude and phase of the positive and negative sideband carriers respectively, incorporate the choice of modulation waveform and anti-aliasing filter and also depend on the constituent interferometer index  $k$  and the decoding delay  $\tau_d$ . The coefficients  $c_{n,k}(\tau_d)$  are then given by:

$$\begin{aligned} c_{n,k}(\tau_d) = & \frac{1}{T_{code}} \int_{-\frac{T_{code}}{2}}^{+\frac{T_{code}}{2}} \left( d(t - \tau_d) \cdot \right. \\ & \left( \int_{-\frac{T_{code}}{2}}^{+\frac{T_{code}}{2}} h_{comb}(t') \cdot \exp[j \cdot s\tilde{\theta}(t - t' + \tau_k)] dt' \right) \cdot \\ & \left. \exp[-j \cdot 2\pi n f_{code} t] \right) dt \end{aligned} \quad (5.14)$$

Once single sideband operation is achieved, one of the sidebands at  $+n$  or  $-n$  will disappear, allowing the desired phase signal  $\varphi_k$  to be demodulated using the arctangent of the complex quadrature signal if the decoding delay  $\tau_d$  is set approximately equal to the time-of-flight delay  $\tau_k$  of the desired constituent interferometer  $k$  plus any additional offset signal processing delay. As a consequence of the MLS code, the coefficients  $c_{n,k}(\tau_d)$  will ideally both reduce to zero when  $\tau_d$  differs from  $\tau_k$  by more than the permitted source separation  $T_{synd}$ . For the parameters of the later experimental implementation, plots of the calculated spatial dependence of  $c_{n,k}(\tau_d)$  will be shown and discussed later in Sec. 5.3.3.

When the positive sideband is chosen for demodulation, the sideband suppression  $S_{sb,n,k}(\tau_d)$  and quadrature signal crosstalk suppression  $S_{cr,n,k}(\tau_d)$ , which should both approach zero in an ideal case, can be defined as:

$$S_{sb,n,k}(\tau_d) = \frac{|c_{-n,k}^*(\tau_d)|}{|c_{n,k}(\tau_d)|} \quad (5.15)$$

$$S_{cr,n,k}(\tau_d) = \frac{\sum_{\substack{k'=1 \\ k' \neq k}}^{k'=k_{max}} (|c_{n,k'}(\tau_d)| + |c_{-n,k'}(\tau_d)|)}{|c_{n,k}(\tau_d)|} \quad (5.16)$$

These suppression values then allow a simple assessment of the modulation waveform and anti-aliasing filter design choices in the later sections of this chapter.

## 5.3. Modulation Waveform and Filter Design

In this section, the design choices for the modulation waveform and the filter arrangement are detailed, starting with the shape of the basic phase modulation waveform template. This is followed by a discussion of the chosen filter impulse responses and concluded by examining the complete phase modulation waveform using the theoretical description developed in the previous section.

### 5.3.1. Modulation Waveform Template Design

In this work, in order to allow the implementation of the previously discussed grace periods, each of the  $y$  MLS code symbols may itself consist of  $x$  phase modulation waveform templates of individual duration  $T_{\text{wf}}$  (see also Fig. 5.1(a)) and the design of these templates will be detailed in this section. As discussed previously in Sec. 4.3, in CDM, the minimal spatial separation between signal sources is proportional to the temporal duration of the code symbols and thus inversely proportional to the modulation bandwidth. Therefore, the individual modulation waveform templates have to be designed with high bandwidth efficiency so that they are as short as possible and thus achieve the highest spatial resolution at a given hardware modulation bandwidth. Furthermore, there is a requirement for the modulation waveform templates to be zero-valued at both start and end of the template so that CDM encoding can be accomplished without discontinuities at code symbol transitions. The only additional requirement due to SSB theory for the design of the modulation waveform template, as discussed previously in Sec. 5.2.1, is odd symmetry around the centre of the template. Therefore, in order for the modulation waveform template to be both bandwidth efficient and capable of SSB operation, a design that is based on an exact Blackman window function [243] and multiplied with a sine function to obtain the required odd symmetry is proposed in this work and outlined in the following.

The exact Blackman window [243],  $W_{\text{B,wf}}(t_i)$ , having even symmetry, for the  $i$ th out of a discrete number of  $D_{\text{wf}}$  samples, with coefficients  $[q_0, q_1, q_2]$  equal to  $\frac{1}{18608} \cdot [7938, 9240, 1430]$ , in the form relevant for this thesis, is given by:

$$W_{\text{B,wf}}(t_i) = \sum_{m=0}^2 q_m \cos[2\pi m t_i] \quad \text{for } t_i = \frac{T_{\text{wf}}}{D_{\text{wf}}} \cdot \left[ -\frac{D_{\text{wf}}}{2}, 0, \frac{D_{\text{wf}}}{2} - 1 \right] \quad (5.17)$$

The exact Blackman window is also shown in the time domain in Fig. 5.2(a), with its frequency spectrum shown in Fig. 5.2(b), for the value of  $D_{\text{wf}} = 8$  samples per modulation waveform template that is used in the later experimental implementation. It can be seen in Fig. 5.2(b) that only three frequency components and no further side-lobes are present in the spectrum, therefore this window function can be considered to be very bandwidth efficient. The Blackman window function [243] is very widely used in signal processing and was therefore used as an initial choice. Nevertheless, in future work, further window functions could also be investigated and may offer even better performance in some cases.



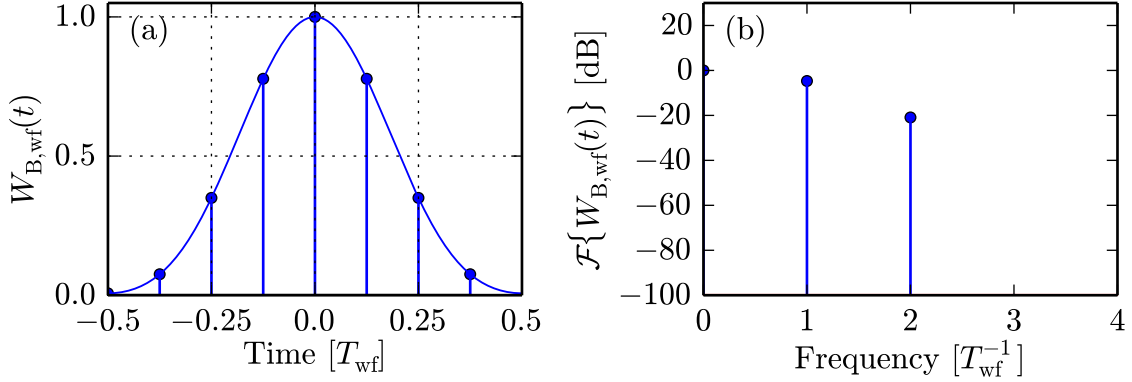


**Figure 5.2.:** Plot of the exact Blackman window  $W_{B,wf}(t_i)$  of Eq. (5.17) in the time domain (a) and the frequency domain (b). In (a), the discrete samples are drawn for  $D_{wf} = 8$  and the continuous line is for  $D_{wf} \rightarrow \infty$ , while (b) is compiled for the case of  $D_{wf} = 8$ .

The exact Blackman window  $W_{B,wf}(t_i)$  of Eq. (5.17) is then multiplied by a sine function of period  $T_{wf}$  to obtain the modulation waveform template with the required odd symmetry, leading to the following expression for the normalised template  $\tilde{\theta}_{wf}(t)$ , with normalisation factor  $G_{wf} \approx 1.7779$ :

$$\tilde{\theta}_{wf}(t_i) = G_{wf} \sin(-2\pi t_i) W_{B,wf}(t_i) \quad \text{for } t_i = \frac{T_{wf}}{D_{wf}} \left[ -\frac{D_{wf}}{2}, 0, \frac{D_{wf}}{2} - 1 \right] \quad (5.18)$$

Here, a DFT-even representation [243], where the last sample is at index  $(0.5D_{wf} - 1)$  and not at  $0.5D_{wf}$ , as in a true-even representation, is used, allowing the modulation waveform template to be repeated seamlessly in the later assembly of the complete modulation waveform. The normalised phase modulation waveform template  $\tilde{\theta}_{wf}(t)$ , given by Eq. (5.18), is plotted in Fig. 5.3(a) with the corresponding spectrum shown in Fig. 5.3(b), where it can be seen that again only three spectral components up to a maximum frequency of  $3T_{wf}^{-1}$  are present. An additional advantage of the chosen design for  $\tilde{\theta}_{wf}(t_i)$  is that there is no DC component visible in Fig. 5.3(b), which is an advantage for practical signal generation, as will be discussed further in Sec. 5.4.2.

To confirm the principle suitability of the phase modulation waveform template  $\tilde{\theta}_{wf}(t_i)$  of Eq. (5.18) for SSB signal processing, the coefficients  $c_{+1}$  and  $c_{-1}$  are calcu-

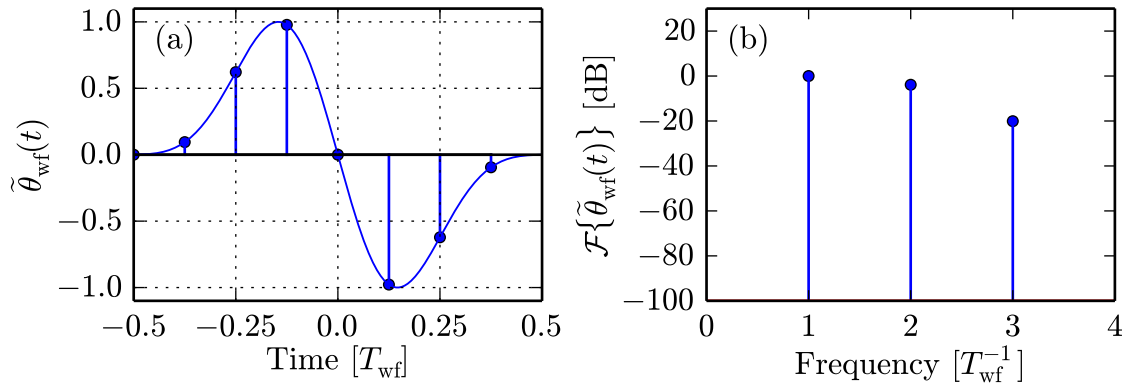


**Figure 5.3.:** Plot of the normalised phase modulation waveform template  $\tilde{\theta}_{wf}(t_i)$  of Eq. (5.18) in the time (a) and frequency (b) domain. In (a), the discrete samples are for  $D_{wf} = 8$  and the continuous line is for  $D_{wf} \rightarrow \infty$ , while (b) is compiled for  $D_{wf} = 8$ .

lated according to the basic SSB equations of Eq. (5.3). Therefore, the fundamental component of the waveform template at positive harmonic index  $n = +1$  in Eq. (5.3) is selected for demodulation, corresponding to a carrier frequency equal to  $T_{\text{wf}}^{-1}$ . A carrier frequency equal to  $T_{\text{wf}}^{-1}$  will also be used in the complete phase modulation waveform discussed later in Sec. 5.3.3. The dependence on the scale factor  $s$  on the coefficient amplitudes is shown in Fig. 5.4(a), where it can be seen that the coefficient  $c_{-1}$  vanishes at  $s = 0.910\pi$ , allowing SSB signal processing to be performed. This is also echoed by Fig. 5.4(b), which plots the corresponding sideband suppression  $S_{\text{sb},+1}$  according to Eq. (5.4).

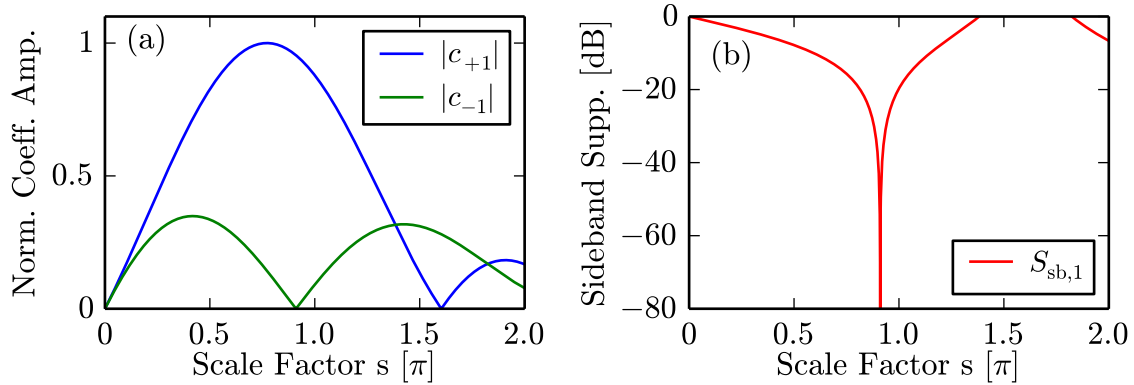


**Figure 5.4.:** Plot (a) of the dependence of the amplitude of coefficients  $c_{+1}$  and  $c_{-1}$  on the scale factor  $s$  for  $\hat{\theta}_{\text{wf}}(t_i)$  of Eq. (5.18) for  $D_{\text{wf}} = 8$ , where the amplitudes are normalised to the maximum of  $c_{+1}$ . (b) shows the corresponding sideband suppression  $S_{\text{sb},+1}$ .

### 5.3.2. Filter Design

In any digital signal processing scheme, analogue reconstruction filtering at the output of a digital-to-analogue converter (DAC) or analogue anti-aliasing filtering at the input of an analogue-to-digital converter (ADC) are prerequisites for proper operation satisfying the Nyquist sampling theorem [242]. In CDM, long ringing periods that commonly occur in analogue filters can lead to inter-symbol interference, where signal energy can penetrate into succeeding code symbols, for both reconstruction and anti-aliasing filtering. This can be the cause of crosstalk between signal sources and cyclic errors due to non-ideal sideband suppression can also occur as a result of these filtering operations.

The requirements for DAC reconstruction filtering and ADC anti-aliasing filtering are compared in the frequency domain in Figs. 5.5(a) and (b), respectively, for the example of the previously shown time-domain signals of Figs. 5.1(a) and (b), which are also repeated in the insets. The dashed vertical lines in Figs. 5.5(a) and (b) illustrate the Nyquist limits for a representation of the signals by  $D_{\text{wf}} = 8$  samples per waveform template, the value used in this thesis for both DAC and ADC sample rates. It can be seen qualitatively from the plotted examples that the proportion of signal content above the Nyquist limit is considerably higher for the incoming ADC signal in Fig. 5.5(b) than for the spectrum of the outgoing phase modulation function at the DAC in Fig. 5.5(a). This is because for the incoming ADC signal  $U_{\text{pd}}(t)$ , the

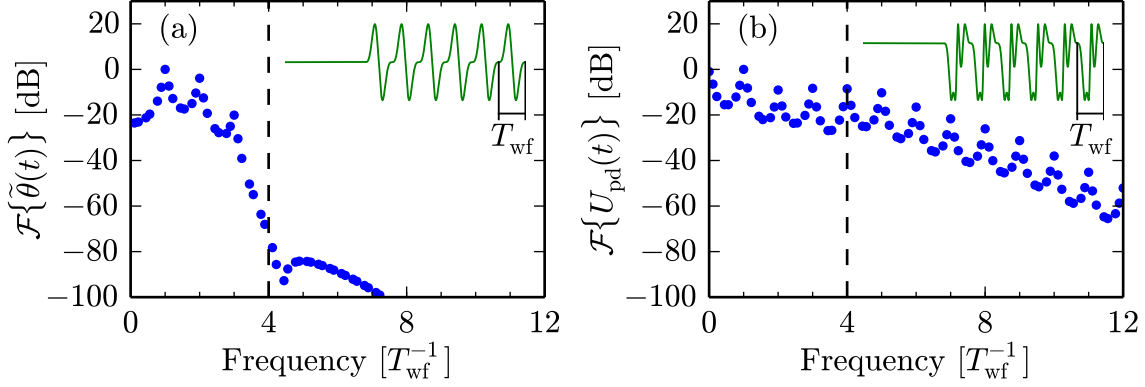


**Figure 5.5.:** A typical example of the Fourier spectra of the phase modulation waveform  $\tilde{\theta}(t)$  and the resulting photo detector signal  $U_{\text{pd}}(t)$  are plotted in (a) and (b), respectively. The corresponding time domain signals were previously used in Figs. 5.1(a) and (b), respectively, and are also sketched in the insets. The plots, calculated for  $D_{\text{wf}} \rightarrow \infty$ , are shown in units of the inverse waveform template duration  $T_{\text{wf}}^{-1}$  and the dashed lines mark the Nyquist limit for a signal representation by  $T_{\text{wf}} = D_{\text{wf}} T_s = 8 T_s$  samples per waveform template.

non-linear nature of the cosine-shaped interferometric transfer function of Eq. (3.3) drastically increases the harmonic content compared to the outgoing phase modulation signal  $\tilde{\theta}(t)$ , driven by the DAC. Therefore the requirements for DAC reconstruction filtering are considerably lower than those for ADC anti-aliasing filtering, making ADC anti-aliasing filtering much more critical to the overall performance of the system. Furthermore, it is also possible to improve ringing due to DAC reconstruction filtering using the modulation waveform pre-shaping technique discussed in Sec. 5.4.2. Therefore, it is assumed that any ringing in the outgoing phase modulation waveform driven by the DAC can be neglected and the calculations in this section focus solely on the characteristics of the ADC anti-aliasing filter.

As previously discussed in Sec. 5.2.3, in an effort to make the anti-aliasing impulse response digitally controllable, reduce ringing and also remove any DC transmission of the filter, a digital filter is inserted after the analogue anti-aliasing filter. Therefore, the resulting combined impulse response  $h_{\text{comb}}(t) = h_{\text{anag}}(t) * h_{\text{dig}}(t)$  is given by the convolution of  $h_{\text{anag}}(t)$ , the analogue filter impulse response, with  $h_{\text{dig}}(t)$ , the digital filter impulse response. For the design of  $h_{\text{dig}}(t)$ , as a compromise between short impulse response and good anti-aliasing performance, a target cut-off frequency of  $2T_{\text{wf}}^{-1}$  was chosen. Also, as previously discussed in Sec. 5.2.3, there is a need to have zero DC transmission in the anti-aliasing filter, resulting in a band-pass characteristic incorporated into the digital filter. The chosen digital filter is based on the previously used exact Blackman window, however, the filter needs a duration of  $D_h = 16 = 2D_{\text{wf}}$  sample periods to achieve the stated requirements, thus resulting in a filter length of  $T_h = 2T_{\text{wf}}$ . Here, for the definition of the digital filter impulse response  $h_{\text{dig}}(t)$ , the exact Blackman window [243],  $W_{\text{B,h}}(t_i)$ , with even symmetry, for the  $i$ th out of a discrete number of  $D_h$  sample periods and with coefficients  $[q_0, q_1, q_2]$  again equal to  $\frac{1}{18608} \cdot [7938, 9240, 1430]$ , is given by:

$$W_{\text{B,h}}(t_i) = \sum_{m=0}^2 q_m \cos[2\pi m t_i] \quad \text{for } t_i = \frac{T_h}{D_h} \cdot \left[ -\frac{D_h}{2}, 0, \frac{D_h}{2} \right] \quad (5.19)$$

To maximise the usable signal energy, the filter response is peaked at the target demodulation carrier frequency of  $T_{\text{wf}}^{-1}$  by multiplying a sine of frequency  $T_{\text{wf}}^{-1}$  to the Blackman window of Eq. (5.19), which also removes any DC transmission of the filter. The frequency of the sine has to be adjusted by a factor of  $D_h D_{\text{wf}}^{-1}$  to achieve a peak at  $T_{\text{wf}}^{-1}$ . Because the digital filter is designed to be applied to non-periodic signals, mathematically, it needs to be defined over an infinite interval, with the digital filter impulse response  $h_{\text{dig}}(t_i)$  set to zero outside the filter length  $T_h$ . Using the normalisation coefficient  $G_h \approx 1.2318$ , this results in  $h_{\text{dig}}(t_i)$  given by:

$$h_{\text{dig}}(t_i) = \begin{cases} G_h \sin\left(2\pi t_i \frac{D_h}{D_{\text{wf}}}\right) W_{\text{B,h}}(t_i) & \text{for } t_i = \frac{T_h}{D_h} \left[ \frac{-D_h}{2}, 0, \frac{D_h}{2} \right] \\ 0 & \text{for } t_i > 0.5T_h \text{ or } t_i < -0.5T_h \end{cases} \quad (5.20)$$

The digital filter response given by Eq. (5.20) is shown<sup>1</sup> in Fig. 5.6(a) for the chosen value of  $D_h = 16$ . It can be seen in the spectrum of Fig. 5.6(b) that this filter peaks at a frequency of  $T_{\text{wf}}^{-1}$ , has minimal DC transmission and that a cut-off of  $\approx 2T_{\text{wf}}^{-1}$  as well as a stop-band attenuation below  $-70$  dB can be achieved. Again, different filter choices using other window functions could also be investigated in future work.

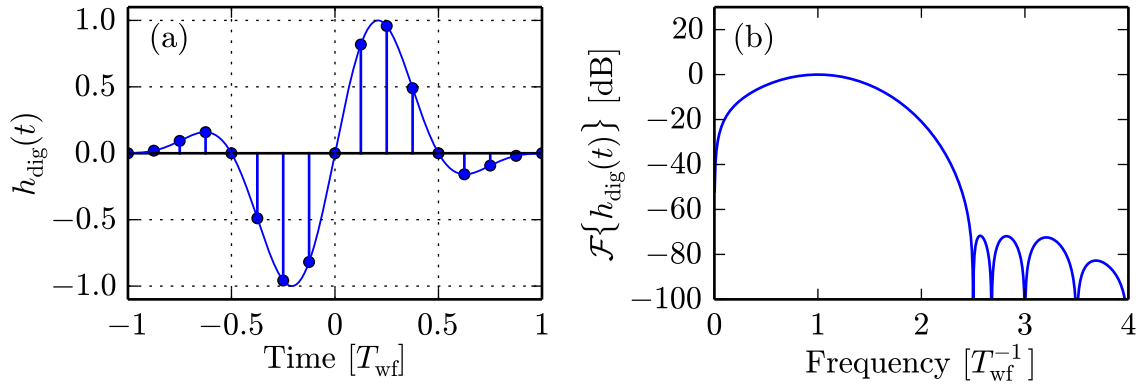


**Figure 5.6.:** Plot of the discrete, normalised digital filter impulse response of Eq. (5.20) in the time domain (a) and frequency domain (b). In (a), the discrete samples are for  $D_h = 16$  and the continuous line is for  $D_h \rightarrow \infty$ , while (b) is compiled for a non-periodic input signal for the case of  $D_h = 16$ . Note the use of units of  $T_{\text{wf}} = 0.5T_h$  to allow comparison with previous graphs.

In order to determine the anti-aliasing filter performance of the filtering arrangement, the frequency spectra of the analogue filter (Mini-Circuits BLP50+) that is used in the later experimental implementation, with impulse response  $h_{\text{anag}}(t)$ , the digital filter  $h_{\text{dig}}(t)$  discussed above, and their combination with impulse response  $h_{\text{comb}}(t)$ , are plotted in Fig. 5.7(a). The analogue impulse response  $h_{\text{anag}}(t)$  was determined using a high-speed oscilloscope and a pulse generator. Here it can be seen that the analogue filter provides the necessary attenuation above the Nyquist frequency. The digital filter has a much tighter characteristic that allows the required control of the filtering characteristic to shorten the impulse response and remove the DC component, however, on its own the digital filter would lead to aliasing for

<sup>1</sup>To assess the performance of the digital filter on a non-periodic input function, the Fourier spectrum has to be evaluated over an infinite period of zeros before and after the filter impulse response shown in Fig. 5.6(a), leading to the continuous spectrum shown in Fig. 5.6(b).

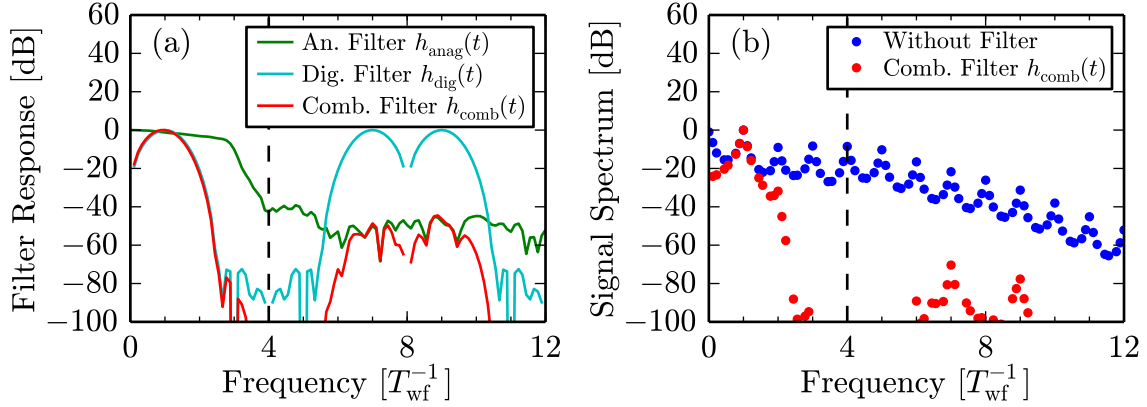


**Figure 5.7.:** To assess the anti-aliasing performance, (a) plots the filter frequency characteristics of the analogue filter, the digital filter and their combination in response to an incoming continuous-time signal. (b) shows the result of the combined filter on the spectrum of the example photo detector signal previously depicted in Fig. 5.5(b). In both (a) and (b), the Nyquist frequency for  $T_{wf} = 8T_s$  is drawn using dashed lines.

frequencies above the Nyquist limit, which would result in a repetition of the filter characteristic at multiples of the sample frequency  $f_s = D_{wf}T_{wf}^{-1}$ . However, it can also be seen in Fig. 5.7(a) that the spectrum of the combined filter, which is the product of both analogue and digital spectra, largely follows the spectrum of the digital filter but additionally attenuates aliased signals with by  $\approx 50$  dB. When this filter is applied to the example ADC signal previously shown in Fig. 5.5(b), it can be seen in Fig. 5.7(b) that with this filtering arrangement the expected aliased signal components are at levels of 70 dB below the main carrier. This is considered acceptable for the purpose of this work, but could be improved by more stringent analogue filtering in future implementations of this scheme, which, on the other hand, also has potential to worsen the ringing performance if not compensated carefully.

Finally, in order to quantify the ringing performance of anti-aliasing filter configuration, Fig. 5.8 draws the resulting filter impulse responses.<sup>2</sup> It can be seen in Fig. 5.8 that  $h_{comb}(t)$  approximates the shape of the digital impulse response  $h_{dig}(t)$ , but, unlike  $h_{dig}(t)$ ,  $h_{comb}(t)$  does show some low-level ringing above  $2T_{wf}$ , as visible in the inset in Fig. 5.8. This exceeds the length of the previously discussed grace periods of length  $T_{grace} = 2T_{wf}$  and therefore has some negative effects on crosstalk and sideband suppression that will be quantified in the next section by calculating the spatial dependence of the carrier amplitude coefficients, later shown in Fig. 5.10. Nevertheless, compared to the case where only the analogue filter would be used, an improvement in the ringing performance can be observed, and this combined anti-aliasing filter configuration is also employed in the later experimental implementation. In this context, an additional correction scheme that would theoretically allow the shortening of the combined filter impulse response to the exact length of the digital filter impulse response by incorporating detailed knowledge of the complete analogue signal processing chain will also be outlined in the discussion in Sec. 5.6.1.

<sup>2</sup>Here, the analogue filter response  $h_{anag}(t)$  is drawn as a continuous-time signal, while the impulse responses of the digital  $h_{dig}(t)$  and combined filters  $h_{comb}(t)$  are ultimately defined in the digital domain and are drawn as discrete-time signals accordingly.

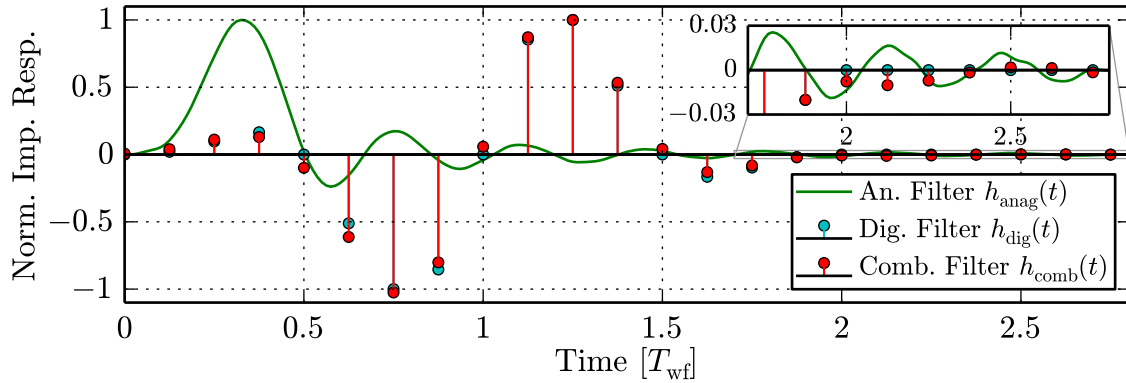


**Figure 5.8.:** The impulse responses of the analogue filter  $h_{\text{anag}}(t)$ , used in the later experimental implementation, the proposed digital filter,  $h_{\text{dig}}(t)$ , and the combined filter,  $h_{\text{comb}}(t)$ , are compared, with the inset illustrating the ringing performance of the individual impulse responses. Here,  $T_{\text{wf}} = D_{\text{wf}}T_s = 8T_s$  is 53.3 ns for a sample frequency of  $f_s = T_s^{-1} = 150$  MHz.

### 5.3.3. Complete Phase Modulation Waveform

In this section, the complete phase modulation waveform is analysed using the theoretical description developed in Sec. 5.2.3, which, as discussed there, is only valid for stationary phase signals  $\varphi(t)$ . Nevertheless, in this work this is sufficient to show that in order to prevent inter-symbol interference due to anti-aliasing filtering, two grace periods for every one evaluated modulation waveform template, as illustrated in Fig. 5.1(e), are required. This leads to a minimum of  $x = 3$  waveforms per code symbol (see also Eq (5.7)). The complete normalised phase modulation waveform  $\tilde{\theta}(t)$  can be straightforwardly assembled from the individual modulation waveform templates  $\tilde{\theta}_{\text{wf}}(t)$ . The resultant waveform  $\tilde{\theta}(t)$  is shown in Fig. 5.1(a) for an MLS code of length  $y = 3$ , whereas for the calculations in this section and the later experimental implementation a MLS code of length  $y = 15$  is used, which theoretically allows  $y = 15$  range channels to be addressed.

With these parameters for  $x$  and  $y$  fixed, the target demodulation carrier frequency of  $1 \cdot T_{\text{wf}}$  of the modulation waveform template  $\tilde{\theta}_{\text{wf}}(t)$ , chosen in Sec. 5.3.1, translates to  $x \cdot y = 45$  repetitions per complete modulation waveform  $\tilde{\theta}(t)$  of length  $T_{\text{code}}$ , according to Eq. (5.7). Therefore, the harmonic index  $n$  for the demodulation will also be  $n = 45$  and the coefficient amplitudes  $c_{n,k}(\tau_d)$  with  $n = \pm 45$  can be calculated according to Eq. (5.14), using the combined anti-aliasing filter impulse response  $h_{\text{comb}}(t)$ . This is shown in Figs. 5.9(a) and (b) as a function of the phase modulation scale factor  $s$  for zero decoding delay  $\tau_d = 0$  for a single interferometer of index  $k = 1$ . Here, single-sideband operation is achieved for a scale factor  $s$  of  $s = 0.910\pi$ , which is the same as the value extracted from Fig. 5.4 for the single modulation waveform template without considering the influence of the anti-aliasing filter.

After the optimal scale factor  $s = 0.910\pi$  is found by evaluating the peak position in Fig. 5.9(b), the spatial dependence of the coefficients  $c_{\pm 45,1}(\tau_d)$  is investigated for the optimum value of  $s$  as a function of the decoding delay  $\tau_d$ . In order to investigate the influence of the anti-aliasing filter choice and associated ringing performance on



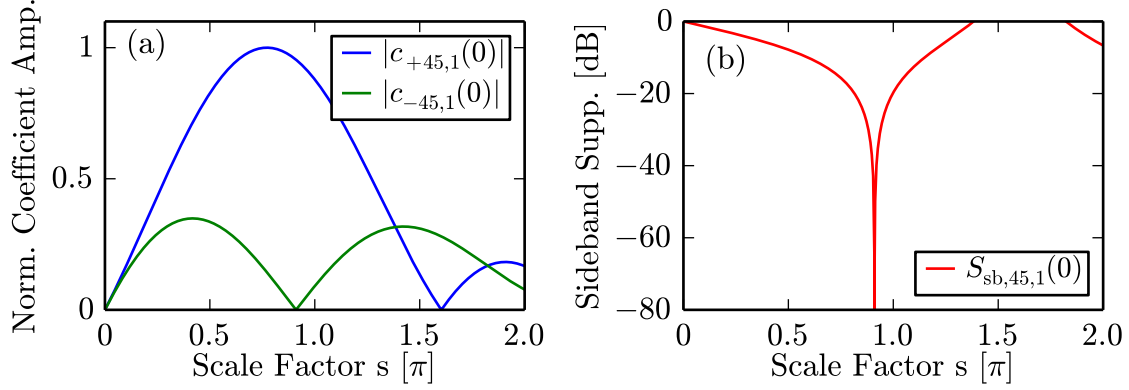


**Figure 5.9.:** (a) plots the dependence of the amplitude of coefficients  $c_{+45,1}(0)$  and  $c_{-45,1}(0)$  on the scale factor  $s$ , calculated using Eq. (5.14) for  $D_{wf} = 8$  and using the combined anti-aliasing filter impulse response  $h_{comb}(t)$ . This is shown for the chosen carrier harmonic  $n = x \cdot y = 45$  for an MLS of code length  $y = 15$  and for a single source,  $k = 1$ , placed at zero time-of-flight delay  $\tau_1 = 0$  and demodulated at  $\tau_d = 0$ . In (a), the amplitudes of the coefficients are normalised to the maximum of  $c_{+45,1}(0)$  and (b) shows the corresponding sideband suppression  $S_{sb,45,1}(0)$ .

the spatial dependence of the coefficients, the coefficients are calculated separately for different filter operations and the results are shown in Fig. 5.10. Here, for the case of analogue filtering only,  $h_{anag}(t)$  is used instead of  $h_{comb}(t)$  in Eq. (5.14), with results shown in Figs. 5.10(a) to (b). For the case of digital filtering only,  $h_{dig}(t)$  is used instead of  $h_{comb}(t)$  in Eq. (5.14), with results shown in Figs. 5.10(c) to (d). Finally, results for the combination of both filters, using  $h_{comb}(t)$  in Eq. (5.14), which is the case that is valid for the later experimental implementation, are shown in Figs. 5.10(e) to (f). The plots for  $x = 3$  waveform templates per code symbols, as used in the later experiments, are shown in Figs. 5.10(b),(d) and (f) on the right. Furthermore, in order to verify the general need for the introduction of the discussed grace periods, the calculations are also carried out for the hypothetical case of  $x = 1$  without any grace period, with results shown in Figs. 5.10(a),(c) and (e) on the left. For the case where  $x = 1$ , the appropriate carrier harmonic for demodulation is  $n = 15$ , while  $n = 45$  is appropriate for  $x = 3$  as discussed before. In each sub-plot of Fig. 5.10, the values of the coefficients  $c_{n,k}(\tau_d)$  are drawn in the upper panel, while the lower panel plots the values of the sideband suppression ratio  $S_{sb,n,k}(\tau_d)$ , given by Eq. (5.15), and the quadrature signal crosstalk suppression ratio  $S_{cr,n,k}(\tau_d)$ , given by Eq. (5.16). In the upper panel, the coefficients for the main source at  $k = 1$  at zero propagation delay  $\tau_{k=1} = 0$  are plotted using solid lines. Also, in order to evaluate crosstalk, additional signal sources, with their resulting coefficient dependencies plotted using dashed lines, are placed regularly with time delays corresponding to OPDs equal to the minimal permissible source separation, i.e. the MLS code symbol length  $T_{symb}$ . Here,  $T_{symb}$  corresponds to  $1 \cdot T_{wf}$  for  $x = 1$  and  $3 \cdot T_{wf}$  for  $x = 3$ .

The need for the introduction of grace periods becomes obvious when comparing the graphs on the left side, i.e. Figs. 5.10(a), (c) and (e), where  $x = 1$ , with the graphs on the right side, i.e. Figs. 5.10(b), (d) and (f), where  $x = 3$ . It can be seen that when there is no grace period, there is strong inter-symbol interference for any filtering arrangement, limiting both the achievable sideband suppression  $S_{sb,15,1}(\tau_d)$  and crosstalk suppression  $S_{cr,15,1}(\tau_d)$  to unacceptable levels. When this is compared to the corresponding graphs on the right side, Figs. 5.10(b), (d) and (f),

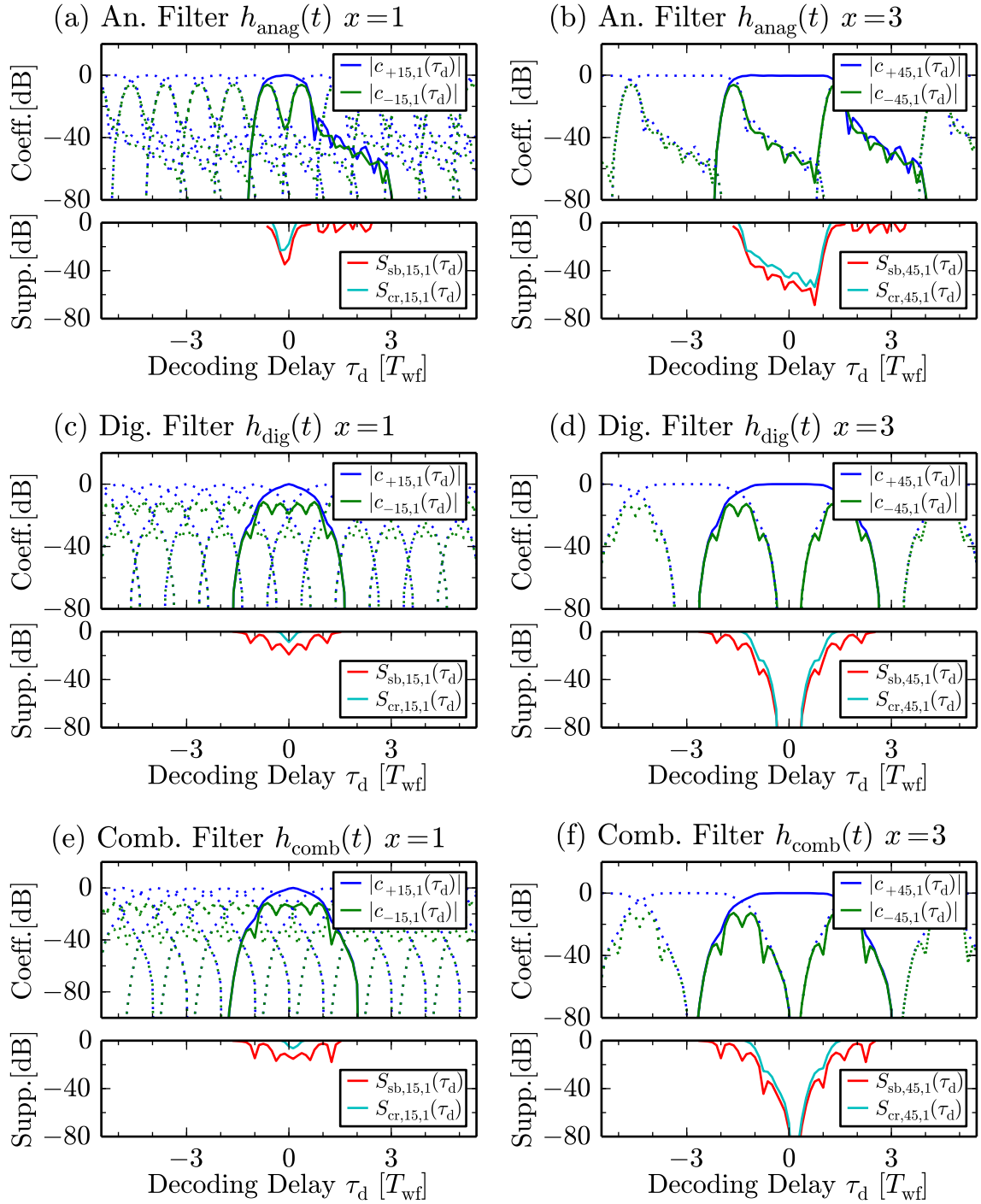


**Figure 5.10.:** Plots of the spatial dependence of the coefficient amplitudes  $c_{\pm n,k}(\tau_d)$ , the sideband suppression  $S_{sb,n,k}(\tau_d)$  and the crosstalk suppression  $S_{cr,n,k}(\tau_d)$  as a function of the decoding delay  $\tau_d$  for a fixed scale factor  $s = 0.910\pi$ . The coefficients are shown for a single source,  $k = 1$ , placed at zero delay  $\tau_{k=1} = 0$  (solid) and for further sources placed equidistantly with separations equal to  $T_{\text{symp}} = xT_{\text{wf}}$  (dashed). The demodulation carrier harmonic  $n$  for an MLS of code length  $y = 15$  is  $n = 15$  for the case without grace period, i.e.  $x = 1$ , shown in (a), (c) and (e), and  $n = 45$  for the case with the previously described grace period, i.e.  $x = 3$ , shown in (b), (d) and (f). This is calculated for three filtering operations individually, for analogue filtering only, using  $h_{\text{anag}}(t)$ , in (a) and (b), for digital filtering only, using  $h_{\text{dig}}(t)$ , in (c) and (d) and for combined analogue and digital filtering, using  $h_{\text{comb}}(t)$ , in (e) and (f).



the positive influence of the grace period on the sideband and crosstalk suppression becomes obvious, confirming the case for their introduction. Furthermore, when comparing the responses for the different anti-aliasing filter arrangements for  $x = 3$  in Figs. 5.10(b), (d) and (f), it can be seen in Fig. 5.10(b) that analogue only filtering has a profound effect on the results. In this case, the asymmetry of the analogue impulse response  $h_{\text{anag}}(t)$ , which is also visible in Fig. 5.8, leads to highly asymmetric coefficient dependencies. Also, the strong ringing in  $h_{\text{anag}}(t)$  limits sideband and crosstalk suppression to values above  $\approx -60\text{dB}$  in the theoretical calculation. This is in contrast to the response of the digital filter only, plotted in Fig. 5.10(d), which exhibits perfect symmetry and where very high sideband and crosstalk suppression values can theoretically be achieved over a wide range of propagation delay values, allowing the OPDs of the constituent interferometers to be placed with very relaxed spatial tolerances. However, as described previously, in practice, a digital filter cannot be used on its own due to the aliasing that would occur. Finally, in Fig. 5.10(f), it can be seen that the combined filter arrangement that is used in the later experiment approximates the ideal behaviour of the digital filter, however, the tolerance band is smaller than in the hypothetical case of digital filtering only. Also, a slight asymmetry can be observed in the calculated values. Nevertheless, these calculations show that the performance improvement in terms of sideband and crosstalk suppression that can be theoretically achieved using grace periods is significant. This therefore also confirms the rationale for the use of the described filter configuration in the experimental work in this chapter.

### 5.3.4. Design Parameter Summary

Table 5.1 shows the chosen design parameters for the assembly of the complete phase modulation waveform  $\tilde{\theta}(t)$ . The spatial resolution resulting from this choice of parameters and the specific experimental details are then discussed in Sec. 5.4.3.

**Table 5.1.:** Design parameters chosen in this thesis for the phase modulation waveform  $\tilde{\theta}(t)$  at a given sampling period of  $T_s = f_s^{-1}$ .

Parameter	Value	Description
$x$	3	Number of waveform templates per code symbol
$y$	15	MLS code length and max. number of range channels
$n$	$x \cdot y = 45$	Harmonic index of the chosen carrier
$D_{\text{wf}}$	8	Number of samples in waveform template
$D_{\text{h}}$	$(x-1) \cdot D_{\text{wf}} = 16$	Number of samples in digital filter impulse response
$T_{\text{wf}}$	$D_{\text{wf}} \cdot T_s$	Length of one modulation waveform template
$T_{\text{h}}$	$D_{\text{h}} \cdot T_s$	Length of the digital filter impulse response
$T_{\text{grace}}$	$T_{\text{h}}$	Length of the grace period
$T_{\text{symb}}$	$x \cdot T_{\text{wf}}$	Length of each code symbol
$T_{\text{code}}$	$y \cdot T_{\text{symb}}$	Length of the whole code

## 5.4. Implementation

This section discusses the details of the experimental implementation. Here, the optical setup is described in Sec. 5.4.1, and the measurement arm configuration is detailed in Sec. 5.4.3. The electronic components can be separated into the signal generation chain and the signal processing chain that will be discussed in Sec. 5.4.2 and Sec. 5.4.4, respectively.

### 5.4.1. Optical Setup

In the optical setup of this implementation, as illustrated in Fig. 5.11, light from a 1552 nm single-mode fibre-coupled diode laser EP1550-NLW-B from Eblana Photonics (for full characterisation see App. B), driven at an output power of 8 mW and temperature controlled to 25° C, enters the interferometer constructed using regular SMF-28-type optical fibre. The setup corresponds to the common LO configuration of Fig. 4.1(c). Here, in one arm, a polarisation controller [100] was constructed and is used to align the linear polarisation direction of the incoming light with the principal polarisation axis of the electro-optic phase modulator (Photline MPZ-LN-10), which has a bandwidth of 10 GHz and which is a lithium niobate travelling-wave phase modulator widely used in the telecoms industry. This is necessary because of the inherent dependence of the voltage-to-phase-modulation transfer function on the polarisation direction in lithium niobate modulators [114], leading to different voltage-to-phase modulation conversion factors for each principal polarisation axis. A further in-fibre polariser is inserted after the phase modulator and also aligned to the principal polarisation axis of the phase modulator in order to filter out any remaining light of the undesired polarisation direction.

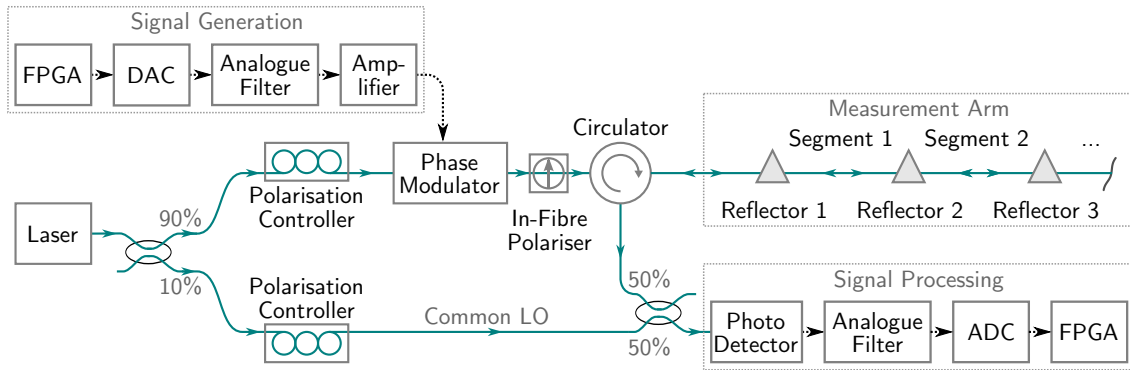


**Figure 5.11.:** Setup used in the experimental implementation in this chapter. Light emitted by the laser diode is split by a directional coupler, where one part is passed to the common LO and another part is guided to a polarisation controller before being phase modulated by the modulation signal from the signal generation chain. After traversing an in-fibre polariser, the modulated light is then guided by a circulator to the measurement arm. Here, following reflection by in-fibre partial reflectors, return light is directed by the circulator towards a directional coupler, where it is mixed with unmodulated light from the common LO that has also been subject to further polarisation control to optimise visibility of the reflector signals. After mixing and photo detection, the resulting signals are then processed in the signal processing chain.

To achieve high sideband suppression for SSB signal processing without cyclic errors, an optimum value for the scale factor of  $s = 0.910\pi$  rad was calculated in Sec. 5.3.3 for the chosen phase modulation waveform. As discussed above, the phase modulation efficiency is dependent on the polarisation direction within the phase modulator in addition to the voltage scaling of the drive signal, thus requiring simultaneous tuning of both quantities. In practice, due to the unknown voltage-to-phase-modulation conversion factor of the phase modulator, the calculated value of  $s$  can only give an indication of the correct value and manual tuning is required. For tuning of both polarisation direction and driving voltage scale, a test signal with phase excursion  $> 2\pi$  is induced in the measurement arm in any of the experimental configurations discussed later in Sec. 5.5. Then the following procedure is performed:

- First, the principal polarisation axis of the phase modulator with the highest phase modulation efficiency is aligned with the output polarisation of the polarisation controller. To achieve this, the phase modulator is driven with the regular phase modulation waveform that allows SSB-CDM signal processing, as described in Sec. 5.3.3, however, at slightly lower than anticipated drive voltage scale. Then, the maximum modulation efficiency of the phase modulator, which should coincide with one of the principle polarisation axes, is found by adjusting the polarisation controller so as to minimise the ellipticity of the measured quadrature signal  $U_{Q,n}(t)$  of Eq. (5.13), when plotted in the complex plane (see also Fig. 3.6).
- The polarisation direction of the in-fibre polariser is then adjusted to coincide with the polarisation direction of the outgoing light from the phase modulator by tuning the FC/PC connector orientation of the fibre link between modulation and polariser until the photo detector signal amplitude is maximised. This is intended to filter out any remaining light that is not aligned with the principle polarisation axis of the phase modulator.
- Finally the drive voltage scaling is increased until  $U_{Q,n}(t)$  appears completely circular in the complex plane and complete sideband suppression is achieved.

While theoretically a single polarisation controller should be sufficient to align the incoming polarisation axis to the principal polarisation axis of the phase modulator, it was found that only the combination of polarisation controller and polariser allowed for drift free and stable operation. However, once all fibre leads were fixed to the table and the above tuning procedure was followed, the experiment did not require any further tuning, even over several weeks. As will be discussed further in Sec. 5.6.1, it is recommended that a phase modulator with polarisation maintaining input fibre is used in future implementations. This avoids the need for the polarisation controller and polariser as well as the tuning procedure described above.

In Fig. 5.11, light leaving the in-fibre polariser is directed by a circulator to the measurement arm. Here, as detailed in Sec. 5.4.3, in-fibre partial reflectors provide the return signals that are then evaluated by this scheme. After returning from the measurement arm, the circulator guides the light towards the signal processing chain that will be detailed in Sec. 5.4.4. Before entering the photo detector, light from the measurement arm is mixed with the light from the common LO. A second

polarisation controller is inserted into the common LO arm and is tuned so that no complete polarisation-induced signal fading [98, 99] (see also Sec. 2.4) occurs in any of the return signals from the measurement arm. It is recognized that in a real-life application, the use of a second polarisation controller in this way, while having allowed the experiments in Sec. 5.5.1 to be carried out, cannot guarantee the absence of polarisation-induced fading in all cases. Potential ways to mitigate this will be further detailed in Sec. 5.6.1.

## 5.4.2. Signal Generation

As illustrated in Fig. 5.11, the signal generation chain driving the phase modulator consists of the field programmable gate array (FPGA), the DAC, an analogue reconstruction filter and a high-frequency amplifier. The FPGA controls both the signal generation and processing to ensure precisely synchronised modulation and demodulation, which is a necessity in CDM. The working principle of an FPGA is also outlined in App. C. In this implementation, an Altera Cyclone IV FPGA on a Terasic DE2-115 development board was used in conjunction with a data acquisition daughter board containing the 14 bit ADC and 14 bit DAC, both running at a clock and sample frequency of  $f_s = T_s^{-1} = 150$  MHz. With the help of Table 5.1 and Eq. (5.7), this yields a waveform template repetition frequency of  $T_{wf}^{-1} = D_{wf} T_s^{-1} = 18.75$  MHz, a code symbol repetition frequency of  $T_{symb}^{-1} = (x \cdot T_{wf})^{-1} = 6.25$  MHz and a code repetition frequency of  $T_{code}^{-1} = (y \cdot T_{symb})^{-1} = 417$  kHz. As discussed in Sec. 5.3.1 a target carrier of  $1 \cdot T_{wf}$  is chosen, leading to a demodulation carrier  $C_n(t)$  of Eq. (5.11) at harmonic index  $n = x \cdot y = 45$  and frequency  $n \cdot T_{code}^{-1} = 18.75$  MHz.

The DAC is connected to an analogue low-pass reconstruction filter (Mini-Circuits BLP-90+) with a cut-off frequency of 90 MHz. While this cut-off frequency is not ideally situated for the Nyquist frequency of  $0.5f_s = 75$  MHz no other filter was available, however, the correction procedure outlined below also mitigates against this apparent drawback. After passing the reconstruction filter, the signal is amplified by a high-frequency amplifier (Mini-Circuits ZHL-32A; Gain: 25 dB; Passband: 0.05 to 130 MHz) to boost the drive voltage of the phase modulator to reach the required phase modulation depth of  $s = 0.910\pi$ , determined in Sec. 5.3.3. For the operation of the amplifier it is advantageous that there is no DC component in the modulation waveform  $\theta(t)$ , as discussed in Sec. 5.3.1, otherwise non-linear behaviour in the amplifier could result.

In general, because every component in the signal generation chain introduces its own specific frequency characteristic, in particular the high-frequency amplifier, the resulting waveform at the input of the phase modulator will be distorted. This can be seen in Fig. 5.12, where ringing at the end of the depicted code symbol can be observed that can lead to inter-symbol interference. To counteract this non-ideal frequency response, the waveform transmitted by the DAC is digitally pre-shaped incorporating the measured impulse response of the signal generation chain  $h_{sg}(t)$ . To measure  $h_{sg}(t)$ , a singular, non-zero impulse of one sample was generated by the DAC and the resulting response after the amplifier is recorded using an oscilloscope of input impedance  $50 \Omega$ . Then, to digitally pre-shape the normalised phase modulation

waveform  $\tilde{\theta}(t)$ , the following procedure is performed:

- First, the reciprocal  $[H_{\text{sg}}(f)]^{-1}$  of the complex Fourier transform  $H_{\text{sg}}(f) = \mathcal{F}\{h_{\text{sg}}(t)\}$  of the measured impulse response  $h_{\text{sg}}(t)$  is calculated.
- Then the reciprocal spectrum  $[H_{\text{sg}}(f)]^{-1}$  is multiplied with the complex spectrum of the desired output signal  $\mathcal{F}\{\tilde{\theta}(t)\}$ .
- Finally, the inverse Fourier transform of the above product results in the pre-shaped output signal  $\mathcal{F}^{-1}\{[H_{\text{sg}}(f)]^{-1} \cdot \mathcal{F}\{\tilde{\theta}(t)\}\}$ .

The result of this procedure is shown in Fig. 5.12, showing a marked improvement in the fidelity of the output waveform that almost completely overlaps with the desired theoretical waveform where pre-shaping is carried out.

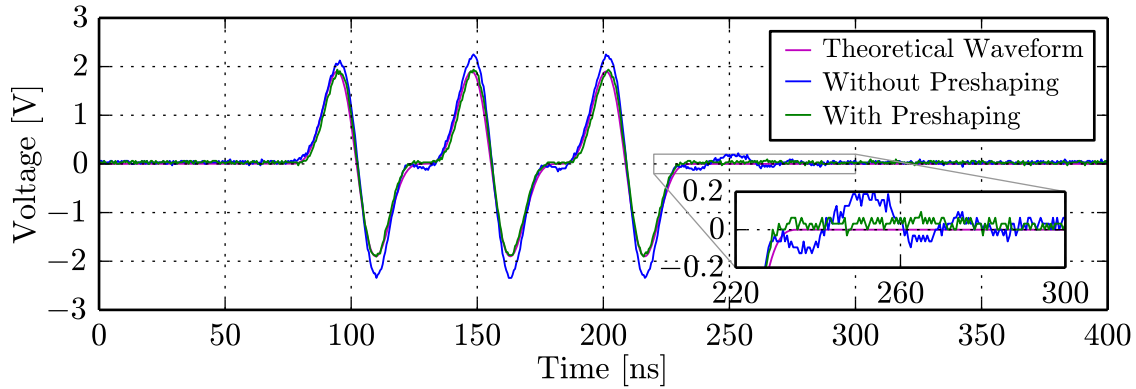


**Figure 5.12.:** Output signal of the signal generation chain after the amplifier, measured with an oscilloscope. Here the measured signal overlaps very well with the appropriately scaled theoretical phase modulation waveform  $\tilde{\theta}(t)$  (see Sec. 5.3.3) for the case with waveform pre-shaping, but show distortions and ringing without pre-shaping, which is particularly evident in the inset.

It should be noted that due to the lack of knowledge of how the impulse response is translated into the optical domain by the phase modulator, the pre-shaping procedure outlined above is incomplete. It is plausible the phase modulator has a reasonably flat frequency response over the relevant frequency region, as the maximum bandwidth of the phase modulator is 10 GHz and thus far away from the modulation bandwidths used here, however, there is no data from the manufacturer available in this regard. Also, as the characteristic impedance of the phase modulator is given as  $40\ \Omega$  and the high-frequency amplifier is designed for  $50\ \Omega$ , thus there is further uncertainty about the actual transmission from the amplifier to the phase modulator, in particular the possibility of RF signal reflections. In future implementations, it is therefore recommended to determine the optical impulse response of the complete signal generation chain, including the phase modulator, in order to remove these uncertainties. This could be achieved using a procedure that will be outlined in the discussion in Sec. 5.6.1.

### 5.4.3. Measurement Arm Configuration

In unipolar-bipolar CDM for multiple reflectors that are correctly positioned, no discernible crosstalk should occur. This is the case when the OPDs of the constituent

interferometers correspond to an equidistant grid with individual time-of-flight differences of one MLS code symbol length  $T_{\text{symb}}$ , with  $T_{\text{symb}} = xT_{\text{wf}} = xD_{\text{wf}}T_s$  according to Table 5.1. The lack of crosstalk theoretically expected for this case is also evident when comparing the dashed and the solid lines in the upper panel in Fig. 5.10(f). Additionally, it can be observed in Fig. 5.10(f) that there should be a tolerance band in the positioning of the partial in-fibre reflectors resulting from the parameter choice in this work. The unit fibre segment length  $l_s$ , corresponding to a return time-of-flight of duration  $T_{\text{symb}}$  between the segment reflectors, with sample frequency  $f_s = T_s^{-1}$ , fibre group index of refraction  $n_g = 1.46$  and vacuum speed of light  $c_0$ , is then given by:

$$l_s = \frac{c_0}{2n_g} \cdot T_{\text{symb}} = \frac{c_0 \cdot xD_{\text{wf}}}{2n_g \cdot f_s} = \frac{2.47 \cdot 10^9 \text{ m s}^{-1}}{f_s} \quad (5.21)$$

For the parameters in this experimental implementation with  $f_s = 150 \text{ MHz}$ , this equates to  $l_s = 16.5 \text{ m}$ . Thus, neighbouring reflectors need to be placed equidistantly on a grid with a separation of  $l_s$  for proper operation of this technique. In general, there also exists an additional offset signal processing delay for all range channels, which can easily be accounted for by adjusting the decoding delays in the FPGA signal processing. It can be seen in Eq. (5.21) that with the modulation waveform parameters fixed according to Table 5.1, there are no other fundamental limitations influencing the minimally achievable unit fibre segment length  $l_s$  in Eq. (5.21) apart from the sample frequency  $f_s$ . Thus  $l_s$  is inversely proportional to  $f_s$  and independent of the MLS code length  $y$  of Eq. (5.5). The maximum number of reflectors that can be addressed is then given by the MLS code length  $y$  and subsequently the maximum number of fibre segments that can be addressed is  $y - 1$ . Range channels where no reflector is placed do not produce a signal and are of no concern.

In this work, using the common LO configuration of Fig. 4.1(c), where a strong local oscillator provides considerable heterodyne gain, it is assumed that the reflectivities of the reflectors are sufficiently small not to substantially reduce the incident light of other reflectors or cause interference between unintended path combinations or multiple reflections, as previously discussed in Sec. 4.1. As the later experimental results in Fig. 5.19 show, in the current implementation, making use of the heterodyne gain phenomenon previously discussed in Sec. 3.1.1, the technique can be expected to work well down to reflectivities of  $-45 \text{ dB}$  (0.003%). In the experiments in this chapter, pairs of FC/PC connectors that are slightly detuned to achieve weak back reflections are used. This approach is only feasible in a lab environment due to its instability and the extensive tuning it requires, where further options for in-fibre partial reflectors have also been discussed in Sec. 4.1.

#### 5.4.4. Signal Processing

The signal processing is illustrated in Fig. 5.13. After photo detection (New Focus 1592; Gain:  $1100 \text{ V W}^{-1}$ ; Passband:  $10 \text{ kHz}$  to  $3.5 \text{ GHz}$ ), the electrical signal is filtered with an analogue anti-alias filter (Mini-Circuits BLP-50+ with cut-off frequency  $50 \text{ MHz}$ ), characterised by the impulse response  $h_{\text{anag}}(t)$ , and then digitized at sample

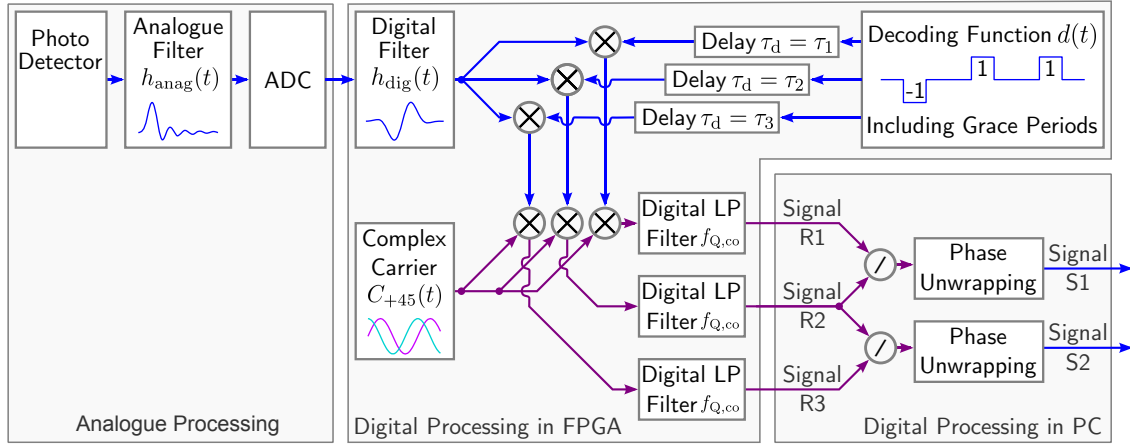


**Figure 5.13.:** Outline of signal processing implementation (compare also with Fig. 5.1), illustrated for the decoding of signals from three reflectors R1, R2 and R3. Here, real signals are drawn in blue, while complex signals are drawn in magenta. After analogue anti-aliasing filtering with impulse response  $h_{\text{anag}}(t)$  and digitisation by the ADC, the photo detector signal enters the FPGA. Here, after digital filtering with impulse response  $h_{\text{dig}}(t)$ , the signals are separated into three range channels for R1, R2 and R3 by delaying the multiplication with the decoding function  $d(t)$  by decoding delays  $\tau_d$  equal to  $\tau_1$ ,  $\tau_2$  and  $\tau_3$ , respectively. Each range channel is subsequently demodulated by multiplication with the complex carrier  $C_{+45}(t)$  and finally digitally low-pass filtered at quadrature cut-off frequency  $f_{Q,\text{co}}$ . After being transmitted from the FPGA to a PC, the quadrature signals of R1, R2 and R3 are subject to a complex division to subtract the phases and finally phase unwrapping, resulting in the desired phase signals for two segments S1 and S2.

frequency  $f_s = 150$  MHz by the ADC before being transmitted to the FPGA. Here, as previously discussed in Sec. 5.3.2, further digital filtering, characterised by the impulse response  $h_{\text{dig}}(t)$ , is carried out, resulting in the combined impulse response  $h_{\text{comb}}(t) = h_{\text{anag}}(t) * h_{\text{dig}}(t)$  for the anti-aliasing filtered photo detector signal  $U_{\text{aa}}(t)$  of Eq. (5.9). Separately for each range channel,  $U_{\text{aa}}(t)$  is then multiplied with delayed versions of the decoding function, given by  $d(t - \tau_d)$  in Eq. (5.10). For each range channel the decoding delay  $\tau_d$  corresponds to  $\tau_d = \tau_k$ , the time-of-flight to the  $k$ th reflector. As discussed in Sec. 5.2.2 and also observable when comparing Figs. 5.1(e) to (i) with Figs. 5.1(j) to (n), in unipolar-bipolar MLS coding the autocorrelation for code iterations with different code delays is zero and out-of-range signals should cancel, leaving, in theory, only the signal from the reflector at the desired range, i.e. with the correct delay  $\tau_d = \tau_k$ , to accumulate in the corresponding range channel.

Following decoding into range channels, the complex quadrature signals  $U_{Q,n}(t, \tau_d)$  of Eq. (5.13) results from the demodulation with the complex carrier  $C_n(t)$  of Eq. (5.11) and subsequent complex digital low-pass filtering at cut-off frequency  $f_{Q,\text{co}}$ , according to Eq. (5.12). Here, the chosen carrier harmonic for demodulation is  $n = +45$ . Care has to be taken to demodulate a positive carrier harmonic  $c_{+n,k}(\tau_d)$  with a positive complex frequency and vice versa to obtain meaningful results, as this was an error causing delay during the practical implementation. As previously discussed, the chosen parameters according to Table 5.1 lead to a possible maximum quadrature cut-off frequency  $f_{Q,\text{co,max}}$ , according to Eq. (5.12), of  $f_{Q,\text{co,max}} = 0.5T_{\text{code}}^{-1} = 208$  kHz. It will be detailed in the discussion of the later experiments in Sec. 5.5.1 that in this work quadrature noise can lead to spurious unwrappings (see also App. D.2) that requires the low-pass filter cut-off frequency of

the complex quadrature signal to be significantly lowered to  $f_{Q,co} = 20$  kHz.

In the current implementation, due to capacity limitations on the used FPGA, a total of 12 range channels can be interrogated simultaneously, and, as can be seen in Fig. 5.13, the filtered complex quadrature signals, at a data rate of 50.4 kHz each, are then transferred serially from the FPGA to a personal computer (PC) for further processing. This was done in order to limit FPGA programming complexity, however, in future implementations all digital signal processing could equally be performed on the FPGA. In the current implementation, the transfer of data from the FPGA to the PC and the associated buffering constituted a bottleneck, limiting the continuous recording time to less than a second. However, this is only a technological problem that could be solved using faster data transfer links in future implementations. Finally, in order to evaluate segment data, the phases of neighbouring range channels are subtracted by complex division of the quadrature signals on the PC. This is followed by complex phase determination using the arctan function and phase unwrapping [112], resulting in the desired phase signals for each fibre segment.

### 5.4.5. Implementation Parameter Summary

Table 5.2 shows the signal processing implementation parameters used in this chapter.

**Table 5.2.:** Signal processing implementation parameters for the demonstration of the CDM technique.

Parameter	Value	Description
$f_s$	150 MHz	Digital hardware sample frequency
$f_{wf} = T_{wf}^{-1}$	18.75 MHz	Waveform template repetition frequency
$T_{symb}^{-1}$	6.25 MHz	Code symbol repetition frequency
$f_{code} = T_{code}^{-1}$	417 kHz	Repetition frequency of the whole code
$f_{Q,co,max}$	208 kHz	Maximum possible quadrature filter cut-off frequency
$f_{Q,co}$	20 kHz	Used quadrature filter cut-off frequency
$l_s$	16.5 m	Unit fibre segment physical length

## 5.5. Experiments

In this section, results from an experimental demonstration of the proposed combined SSB-CDM signal processing technique will be presented. First, in Sec. 5.5.1, a detailed analysis of linearity, noise and crosstalk performance for a configuration with only a single reflector present is carried out, evaluating the best case performance that can, in principle, be expected using the proposed technique and allowing theoretical predictions originating from the previous sections to be tested. This is followed in Sec. 5.5.2 by characterising the performance for multiple reflectors, which is more relevant for FSI applications, in a suitable test setup. Finally, in



Sec. 5.5.3, the multiplexing of four long-gauge length fibre optic strain sensors in an FSI configuration will be trialled. A critical discussion of both these experiments and future improvements to the implementation will then be carried out in Sec. 5.6.

### 5.5.1. Single Reflector Measurements

**Linearity:** To analyse the linearity and noise properties of a system where only a single reflector is present, the measurement arm configurations R1 to R5 that are illustrated in Fig. 5.14 are used. Here, up to four fibre segments that have FC/PC connectors on both ends and that are of unit fibre segment length  $l_s$  can be used, where  $l_s$  equals 16.5 m according to Eq. (5.21) for the experimental parameters described there. In each measurement configuration R1 to R5, only a single signal from the respective open FC/PC connector fibre tip reflection at positions 1 to 5 is present in the measurement signal. The other FC/PC connectors are in close contact and therefore ideally return no signal. The signals are measured for a total of 36 equidistant range channels, recorded sequentially in three sessions for the maximum number of 12 range channels that are implemented on the FPGA. Each range channel is separated by four samples or  $0.5 \cdot T_{wf}$ , corresponding to a physical distance of 2.75 m between range channels. In order to introduce a phase signal sweep, required to equalise the point density in the later plots of the quadrature ellipses, an additional slow (33 Hz) laser injection current modulation of the source can be used.

Polar scatter plots (see also Fig. 3.6) of the complex quadrature signals  $U_{Q,45}(t, \tau_d)$  of Eq. (5.13), with  $n = 45$  according to Table 5.1 and  $\tau_d = \tau_k$ , where  $k = 1 \dots 5$  for

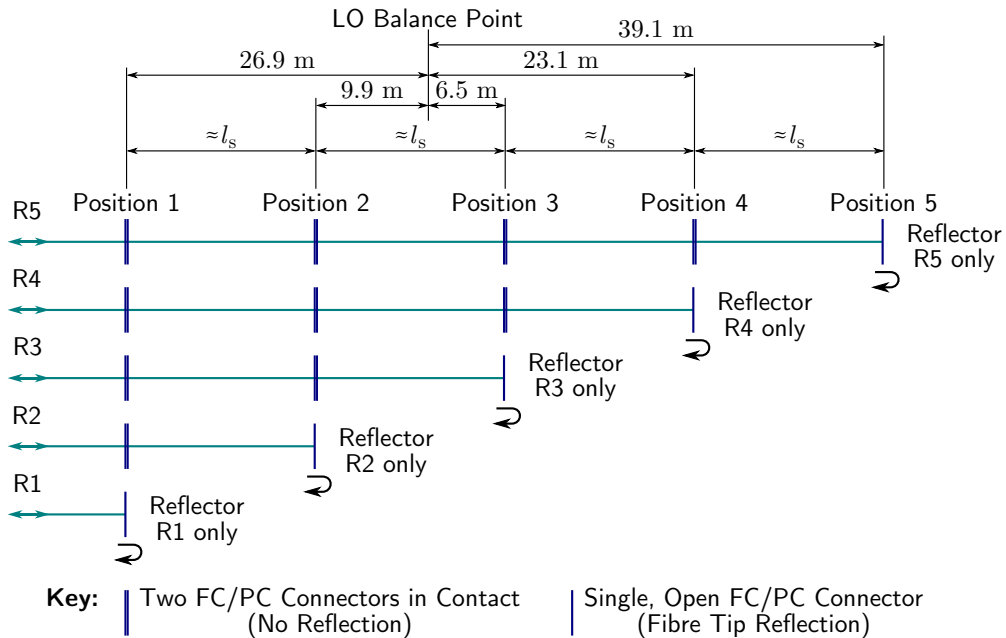


**Figure 5.14.:** Five measurement arm configurations for single reflector measurements in conjunction with the setup of Fig. 5.11. Here, for each configuration R1 to R5, a single return signal occurs where the respective FC/PC connector at position 1 to 5 is left open, while no reflection should result from the other connectors that are in close contact. Also shown are the physical distances of positions 1 to 5 with respect to the common LO balance point (see also Fig. 4.1).

the time-of-flights to the respective reflector of the five configurations R1 to R5, are then used to determine the achievable linearity of the technique. These are shown in Fig. 5.15(a), where the blue dots trace the end-points of every quadrature signal phasor over a period of 0.5 s, with the quadrature signal low-pass filtered at a bandwidth of  $f_{Q,co} = 20$  kHz. The green lines then represent the angular average of this data over 30 angular sectors, with both plots normalised to the mean phasor amplitude. The differences in noise in R1 to R5 will be analysed in the next section, however, it can be seen qualitatively that all plots appear centred and circular and should therefore result in highly linear interferometric phase measurements with low cyclic error magnitudes. To quantitatively determine the magnitude of the remaining cyclic errors, the dependence of the complex phasor amplitude on the phasor angle for the angular averaged quadrature data was fitted to the cyclic error model given by Eq. (3.8). The results of this fitting procedure can be inspected in Fig. 5.15(b). Here, a very good agreement can be seen between the fitted model, drawn using continuous lines, and the measured angular averaged phasor amplitude values, drawn using dots of the same colour. This very close match is particularly obvious for the curves for R2 and R3 due to the lack of noise, and proves that the signal properties in regards to linearity can be very well described by the model given by Eq. (3.8). Using this model, the resulting angular distortions are shown in Fig. 5.15(c), where it can be determined that the maximum angular errors are  $\pm 30$  mrad for R1 and below  $\pm 20$  mrad for R2 to R5. It can further be seen in Fig. 5.15(c) that the angular distortion of the signal from R1 is dominated by a sine of frequency one per cycle,

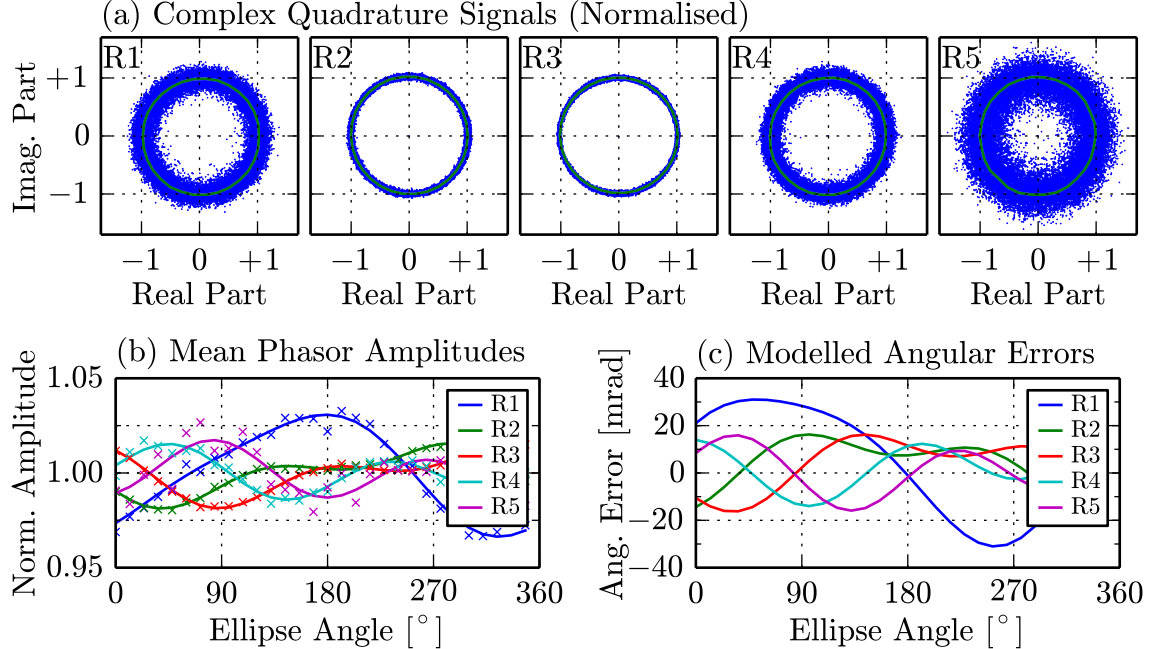


**Figure 5.15.:** (a) shows a scatter plot of the complex quadrature signals for the single reflector configurations R1 to R5 according to Fig. 5.14. Here, the locations of the tip of the complex quadrature phasor are traced over 0.5 s, normalised to the mean quadrature amplitude. This is represented by the blue dots, while the green lines plot the angular average of this data over 30 angular sectors. (b) shows the normalized quadrature amplitudes for R1 to R5 for the angular averaged data using crosses, while the fits of this data to the ellipse model of Eq. (3.8) are drawn using lines of the same colour. (c) then plots the angular errors calculated using this model.

which on closer analysis corresponds to a lateral displacement of the ellipse drawn in Fig. 3.6(b) and described by a non-zero coefficient  $a_3$  in Eq. (3.8). In contrast, the angular errors of the signals from R2 to R5 are dominated by two-cycle non-linearity errors, which can be seen to be a result of a non-zero coefficient  $a_2$  in Eq. (3.8) that controls the ellipticity of the complex quadrature signal plot.

To investigate the positioning tolerance for the reflectors, the spatial dependence of the ellipticity and lateral displacement of the complex quadrature ellipses are characterized by plots of the coefficient ratios  $a_2/a_1$  for ellipticity, shown in Fig. 5.16(a), and  $a_3/a_1$  for lateral displacement of the ellipse, shown in Fig. 5.16(b). Here  $a_1$  is the amplitude of the desired exponential term and is used to normalise the amplitudes  $a_2$  and  $a_3$  of the undesired exponential terms in Eq. (3.8). Note that in both graphs, the results from the five individual measurement configurations R1 to R5 are plotted into a single graph and that the coefficient ratios are only drawn near the reflector positions where the signal is sufficiently strong to calculate the coefficients. As will be discussed below, the coefficient ratio  $a_2/a_1$  directly corresponds to the achievable sideband suppression and it can be seen in Fig. 5.16(a) that the spatial dependence of the ratio  $a_2/a_1$ , including the flat plateau at  $\approx -40$  dB over four range channels, appears broadly similar for all five measurements R1 to R5. In this experiment, the distances between the four evaluated range channels that form the plateaus correspond to  $3 \cdot 2.75 \text{ m} \approx 8 \text{ m}$ . Fig. 5.16(b) then plots the coefficient ratio  $a_3/a_1$ , which, as discussed above, is a measure of the lateral displacement of the complex quadrature ellipse and thus, as illustrated in Fig. 3.6, an indication for the presence of a stationary offset signal within the respective range channel. At this point, it is unclear where this offset signal originates, whether from within the signal processing or from crosstalk by parasitic reflections, however, it can be seen in Fig. 5.16(b) that the coefficient ratio  $a_3/a_1$  decreases from R1 through to R5, which equals a reduction in the discussed offset signal. This explains the decrease of the one-cycle non-linearities from R1 through to R5 that is visible in Fig. 5.15(c). Therefore, from Fig. 5.16 it can be concluded that the flat plateau in the spatial dependence of both  $a_2/a_1$  and  $a_3/a_1$  values permits a linearity performance comparable to Fig. 5.15 to be obtained over a relatively wide reflector positioning tolerance band of  $\approx 8 \text{ m}$ .

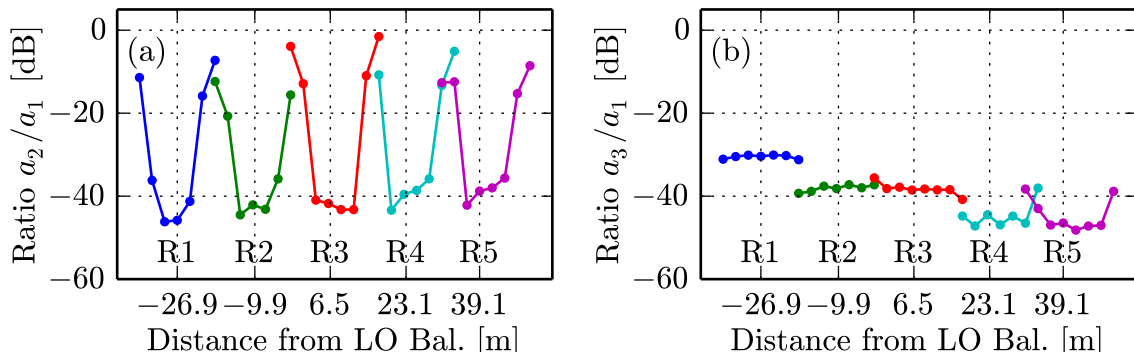


**Figure 5.16.:** Logarithmic plot of the measured coefficient ratios  $a_2/a_1$  in (a) and  $a_3/a_1$  in (b) resulting from the fit of the ellipse model according to Eq. (3.8). In both (a) and (b), the results for the five measurement configurations R1 to R5 are drawn into one graph as a function of the physical distance to the LO balance point and only the data points around the reflectors with sufficient signal amplitude to calculate the coefficients are shown.

The coefficient ratio  $a_2/a_1$  directly corresponds to the sideband suppression  $S_{\text{sb},45,k}(\tau_d)$ , given by Eq. (5.15) for the relevant harmonic index  $n = 45$ , a fact that becomes obvious when comparing the coefficients  $a_1$  and  $a_2$  of the exponential terms in Eq. (3.8) with coefficients  $c_{+n,k}(\tau_d)$  and  $c_{-n,k}^*(\tau_d)$  of the exponential terms in Eq. (5.13). This allows for a convenient method of testing the theoretical approach that was developed in this chapter in Sec. 5.2.3. The spatial dependence of  $S_{\text{sb},45,k}(\tau_d)$ , predicted by Eq. (5.15), and the measured  $a_2/a_1$  coefficient ratios, first shown in Fig. 5.16(a), are compared in the upper panels of Figs. 5.17(a) to (e) for R1 to R5, respectively. The corresponding lower panels then plot, on the same logarithmic scale, the spatial dependence of the quadrature signal amplitude  $|U_{Q,45}|$  of Eq. (5.13), normalised to the peak value. Note that only a straightforward conversion between spatial dependence in metres and corresponding time-of-flight, including the appropriate offset distances to the reflectors R1 to R5, was conducted to allow the measured data points and the theoretical predictions to be drawn on top of each other, but that no further alteration of the plots was performed. Using the combined anti-aliasing filter impulse response  $h_{\text{comb}}(t)$ , detailed in Sec. 5.3.2, the sideband suppression  $S_{\text{sb},45,1}(\tau_d)$  was calculated according to Eq. (5.15) both for the optimal value of the phase scale factor  $s$  of  $s = 0.910\pi$  and for a non-optimum scale factor of  $s = 0.904\pi$ , with this value chosen by a visual fit in the top panels in Fig. 5.17. The curve for  $s = 0.910\pi$  is equal to the one previously depicted in Fig. 5.10(f) and drawn in Fig. 5.17 using black dotted lines, while the curve for the non-optimum scale factor  $s = 0.904\pi$  is drawn using continuous black lines. It can be seen in the top panels in Fig. 5.17 that the curves for  $s = 0.910\pi$  and  $s = 0.904\pi$  only substantially differ in the plateau height and that for  $s = 0.904\pi$  the calculated sideband suppression agrees well with the measured coefficient ratio  $a_2/a_1$  values.

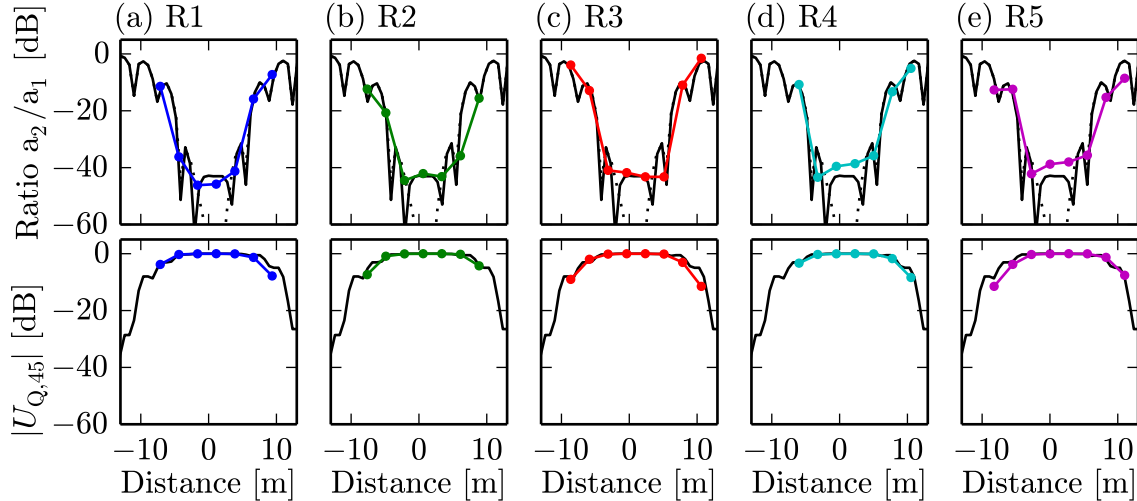


**Figure 5.17.:** A comparison of the measured coefficient ratio  $a_2/a_1$  for R1 to R5, previously depicted in Fig. 5.16(a), with the calculated sideband suppression ratios  $S_{\text{sb},45,k}(\tau_d)$  of Eq. (5.15) shown in the upper panels. Here, the plots for the coefficient ratio  $a_2/a_1$  are drawn in colour, while the sideband suppression ratios  $S_{\text{sb},45,k}(\tau_d)$  are drawn in black, with the curve calculated for the non-optimal phase scale factor  $s$  of  $s = 0.904\pi$ , drawn using black continuous lines and with the curve calculated for the optimal value of  $s = 0.910\pi$ , similar to Fig. 5.10(f), drawn using black dotted lines. The corresponding lower panels then show the measured quadrature amplitude  $|U_{Q,45}|$ , along with the predicted curves, overlapping for both  $s = 0.904\pi$  and  $s = 0.910\pi$ , in black.

The generally good agreement of the height of the plateaus with the calculated curve for  $s = 0.904\pi$  leads to the conjecture that the appearance of the plateau is due to a non-perfect setting of the modulation scale factor  $s$  and associated polarisation control, as detailed in Sec. 5.4.1 and Sec. 5.4.2, however, the setting of  $s$  was still achieved to within 0.7 % of the optimum value. The lower panels of Fig. 5.17 then plot the spatial dependence of the quadrature amplitude  $|U_{Q,45}|$ . Here, the measured values are compared with the theoretically calculated values using the theory of Sec. 5.2.3, drawn in black, where in this case both theoretical curves for  $s = 0.904\pi$  and  $s = 0.910\pi$  lie on top of each other. The spatial dependence of  $|U_{Q,45}|$  also shows a very good agreement with the theoretical predictions. Furthermore, because the reduction of the quadrature amplitude in the lower panels is more than an order of magnitude less than the observed changes in the coefficient ratio  $a_2/a_1$ , also confirms that the observed spatial dependence of the measured coefficient ratio  $a_2/a_1$  is completely unrelated to the drop in  $|U_{Q,45}|$ . The results shown in Fig. 5.17, with the very good fit of the width of the peak shapes as well as the peak symmetry for all five measurements R1 to R5 as well as the good overlap of the spatial dependence of the calculated quadrature amplitude values, highlight the power of the theoretical approach developed in Sec. 5.2.3. In general, both peak width and peak asymmetry are highly dependent on the filter choice, as can be seen in Fig. 5.10. Therefore the results shown also indicate that the combined filter impulse response  $h_{\text{comb}}(t)$  is correctly modelled in Sec. 5.3.2.

**Quadrature and Phase Noise:** As well as providing a measure of linearity, the plots of the complex quadrature signal shown in Fig. 5.15(a) also yield qualitative information about the noise present in the quadrature signals. In Fig. 5.15(a) it can be observed that quadrature noise varies considerably for the single reflector configurations R1 to R5. The properties of quadrature noise are discussed further in App. D.1. In general, strong quadrature noise increases the likelihood of spurious phase unwrappings, as explained in App. D.2. A single spurious phase unwrapping can lead to a permanent phase error of  $\pm 2\pi$  that cannot be unambiguously corrected in post-processing and thus needs to be prevented in the first place by sufficiently averaging the quadrature signal. In this work, the onset of spurious phase unwrappings required the reduction of the quadrature signal bandwidth from its maximum value of  $f_{Q,\text{co,max}} = 208 \text{ kHz}$ , as given by Eq. (5.12), down to  $f_{Q,\text{co}} = 20 \text{ kHz}$ , only 9.6 % of the maximally possible cut-off frequency  $f_{Q,\text{co,max}}$ . In order to mitigate this considerable performance limitation, a thorough understanding of the origins of the quadrature noise is required, which will be investigated below. Following on from this, options for allowing larger bandwidths in future work will be discussed in Sec. 5.6.1.

In addition to the dependency of the quadrature noise on reflector position when a single reflector is present, as evident in Fig. 5.15(a), it was also observed in other experiments with multiple reflectors, detailed in Sec. 5.5.2, that the quadrature noise level in any one range channel is dependent on the signal levels of other reflectors present at different ranges. This leads to the conclusion that there is considerable leakage of quadrature noise from the originating signal source to other range channels. To investigate this, the same measurement with five single reflector configurations R1 to R5 of Fig. 5.14, previously used to analyse linearity, is evaluated with regard

to quadrature and phase noise. Fig. 5.18(a) plots the root-mean square (RMS) signal amplitudes, normalised to the respective peak RMS signal amplitude, for all 36 range channels used. Here it can be seen qualitatively that the RMS signal amplitude in the baseline is dependent on the position of the originating single reflector.

This dependence is quantified in Fig. 5.18(b), where the average baseline value is plotted as a function of the OPD  $\eta$ . Here, for the common LO FSI configuration of Fig. 4.1(c),  $\eta$  is twice the physical distance to the LO balance point multiplied by the group index of refraction  $n_g = 1.46$ . To obtain the baseline RMS amplitude data, only the average of the four rightmost range channels, which are also marked in Fig. 5.18(a), are used, as these channels are positioned beyond the fibre tip reflection and no physical return signals can originate here. Therefore these values should not be influenced by parasitic reflections from the other connectors that are assumed to be in close contact in Fig. 5.14. In Fig. 5.18(b), a linear least square fit of this data is also drawn using a continuous line. In general, for Figs. 5.18(b) and (c) and for later figures, the OPD dependence of measurements is verified using least-square fits against the absolute OPD value  $|\eta|$ . For a generic measurand  $Y$ , the linear or quadratic least square fits are described by the following equation, where for a linear

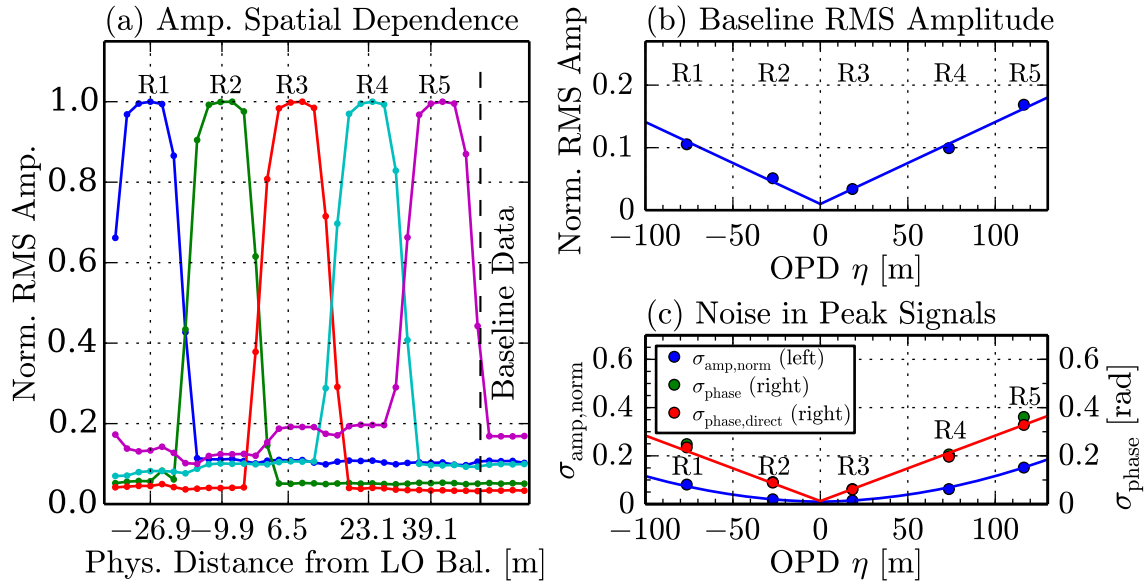


**Figure 5.18.:** For the five single reflector configurations R1 to R5 of Fig. 5.14 in a single plot, (a) shows the RMS values of the complex quadrature amplitudes in each of the 36 interrogated range channels, with the amplitudes normalised to the respective peak values. (b) then plots the RMS amplitude of the baseline, with values averaged over the four rightmost points that are also marked in (a), as a function of the distance of the originating reflector from the LO balance point. Finally, for the reflector signals evaluated at the respective peak range channel, (c) plots the standard deviation of the amplitude noise  $\sigma_{amp,norm}$  due to quadrature noise, normalised to the mean quadrature amplitude, and, on the secondary y-axis, the standard deviation of the apparent phase noise  $\sigma_{phase}$ . (c) also plots the direct phase noise levels  $\sigma_{phase,direct}$ , which exclude excess phase noise caused by quadrature noise and were computed using the model detailed in App. D.1. For each range channel, all noise standard deviation levels in (c) were determined for noise frequencies between 1 kHz and 20 kHz and in both (b) and (c), the solid lines represent linear or quadratic least square fits, according to Eq. (5.22), of the OPD dependence of the measurements.

fit the coefficient  $Y_2$  equals zero:

$$Y(\eta) = Y_0 + Y_1 \cdot |\eta| + Y_2 \eta^2 \quad (5.22)$$

It can be seen in Fig. 5.18(b) that the normalised RMS signal amplitude in the baseline for each of the configurations R1 to R5 shows a largely proportional dependence on the absolute OPD  $|\eta|$  with only a very small offset value  $Y_0$  in Eq. (5.22) of  $Y_0 = 0.001$ . This confirms that the signal levels in the baseline are, to a large part, OPD dependent, indicating that the baseline noise is not caused by a constant background noise source but rather by quadrature noise leakage that is linearly dependent on the absolute OPD of the originating reflector.

Furthermore, Fig. 5.18(c) evaluates amplitude and phase noise in the reflector signals themselves at the respective peak range channel, also as a function of the reflector OPD  $\eta$ . Here, the standard deviation of the complex amplitude noise  $\sigma_{\text{amp}}$  is normalised by the mean quadrature amplitude to obtain  $\sigma_{\text{amp,norm}}$ . Also the standard deviation of the apparent phase signal  $\sigma_{\text{phase}}$  is plotted in units of rad on the secondary axis in Fig. 5.18(c). Additionally, Fig. 5.18(c) plots the direct phase noise standard deviation  $\sigma_{\text{phase,direct}}$ , where direct phase noise that is thought to be caused by laser frequency noise is separated from excess phase noise that is thought to be induced by the quadrature noise. To obtain  $\sigma_{\text{phase,direct}}$ , the contributions of the excess phase noise are subtracted according to the model detailed in App. D.1. Both quadrature and phase data have been filtered to only take into account noise frequencies above 1 kHz, where environmental and  $1/f$  noise is subdued, and below the quadrature filter cut-off frequency  $f_{\text{Q,co}} = 20$  kHz. In this frequency range, the signals generally exhibit a flat noise floor. Again, in Fig. 5.18(c), a linear least square fit of the direct phase noise  $\sigma_{\text{phase,direct}}$  is shown using a continuous line. The linear fit of the direct phase noise shows a very good agreement with the ideally linear dependence on  $|\eta|$ , with an offset value  $Y_0$  in Eq. (5.22) of  $Y_0 = 0.006$  rad and a slope of  $Y_1 = 0.0030 \text{ rad m}^{-1}$ . For future reference, this also equates to a phase noise slope value of  $22 \mu\text{rad} \cdot \text{Hz}^{-0.5} \text{ m}^{-1}$ . A quadratic least square fit according to Eq. (5.22) of the normalised amplitude noise  $\sigma_{\text{amp,norm}}$  also shows very good agreement with the measured data in Fig. 5.18(c). Whilst the reason for this quadratic behaviour is not clear at this point and a single measurement would not warrant such a claim, a quadratic OPD dependence of  $\sigma_{\text{amp,norm}}$  is also found in Fig. 6.18(b) in Chap. 6 for the sinusoidal optical frequency modulation technique presented there. Therefore the quadratic behaviour is thought to be a general phenomenon that will also be discussed further in Chap. 6. In summary, the experiments visualised in Fig. 5.18 confirm a linear or quadratic OPD dependence of the leaked baseline RMS signal amplitude as well as of the amplitude and phase noise in the reflector signal themselves, proving that, with only a single reflector present, the noise behaviour is dominated by an OPD-dependent noise source.

In order to additionally investigate any dependence of the noise behaviour on the return signal amplitude and to characterise the performance of the technique for low signal powers, a further experiment, using the measurement configuration R3 in Fig. 5.14, was conducted. In this experiment, the return power of the fibre tip reflector was successively lowered by inducing bend loss in the fibre lead. The return



power levels range from  $-15$  dB (3.5 %) for the fibre tip Fresnel reflection without additional attenuation to  $-57$  dB (0.0002 %), as measured by a power meter instead of the photo detector in Fig. 5.11 and with the common LO arm disconnected. The spatial dependence of the average RMS signal amplitude over 20 range channels at each of the four return power settings is shown in Fig. 5.19(a), with the RMS amplitude normalised to the respective peak power. Comparing the measurements from  $-15$  dB to  $-45$  dB, the normalised RMS amplitude baseline values can be seen to remain largely constant. Only at  $-57$  dB does this relationship start to break down. This behaviour is quantified in Fig. 5.19(b), where the average normalised baseline RMS amplitude value is plotted as a function of the return power. To obtain these values, only the average of the four rightmost range channels, which are also marked in Fig. 5.18(a), are again used to calculate the baseline RMS amplitudes. Finally, similar to Fig. 5.18(c), for the peak range channel as a function of return power for noise frequencies between 1 kHz and 20 kHz, Fig. 5.19(c) plots the standard deviation of the amplitude noise  $\sigma_{\text{amp,norm}}$ , normalised by the mean quadrature amplitude, and the phase noise standard deviations  $\sigma_{\text{phase}}$  and  $\sigma_{\text{phase,direct}}$ , as detailed in App. D.1, on the secondary y-axis. It can be seen that the quadrature noise power dependency mimics the variation of the baseline RMS amplitude in Fig. 5.19(b), and that the apparent phase noise also shows an increase for low return powers. Fig. 5.19(c) shows that the direct phase noise levels  $\sigma_{\text{phase,direct}}$ , caused by laser

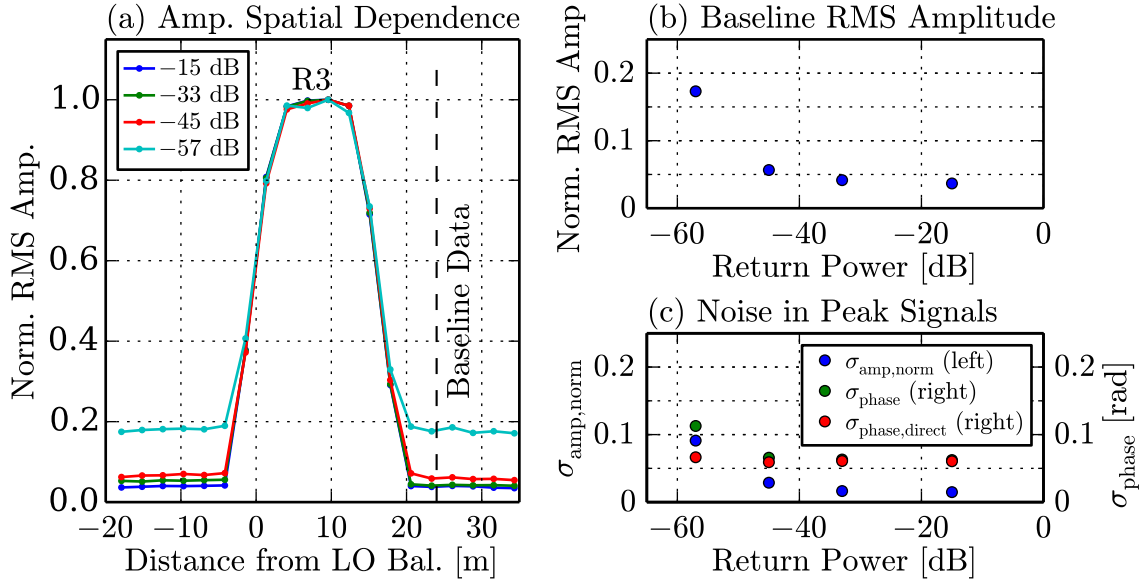


**Figure 5.19.:** For variable return powers of the single reflector configuration R3 of Fig. 5.14 in a single plot, (a) plots the root-mean square (RMS) values of the complex quadrature amplitudes in each of the 20 interrogated range channels, with the amplitudes normalised to the respective peak values. (b) then plots the height of the baseline, with values averaged over the four rightmost points that are also marked in (a), as a function of the return power. Finally, for the reflector signals evaluated at the respective peak range channel, (c) plots the standard deviation of the variation of the complex quadrature amplitude  $\sigma_{\text{amp,norm}}$  due to quadrature noise, normalised to the mean quadrature amplitude, and, on the secondary y-axis, the standard deviation of the apparent phase noise  $\sigma_{\text{phase}}$ . Here, all noise levels in (c) were determined for noise frequencies between 1 kHz and 20 kHz. Additionally, (c) also plots the direct phase noise levels  $\sigma_{\text{phase,direct}}$ , which excludes excess phase noise caused by quadrature noise and was computed using the model detailed in App. D.1.



frequency noise, are independent of the return signal power, therefore the increase in phase noise at low power levels can be entirely attributed to the strong increase in quadrature noise. In summary, the experiment visualised in Fig. 5.19 shows that the noise behaviour for strong to medium return power levels, i.e.  $-15$  dB to  $-45$  dB, is independent of the signal power and this behaviour only starts to break down at very low return signal powers below  $-45$  dB.

From the experiments shown in Fig. 5.18 and Fig. 5.19 it can be deduced that the noise behaviour for low return powers, i.e.  $-45$  dB or above, is dominated by a noise source that is dependent on the absolute distance of the originating reflector from the LO balance point. This rules out direct crosstalk from spurious reflections outside the measurement arm, shot noise, laser intensity noise as well as detector and signal processing noise as possible causes, because all of these would not show any dependence on the distance of the interrogated reflector to the LO. This only leaves laser frequency noise, with its conversion into phase noise at non-zero OPD, as a possible noise source. However, laser frequency noise, on its own, cannot explain the signal leakage into other range channels, evident in Fig. 5.18(b), or the increase in quadrature noise in the reflector signals, evident in Fig. 5.18(c), which, as discussed previously, ultimately limits the achievable quadrature signal low-pass filter cut-off frequency  $f_{Q,co}$  in this technique.

It has been discovered by Kirkendall *et al.* [244] and also discussed in Liao *et al.* [212] that for high-channel count, i.e. low duty-cycle, time-division multiplexing (TDM) systems (see also Sec. 4.2) the multitude of carrier harmonics that result from the inherent gating in TDM can considerably decrease the phase sensitivity. This is because high-frequency laser phase noise can become aliased into the signal band by higher carrier harmonics. This noise behaviour is a fundamental property of any TDM multiplexed system and cannot be corrected by anti-aliasing filtering [244]. It has further been determined by Kirkendall *et al.* [244] that the aliased noise level increases with the square root of the duty cycle and thus with the square root of the maximum number of signal sources that can be multiplexed. Similar to TDM, the number of carrier harmonics in CDM is also dependent on the maximum number of signal sources that can be multiplexed, which is equivalent to the MLS code length  $y$  given by Eq. (5.5). Therefore, it is presumed that the phenomenon of high-frequency noise aliasing can also be observed in the presented CDM experiments. In general, any aliased high-frequency phase noise will be the sum of noise contributions from many different carrier harmonics and will thus be uncorrelated to the desired phase signal. In this work, it is therefore assumed that the observed quadrature noise is dominated by aliased high-frequency laser phase noise. However, for low powers, quadrature noise might additionally result from other noise, such as shot or electronic noise. In either case, the quadrature noise is presumed to be uncorrelated to the desired phase signal and can cause excess phase noise as discussed in App. D.1.

In summary, since aliased high-frequency phase noise should affect every range channel equally, both on-peak amplitude noise in Fig. 5.18(c) and off-peak RMS signal amplitude leakage into the baseline evident in Figs. 5.18(a) and (b) could be explained using aliased high-frequency phase noise. Also, because the magnitude of the aliased high-frequency phase noise is proportional to the OPD, the strength of

the RMS amplitude leakage should be proportional to the LO position, as observed in Fig. 5.18(b). It can thus be concluded that at medium to high return power levels, i.e.  $\geq -45$  dB, the bulk of the quadrature noise, which in this work limits the quadrature signal cut-off frequency  $f_{Q,co}$  and thus the measurement bandwidth of the technique, is likely to be caused by aliased high-frequency laser phase noise.

**Crosstalk in Quadrature Signals:** In this section, results of an investigation into direct signal crosstalk in the complex quadrature signal are presented, allowing the comparison of the bipolar-bipolar MLS coding arrangement, used in prior phase-modulated MLS techniques [1,204], and the unipolar-bipolar MLS coding arrangement used in this work (see also Sec. 5.2.2). Additionally, these measurements also allow the theoretical predictions on the crosstalk suppression  $S_{cr,45,k}(\tau_d)$ , given by Eq. (5.16) and plotted in Fig. 5.10(f), to be tested.

The setup used for the crosstalk experiment is shown in Fig. 5.20, where a sinusoidal test signal of frequency 70 Hz and amplitude 19 rad is introduced by a Piezo-electric transducer (PZT). In this case, the resulting quadrature signal of the signal returned by the fibre tip reflection at position 0 contains many Bessel harmonics (see also Eq. (3.9)) and crosstalk at the Bessel harmonic frequencies into the complex quadrature signals at positions  $\pm 1$  and  $\pm 2$  is then evaluated. Both bipolar-bipolar and unipolar-bipolar MLS coding arrangements were implemented in the FPGA for a MLS code length of  $y = 15$ . Because in this experiment, data had to be recorded over long time periods to sufficiently lower the noise floor, a specially adapted FPGA implementation, where only 3 range channels are evaluated and where the output data was downsampled to a data rate of 5 kHz, had to be used, in order to allow continuous serial transfer of the data to the PC over 500 s.

Figs. 5.21(a) and (b) show the Fourier spectra resulting from the crosstalk measurements according to Fig. 5.20 for bipolar-bipolar and unipolar-bipolar MLS coding arrangements, respectively, plotting both the desired quadrature signals at position 0 and the crosstalk into range channels corresponding to positions  $\pm 1$ . It can be observed qualitatively in both Figs. 5.21(a) and (b) that the crosstalk is approximately constant for all Bessel harmonics. Also, in both Figs. 5.21(a) and (b), the zoom of

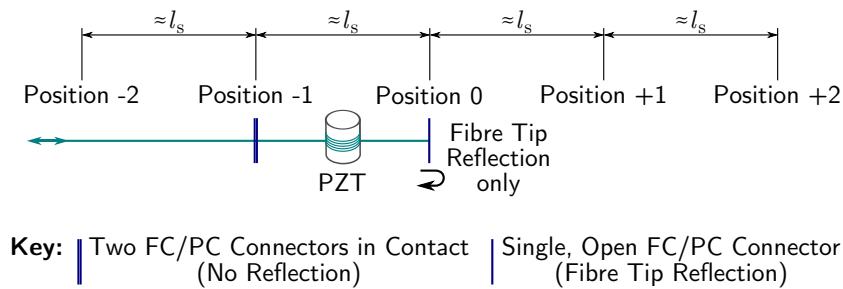


**Figure 5.20.:** Measurement arm configuration for the crosstalk experiment in conjunction with the setup shown in Fig. 5.11. Here, only one physical signal source due to the fibre tip reflection at position 0 is ideally present in the return signal. A PZT fibre stretcher is used to introduce a sinusoidal phase signal of frequency 70 Hz and amplitude 19 rad. Quadrature signal crosstalk that originates from the return signal of the fibre tip reflection into the range channels corresponding to positions  $\pm 1$  and  $\pm 2$ , at multiples of the unit fibre segment length  $l_s = 16.5$  m according to Eq. (5.21), is then evaluated in this experiment.

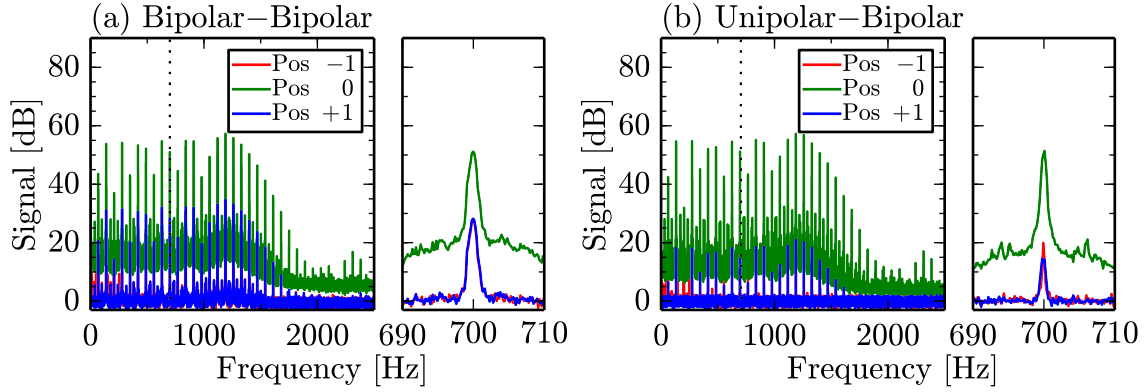


**Figure 5.21.:** Fourier spectra of the crosstalk measurements, showing the original quadrature signal at position 0 as well as the signals corresponding to positions  $\pm 1$  that exhibit crosstalk. Here, (a) shows the case for a bipolar-bipolar coding arrangement, while (b) shows the case for unipolar-bipolar coding. In both (a) and (b), the peak marked by the vertical dotted line at 700 Hz is shown enlarged to the right of the main plot.

the exemplary peak at 700 Hz, shown on the right of each main plot, confirms that the crosstalk for the bipolar-bipolar coding arrangement is indeed higher than for the unipolar-bipolar coding arrangement.

The crosstalk suppression is further quantified in Fig. 5.22, where extracted peak crosstalk values are plotted as a function of the Bessel harmonic index for all 24 Bessel peaks present in Figs. 5.21(a) and (b). From Fig. 5.22(a) for position  $-1$  a mean crosstalk suppression value of  $-23.6$  dB and for position  $+1$  in Fig. 5.22(b) a mean crosstalk suppression of  $-22.8$  dB can be extracted in the bipolar-bipolar MLS coding arrangement, which, for both positions shows little dependence on the Bessel harmonic index. These values are in very good agreement with the crosstalk

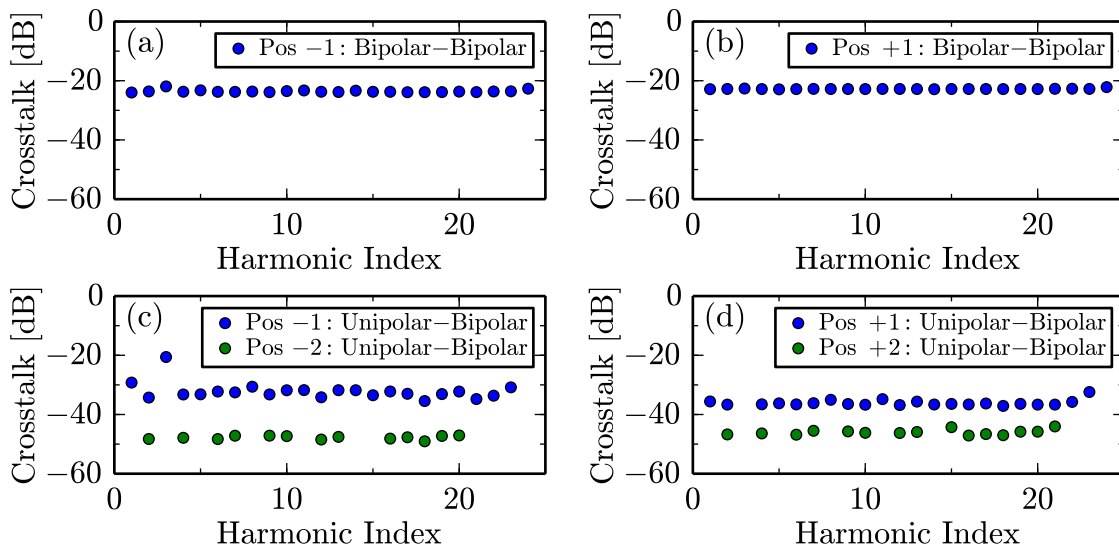


**Figure 5.22.:** Evaluation of crosstalk levels in the quadrature signal peaks as a function of the Bessel harmonic index. Here, only data points for peaks at least 3 dB above the noise floor are drawn. (a) and (b) plot the crosstalk levels for a bipolar-bipolar coding arrangement for positions  $-1$  and  $+1$ , respectively. (c) and (d) plot the crosstalk levels for unipolar-bipolar coding, here both for positions  $-1$  and  $-2$  in (c) and for positions  $+1$  and  $+2$  in (d).

suppression  $S_{\text{cr,bp-bp}} = -23.5 \text{ dB}$  predicted for the case of  $y = 15$  by Eq. (5.6), proving that the current experimental configuration can in principle measure correct crosstalk suppression values.

Figs. 5.22(c) and (d) then show crosstalk plots for the unipolar-bipolar coding arrangement that was used in this work. Here, an additional measurement at positions  $\pm 2$  was also carried out. Some Bessel harmonic peaks can be seen to be very weak in Fig. 5.21(b), and the resulting crosstalk level values that are either buried in the noise floor or do not rise at least 3 dB above the noise floor are not drawn. The measurements of Figs. 5.22(c) and (d) confirm that crosstalk is also uniform across all Bessel harmonics for unipolar-bipolar coding. Mean crosstalk values of  $-32.1 \text{ dB}$  and  $-47.8 \text{ dB}$  can be determined from Fig. 5.22(c) for positions  $-1$  and  $-2$ , respectively, while mean values of  $-36.1 \text{ dB}$  and  $-46.0 \text{ dB}$  are found from Fig. 5.22(d) for positions  $+1$  and  $+2$ , respectively. These values are not in agreement with the theoretical prediction of zero crosstalk  $S_{\text{cr,up-bp}} = -\infty$  expected from Eq. (5.6) and also don't correspond to the calculation of a crosstalk suppression  $S_{\text{cr,45,k}}(\tau_d)$  of  $-70 \text{ dB}$  expected when taking the combined anti-aliasing filter impulse response into account, as plotted in Fig. 5.10(f). The fact that the crosstalk suppression increases with distance from the originating source further indicates that this mismatch is due to non-ideal control of the DAC signal generation chain or the anti-aliasing filter impulse response for the ADC, as discussed in Sec. 5.4.2 and Sec. 5.4.4, respectively. Here, any remaining ringing in the respective impulse response could straightforwardly explain the observed behaviour. Nevertheless, crosstalk suppression values in the quadrature signals of  $-32 \text{ dB}$  and below have been demonstrated, which is an improvement compared to the bipolar-bipolar approach used in prior phase-modulated CDM implementations [1, 204]. Also, as will be shown in the next section and in App. D.3, the resulting crosstalk in the phase signals, which is more relevant to practical operation, is often at considerably lower levels than quadrature crosstalk, at least for non-stationary phase signals. However, crosstalk suppression of the quadrature signal could be improved in future work through better control of the experimental parameters in order to remove ringing of the filter impulse response, as will be discussed further in Sec. 5.6.1.

### 5.5.2. Multiple Reflector Measurements

While the previous section investigated the performance of the proposed technique for the case of only a single reflector present in the system, thus demonstrating the best case performance levels that can, in principle, be expected, the current section investigates the performance with multiple reflectors present, which is more relevant to future FSI applications. Here, the achievable linearity, noise and crosstalk performance for four reflectors is investigated. Then the dynamic performance limits of the present implementation are determined and, finally, the recovery of the segment signals from the reflector signals is demonstrated.

**Measurement Arm Configuration:** The measurement arm configuration used for these experiments is shown in Fig. 5.23. Here four interferometric signals arise from four reflectors R1 to R4 at positions 1 to 4 relative to the LO balance point. While

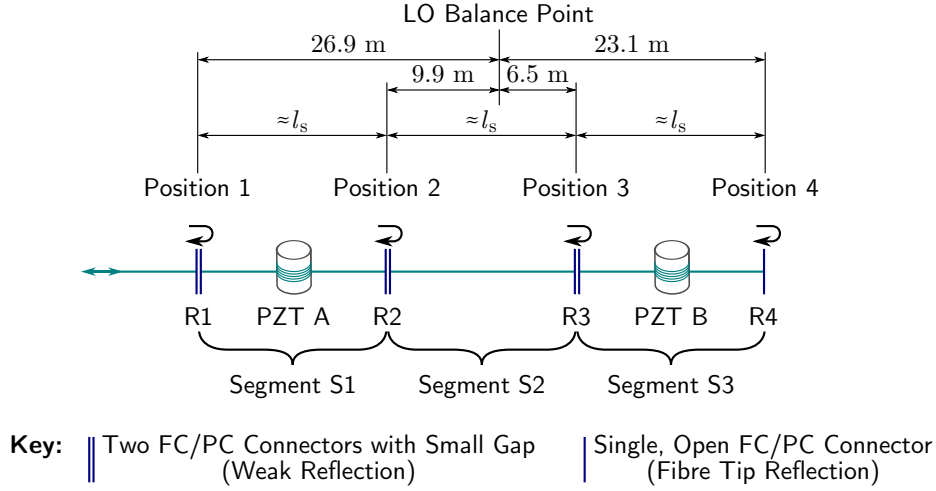


**Figure 5.23.:** Measurement arm configuration for multiple reflector experiments in conjunction with the setup shown in Fig. 5.11. Here, four physical return signals are introduced by reflectors R1 to R4. These originate from the fibre tip reflection at position 4 and from the three FC/PC connectors at positions 1 to 3 that are adjusted with a small gap to yield a weak reflection. Three fibre segments S1 to S3 of physical length  $l_s = 16.5$  m are then formed between the four reflectors R1 to R4, with PZT A inserted into S1 and PZT B inserted into S3 as test signal sources.

the signal from R4 is simply due to the Fresnel fibre tip reflection of an open FC/PC connector, the signals for R1 to R3 are obtained by leaving a small gap between two FC/PC connectors. In this case, the reflectors are not in direct contact so that a Fresnel reflection can be obtained, but are still sufficiently close for transmission losses to be minimised. This approach is low-cost and simple, but suffers from lack of stability, with further options for in-fibre reflectors discussed in Sec. 5.6.1. In total, three fibre segments S1 to S3 of physical length 16.5 m, according to the unit segment length  $l_s$  of Eq. (5.21), are then formed between the four reflectors R1 to R4. For all measurements in this section, a sinusoidal test signal of frequency 370 Hz and amplitude 13.7 rad was introduced into S1 by PZT A and a sinusoidal test signal of frequency 570 Hz and amplitude 19.8 rad was introduced into S3 by PZT B.

**Linearity of Reflector Signals:** Similar to Fig. 5.15 for the case of a single reflector, Fig. 5.24 can be used to analyse the linearity of the technique for multiple reflectors. Here, Fig. 5.24(a) again plots the complex quadrature phasor tip traces over 0.5 s using blue dots, with the angular average over 30 angular sectors drawn using green lines. In contrast to Fig. 5.15(a), the plots Fig. 5.24(a) are not normalised and are drawn in the original signal processing units. It can be seen qualitatively that the four plots again appear broadly circular and centred on the origin. To quantitatively determine the magnitude of the remaining cyclic errors analogous to Fig. 5.15, the dependence of the complex phasor amplitude, normalised to the mean phasor amplitude, on the phase angle is plotted using crosses in Fig. 5.24(b) for the angular averaged quadrature data. Also, these values are again fitted to the cyclic error model given by Eq. (3.8), with these fitted curves drawn in Fig. 5.24(b) using continuous lines of the same colour. The calculated angular errors using this model are then shown in Fig. 5.24(c), exhibiting magnitudes of up to  $\pm 30$  mrad, which is comparable to the results for single reflectors, plotted in Fig. 5.15(c). While the exact shape of the angular distortion curves in Fig. 5.24(c) appears unrelated to the curves in

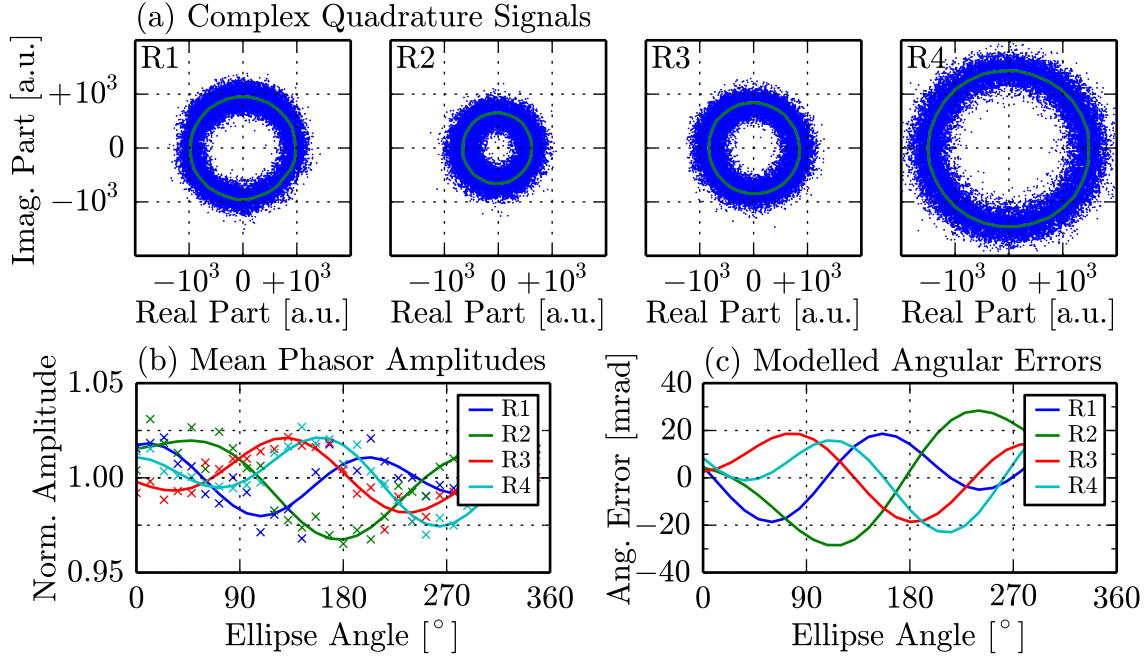


**Figure 5.24.:** Scatter plot of complex quadrature signals originating from the four reflectors R1 to R4 in the multiple reflector configuration according to Fig. 5.23. Here, for every reflector, (a) traces the locations of the tip of the complex quadrature phasor over 0.5 s using original signal processing units. This is represented by the blue dots, while the green lines show the angular average of this data over 30 angular sectors. (b) plots the normalized quadrature amplitudes for R1 to R4 as a function of complex phasor angle for the angular averaged data from (a) using crosses, while the fit of this data with the ellipse model of Eq. (3.8) is drawn using continuous lines of the same colour. Finally, in (c) the angular errors calculated using this model are shown.

Fig. 5.15(c), it can, however, be concluded that the magnitude of the cyclic errors appears largely unaffected by the presence of multiple reflectors.

**Noise of Reflector Signals:** It can be seen qualitatively in the polar plots in Fig. 5.24(a) that the mean signal amplitude varies for the return signals from the four reflectors. Fig. 5.24(a) also shows that the quadrature noise appears broadly similar in all four plots, regardless of the mean signal amplitude. This behaviour is quantified in Figs. 5.25(a) and (b), which plot the mean complex quadrature signal amplitude and the standard deviation  $\sigma_{\text{amp}}$  of the complex quadrature signal amplitude, respectively. Here, the units in both Figs. 5.24(a) and (b) are the original signal processing units and  $\sigma_{\text{amp}}$  is again computed for noise frequencies between 1 kHz and 20 kHz. The differences in reflector effective powers by up to a factor of two, evident in Fig. 5.25(a), are likely to be the result of the tuning differences of the individual reflectors, unavoidable with the type of reflector used here. Also, the effective powers of the reflector signals may be affected by polarisation changes within the fibre, which can only partially be compensated using the second polarisation controller in the common LO that was shown in Fig. 5.11. In theory, differences in reflector effective return powers can be tolerated, as they do not directly affect the retrieval of the phase information. In practice, however, due to the observed leakage of quadrature noise, a weak reflector signal may be subject to strong quadrature noise induced by other reflectors, which can lead to spurious phase unwrappings (see also App. D.2). For these reasons, a minimum return signal level that is dependent

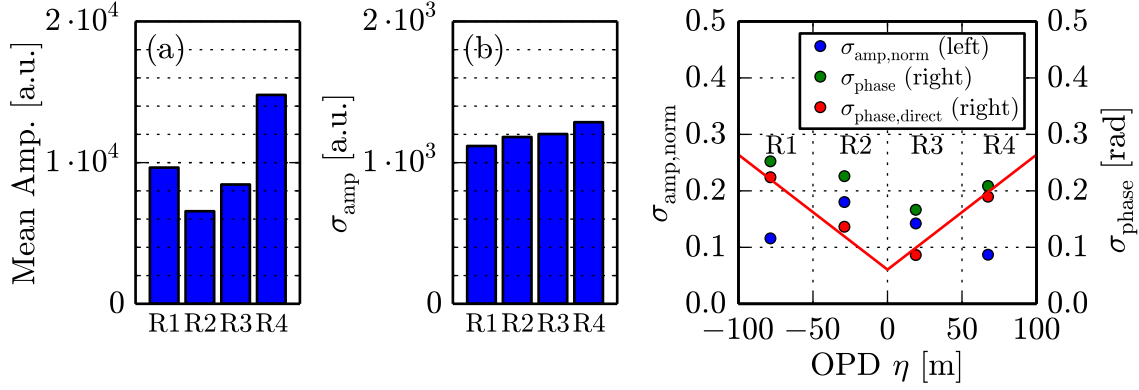


**Figure 5.25.:** The mean amplitudes of the complex quadrature signals are plotted in (a) as a bar chart for the four reflectors R1 to R4, using original signal processing units. (b) then shows the corresponding standard deviation of the amplitude noise  $\sigma_{\text{amp}}$  of the same data and in the same units as (a). Analogous to Fig. 5.18(c), (c) illustrates the noise present in the reflector signals as a function of the OPD. Here  $\sigma_{\text{amp}}$  of (b) is normalised using the mean quadrature amplitude of (a), yielding  $\sigma_{\text{amp,norm}}$ , and, on the secondary y-axis, the standard deviation of the apparent phase noise  $\sigma_{\text{phase}}$  is also plotted. Additionally, (c) also shows the direct phase noise standard deviation  $\sigma_{\text{phase,direct}}$ , where the influence of quadrature noise was compensated using the model detailed in App. D.1. A linear least square fit of  $\sigma_{\text{phase,direct}}$  according to Eq. (5.22) against the OPD is also shown in (c) using the red continuous line. Both amplitude and phase noise levels were determined for noise frequencies between 1 kHz and 20 kHz.

on the particular effective return power constellation, the OPDs of the reflectors and on the averaging defined by the quadrature signal cut-off frequency  $f_{Q,\text{co}}$  is required for reliable operation of the technique.

It can be seen in Fig. 5.25(b) that the complex quadrature phasor amplitude noise  $\sigma_{\text{amp}}$  levels are broadly similar for all four reflectors, with little discernible influence of either the effective power that is plotted in Fig. 5.25(a) or the distance from the LO balance point. In line with the previous arguments in Sec. 5.5.1, this remarkable behaviour can be explained by quadrature noise that is caused by aliased high-frequency laser phase noise. In this case, the resultant quadrature noise from any one reflector would be evenly distributed over all range channels. The quadrature noise contribution due to aliased high-frequency laser phase noise from each originating reflector is proportional to the individual reflector effective power as well as its OPD. The common quadrature noise level that then affects all reflector signals equally is thought to be the quadratic sum of all quadrature noise contributions from the individual reflectors. Therefore, in practical FSI applications, quadrature noise is dominated by strong reflectors with large OPDs.

Fig. 5.25(c) then quantifies the contribution of the quadrature noise onto the resulting phase noise of the reflector signals. As detailed in App. D.1, quadrature noise can cause excess phase noise that is proportional to the normalised complex quadrature signal amplitude noise  $\sigma_{\text{amp,norm}}$ . Fig. 5.25(c) then plots  $\sigma_{\text{amp,norm}}$ , determined from the data shown in Figs. 5.25(a) and (b), and, on the secondary y-axis, the standard deviation of the apparent phase noise  $\sigma_{\text{phase}}$ , where both  $\sigma_{\text{amp,norm}}$  and  $\sigma_{\text{phase}}$  are computed for noise frequencies between 1 kHz and 20 kHz. Using the model of App. D.1 then yields  $\sigma_{\text{phase,direct}}$ , the phase noise standard deviation solely due to laser frequency noise where the excess phase noise due to quadrature noise is com-



pensated, which is also plotted against the secondary y-axis. A linear least square fit according to Eq. (5.22) of  $\sigma_{\text{phase,direct}}$  against the OPD  $\eta$  is also shown in Fig. 5.25(c), drawn using the continuous red line. Similar to linear fit of  $\sigma_{\text{phase,direct}}$  in Fig. 5.18(c) for the case where only a single reflector is present, the fit of  $\sigma_{\text{phase,direct}}$  in Fig. 5.25(c) for multiple reflectors also results in a good agreement for the linear dependency of  $\sigma_{\text{phase,direct}}$  on the OPD. However, for the case of multiple reflectors a large offset value of  $Y_0 = 0.060$  rad is present, ten times the value for the corresponding single reflector experiment in Fig. 5.18(c). The reasons for this offset value in  $\sigma_{\text{phase,direct}}$  is not understood, but is likely to be due to shortcomings in the validity of the assumptions that are required for the application of the model of App. D.1. In this case, a partial correlation between quadrature noise components of the individual reflectors would invalidate the assumption of random quadrature noise phase that is used in App. D.1, with this question requiring further theoretical and experimental analysis. Nevertheless, it can be concluded from Fig. 5.25(c) and previous sections that the phase noise behaviour for a FSI configuration with multiple reflectors is a complex and not well-understood interplay of laser phase noise and quadrature noise, mainly caused by high-frequency aliased laser phase noise and which can furthermore also leak into other reflectors in the system.

**Reflector Signal Time Traces, Spectra and Crosstalk:** After analysing linearity and noise of the multiple reflector experiment shown in Fig. 5.23, the time traces of the four reflector phase signals are plotted in Fig. 5.26(a) over a period of 20 ms. Here, it can be seen that the signal from R1 carries no excitation, while the signals for R2 and R3 carry the test signal at 370 Hz of PZT A and that the signal for R4 carries the combined test signals of PZT A at 370 Hz and from PZT B at 570 Hz. For comparison with later work, Fig. 5.26(b) then plots the apparent phase noise levels in the reflector signals, previously shown in Fig. 5.25(c), however, now in units of  $\text{mrad} \cdot \text{Hz}^{-0.5}$  for phase noise frequencies between 1 kHz and 20 kHz. Here, broadly comparable phase noise levels for all four reflector signals can be observed.

The Fourier spectra of the phase signals, computed over the whole recording time of 0.5 s, are shown in Fig. 5.26(c) on a logarithmic frequency scale in units<sup>3</sup> of  $\text{dB}_{\text{rad}}$ . Here a Blackman window [243] was applied before the Fourier transform to reduce peak broadening due to spectral leakage. It can be seen in the spectra in Fig. 5.26(c) that  $1/f$  noise at low frequencies gradually converges into a flat noise floor above  $\approx 100$  Hz for all four reflector signals and that non-linear harmonics of the phase signal are at least 50 dB below the main peaks. Figs. 5.26(d) and (e) then enlarge the spectrum around the test signal peaks on a non-logarithmic frequency scale, with Fig. 5.26(d) showing the presence of the 370 Hz signal of PZT A for R2, R3 and R4, while Fig. 5.26(e) shows that the 570 Hz signal of PZT B is only present for R4.

In general, as detailed in App. D.3, due to the rules of phasor addition, crosstalk into phase signals does not only depend on the quadrature crosstalk suppression, but also on the phase signal waveforms of both the signals from which the crosstalk originates and the phase signal that is subjected to the crosstalk as well as the relative effective power ratio between them. It can be seen in the experimental

<sup>3</sup>For a phase value  $\varphi$  in units of rad, the value in units of  $\text{dB}_{\text{rad}}$  is given by  $20 \cdot \log_{10}[\varphi]$



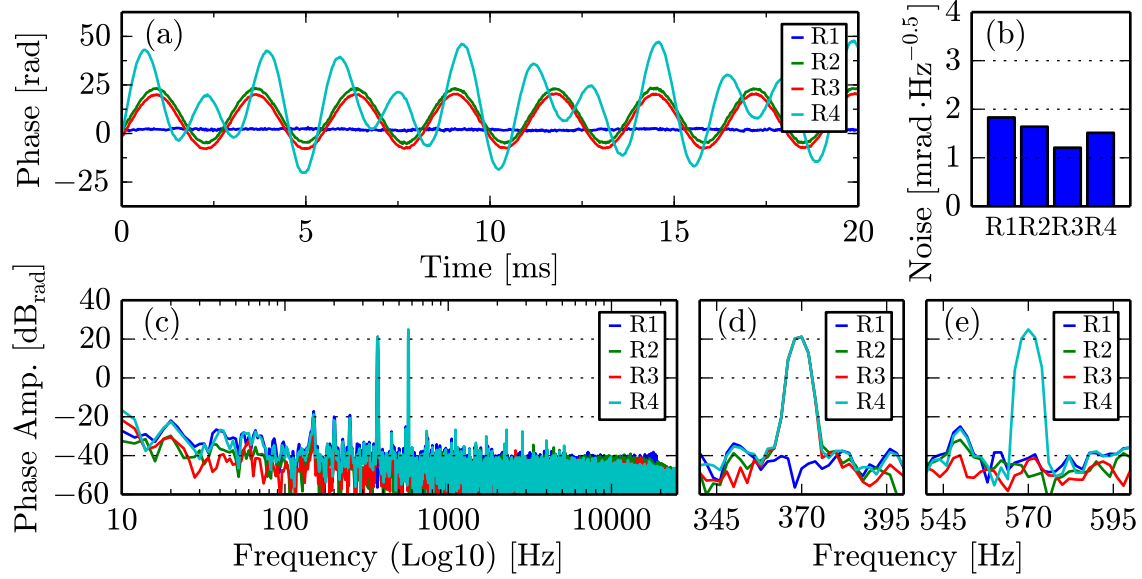


**Figure 5.26.:** Plot of the time trace of the phase signals from reflectors R1 to R4 in response to sinusoidal test signals at frequencies 370 Hz and 570 Hz, introduced by PZT A and B in Fig. 5.23, respectively. The bar chart in (b) plots the phase noise level, with data previously used in Fig. 5.25(c), now in units of  $\text{mrad} \cdot \text{Hz}^{-0.5}$ , for noise frequencies between 1 kHz and 20 kHz. (c) then plots the Fourier spectra (computed over 0.5 s) of the four phase signals on a logarithmic frequency scale, while (d) and (e) plot enlarged versions of the two main peaks in (c), at 370 Hz and 570 Hz, respectively, on a non-logarithmic scale.

results in Figs. 5.26(c), (d) and (e) that crosstalk levels in the phase signals were found to be at, or below, the noise floor level at  $-40 \text{ dB}_{\text{rad}}$  and thus, for the peak signals at 370 Hz and 570 Hz, a crosstalk suppression in the phase signals of at least  $-60 \text{ dB}$  was demonstrated for the particular experimental conditions. Furthermore, the analysis in App. D.3, especially Fig. D.4, confirms that, even if the worst-case quadrature crosstalk suppression of  $-32 \text{ dB}$ , derived from Fig. 5.22(c), is applied throughout, crosstalk induced signal components are expected to mostly stay well below  $-40 \text{ dB}_{\text{rad}}$ . Crosstalk signal contributions are therefore expected to be below the noise floor of the data shown in Fig. 5.26(c), confirming the validity of the experimental findings. Further experimental characterisation of phase signal crosstalk would require longer measurement periods to lower the noise floor sufficiently to identify crosstalk contributions that are currently beyond the limits of detection.

**Dynamic Characteristics:** As previously described in Sec. 3.1.4, the calculation of the bandwidth requirements of the complex quadrature signal is non-trivial and can be approximated by Carson’s rule of Eq. (3.4) for the simplified case of a sinusoidal phase signal. In the experimental setup of Fig. 5.23, two sinusoidal phase signals of frequency 370 Hz and amplitude 13.7 rad and of frequency 570 Hz and amplitude 19.8 rad, introduced by PZT A and B, respectively, are present. According to Carson’s rule, PZT A requires a quadrature bandwidth of  $B_Q = 5.4 \text{ kHz}$  and PZT B requires  $B_Q = 11.9 \text{ kHz}$ . It is assumed that the quadrature bandwidth requirement for the signal of reflector R4, where phase signals from both PZT A and PZT B are present, can be approximated by the sum of the bandwidth requirements for the individual sinusoidal phase signals, resulting in  $B_Q = 17.3 \text{ kHz}$ .

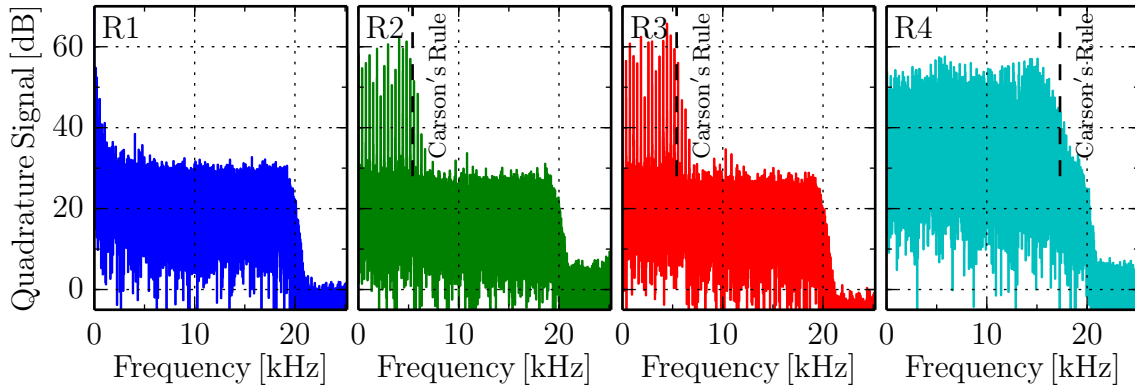


**Figure 5.27.:** The Fourier spectra of the complex quadrature signals for the four reflectors R1 to R4 are shown, which are subject to low-pass filtering in the FPGA at quadrature filter bandwidth of  $f_{Q,co} = 20$  kHz. For R2, R3 and R4 the calculated bandwidth requirements according to Carson's rule of Eq. (3.4) are marked using the dashed line.

To compare the calculated quadrature bandwidth requirements with the experimental data, the Fourier spectra of the reflector complex quadrature signals are plotted in Fig. 5.27 for the four reflectors R1 to R4. It can be seen in Fig. 5.27 that the quadrature signal spectra broadly adhere to the respective bandwidths defined by Carson's rule, which are marked by the dashed lines for R2, R3 and R4. In combination with the plots of the phase signals in Fig. 5.26, Fig. 5.27 confirms that the proposed signal processing technique can indeed reproduce phase signals of a quadrature bandwidth  $B_Q$ , according to Eq. (3.4), of at least 87% of the quadrature low-pass filter cut-off frequency  $f_{Q,co}$  without distortions. Since the consequences of not adhering to the bandwidth requirements, such as spurious phase unwrappings, are potentially more serious in interferometric signal processing than in communication engineering, it is proposed, as used here, to generally maintain a safety margin of 10% to 15% for the quadrature bandwidth limit  $B_Q$  of the phase signals relative to the given quadrature low-pass filter cut-off  $f_{Q,co}$ .

**Segment Signals:** Analogous to the reflector phase signals shown in Fig. 5.26, Fig. 5.28 shows the corresponding segment phase signals, obtained by subtracting reflector signals as explained in Sec. 5.4.4. Fig. 5.28(a) plots the segment signals in the time domain over a period of 20 ms and now directly reproduces the phase signals from PZT A and PZT B in segments S1 and S3, respectively. Also, the signal for segment S2 shows the complete suppression of the test signal of PZT A, which is present in both constituent reflectors R2 and R3 of segment S2, as visible in Fig. 5.26(a). Fig. 5.28(b) then plots the phase noise levels in the segment data, again for phase noise frequencies between 1 kHz and 20 kHz. Similar to the reflector phase noise levels shown in Fig. 5.26(b), the segment data phase noise levels show little discernible OPD dependence, with mostly constant phase noise levels up to a maximum value of  $2.2 \text{ mrad} \cdot \text{Hz}^{-0.5}$ . Fig. 5.28(c) then plots the Fourier spectra, again computed over the whole recording time of 0.5s, on a logarithmic frequency scale. The two main peaks at 370 Hz and 570 Hz, introduced by PZT A and PZT B, are then enlarged in Fig. 5.28(d) and Fig. 5.28(e), respectively, on a non-logarithmic frequency scale. Fig. 5.28(d) and Fig. 5.28(e) show that the two test signals in segments S1 and S3 can be completely separated by the signal processing and also

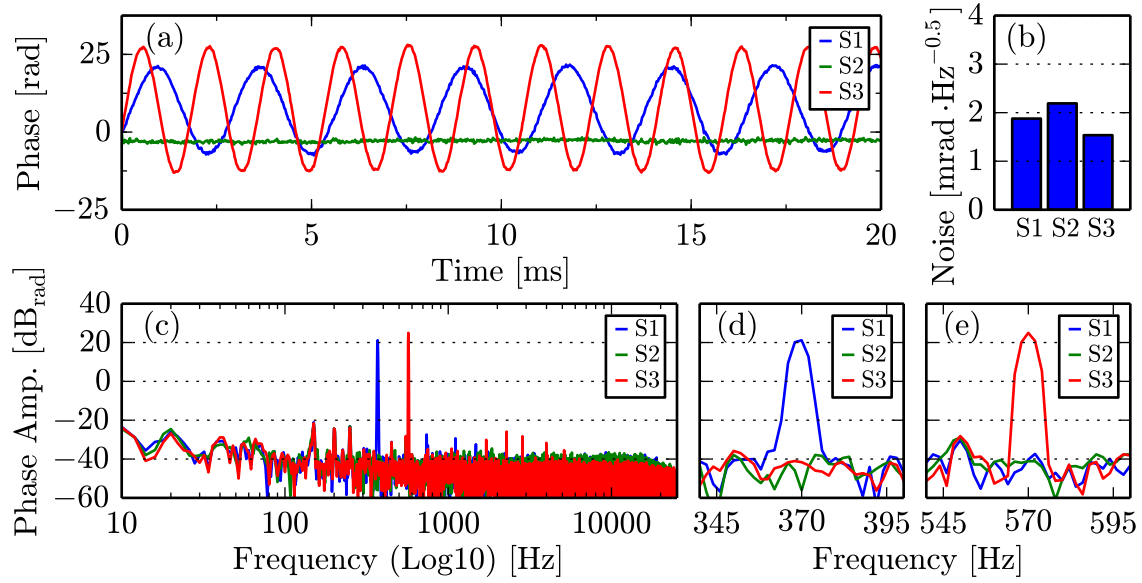


**Figure 5.28.:** Plot of the time trace of the phase signals from segments S1 to S3 in response to sinusoidal test signals at frequencies 370 Hz and 570 Hz, introduced by PZT A and B in Fig. 5.23, respectively. The bar chart in (b) plots the phase noise level in the segment data in units of  $\text{mrad} \cdot \text{Hz}^{-0.5}$ , for noise frequencies between 1 kHz and 20 kHz. (c) then plots the Fourier spectra (computed over 0.5 s) of the three phase signals on a logarithmic frequency scale, while (d) and (e) plot enlarged versions of the two main peaks in (c), at 370 Hz and 570 Hz, respectively.

confirms the absence of crosstalk in the segment phase signals.

When comparing the Fourier spectra of the segment data in Fig. 5.28(c) with the spectra of the reflector signals in Fig. 5.26(c), it can be seen that, while the flat noise floor above  $\approx 100$  Hz appears comparable in both cases, the  $1/f$  noise below  $\approx 100$  Hz differs considerably. For segment data it can be seen in Fig. 5.28(c) that  $1/f$  noise components appear mostly similar across all three segments, indicating that the  $1/f$  phase noise signals might be the same in all three segments. This is further investigated in Fig. 5.29, where Fig. 5.29(a) repeats the plot of the Fourier spectra of Fig. 5.28(c) in order to compare this with the case where the phase signal of segment S2, where no test signal was induced, is taken as a reference segment and subtracted from the phase signals for S1 and S3 before calculating the Fourier spectra. A similar approach to suppress low-frequency laser phase noise has also previously been demonstrated by Wuchenich *et al.* [202] using a digital heterodyne CDM technique (see also Sec. 4.3).

The resulting suppression of low-frequency phase noise is demonstrated in Fig. 5.29(b), showing that  $1/f$  noise, along with higher 50 Hz harmonics likely to be due to mains interference, can be largely suppressed with the help of the reference measurement and that a mostly flat phase noise floor at low frequencies results. This behaviour can be easily explained by low-frequency laser phase noise that is faithfully reproduced by the signal processing and partially corrected when the reflector signals are subtracted to obtain the segment data. However, in this case the segment data still carries a residual laser phase noise contribution that is proportional to the segment length. This residual laser phase noise is, at least at low frequencies, similar in all segments, and can be corrected by subtraction

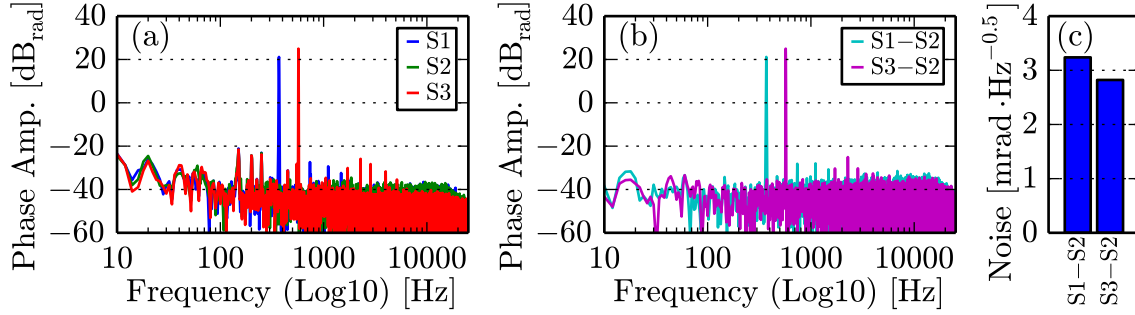
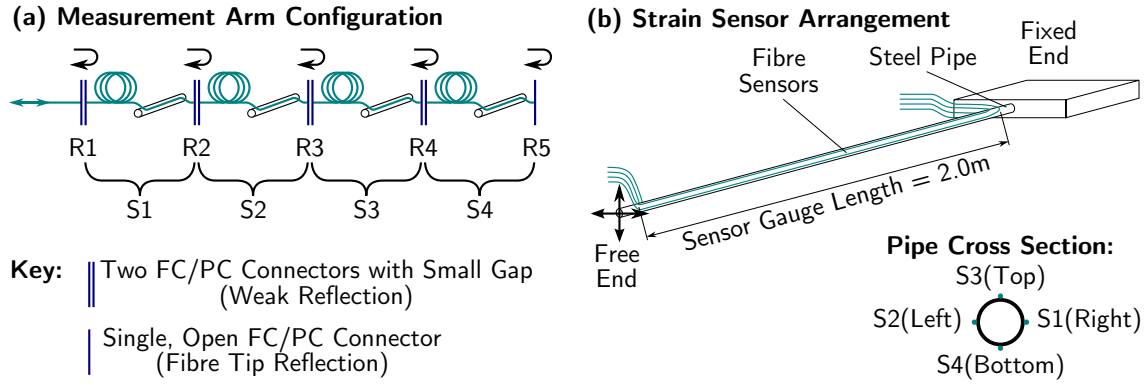


**Figure 5.29.:** (a) repeats the plot of the Fourier spectra over three phase signals on a logarithmic frequency scale, previously shown in Fig. 5.28(c), in order to compare this with (b), where the phase signal of segment S2 is subtracted from the phase signals for segments S1 and S3 before calculating the Fourier transform. (c) shows the direct phase noise levels for the corrected signals of (b) for noise frequencies between 1 kHz and 20 kHz.

of an appropriate reference measurement of similar segment length. A drawback of this subtraction process is, however, a general increase of the segment phase noise floor, measured for frequencies between 1 kHz and 20 kHz. An increase by  $\sqrt{2}$  would be expected when subtracting signals with uncorrelated phase noise and an increase on this scale is found by comparing the phase noise levels plotted in Fig. 5.29(c) and Fig. 5.28(b), where worst-case phase noise levels can be seen to increase from  $2.2 \text{ mrad} \cdot \text{Hz}^{-0.5}$  to  $3.2 \text{ mrad} \cdot \text{Hz}^{-0.5}$  for the case where a reference segment is used. Because low-frequency phase noise can be corrected well, it appears that the correlation of the phase noise is strong for low frequencies but that the degree of correlation reduces for higher noise frequencies. Here, the slight increase in the phase noise floor for high frequencies in Fig. 5.29(b) is a further indication of this phenomenon, however, a comprehensive explanation of this is not straightforward and should be a topic of future research. In summary, the measurements shown here confirm that the principle of the FSI approach proposed in this work, which requires the numerical subtraction of measured reflector phase signals to obtain the desired segment phase signals, appears to work very well in practice and may even be useful for suppressing low-frequency laser phase noise.

### 5.5.3. FSI Strain Measurements

Finally, to conclude the experimental section of this chapter, the SSB-CDM signal processing system was used to make exemplary FSI strain measurements, which also illustrates its potential use as long-gauge length interferometric strain sensor (see also Sec. 2.4). The sensor configuration for this experiment is shown in Fig. 5.30. Here, Fig. 5.30(a) shows the measurement arm configuration, in conjunction with Fig. 5.11, where four fibre segments S1 to S4 of unit fibre segment length  $l_s = 16.5 \text{ m}$ , according to Eq. (5.21), are formed between five reflectors R1 to R5. Again, FC/PC connectors that are tuned to return a small reflection while maintaining high transmission are employed as the first four reflectors R1 to R4, while the fibre tip Fresnel reflection is used for R5. In each of the four segments, a section of fibre is used for strain sensing, while the remainder of the fibre is rolled up and thus remains inactive.



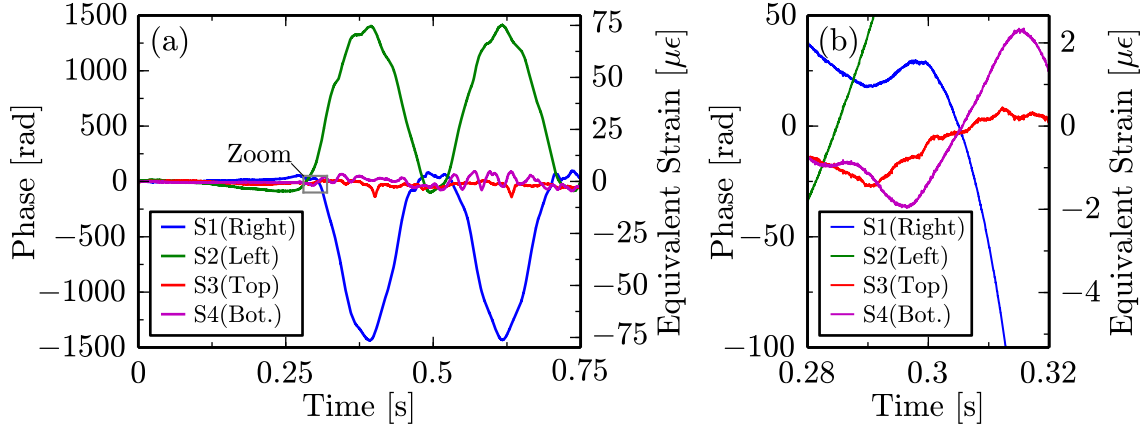
**Figure 5.30.:** The measurement arm configuration for the FSI experiment, in conjunction with the setup shown in Fig. 5.11, is shown in (a). Here five physical signal sources are introduced by reflectors R1 to R5. For R1 to R4 these originate from the reflections of the four FC/PC connectors that are adjusted with a small gap to yield a weak reflection and for R5 from the fibre tip reflection. Four fibre segments S1 to S4 of physical length  $l_s = 16.5$  m, according to Eq. (5.21), are then formed between the five reflectors and act as fibre strain sensors for part of their length, while the remainder of the fibre is rolled up. (b) then shows the arrangement of the four fibre strain sensors of active gauge length 2 m, attached to the four opposite sides of a steel pipe, as also illustrated in the cross section, with the pipe fixed on one end and free to move on the other.

Fig. 5.30(b) illustrates the sensing arrangement, with the sensitive parts of the fibre segments corresponding to a gauge length  $l_g = 2.0$  m. Here, the strain sensing sections of the four segments S1 to S4 are attached to four opposing sides of a steel pipe of outer diameter  $3/4'' = 19.05$  mm, as additionally illustrated in the cross section in Fig. 5.30(b), with the steel pipe fixed at one end but free to vibrate at the other. This experiment is designed to obtain test signals of low frequency but with high signal amplitudes. Signals of these characteristics are expected to be encountered in many real applications of long-gauge length interferometric strain sensing, particularly for large engineering structures.

Example measurements using the sensing arrangement in Fig. 5.30 are shown in Fig. 5.31. The phase data measured by the fibre segment sensors is plotted on the primary y-axis and corresponds to equivalent strain data with units shown on the secondary y-axis. Here, the strain change  $\Delta\epsilon(t) = \epsilon(t) - \epsilon(t_0)$  can be calculated from the measured phase signal change  $\Delta\varphi(t) = \varphi(t) - \varphi(t_0)$  relative to the measurement start time  $t_0$ , using the following equation adapted from Kirkendall *et al* [30]:

$$\Delta\epsilon(t) = \frac{\Delta\varphi(t) \cdot \lambda_0}{2l_g \cdot 2\pi \cdot n_g \cdot \kappa} \quad (5.23)$$

Here  $\lambda_0 = 1552$  nm is the vacuum wavelength of the laser light, where the values  $n_g = 1.46$  for the fibre group index and  $\kappa = 0.795$  for the fibre strain sensitivity factor  $\kappa$ , according to Roths *et al* [97] for SMF-28 type fibre, are also used. An additional factor of two is included in the denominator because in an FSI configuration the light passes the sensor gauge length  $l_g$  twice. In general, it can be seen in Eq. (5.23) that the strain sensitivity in interferometric strain sensing is inversely proportional to the sensor gauge length  $l_g$ , allowing very large strain sensitivities to be achieved with long-gauge length strain sensors. In Fig. 5.30(a) it is shown how the steel pipe



**Figure 5.31.:** Example strain measurement using the sensing arrangement illustrated in Fig. 5.30 for a horizontal excitation, recorded at a quadrature bandwidth of 20 kHz. Here, the phase signals from the four segments S1 to S4 are directly plotted in (a), with the secondary y-axis showing the equivalent strain values for a sensor gauge length of  $l_g = 2.0$  m, calculated according to Eq. (5.23). (b) then shows an enlarged version of the region marked in (a).

vibrates horizontally, resulting in large signals for S1 and S2 at a frequency of about 4 Hz after manual excitation after  $\approx 0.3$  s. Fig. 5.30(b) then shows an enlarged plot of the region that is also marked in Fig. 5.30(a) in order to allow visual inspection of the measurement quality. On closer analysis, using a separate measurement with the same configuration according to Fig. 5.30 but without any manual excitation, typical instantaneous phase noise standard deviations of 0.4 rad, or equivalent instantaneous strain noise below  $0.02 \mu\epsilon$ , can be determined over the total measurement bandwidth up to 20 kHz. When noise is evaluated for noise frequencies between 1 kHz and 20 kHz the standard deviation of the phase noise drops to 0.29 rad. This corresponds to phase noise levels of  $2.1 \text{ mrad} \cdot \text{Hz}^{-0.5}$ , which is comparable to the previous phase noise levels shown in Fig. 5.28(b).

One potential application for the FSI technique is thought to be interferometric curvature or shape sensing, which is based on the measurement of the differential strain in optical fibres attached to opposing sides of a curving structure. In order to demonstrate the potential of the technique in this area, the measurement previously shown in Fig. 5.30 is re-evaluated to obtain tip displacement data of the free end of the steel pipe illustrated in Fig. 5.30(b). Here, the simple cantilever model also used by Blanchard *et al.* [26], where the cantilever length is equal to the sensor gauge length  $l_g = 2.0$  m was used. Using Eq. (5.23), this can then be expressed as:

$$\Delta l_{\text{tip}} = \frac{\Delta\varphi(t) \cdot l_g \cdot \lambda_0}{6\pi \cdot n_g \cdot \kappa \cdot d_{\text{core}}} \quad (5.24)$$

Here,  $\Delta l_{\text{tip}}$  is the tip displacement along one Cartesian direction relative to the displacement at the start of the measurement, with the measured phase signal difference  $\Delta\varphi(t)$  defined analogous to Eq. (5.23). Here, for an optical fibre of outer radius  $125 \mu\text{m}$  (including coating), the relevant distance between the fibre cores  $d_{\text{core}}$  is the pipe diameter 19.05 mm plus twice the fibre radius, thus  $d_{\text{core}} = 19.30$  mm.

Eq. (5.24) was used to calculate tip displacement values for horizontal (Segments: S2 – S1) and vertical (Segments: S4 – S3) movement of the steel pipe. The results



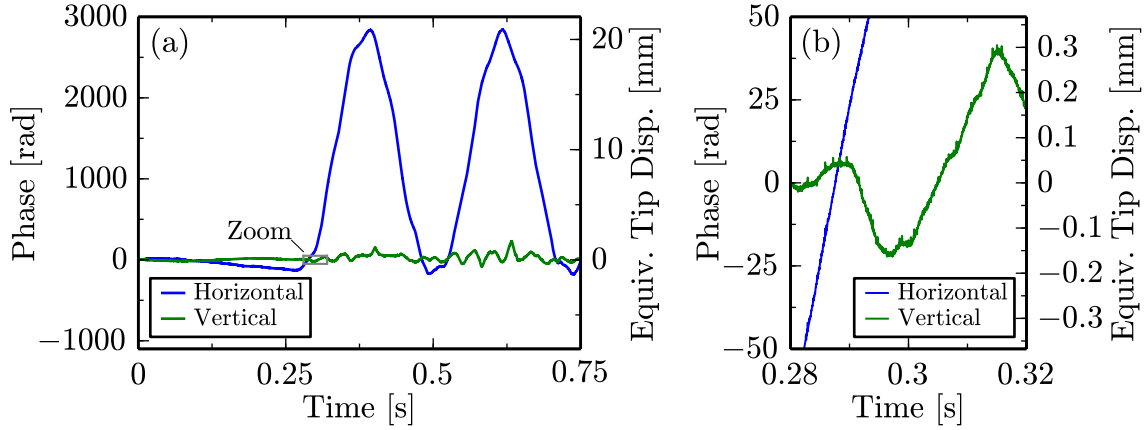


**Figure 5.32.:** Example tip displacement measurement using the sensing arrangement illustrated in Fig. 5.30 for a horizontal excitation, recorded at a quadrature bandwidth of 20 kHz. Here, the measured differential strain signals are plotted in (a), with the secondary y-axis showing the tip displacement values of the steel pipe calculated according to Eq. (5.24). (b) then shows an enlarged version of the region marked in (a).

of this re-evaluation for tip displacement measurements are shown in Fig. 5.32, where the measured phase differences are plotted in units of rad on the primary y-axis and the equivalent tip displacement values are plotted in units of mm on the secondary y-axis. Here, in Fig. 5.32(a), a maximum tip displacement of 20 mm in the horizontal direction can be observed, obtained after manually releasing the pipe from its initially curved position at about 0.25 s. It can also be seen in Fig. 5.32(a) that there is little movement in the vertical direction. Fig. 5.32(b) then allows a closer inspection of the measurement quality by enlarging the area also marked in Fig. 5.32(a), where some signal spikes that are thought to be due to data transmission errors are also visible. When the measurement without excitation that was previously used to determine the strain noise standard deviation is evaluated for tip displacement, a standard deviation of the tip displacement of  $4\text{ }\mu\text{m}$  can be found. Unfortunately, no further independent measurement of the tip displacement was carried out at the time of the experiment. Nevertheless, the value of 20 mm peak to peak tip displacement appeared to be in the right order of magnitude with the visually perceived tip displacement. In any future curvature sensing demonstration an independent verification measurement, possibly using free-space interferometric vibrometry, such as the technique proposed in Chap. 7, for direct tip displacement measurements would be highly recommended.

## 5.6. Discussion and Future Work

### 5.6.1. Discussion and Improvements to Current Work

**Polarisation Sensitivity:** The optical setup used in this work, as shown in Fig. 5.11, is relatively complicated, employing a polarisation controller and in-fibre polariser to maintain a stable phase modulation depth of the phase modulator output. This was necessary because of the strong inherent dependence of the phase modulation efficiency on the polarisation of the incoming light, typical of most electro-optic phase modulators [114]. In future implementations it is strongly recommended to

use a phase modulator with a polarisation-maintaining fibre input lead and employ a wholly polarisation-maintaining link, including the directional coupler, between the laser and the phase modulator input in Fig. 5.11. This would allow operation without any polarisation controlling and filtering equipment, both before and after the phase modulator, also avoiding the complicated tuning procedure outlined in Sec. 5.4.1 as well as ensuring that the setup will be tolerant to any drift in the polarisation properties. In future implementations, regular single-mode fibre could then be used after the phase modulator, for the remainder of the optical setup. However, the separate issue of how to prevent polarisation-induced fading [98, 99] might require further use of polarisation-maintaining fibre as discussed below.

In the setup shown in Fig. 5.11, a second polarisation controller was inserted into the common LO arm and tuned to optimize visibility across all participating reflectors in the measurement arm. While this procedure was sufficient to compensate polarisation-induced fading during this work, it is recognized that in a real-life application, the use of a second polarisation controller in this way cannot guarantee the absence of polarisation-induced fading. This would require the use of polarisation-maintaining fibre throughout the measurement arm and the remaining optical setup. Alternatively, polarisation-diversity detection [101] could be employed, where three detectors with linear polarisation filters that are individually offset by  $60^\circ$  are used, and where there is certainty that no complete fading can occur. This would avoid the use of expensive polarisation-maintaining fibre and couplers in the measurement arm and remaining setup, but would, however, require three photo detectors, analogue filters and ADCs in the signal processing chain.

**Choice of In-Fibre Reflector:** In the experiments in this chapter, pairs of FC/PC connectors that are slightly detuned to achieve weak back reflections are employed as partial in-fibre reflectors. This approach, while being low-cost and simple to set up, lacks stability and is therefore only applicable to a lab environment. For future implementations and real-life applications, the use of weak, broadband fibre Bragg gratings (FBGs), as used in Chap. 6, or other types of in-fibre partial reflector that have been reviewed in Sec. 4.1 are recommended to ultimately allow cost-effective and mechanically stable FSI sensing fibres. The permissible tolerances of the reflectivities for the partial in-fibre reflectors in the measurement arm should theoretically be very large. However, the discussed onset of quadrature noise that can also be seen in Fig. 5.24(a) and the associated requirement to prevent spurious phase unwrappings (see also App. D.2) at all times considerably lowers the permissible variances in the reflectivity values, with leaked quadrature noise from strong reflectors at large OPDs overshadowing the return signals from weaker reflectors. Additionally, the effective signal powers will also be affected by differences caused by polarisation mismatch.

**Spatial Resolution:** In order to improve the spatial resolution, i.e. reduce the unit fibre segment length  $l_s$ , with all other parameters of Table 5.1 unchanged, the speed of the signal processing would need to be increased. If the current signal generation and signal processing sample frequency  $f_s = 150$  MHz is scaled up by a factor  $\rho$  to  $f_s = \rho \cdot 150$  MHz,  $l_s$  will reduce to  $l_s = \frac{16.5 \text{ m}}{\rho}$ , according to Eq. (5.21). The maximally possible quadrature signal frequency  $f_{Q,\text{co,max}}$  of Eq. (5.12) will also increase when



the signal processing is scaled up by a factor  $\rho$  to  $f_{Q,co,max} = 3.125 \text{ MHz} \cdot \frac{\rho}{y}$ , where the MLS code length  $y$ , according to Eq. (5.5), determines the maximum number of range channels that can be separated. In this context, signal generation and processing at many GHz clock frequencies is state of the art in optical communications technology and has also been demonstrated for optical measurement applications [245]. If crosstalk or linearity expectations are lowered, a further option for improving the spatial resolution is the amendment of other signal processing parameters given by Table 5.1, in particular the number of waveform templates per code symbol  $x$  or the number of samples per waveform template  $D_{wf}$ . Here, any impact on the expected linearity and crosstalk performance can be conveniently analysed using the theoretical description developed in Sec. 5.2.3, using plots similar to Fig. 5.10.

**Signal Generation and Processing Impulse Responses:** Better control of both the signal generation and processing impulse responses may lead to improvements in both linearity and crosstalk due to a reduction of inter-symbol interference caused by ringing, with some ringing still visible in the inset in Fig. 5.8. In the current implementation, there is a lack of knowledge of how the electrically measured impulse responses transform to and from the optical domain, both at the phase modulator and at the photo detector. Therefore all measured impulse responses used so far in this work are incomplete in this regard. A possible method of measuring the complete impulse responses, including the optical domain, could involve the use of an active homodyne approach (see Sec. 3.2.3) in a simple Mach-Zehnder interferometric configuration, as illustrated in Fig. 3.9. Here, the PZT keeps the interferometer in quadrature (see also Sec. 3.1.1), so that there is linear signal transmission from the electrical to the optical domain. Using a high-speed oscilloscope and photo detector with measurement bandwidths well above the phase modulation bandwidth used would then allow the measurement of the complete impulse response of the signal generation chain as a result of an impulse introduced by the DAC. Following this, the regular photo detector and signal processing chain used for this implementation could be connected to the active homodyne setup to allow a corresponding measurement of the complete impulse response of the combined signal generation and processing chains by evaluating the ADC signal on the FPGA. Using these two measurements it is then possible to mathematically determine the impulse response of the signal processing chain only, which has been referred to as  $h_{anag}(t)$  in the previous sections, and which would then include the optical and electrical response of the photo detector.

The enhanced knowledge of the impulse response of the signal generation chain will be useful in improving the pre-shaping technique outlined in Sec. 5.4.2. Also, measurement of the impulse response  $h_{anag}(t)$  of the signal processing chain could enhance the quality of the theoretical predictions, such as those shown in Fig. 5.10. In a further step, the knowledge of  $h_{anag}(t)$  could be used to implement a pre-shaping procedure, similar to the one that was used in the signal generation chain and whose principle effectiveness in reducing ringing is evident in Fig. 5.12, to be applied to the signal processing chain as well. This would potentially allow the realisation of an effective combined impulse response  $h_{comb}(t)$  that would completely adhere to the design of the digital impulse response  $h_{dig}(t)$  (see Sec. 5.3.2). This would make  $h_{comb}(t)$  completely digitally controllable and should theoretically achieve the total

elimination of any ringing, which is currently still present in Fig. 5.8.

**Quadrature Bandwidth and Dynamic Range:** For the originally proposed applications of FSI in strain and shape sensing of large engineering structures, the most critical issue in the current implementation is thought to be the occurrence of quadrature noise due to aliased high-frequency laser phase noise. Quadrature noise can cause excess phase noise, as discussed in App. D.1. Also, as discussed before, quadrature noise can lead to a reduction in the reflectivity tolerances of the constituent reflectors, but, more importantly, it limits the usable quadrature signal cut-off frequency  $f_{q,co}$ . In this implementation, the reduction of  $f_{q,co}$  from its maximum value  $f_{q,co,max}$  by over a factor of 10, as discussed in Sec. 5.4.4, was necessary to prevent spurious phase unwrappings (see App. D.2) at all times.

For a given quadrature bandwidth  $B_Q$ , the permissible amplitude of a sinusoidal phase signal is approximated by Carson's rule of Eq. (3.4). For the value of the quadrature cut-off frequency  $f_{Q,co} = 20$  kHz used in this implementation, including the safety margin of 15% discussed in Sec. 5.5.2,  $B_Q$  equals 17 kHz. Fig. 3.5 plots the permissible amplitude range for a sinusoidal phase signal in this case. For an example 4 Hz sinusoidal strain signal, similar to the fundamental vibration component in Fig. 5.31(a), the maximum amplitude is 4.3 krad according to Fig. 3.5, which, using Eq. (5.23), equates to a strain amplitude of  $0.23 \text{ m}\epsilon$  for the sensor gauge length  $l_g = 2.0$  m that was used. If the theoretically largest possible quadrature cut-off frequency  $f_{Q,co,max} = 208$  kHz according to Sec. 5.4.4, with a corresponding quadrature bandwidth of  $B_Q = 177$  kHz, could be used, the permissible strain amplitude would increase to  $2.3 \text{ m}\epsilon$  for a 4 Hz example signal according to Fig. 3.5.

It should be noted that in the common LO FSI configuration of Fig. 4.1(c) implemented in this work, any measured reflector signal carries the signal contributions from all previous reflector signals, as can be seen in Fig. 5.26(a), where the signal from reflector R4 carries both contributions from PZT A and PZT B in Fig. 5.23. Therefore, the dynamic range available in any one fibre segment is dependent on the phase signals in other segments and the available quadrature bandwidth is shared by all fibre segment sensors present in the sensing fibre. This is a considerable limitation in any practical application as the required quadrature bandwidth  $B_Q$  will need to be specified high enough to encompass the sum of the phase signals of all fibre segment sensors. This could be mitigated in future work by the use of direct segment interference, as will be detailed in Sec. 5.6.2.

Because, as discussed in Sec. 5.5.1, the quadrature noise is thought to be the result of aliased high-frequency laser phase noise [212, 244], which itself is due to laser frequency noise in an OPD-imbalanced setup, the simplest way to improve the dynamic performance of the technique would be to employ a laser with lower intrinsic frequency noise. The laser used in this implementation was measured in App. B to have a linewidth of 0.6 MHz, while the linewidth specified by the manufacturer is 0.2 MHz. As detailed in App. B, it is thought that this performance reduction is due to current noise of the laser driver (Profile LDC200). If this is correct, the use of a better laser driver could improve laser frequency noise performance by up to a factor of 3. This, in turn, would lower the standard deviation of the laser phase

noise, which is proportional to the laser frequency noise, also by a factor of up to 3. In general, for a flat phase noise floor, an increase in the phase noise bandwidth by a factor of  $\rho$  would increase the instantaneous phase noise standard deviation by a factor of  $\sqrt{\rho}$ . Therefore, a reduction in the instantaneous phase noise standard deviation, which for aliased high-frequency noise should be directly proportional to the instantaneous quadrature noise standard deviation, by a factor of 3 through the use of a better laser driver should result in an increase of the achievable quadrature bandwidth by a factor of 9. This is close to the maximally possible frequency  $f_{Q,co,max} = 208 \text{ kHz}$  for the current system parameters. Therefore, there is reason to believe that the performance could be improved even for the current laser diode simply by using a driver with improved noise characteristics. Furthermore, the use of integrated external cavity lasers that can also be comparatively cost-effective could improve phase noise performance [246] by several orders of magnitude. Another option to reduce quadrature noise would be the use of a low-coherence source in an OPD-balanced compensating FSI configuration, as will be outlined in Sec. 5.6.2.

**Phase Noise and Dynamic Strain Sensitivity:** In Sec. 5.5.3, typical instantaneous phase noise standard deviations for a fibre segment were found to be 0.4 rad over all frequencies up to 20 kHz, which incorporates, as evident in Fig. 5.28(c), strong contributions from  $1/f$  noise at low frequencies. This is lowered to 0.29 rad for noise frequencies between 1 kHz and 20 kHz, where a flat phase noise floor is present. In general, the statement of a dynamic strain sensitivity value per  $\sqrt{\text{Hz}}$ , which is the conventional means of comparing different strain sensors, requires a flat noise floor to be meaningful. In FSI long-gauge length strain sensing, low frequency phase signals are expected to be dominant, therefore any dynamic strain sensitivity value that is relevant must also include low frequencies. As demonstrated in Fig. 5.29(b) it is possible to compensate low-frequency laser phase noise and obtain a flat noise floor down to low frequencies by subtracting the phase signal of the desired segment from the measurement of a reference segment. The resulting mostly flat noise floor then allows the extension of the validity of the measured phase noise level of  $3.2 \text{ mrad} \cdot \text{Hz}^{-0.5}$ , originally valid only for noise frequencies between 1 kHz and 20 kHz, down to low frequencies. Using this value of  $3.2 \text{ mrad} \cdot \text{Hz}^{-0.5}$  then permits the statement of a dynamic strain sensitivity value of  $0.17 \text{ n}\epsilon \cdot \text{Hz}^{-0.5}$ , now valid from low frequencies up to 20 kHz, using Eq. (5.23) for the demonstrated sensor gauge length of  $l_g = 2.0 \text{ m}$ . If the whole fibre segment length of  $l_s = 16.5 \text{ m}$  is used for strain sensing, the sensitivity would improve to  $21 \text{ p}\epsilon \cdot \text{Hz}^{-0.5}$ . The presented long-gauge length interferometric sensor system, in line with most fibre strain sensors (see Sec. 2.1), suffers from a strong inherent sensitivity to temperature due to the material properties of silica optical fibres. This can negatively affect strain measurements and temperature-strain discrimination has not yet been addressed in this scheme. Possible options, such as a two-wavelength approach, are reviewed by Jones [21]. However, temperature-induced variations of the laser emission wavelength can be compensated by the proposed reference segment measurement as described before and should then cause no concern.

When compared to high-end optical hydrophone applications, where sensitivities below  $1 \mu\text{rad} \cdot \text{Hz}^{-0.5}$  [96] have been obtained using an OPD-balanced active homo-

dyne approach (see also Sec. 3.2.3), the obtained phase noise levels of  $3.2 \text{ mrad} \cdot \text{Hz}^{-0.5}$  are not very good. This difference in performance is primarily attributed to the use of an internal cavity diode laser in an OPD-imbalanced setup, where internal cavity diode lasers, such as DFB diode lasers, are known to have phase noise levels orders of magnitude higher than solid state Nd:YAG lasers commonly used for fibre optic hydrophones [30, 246]. Also, in high-end strain sensing applications, active FBG-based fibre laser sensors have achieved dynamic strain sensitivities as low as  $7 \text{ f}\epsilon \cdot \text{Hz}^{-0.5}$ . However, apart from the high-end systems discussed above, when compared to other cost-effective strain sensing techniques, such as regular FBG-based strain sensing, the achieved dynamic strain sensitivities of the proposed approach, well below the  $\text{n}\epsilon \cdot \text{Hz}^{-0.5}$  level, compare very well. Here, wavelength-based FBG interrogation (see Sec. 2.3) can reach dynamic sensitivities [65] as low as  $5 \text{ n}\epsilon \cdot \text{Hz}^{-0.5}$  [65, 247], while interferometric FBG interrogation (see also Sec. 2.3), which, in common with the proposed FSI technique does not provide absolute strain values, has also been shown to achieve sensitivities in the  $\text{n}\epsilon \cdot \text{Hz}^{-0.5}$  range [65, 248, 249], but requires a separate readout interferometer per sensor, which is very impractical. Therefore, it can be said that the dynamic sensitivity of the proposed FSI technique is comparable to or surpasses most other cost-effective strain sensing applications and could be further improved by a reduction in laser frequency noise as outlined before. Furthermore, the proposed FSI technique has already demonstrated the stated strain sensitivities for frequencies up to 20 kHz and has the potential to reach much higher bandwidths, therefore also promising usefulness for high-speed applications.

**Linearity and Crosstalk:** Maximum non-linearity errors were found to be  $\pm 0.03 \text{ rad}$  in Fig. 5.15(c) for the current implementation. Using Eq. (5.23) and realizing that systematic errors, such as cyclic errors, in the reflector data can enter the segment data twice in the worst case, the maximum systematic phase error can be given as  $\pm 0.06 \text{ rad}$ , or  $4 \text{ n}\epsilon$  for the gauge length of  $l_g = 2.0 \text{ m}$  used in the current FSI implementation. Also, because the magnitude of the cyclic error can never exceed  $0.5\pi$  and is non-cumulative, this systematic error is bound in magnitude to below  $0.17 \mu\epsilon$  for the gauge length of  $l_g = 2.0 \text{ m}$ , even in a worst-case scenario, however, these systematic errors values obviously require the total absence of spurious phase unwrappings (see also App. D.2). It is also worth noting that strain noise and systematic errors scale inversely with the sensor gauge length, leading to even higher strain sensitivities and reduced systematic errors for longer sensor gauge lengths.

In this work, crosstalk suppression levels in the phase signals below  $-60 \text{ dB}$  were demonstrated even though crosstalk suppression levels in the quadrature signals were found to be as high as  $-32 \text{ dB}$ . The reasons for this behaviour are explained in App. D.3, where the simulation performed there confirms that phase signal crosstalk suppression levels below  $-60 \text{ dB}$  can indeed be expected for the current experimental implementation. This compares well with prior work in phase-modulated CDM, where Wuchenich *et al.* [202] demonstrated a crosstalk suppression ratio in the phase signal of  $-52 \text{ dB}$  using a digitally enhanced heterodyne interferometry technique (see also Sec. 4.3). For the originally proposed applications of strain and shape sensing for large engineering structures, systematic error levels due to cyclic errors and crosstalk on the scales seen in this work can be deemed negligible, but nevertheless future

applications in other application areas might benefit from further improvement using some of the measures discussed in this section.

### 5.6.2. Future Research Directions

Apart from implementing the improvements to the current setup outlined in the previous section, the following conceptual changes could also be investigated in future research to see if performance in FSI applications can be enhanced. Also, the proposed concepts may open up new application areas of SSB-CDM signal processing outside FSI for large engineering structures. In general, there is also the option to combine FSI with regular FBG sensing operating at other wavelengths to obtain both short-gauge and long-gauge length strain information from the same sensing fibre. In contrast to the common LO configuration of Fig. 4.1(c) that was used so far in this work and where the signals returning from the in-fibre partial reflectors interfere with a strong common LO, the newly proposed configurations rely on direct interference between individual reflector signals. The main advantage of this is that the system is approximately OPD-balanced, which should reduce overall laser phase noise even though more intrinsically noisy low-coherence sources will be used. Furthermore, the dynamic range for each sensor is not shared with other sensors in the sensing fibre, as is the case for the common LO configuration discussed in the previous section. Also, because the return reflector signals travel to and from the fibre segment together and their paths only differ while traversing the actual fibre segment, much greater polarisation overlap can be expected in many cases, easing the problem of polarisation-induced signal fading discussed before. However, as detailed in Sec. 4.1, the return signals of the in-fibre partial reflectors do not experience heterodyne gain, i.e. effective amplification by a strong LO signal, therefore the reflectivities need to be larger and the potential for undesired path combinations and multiple reflections to distort the measurements is greater.

In the three previously reviewed basic FSI configurations of Fig. 4.1, the reflector signals interfere directly in the configurations of Figs. 4.1(a) and (b), theoretically permitting the advantages discussed above. Out of these two configurations, the direct FSI configuration of Fig. 4.1(a) is deemed incompatible with the current SSB-CDM technique, because the current SSB-CDM technique requires the interference of the phase-modulated light with unmodulated LO light. However, the compensating configuration of Fig. 4.1(b), using a low-coherence source, is compatible with SSB-CDM because here an unmodulated LO is provided by the light bypassing the phase modulator in the compensating interferometer. The principle setup for a FSI configuration implementing the compensating FSI configuration of Fig. 4.1(b) is plotted in Fig. 5.33(a). Here the delay  $\tau_{\text{comp}}$  in the compensating interferometer is chosen to compensate the OPD  $\eta = 2n_g l_s$  over one fibre segment, with a fibre group index of refraction  $n_g$  and with the unit fibre segment length  $l_s$  of Eq. (5.21). Because all desired segment signals are approximately OPD-balanced, the low-coherence properties of the illuminating light suppresses signals from all other path combinations as well as multiple reflections. Furthermore, the use of an approximately OPD-balanced setup should mostly eliminate direct laser phase noise, as well as

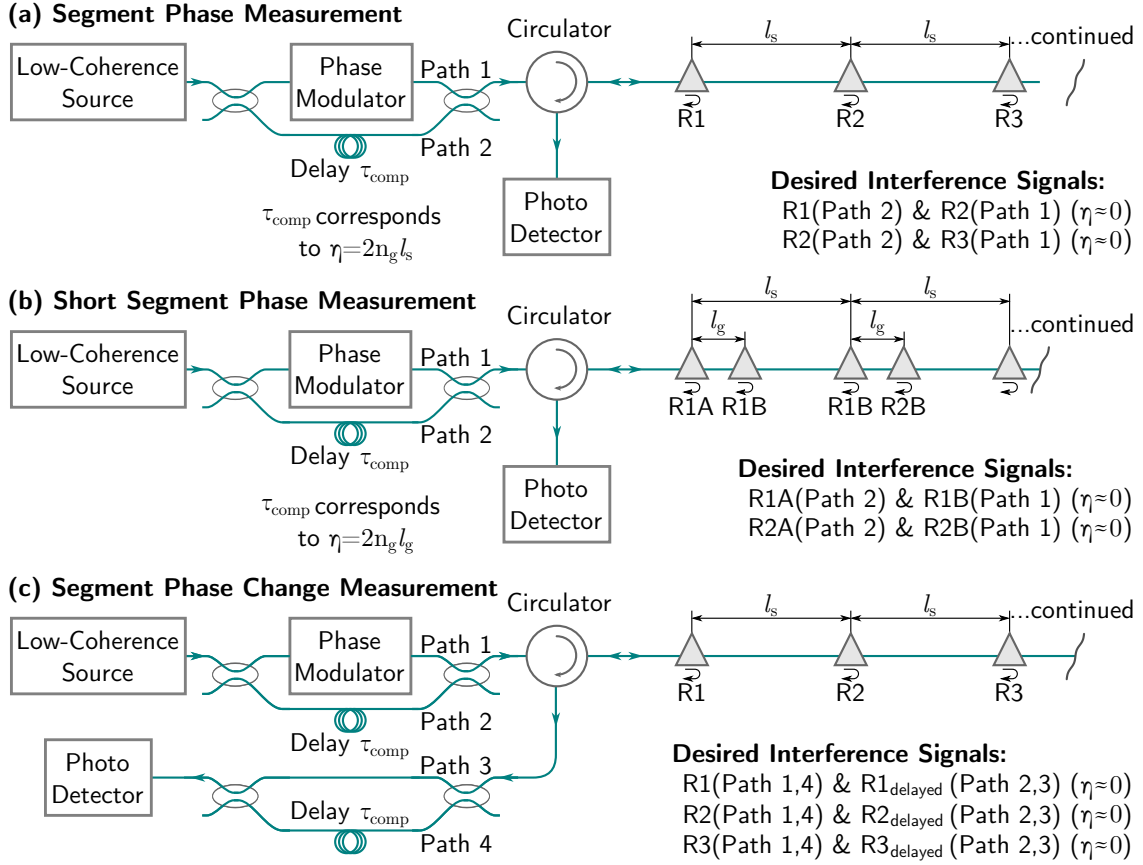


**Figure 5.33.:** Proposed future extensions to the FSI concept, employing a low-coherence source and fibre of group index of refraction  $n_g$ . Here, (a) implements the compensating FSI configuration of Fig. 4.1(b) for fibre segments corresponding to the unit segment length  $l_s$ , according to Eq. (5.21). (b) highlights the possibility of shortening the fibre sensors to a user-definable gauge length  $l_g$ , while still maintaining a sensor spacing of unit fibre segment length  $l_s$ . In (c), a second compensating interferometer is used to interfere the signals returned from the same reflector but separated by a user-definable delay time  $\tau_{\text{comp}}$ , resulting in a direct measurement of the phase change rate.

associated aliased high-frequency phase noise causing quadrature noise. This should ease the previously discussed bandwidth limitations caused by quadrature noise. The required low coherence could be a natural property of the source or could be introduced artificially through additional modulation [135]. However, due to the fibre couplers used, a compensating configuration introduces additional losses

The compensating FSI configuration of Fig. 5.33(a) can also be altered to multiplex fibre sensors with shorter gauge lengths by changing the delay  $\tau_{\text{comp}}$  in the compensating interferometer. This is illustrated in Fig. 5.33(b), where the interference signals from pairs of reflectors that are separated by the reduced sensor gauge length  $l_g$  is evaluated and the delay  $\tau_{\text{comp}}$  is appropriately adjusted to correspond to the OPD  $\eta = 2n_g l_g$  over the reduced sensor gauge length only. In order to implement SSB-CDM, the distances between the reflector pairs still need to adhere to the unit segment length  $l_s$ , but there are no further limitations on  $l_g$  other than that the coherence length of the source has to be much lower than  $2n_g l_g$ . This approach could potentially be applied to the multiplexing of short-gauge length Fabry-Perot sensors (see also Sec. 2.4), where surplus optical fibre between sensors is of no concern.

Finally, the setup shown in Fig. 5.33(c) shows a configuration employing two compensating interferometers that can be used to directly measure the phase difference, i.e. the rate-of-change, of a segment signal over a user-definable delay time  $\tau_{\text{comp}}$ . Here, for every reflector, there is approximate OPD-balance between the phase-modulated arm of the interferometer (Path 1 and Path 4) and the LO (Path 2 and Path 3), while other path combinations are suppressed when the coherence time of the light is much smaller than  $\tau_{\text{comp}}$ . This results in a separate interference signal for every participating reflector, however, because the reflection of the phase-modulated light of path 1 is initially not delayed, while the reflection of the LO light of path 2 is delayed by  $\tau_{\text{comp}}$ , the phase of the resulting interference signals will be non-zero only if there is a non-zero rate of change of the reflector phase signals. The rate-of-change signal over any segment can then be obtained by numerical subtraction of the measured rate-of-change signals from the reflectors and the sensitivity can be adjusted by changing the delay  $\tau_{\text{comp}}$ . This approach could have advantages in applications where the rate-of-change of a strain signal or a velocity signal is the primary measurand. Also, for high-frequency signals, the direct measurement of rate-of-change phase signals provides an inherent suppression of large undesired low-frequency phase signals, which could lead to lower quadrature bandwidth requirements in many cases. Furthermore, because the interfering light travels exactly the same fibre path no polarisation-induced fading is expected as long as polarisation changes over the delay time  $\tau_{\text{comp}}$  can be ruled out.

## 5.7. Summary

A novel signal processing technique that combines code-division multiplexing to separate signals from multiple sources and single-sideband homodyne processing to perform interferometric phase measurements, achieving both functions using only a single phase modulator, was presented in this chapter. The scheme is primarily aimed at FSI applications, such as strain and shape sensing in large engineering structures, but further extensions to other applications have also been discussed.

A detailed theoretical description of the technique has been presented that allows the calculation of relevant design parameters, with special emphasis on the anti-aliasing filtering necessary in any digital signal processing system. The various design choices for signal generation and processing have been described extensively and analysed using the theoretical approach developed. After describing the implementation details, experiments with several measurement configurations to characterise different performance aspects of the technique were carried out. This was followed by a comprehensive discussion of the limitations of, and possible improvements to, the current implementation, before novel concepts for future research work were proposed. In the experimental sections, using a cost-effective laser diode and phase modulator, up to four fibre segments of length  $l_s = 16.5$  m were multiplexed with typical phase noise levels of  $3.2 \text{ mrad} \cdot \text{Hz}^{-0.5}$  and a maximum quadrature bandwidth of 20 kHz was demonstrated. Crosstalk suppression in the phase signals was found to be below  $-60$  dB and the cyclic errors in the reflector signals were at a maximum of  $\pm 0.03$  rad, leading to worst-case systematic distortion in the segment data of  $\pm 0.06$  rad. When, as in the experimental demonstration, a reduced sensor gauge length of  $l_g = 2.0$  m is used, these noise levels equate to a strain sensitivity of  $0.17 \text{ n}\epsilon \cdot \text{Hz}^{-0.5}$  and the system has been applied to an example strain and tip displacement measurement of a vibrating steel pipe cantilever.

The main limitation of the scheme in its current implementation was found to be aliased high-frequency laser phase noise. This severely limited the achievable quadrature bandwidth to less than 10% of the theoretically possible bandwidth, however, it is thought that through the use of a better laser driver, and/or better laser diodes, this could be easily improved. The current implementation theoretically allows the multiplexing of 14 fibre segments without altering the signal processing parameters, and faster digital signal generation and processing hardware could be employed in order to reduce the minimum fibre segment length  $l_s$  in future implementations. Because the combined cost of all the equipment used in this prototype was less than £6k, the possibility of a cost-effective strain measurement system has been successfully demonstrated.



# 6. Sinusoidal Optical Frequency Modulation Technique for Fibre Segment Interferometry

## 6.1. Introduction

In this chapter, a novel range-resolved interferometric signal processing technique is proposed and several experiments are demonstrated, including an application to the fibre segment interferometry (FSI) approach that forms the main theme of this thesis. In contrast to the code-division multiplexing (CDM) technique presented in the previous chapter, where direct phase modulation was used, the approach in this chapter is based on sinusoidal optical frequency modulation (SFM) of the light illuminating one or more interferometers of non-zero OPD (see also Sec. 3.1.2). Here, for each constituent interferometer, the optical frequency modulation induces an OPD-dependent phase modulation waveform and the interference signals resulting from this can then be used as range-dependent carriers to demodulate the desired interferometric phase signals. This allows the use of a very simple optical setup to interrogate long-gauge length interferometric sensors (see also Sec. 2.4) in a self-referencing interferometric configuration (see also Sec. 3.1.3) that offers high stability and down-lead insensitivity. In this work, optical frequency modulation is induced by injection current modulation of a diode laser, with further methods for optical frequency modulation discussed in Sec. 3.1.2.

As the review of this area in Sec. 4.4 showed, prior work has been performed using both linear or sinusoidal optical frequency modulation waveforms. Here, linear techniques are conceptually simple but suffer from the difficulty of introducing a clean linear frequency sweep due to their high harmonic frequency content [174]. Sinusoidal range-resolved signal processing techniques, such as the approach used by Sakai *et al.* [128], on the other hand use only a single modulation frequency component, which greatly reduces complexity, but require gating with a rectangular window function to select the relevant sections of the interference signals for evaluation. As also discussed in Sec. 4.4, previously demonstrated range-resolved approaches, using both linear and sinusoidal modulation, require the OPDs of the constituent interferometers to adhere to a discrete set of permitted OPD values. In particular, the sinusoidal approach by Sakai *et al.* [128] requires tuning of the phase carrier amplitude to fit integer multiples of the carrier waveform inside the rectangular

window function. The technique proposed in this chapter builds upon this idea of windowing, however, it is shown that using a non-rectangular, smooth window function, which can easily be applied to the photo detector signal using digital signal processing, the restriction of fitting integer carrier multiples within the window period vanishes. Additionally, demodulation is now performed using a time-variant carrier frequency that approximately matches the complex interferometric signal expected at the photo detector for the OPD of the desired interferometer. Together, these measures allow continuous and independent variation of the OPDs, subject to a minimum separation, of one or more interferometers. Therefore the necessity to adhere to a discrete OPD grid as in prior work is removed, greatly increasing the flexibility and practicality of the approach. Furthermore, when compared to other interferometric multiplexing techniques, such as time-division or code-division multiplexing, both reviewed in Chap. 4, where spatial resolution is proportional to the processing bandwidth, spatial resolution in optical frequency modulation approaches, such as in the proposed technique, is proportional to the optical frequency modulation amplitude, thus becoming a property of the laser source. In this way, as will be shown, many GHz of optical frequency modulation amplitude can be harnessed to improve spatial resolution whilst using digital signal processing hardware that only needs to be capable of much lower processing bandwidths, effectively decoupling spatial resolution from processing bandwidth.

In this chapter, the theory of the SFM technique is explained in detail in Sec. 6.2, including numerical modelling of expected linearity and crosstalk performance. In Sec. 6.3, an experiment using a nested Mach-Zehnder (MZ) configuration with three constituent interferometers is used to demonstrate the working principle of the signal processing as well as procedures that are required to operate the technique, such as finding the correct demodulation parameters. Also, in this section, experimental results of phase measurements as well as quantitative measurements of the achievable linearity, crosstalk and tolerance against instrumental drift are presented. Following this, in Sec. 6.4, a simple, single MZ interferometric configuration is used for quantitative measurements of noise as a function of signal power and OPD. In general, the use of transmissive MZ interferometers in Sec. 6.3 and Sec. 6.4 for the characterisation of the signal processing technique is very versatile and offers very high signal powers. It is therefore an ideal test-bed before finally applying the technique to a reflective FSI configuration in an experiment using six fibre segment strain sensors that is presented in Sec. 6.5. Here, the capabilities of the technique are demonstrated by measuring the speed-of-sound in a suspended metal rod. In contrast to the CDM approach in Chap. 5, a fibre segment length  $l_s$  of 12.5 cm is demonstrated here, an improvement of more than two orders of magnitude, using the same basic FPGA signal processing hardware. Furthermore, the use of low-reflectivity, broadband fibre Bragg gratings (FBGs) (see Sec. 2.3), all inscribed at the same wavelength, to act as partial in-fibre reflectors (see also Sec. 4.1) could prove beneficial for future applications. A thorough discussion of the achieved performance and options for future improvements is held in Sec. 6.6 before a brief concluding summary in Sec. 6.7.

## 6.2. Theory

### 6.2.1. Basic Equations

This section discusses the derivation of the basic equations of the proposed SFM technique, before a detailed explanation of the range-dependent behaviour of the resulting interference signals is presented in Sec. 6.2.2. Here, the key equations from the analysis of sinusoidal optical frequency modulation by Zheng [121] are restated in the notation of this thesis, with their detailed derivation also shown in App. E. In this work, this previous analysis [121] is then extended to describe multiple interferometers and to include the complete demodulation process of the proposed SFM technique. This can be split into four distinct phases:

Modulation: A sinusoidal optical frequency modulation causes a phase modulation waveform of OPD-dependent amplitude in each constituent interferometer.

Photo Detection: The characteristic signals resulting from the constituent interferometers are recorded, digitised and compensated for signal processing delays.

Windowing: A smooth window function is applied to the photo detector signal.

Demodulation: By applying a range-dependent complex carrier function to the windowed signal and then passing the signal through a low-pass filter, the complex quadrature signal can be obtained that directly encodes the desired phase information for each constituent interferometer.

Fig. 6.1 illustrates typical signals at each intermediate processing step in this section, while the used signal processing implementation is also shown later in Fig. 6.8.

**Modulation:** The optical frequency  $f_{\text{opt}}(t)$ , emitted by a source of optical centre frequency  $f_{\text{opt},c}$ , subject to sinusoidal optical frequency modulation of optical frequency modulation amplitude  $\Delta f_{\text{opt}}$ , at modulation frequency  $f_m$ , is given by:

$$f_{\text{opt}}(t) = f_{\text{opt},c} + \Delta f_{\text{opt}} \sin[2\pi f_m t] \quad (6.1)$$

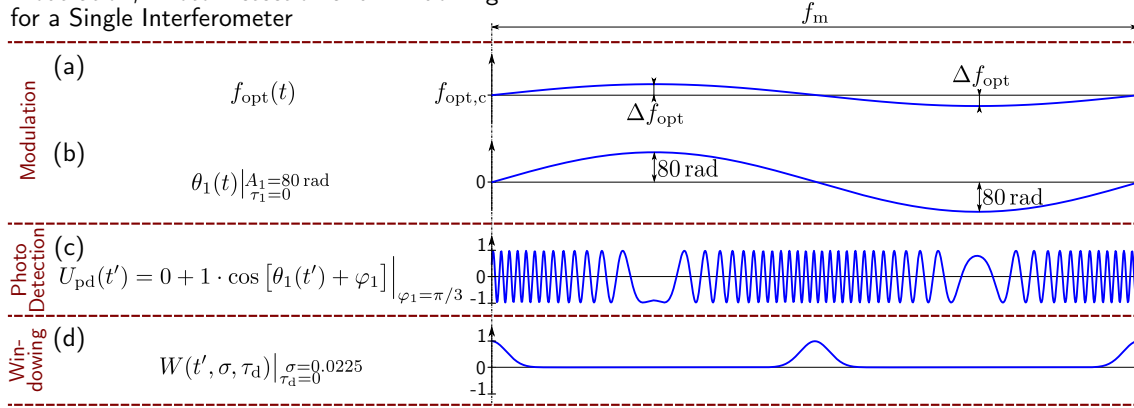
The frequency modulation waveform of Eq. (6.1) is also illustrated in Fig. 6.1(a). For each of the  $k = 1 \dots k_{\text{max}}$  constituent interferometers with average time-of-flight delays  $\tau_k$  between the respective interferometer arms, the applied optical frequency modulation (see also Sec. 3.1.2) then results in the phase modulation function  $\theta_k(t)$ , extended from Eq. (E.11) in App. E, using the assumptions stated there:

$$\theta_k(t) = A_k \sin[2\pi f_m (t - 0.5\tau_k)] \quad (6.2)$$

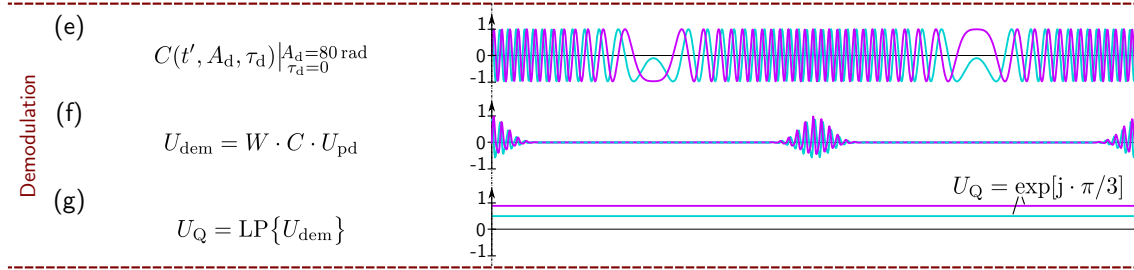
Here, the phase carrier amplitude,  $A_k$ , in units of rads, was extended from Eq. (E.12) in App. E and is the amplitude of the sinusoidal phase modulation waveform that results from the applied sinusoidal optical frequency modulation for the OPD  $\eta_k$  of the  $k$ th interferometer, using the vacuum speed of light  $c_0$ :

$$A_k = \frac{2\Delta f_{\text{opt}}}{f_m} \sin\left[\frac{\pi f_m \eta_k}{c_0}\right] \approx \frac{2\pi \Delta f_{\text{opt}} \eta_k}{c_0} \quad \text{for } \eta_k \ll \frac{c_0}{\pi f_m} \quad (6.3)$$

### Modulation, Photo Detection and Windowing for a Single Interferometer



### Range-Resolved Demodulation (In-Range: $A_d = 80 \text{ rad} = A_1$ and $\tau_d = \tau_1 = 0$ ):



### Range-Resolved Demodulation (Out-of-Range: $A_d = 40 \text{ rad} \neq A_1$ and $\tau_d = \tau_1 = 0$ ):

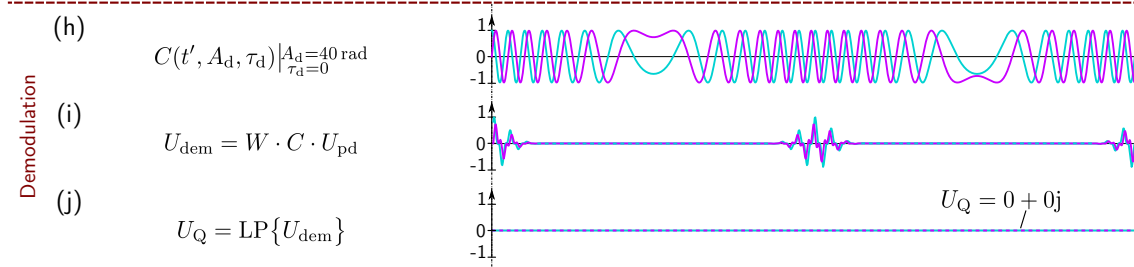


**Figure 6.1.:** Illustration of typical signals at intermediate stages of the signal processing with a detailed description given in the main text. For illustrative purposes, the plotted signals originate from a single interferometer  $k = 1$  with zero time-of-flight  $\tau_1 = 0$  and are evaluated at stationary phase value  $\varphi_1 = \pi/3$  for  $RP_{\text{off}} = 0$  and  $RP_{\text{eff},1} = 1$ . In this figure, real functions are drawn in blue, while for complex functions, cyan (real) and magenta (imaginary) line colours are drawn and all signals, with the exception of (a) and (b), are drawn normalised and unitless.

The figure shows the modulation and demodulation for a single interferometer with an OPD  $\eta_1$  resulting in a phase carrier amplitude  $A_1 = 80 \text{ rad}$ . (a) plots the applied sinusoidal optical frequency modulation, (b) shows the resulting phase modulation, while (c) plots the photo signal for this case, with the window function for a width parameter of  $\sigma = 0.0225$  drawn in (d). (e) to (g) then show the resulting signals for in-range demodulation ( $A_d = 80 \text{ rad} = A_1$ ), with the carrier used shown in (e), the demodulated signal shown in (f), while (g) then shows the complex quadrature signal, i.e. the low-pass filtered (LP) version of (f). Analogous to (e) to (g), (h) to (j) show the corresponding signals for out-of-range demodulation ( $A_d = 40 \text{ rad} \neq A_1$ ).

Thus, for  $\eta_k$  small relative to  $c_0(\pi f_m)^{-1}$ , i.e. for time-of-flights  $\tau_k$  small relative to the modulation period  $T_m$ ,  $A_k$  is independent of the modulation frequency,  $f_m$ , but proportional to the optical frequency modulation amplitude of the source,  $\Delta f_{\text{opt}}$ , as well as the OPD  $\eta_k$  of the  $k$ th interferometer. The latter property permits range-resolved interferometry to be performed with this technique. In general, the use of the phase carrier amplitude,  $A_k$ , instead of directly using OPD or time delay units in the theoretical description allows an abstract analysis of the characteristics of the signal processing, in particular with regard to spatial resolution (detailed in Sec. 6.2.3 later), independent of the source specific parameter  $\Delta f_{\text{opt}}$ . An example phase modulation waveform is illustrated in Fig. 6.1(b) for a single interferometer ( $k = 1$ ) with OPD  $\eta_1$  and for a frequency modulation amplitude  $\Delta f_{\text{opt}}$  that leads to a phase carrier amplitude  $A_1 = 80$  rad, a value typical for the later experiments.

**Photo Detection:** After photo detection, the photo detector signal is digitized, where, in contrast to the CDM signal processing technique presented in Chap. 5, anti-aliasing does not appear to be critical to the experiments in the SFM technique. Therefore anti-aliasing filtering is not included in the theoretical description at this stage. Furthermore, in future work, any detrimental effects could be compensated using an additional digital input filter, as discussed in Sec. 6.6.1. For proper operation of the proposed technique any signal processing delay  $\tau_{\text{sp}}$  that occurs after modulation will need to be compensated. Without loss of generality,  $\tau_{\text{sp}}$  can be set to include all analogue and digital delays occurring between modulation and signal processing. In this theoretical treatment all signals after modulation are considered to be fully compensated for  $\tau_{\text{sp}}$  by introducing the compensated time variable  $t'$ , which bears the following relation with the regular time variable  $t$ :

$$t' = t - \tau_{\text{sp}} \quad (6.4)$$

An experimental method to a priori determine the signal processing delay  $\tau_{\text{sp}}$  using demodulation maps will then be presented in Sec. 6.3.1. Extending Eq. (E.6) in App. E for  $k_{\text{max}}$  constituent interferometers, the resulting photo detector signal,  $U_{\text{pd}}(t')$ , compensated for the signal processing delay  $\tau_{\text{sp}}$ , is then given by:

$$\begin{aligned} U_{\text{pd}}(t') &= RP_{\text{off}} + \sum_{k=1}^{k_{\text{max}}} \left( RP_{\text{eff},k} \cdot \cos \left[ \theta_k(t') + \varphi_k(t') \right] \right) \\ &= RP_{\text{off}} + \sum_{k=1}^{k_{\text{max}}} \left( RP_{\text{eff},k} \cdot \cos \left[ A_k \sin[2\pi f_m(t' - 0.5\tau_k)] + \varphi_k(t') \right] \right) \end{aligned} \quad (6.5)$$

The photo detector responsivity  $R$ , the stationary offset power  $P_{\text{off}}$  as well as the effective interferometric power  $P_{\text{eff},k}$  in Eq. (6.5) were first introduced in the context of Eq. (3.3).  $P_{\text{eff},k}$  depends on the individual power ratio as well as the mutual coherence and polarisation overlap between the two interferometer arms for each of the  $k_{\text{max}}$  constituent interferometers. The desired phase signal for the  $k$ th constituent interferometer is represented by  $\varphi_k(t')$ , while  $\theta_k(t')$  is given by Eq. (6.2). Fig. 6.1(c) then shows a typical photo detector signal  $U_{\text{pd}}(t')$  resulting from the previous example for the phase modulation waveform  $\theta_1(t)$  for an example stationary phase value  $\varphi_1 = \pi/3$ . Here, for illustrative purposes, no intensity offset  $RP_{\text{off}} = 0$  and full visibility  $RP_{\text{eff},1} = 1$  is also assumed.

**Windowing:** As will become more apparent later, a key step in the SFM approach is the application of a smooth window function  $W(t', \sigma, \tau_d)$  to  $U_{pd}(t')$ , with given demodulation delay  $\tau_d$ . In this implementation, for each modulation period of duration  $T_m = f_m^{-1}$ , a window function containing two individual windows that are centred on the two points of the highest gradients in the sinusoidal optical frequency modulation waveform of Fig. 6.1(a), where the photo detector signal  $U_{pd}(t)$  most rapidly changes, is used, as illustrated in Fig. 6.1(d). The individual windows are of Gaussian shape, with a width specified by the width parameter  $\sigma$ , the Gaussian standard deviation. The complete window function,  $W(t', \sigma, \tau_d)$ , periodic in  $T_m$  and  $2T_m$  and incorporating both Gaussian windows, is then given by:

$$W(t', \sigma, \tau_d) = \sum_{n=-\infty}^{\infty} \left\{ \exp \left[ -\frac{1}{2} \left( \frac{(t' - \tau_d) - nT_m}{T_m \sigma} \right)^2 \right] + \exp \left[ -\frac{1}{2} \left( \frac{(t' - \tau_d) - (n+0.5)T_m}{T_m \sigma} \right)^2 \right] \right\} \quad (6.6)$$

In contrast to prior work [128, 175], as reviewed in Sec. 4.4, a smooth window function is used in this approach, which, as will be detailed later in Sec. 6.2.2, is a key improvement. In this particular implementation, a Gaussian window function was chosen because it is a conceptually simple window function and because it can be easily customised by the window width parameter  $\sigma$ , where a larger value of  $\sigma$  results in a broader window function. Furthermore, the use of two Gaussian windows allows a higher carrier-to-noise (CNR) ratio, rather than using only a single window as in prior work [128, 175]. It is stressed that the version of  $W(t', \sigma, \tau_d)$  above is only an initial choice and other window functions remain to be explored, as will be discussed later in Sec. 6.6.1. It will be shown in Sec. 6.3.2 that for the current experimental implementation, the best choice of  $\sigma$  is approximately  $\sigma \approx 0.0225$ , therefore this value is used in the following theoretical analysis. It is, however, emphasized that, as also experimentally confirmed in Sec. 6.3.2, the technique can be made to work over a wide range of the parameter  $\sigma$  with only small performance penalties.

**Demodulation:** In the presented SFM approach, unlike regular heterodyne interferometry (see also Sec. 3.1.4), where a complex carrier of fixed frequency is used for electronic demodulation, the complex carrier,  $C(t', A_d, \tau_d)$ , used in this approach is time-variant and periodic within the modulation period,  $T_m = f_m^{-1}$ . When the  $k$ th constituent interferometer is to be demodulated, the demodulation phase carrier amplitude  $A_d$  is chosen to approximately match the phase carrier amplitude  $A_k$ , i.e.  $A_d \approx A_k$ , and the demodulation delay  $\tau_d$  is chosen to approximately match half of the time-of-flight delay  $\tau_k$  of that interferometer, i.e.  $\tau_d \approx 0.5\tau_k$ . In this case, both  $A_d$  and  $\tau_d$  match the corresponding terms in the phase modulation waveform of Eq. (6.2) that results from the applied sinusoidal optical frequency modulation for that interferometer. The complex demodulation carrier function  $C(t', A_d, \tau_d)$  then resembles a complex version of the interferometric signal expected at the photo detector (see also Fig. 6.1(c)) for the desired interferometer and is given by:

$$C(t', A_d, \tau_d) = \exp \left[ j \cdot A_d \sin[2\pi f_m(t' - \tau_d)] \right] \quad (6.7)$$

For the previous example, the carrier  $C(t', A_d, \tau_d = 0)$  for in-range demodulation of  $U_{pd}(t')$  at  $A_d = 80 \text{ rad} = A_1$  is plotted in Fig. 6.1(e), while Fig. 6.1(h) shows the carrier

function for an example out-of-range demodulation amplitude of  $A_d = 40 \text{ rad} \neq A_1$ .

After the windowed photo detector signal  $W(t', \sigma, \tau_d)U_{pd}(t')$  is multiplied with  $C(t', A_d, \tau_d)$ , the resulting demodulated signal is represented by  $U_{dem}(t', \sigma, A_d, \tau_d)$ . Finally,  $U_{dem}(t', \sigma, A_d, \tau_d)$  is low-pass (LP) filtered with cut-off frequency  $f_{Q,co} \leq f_{Q,co,max} = 0.5f_m$ , resulting in the complex quadrature signal  $U_Q(t', \sigma, A_d, \tau_d)$ . Therefore  $U_Q(t', \sigma, A_d, \tau_d)$  can be seen as the baseband component of the demodulated signal  $U_{dem}(t', \sigma, A_d, \tau_d)$  around frequency 0. Expressing the cosine function in  $U_{pd}(t')$  of Eq. (6.5) using complex exponential terms,  $U_Q(t', \sigma, A_d, \tau_d)$  is given by:

$$\begin{aligned} U_Q(t', \sigma, A_d, \tau_d) &= \text{LP} \left\{ U_{dem}(t', \sigma, A_d, \tau_d) \right\} = \text{LP} \left\{ C(t', A_d, \tau_d) W(t', \sigma, \tau_d) U_{pd}(t') \right\} \\ &= \text{LP} \left\{ W(t', \sigma, \tau_d) R P_{\text{off}} \exp \left[ j \cdot A_d \sin[\omega_m(t' - \tau_d)] \right] + \right. \\ &\quad \left. \sum_{k=1}^{k_{\text{max}}} 0.5 W(t', \sigma, \tau_d) R P_{\text{eff},k} \left( \exp \left[ j \left( A_d \sin[2\pi f_m(t' - \tau_d)] - A_k \sin[2\pi f_m(t' - 0.5\tau_k)] - \varphi_k(t') \right) \right] + \right. \right. \\ &\quad \left. \left. \exp \left[ j \left( A_d \sin[2\pi f_m(t' - \tau_d)] + A_k \sin[2\pi f_m(t' - 0.5\tau_k)] + \varphi_k(t') \right) \right] \right) \right\} \end{aligned} \quad (6.8)$$

The demodulated signal  $U_{dem}(t', \sigma, A_d, \tau_d)$  and the resulting low-pass filtered complex quadrature signal  $U_Q(t', \sigma, A_d, \tau_d)$  for the previous example cases are also plotted in Figs. 6.1(f) and (g), respectively, for in-range demodulation and in Figs. 6.1(i) and (j) for out-of-range demodulation. As will be discussed in detail later, for in-range demodulation, the non-zero average or baseband signal component visible for both real and imaginary signals in  $U_{dem}(t', \sigma, A_d, \tau_d)$  in Fig. 6.1(f) carries the phase information of the desired phase signal  $\varphi_1$ . This phase signal can then be retrieved from the resulting low-pass filtered complex quadrature signal  $U_Q(t', \sigma, A_d, \tau_d)$  shown in Fig. 6.1(g). This is in contrast to out-of-range modulation, where  $U_{dem}(t', \sigma, A_d, \tau_d)$  in Fig. 6.1(i) can be seen to carry no average or baseband component and consequently results in  $U_Q(t', \sigma, A_d, \tau_d)$  with zero complex amplitude visible in Fig. 6.1(j).

In order to simplify Eq. (6.8) relevant to typical conditions in the later experiments, the phase shifts in the sines caused by both  $\tau_d$  and  $\tau_k$  can be considered negligible, i.e.  $|\tau_d| \ll T_m$  and  $|\tau_n| \ll T_m$  relative to the modulation period  $T_m = f_m^{-1}$ . These assumptions will be used in the remainder of this chapter and allow rewriting of Eq. (6.8) using generic complex exponential terms,  $E(t', A, \varphi(t'))$ , given by:

$$E(t', A, \varphi(t')) = \exp \left[ j \left( A \sin[2\pi f_m t'] + \varphi(t') \right) \right] \quad (6.9)$$

Here, the sinusoidal amplitude  $A$  is representative of any combination of  $A = A_d + [0, \pm A_k]$  occurring in the simplified version of the quadrature signal  $U_Q(t', \sigma, A_d)$  given below, where the described assumptions of zero  $\tau_d$  and  $\tau_k$  were used:

$$\begin{aligned} U_Q(t', \sigma, A_d) &= \text{LP} \left\{ U_{dem}(t', \sigma, A_d) \right\} = \text{LP} \left\{ C(t', A_d, 0) W(t', \sigma, 0) U_{pd}(t') \right\} \\ &\approx \text{LP} \left\{ W(t', \sigma, 0) R P_{\text{off}} E(t', A_d, 0) + \sum_{k=1}^{k_{\text{max}}} 0.5 W(t', \sigma, 0) R P_{\text{eff},k} \left( E(t', (A_d - A_k), -\varphi_k(t')) + E(t', (A_d + A_k), \varphi_k(t')) \right) \right\} \end{aligned} \quad (6.10)$$

When the demodulation phase carrier amplitude  $A_d$  of the complex carrier function  $C(t', A_d, 0)$  of Eq. (6.7) is chosen to approximately match the phase carrier amplitude of the desired  $k$ th interferometer, i.e.  $A_d = A_k$ , the sinusoidal part of the complex exponential term  $E(t', (A_d - A_k), -\varphi_k(t'))$  in the approximated version of the complex quadrature signal  $U_Q(t', \sigma, A_d)$ , given by Eq. (6.10), vanishes because  $A = A_d - A_k \approx 0$ . The desired phase signal,  $\varphi_k(t)$ , is then directly encoded in Eq. (6.10) by the baseband signal component of this term  $E(t', (A_d - A_k), -\varphi_k(t')) = \exp[-j \cdot \varphi_k(t')]$ . However, the presence of the other complex exponential terms with  $A \neq 0$  in Eq. (6.10) prohibits straightforward phase extraction, because, in general, each of these terms also adds its own baseband signal components to  $U_{\text{dem}}(t', \sigma, A_d)$  and thus to  $U_Q(t', \sigma, A_d)$ . If, however, the window function,  $W(t', \sigma, 0)$ , is chosen such that the baseband components of all complex exponential terms with sufficiently large sinusoidal amplitudes  $A$  are suppressed in Eq. (6.10), then only the previously mentioned term  $E(t', (A_d - A_k), -\varphi_k(t')) = \exp[-j \cdot \varphi_k(t')]$  that carries the desired phase information contributes significantly to the baseband component of  $U_{\text{dem}}(t', \sigma, A_d)$ . Therefore,  $U_Q(t', \sigma, A_d)$  will only carry phase information from the desired interferometer and undesired crosstalk from the baseband components of other complex exponential terms in Eq. (6.10) can be avoided. In this case  $\varphi_k(t')$  can be recovered using an arctan function on the complex quadrature signal  $U_Q(t', \sigma, A_d)$ . This is the key working principle of this technique and the baseband crosstalk suppression behaviour of the window function will be quantified and explained in detail in the following section.

## 6.2.2. Demodulation Process

**Baseband Suppression Properties of a Single Complex Exponential Term:** Before discussing the complete demodulation represented by all terms in the approximated complex quadrature signal of Eq. (6.10), it is instructive to first investigate the effect of the window function,  $W(t', \sigma, 0)$ , on the suppression of the baseband component of a single, generic complex exponential term  $E(t', A, \varphi(t'))$  of Eq. (6.9). This is illustrated in Fig. 6.2 for the term  $E(t', 36, 0)$  for an example sinusoidal amplitude value of  $A = 36$  rad, where this value was also chosen to tie in with the discussion later in this section. Fig. 6.2(a) plots the real and imaginary parts of  $E(t', 36, 0)$  as well as  $W(t', 0.0225, 0)$ , given by Eq. (6.6), for width  $\sigma = 0.0225$ , in the time domain, while Fig. 6.2(b) compares the corresponding Fourier spectra with and without application of  $W(t', 0.0225, 0)$ . It has been verified that the phase term  $\varphi(t')$  in Eq. (6.9) has no influence on baseband suppression and can thus be neglected in this discussion and set to zero. In general, the application of the smooth window function results in a distinctly peaked signal spectrum with maxima at frequencies  $\approx \pm A f_m$  and it can clearly be seen in Fig. 6.2(b) that the application of the smooth window function on  $E(t', 36, 0)$  strongly suppresses any baseband signal component. In this example, the baseband suppression ratio  $S_{\text{bb}}$ , between the peaks at  $\approx \pm 36 f_m$  and the value at frequency 0, also marked in Fig. 6.2(b), is  $S_{\text{bb}} = -143$  dB.

Additionally Fig. 6.2(a) plots an example of the single rectangular window/gating function  $\Pi(t')$  that was used in prior work by Sakai *et al.* [128] and Fig. 6.2(b)



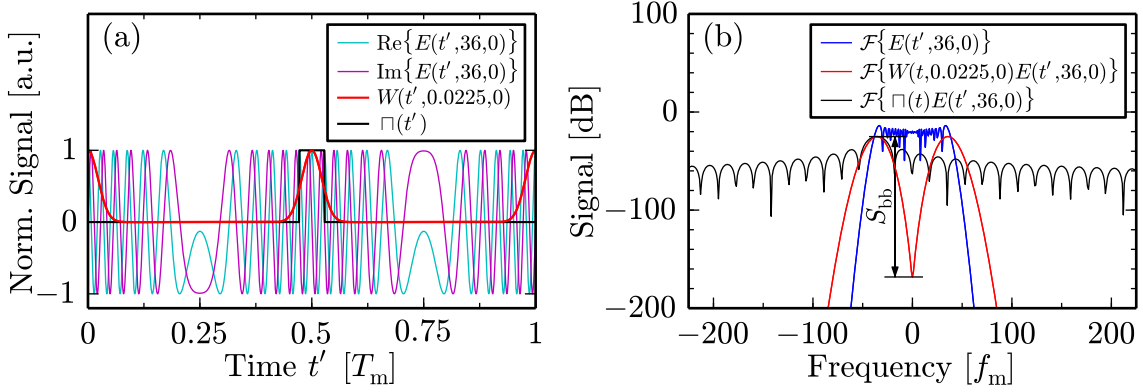


**Figure 6.2.:** Illustration of the effect of windowing on a single complex exponential term  $E(t', 36, 0)$ . (a) plots the real and imaginary part of  $E(t', 36, 0)$  over one modulation period  $T_m$  as well as the smooth window  $W(t', 0.0225, 0)$  and, additionally, a rectangular window  $\Pi(t')$  for comparison with prior work. (b) compares the corresponding spectra of  $E(t', 36, 0)$  with and without application of  $W(t', 0.0225, 0)$  or  $\Pi(t')$ . Here  $S_{bb} = -143$  dB for  $W(t', 0.0225, 0)$  is also marked.

then shows the corresponding spectrum after application of  $\Pi(t')$ . In Fig. 6.2(b), when comparing the Fourier spectrum resulting from the application of the smooth window function  $W(t', 0.0225, 0)$  with that resulting from  $\Pi(t')$ , the differences in the magnitudes of the sidelobe components for the two types of windows are obvious. Here, the smooth window function produces virtually no sidelobe components, while these are of considerable magnitude for the rectangular window function and only decay very slowly. In prior work [128], as detailed in Sec. 4.4 and illustrated in Fig. 4.7, the occurrence of sidelobe components required the placement of multiple sources on an integer OPD grid. In contrast, the avoidance of sidelobe components through the use of a smooth window function permits continuously variable placement of the OPDs of constituent interferometers, subject to a minimum OPD separation, which is a key advantage of the proposed technique.

For the Gaussian window function  $W(t', \sigma, 0)$  of Eq. (6.6) that is used in this work, Fig. 6.3 then quantifies the baseband suppression ratio  $S_{bb}$  by plotting the dependence of  $S_{bb}$  on the sinusoidal amplitude  $A$  of the generic complex exponential term  $E(t', A, 0)$  after application of  $W(t', \sigma, 0)$  for various values of the width parameter  $\sigma$  and without any windowing ( $\sigma \rightarrow \infty$ ). In Fig. 6.3, the example value  $S_{bb} = -143$  dB of Fig. 6.2(b) can then easily be extracted from the curve for  $\sigma = 0.0225$  at  $A = 36$  rad.

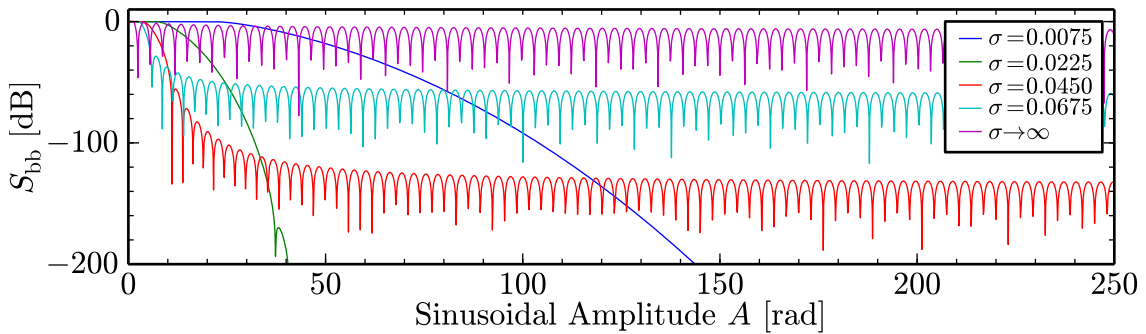


**Figure 6.3.:** The baseband suppression ratio  $S_{bb}$  resulting from the application of  $W(t', \sigma, 0)$  of Eq. (6.6) to a generic complex exponential term  $E(t', A, 0)$  of Eq. (6.9) is plotted as a function of sinusoidal amplitude  $A$  for various width parameters  $\sigma$  and without windowing, i.e.  $\sigma \rightarrow \infty$ .

**Complete Demodulation Process:** As described previously, the basic working principle of the proposed SFM technique is the suppression of the baseband signal components of all complex exponential terms in the simplified complex quadrature signal  $U_Q(t', \sigma, A_d)$  of Eq. (6.10), except for the term  $E(t', (A_d - A_k), -\varphi_k(t'))$  that carries the desired phase signal  $\varphi_k(t')$  of the  $k$ th constituent interferometer and where  $A_d - A_k \approx 0$ . The previous results for the baseband suppression on a single, generic complex exponential term  $E(t', A, \varphi(t'))$  can now be extended to include all  $1 + 2k_{\max}$  complex exponential terms that are present in the approximated demodulated signal  $U_{\text{dem}}(t', \sigma, A_d)$  and the resulting quadrature signal  $U_Q(t', \sigma, A_d)$  in Eq. (6.10). This is possible because all complex exponential terms in  $U_{\text{dem}}(t', \sigma, A_d)$  form a linear combination and thus add independently in the Fourier domain. This is illustrated in Fig. 6.4 for two example constituent interferometers with OPDs that result in phase carrier amplitudes of  $A_1 = 83$  rad for interferometer 1 and  $A_2 = 47$  rad for interferometer 2 and with arbitrarily chosen, stationary phase values of  $\varphi_1 = \pi/3$  and  $\varphi_2 = 8\pi/7$ . In this example, the values for  $A_1$  and  $A_2$  were used because they are prime numbers and therefore no simple integer multiple of each other. For this example, the plots on the left in Figs. 6.4(a), (c) and (e) show the photo detector signals  $U_{\text{pd}}(t')$  resulting for the cases where interferometer 1 only, interferometer 2 only and where both interferometers 1 and 2, respectively, are present, along with the window function  $W(t', 0.0225, 0)$  that is used. Figs. 6.4(b), (d) and (f) on the right then show the corresponding Fourier spectra of the demodulated signal  $U_{\text{dem}}(t', \sigma, A_d) = W(t', \sigma, 0)C(t', A_d, 0)U_{\text{pd}}(t')$  with ( $\sigma = 0.0225$ ) and without ( $\sigma \rightarrow \infty$ ) application of the window function. Here, the demodulation carrier function  $C(t', A_d, 0)$  was set to demodulate the first interferometer at  $A_1 = 83$  rad by letting  $A_d = 83$  rad. In all cases in Fig. 6.4,  $U_{\text{pd}}(t')$  was normalised and an offset intensity of  $RP_{\text{off}} = 1$  and full visibility  $RP_{\text{eff},k} = 1$  was assumed.

It can be seen in the spectra of the demodulated signals  $U_{\text{dem}}(t', \sigma, A_d)$  in Figs. 6.4 (b), (d) and (f) that without windowing ( $\sigma \rightarrow \infty$ ) the spectra are widely spread out, whilst for windowing at width parameter  $\sigma = 0.0225$  distinct peaks that correspond to the different complex exponential terms of Eq. (6.10) are observable. As discussed earlier, a complex exponential term of sinusoidal amplitude  $A$  will cause peaks with maxima at  $\pm \approx Af_m$ . Therefore the peaks occurring in the spectra of  $U_{\text{dem}}(t', 0.0225, 83)$  in Figs. 6.4(b), (d) and (f) can be easily traced to the originating complex exponential terms and are labelled according to Table 6.1. Each interferometer causes two unique sets of peaks, No. 1 and No. 5 for interferometer 1 and No. 2 and No. 4 for interferometer 2, while the non-zero offset intensity  $RP_{\text{off}}$  is the cause of peak No. 3 for both interferometers. Fig. 6.4(f), where both interferometers are present, then exhibits all five peaks. Because the first interferometer was chosen for demodulation by letting  $A_d = A_1$ , the desired phase signal is contained in peak No. 5, which is present in Fig. 6.4(b) and (f) and, unlike the other peaks, displays a comb-like structure, visible in the insets, that will be discussed in the following paragraph. As obvious from Table 6.1, peak No. 4 at  $A_d = 36$  rad due to interferometer 2 is the complex exponential term that is closest in the Fourier spectrum to the desired peak No. 5 in Fig. 6.4(f). Thus crosstalk from interferometer 2 into interferometer 1 will be mostly caused by this peak. This crosstalk will ultimately limit the achievable spatial resolution, as discussed

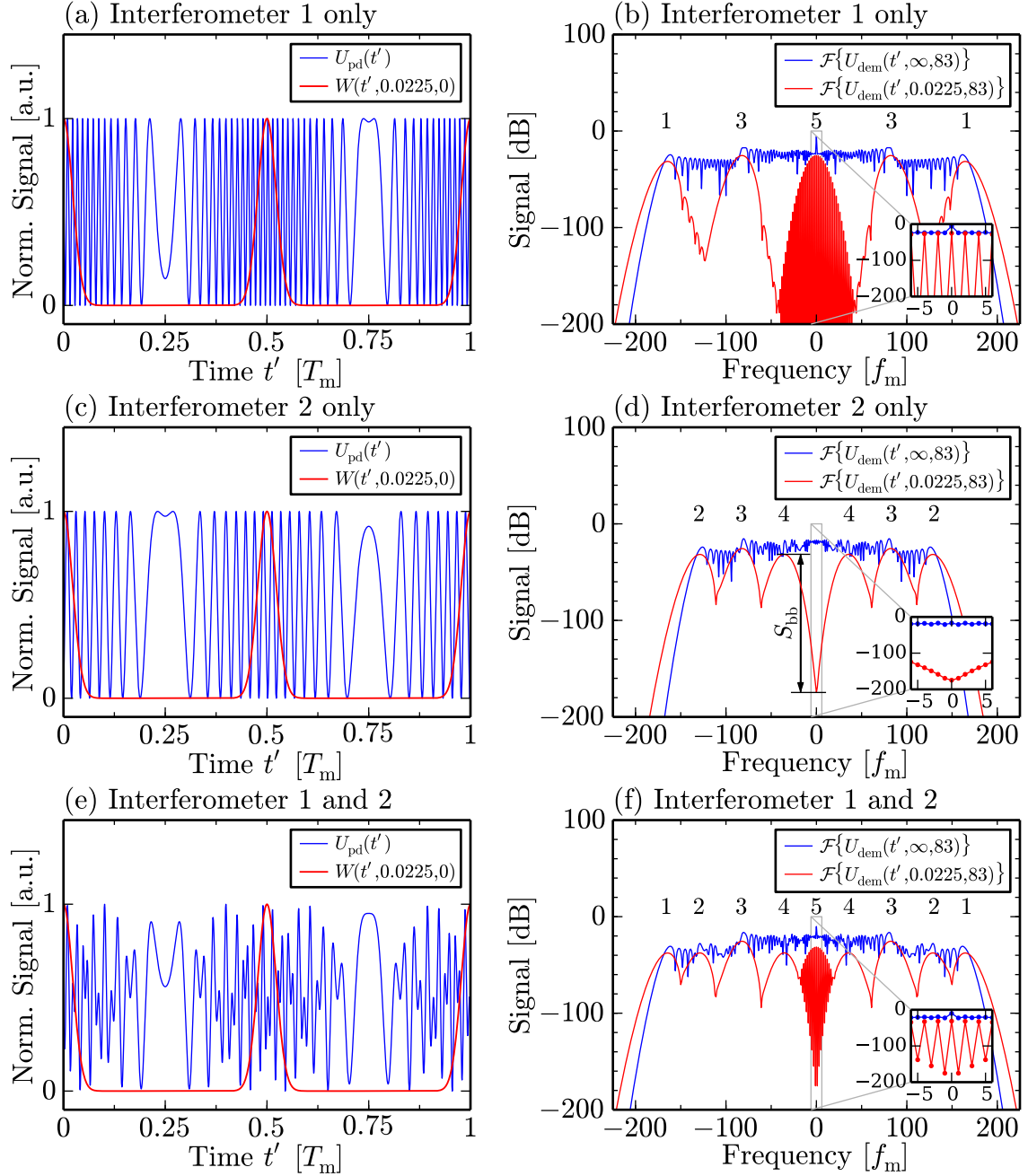


**Figure 6.4.:** Illustration of the complete demodulation process for two constituent interferometers with OPDs that result in phase carrier amplitudes  $A_1 = 83$  rad and  $A_2 = 47$  rad. (a), (c) and (e) plot the window function  $W(t', 0.0225, 0)$  and the normalised photo detector signals  $U_{pd}(t')$  for the cases where interferometer 1 only, interferometer 2 only and both interferometers, respectively, are present. Analogously, (b), (d) and (f) plot the corresponding Fourier spectra of the demodulated signal  $U_{dem}(t', \sigma, A_d) = W(t', \sigma, 0)C(t', A_d, 0)U_{pd}(t')$  of Eq. (6.10) with ( $\sigma = 0.0225$ ) and without ( $\sigma \rightarrow \infty$ ) application of the window function and where the first interferometer was targeted for demodulation by letting  $A_d = 83$  rad. Here, the resulting peaks for the case with windowing are marked with numbers according to Table 6.1. Also, the relevant baseband suppression  $S_{bb}$  that ultimately defines the spatial resolution is marked in (d) and the insets in (b) and (f) reveal the comb-like structure of peak No. 5.

**Table 6.1.:** Complex exponential terms in Eq. (6.10) occurring in Figs. 6.4(b), (d) and (f) for the described example with two constituent interferometers at  $A_1 = 83$  rad and  $A_2 = 47$  rad and where interferometer 1 is demodulated by letting  $A_d = 83$  rad.

Peak No.	Term	Value of $A$	Description
1	$E(t', (A_d + A_1), \varphi_1)$	166 rad	Sum frequency term for $A_1$
2	$E(t', (A_d + A_2), \varphi_2)$	130 rad	Sum frequency term for $A_2$
3	$E(t', A_d, 0)$	83 rad	Term due to offset power $RP_{\text{off}}$
4	$E(t', (A_d - A_2), -\varphi_2)$	36 rad	Difference frequency term for $A_2$
5	$E(t', (A_d - A_1), -\varphi_1)$	0 rad	Difference frequency term for $A_1$

further in Sec. 6.2.3. In general, the quadrature signal crosstalk suppression levels  $S_{\text{cr}}$  then directly correspond to the baseband suppression values  $S_{\text{bb}}$  that are plotted in Fig. 6.3. In Fig. 6.4(d), the baseband suppression ratio  $S_{\text{bb}} = -143$  dB in this example is also marked and the value of  $S_{\text{bb}} = -143$  dB found here is similar to the earlier value for a single complex exponential peak illustrated in Fig. 6.2(b).

It can also be seen from Eq. (6.9) that for peak No. 5 where  $A = 0$  the sinusoidal part of the complex exponential term vanishes, ideally leaving an exponential term  $\exp[-j \cdot \varphi_1(t')]$  that only contains the desired phase signal  $\varphi_1(t')$ . This exponential term would appear as a delta peak at frequency 0 in the Fourier domain, however, this is broadened by the convolution with the periodic window function  $W(t', 0.0225, 0)$ , which leads to a set of carrier harmonics that limit the unambiguous quadrature bandwidth. Because  $W(t', 0.0225, 0)$  of Eq. (6.6) is periodic in  $2f_m$ , a comb-like structure, visible in the insets in Figs. 6.4(b) and (f) arises where every second carrier harmonic is missing, yielding a theoretical unambiguous quadrature bandwidth of  $f_m$ . However, in practice, weak carrier components at  $\pm f_m$  appear due to non-perfect matching of the phase carrier amplitude  $A_k$  of the desired interferometer to the demodulation carrier amplitude  $A_d$ , leading to a usable unambiguous maximum quadrature bandwidth of  $f_{\text{Q,co,max}} = 0.5f_m$ . This is the value that has been previously used for the derivation of Eq.(6.10) and, as discussed there, the extraction of the desired phase signal from the demodulated signal  $U_{\text{dem}}(t', \sigma, A_d)$  then requires low-pass filtering of  $U_{\text{dem}}(t', \sigma, A_d)$  at a cut-off frequency  $f_{\text{Q,co}} \leq f_{\text{Q,co,max}}$ . This yields the complex quadrature signal  $U_Q(t', \sigma, A_d)$  that, using an arctan function, allows the phase signals  $\varphi_k(t')$  to be determined, with this phase signal subsequently subjected to phase unwrapping [112] as a final processing step.

### 6.2.3. Spatial Resolution

The suppression of crosstalk from undesired complex exponential terms after the application of the window function can be quantified by the baseband suppression ratio, as plotted in Fig. 6.3. In order to establish a formula for the minimum OPD separation between constituent interferometers it is necessary to specify an acceptable baseband suppression level  $S_{\text{bb,accept}}$  in the design of the implementation. For a given window width parameter,  $\sigma$ , the corresponding minimum sinusoidal amplitude  $A_{\text{min}}$  at  $S_{\text{bb,accept}}$  can then be extracted from Fig. 6.3 and  $A \geq A_{\text{min}}$  has to be exceeded

by all complex exponential terms in Eq. (6.10) apart from the desired baseband term, where  $A \approx 0$ , in order for the technique to work as specified. The value for  $A_{\min}$  determined in this way can then be inserted into the following formula for the minimum OPD difference  $\Delta\eta_{\min}$  that is derived from the approximated version of Eq. (6.3):

$$\Delta\eta_{\min} \approx \frac{c_0 A_{\min}}{2\pi \Delta f_{\text{opt}}} \quad (6.11)$$

In this technique,  $\Delta\eta_{\min}$  is the minimum OPD that has to be maintained for the first interferometer, and, for multiple constituent interferometers, the minimum OPD separation between constituent interferometers.

This highlights that, in this technique, spatial resolution is dependent on a subjective choice of an acceptable baseband suppression level  $S_{\text{bb,accept}}$ . As an example, at a width parameter  $\sigma = 0.0225$  and for a chosen value of  $S_{\text{bb,accept}} = -200$  dB, Fig. 6.3 yields a value  $A_{\min} = 40$  rad. For an optical frequency modulation amplitude of  $f_{\text{opt}} = 8.4$  GHz, the value obtained in the practical implementation described later, Eq. (6.11) then results in OPD  $\Delta\eta_{\min} = 0.23$  m. However, if an acceptable baseband suppression level of only  $S_{\text{bb,accept}} = -50$  dB is specified,  $A_{\min}$  would reduce to 25 rad for  $\sigma = 0.0225$  according to Fig. 6.3, which results in  $\Delta\eta_{\min} = 0.14$  m. Furthermore, Fig. 6.3 also shows that for  $S_{\text{bb,accept}} = -50$  dB, a choice of  $\sigma = 0.045$  would yield an even lower value of  $A_{\min} = 11$  rad, leading to  $\Delta\eta_{\min} = 0.06$  m. Using baseband suppression curves similar to Fig. 6.3 with a finer  $\sigma$  resolution would then allow the best spatial resolution and the corresponding optimum value of  $\sigma$  to be obtained. In an FSI configuration, where the light traverses the fibre of typical group index of refraction  $n_g = 1.46$  twice, the above values of  $\Delta\eta_{\min}$  correspond to a minimum segment length  $l_s$  of  $l_s = 0.08$  m for  $S_{\text{bb,accept}} = -200$  dB and  $l_s = 0.02$  m for  $S_{\text{bb,accept}} = -50$  dB at  $\sigma = 0.045$ .

#### 6.2.4. Non-Linearity and Crosstalk due to Quantisation Errors

The theoretical treatment in the previous sections has been carried out for ideal conditions where no quantification errors are present. However, in any practical implementation of a digital signal processing system, quantification errors are unavoidable because a digital system will only have a limited number of discrete signal levels available. Assuming that the processing bitwidths of the digital multipliers for the application of the window and carrier function can be made sufficiently large, the actual processing bitwidth in this technique is limited by the initial digitisation of the photo detector signal  $U_{\text{pd}}(t')$  of Eq. (6.5) in the analogue-to-digital converter (ADC). In the following, it will be shown through numerical modelling that, in this technique, the occurrence of quantisation errors is the key phenomenon that is thought to limit the achievable crosstalk and linearity performance and this will also be confirmed by the later experimental results in Sec. 6.3 and Sec. 6.5.

Analogous to Fig. 6.2(b), the Fourier transformed spectra of a windowed complex exponential term  $W(t', \sigma, 0)E(t', 36, 0)$ , with this signal now quantised into  $\pm 2^b$  discrete levels for the processing bitwidth values  $b = [6, 12, 18]$  bit, are plotted in Fig. 6.5(a) for window width parameter  $\sigma = 0.0225$  and in Fig. 6.5(c) for  $\sigma =$

0.045. It can be seen in both Figs. 6.5(a) and (c) that, compared to the respective spectra without quantification also plotted there, the presence of quantisation errors introduces a mostly flat baseline in the spectra at levels that are dependent on the processing bitwidth  $b$ . Furthermore, the corresponding baseband suppression graphs for  $b = [6, 12, 18]$  bit and for the case without quantisation are plotted in analogy to Fig. 6.3 in Fig. 6.5(b) for  $\sigma = 0.0225$  and in Fig. 6.5(d) for  $\sigma = 0.045$ . It can be seen in both Figs. 6.5(b) and (d) that quantisation also introduces a baseline of the achievable baseband suppression values  $S_{bb}$ . These baseline levels do not show any signs of decay with increasing sinusoidal amplitude  $A$  and are independent of the value of  $\sigma$  in both Figs. 6.5(b) and (d). As discussed in Sec. 6.2.2, for multiple constituent interferometers, the baseband suppression  $S_{bb}$  directly corresponds to the quadrature signal crosstalk suppression  $S_{cr}$ . For all graphs in Fig. 6.5 it can be concluded that, for every doubling in the number of quantisation levels, i.e. the processing bitwidth  $b$  increasing by a value of 1, the baseline levels and therefore the suppression values  $S_{cr}$  and  $S_{bb}$  are lowered by approximately 6 dB or a factor of 2.

It can be concluded from the lack of decay of the baseband suppression with  $A$  that undesired contributions from all other complex exponential terms in Eq. (6.10) will be present in the complex quadrature signal of the desired interferometer for a digital signal processing system with limited processing bitwidth. This includes stationary contributions from the complex exponential term  $RP_{off}E(t', A_d, 0)$  for a non-zero offset power  $P_{off}$  and crosstalk from other constituent interferometers due to the remaining complex exponential terms in Eq.(6.10). While it was shown

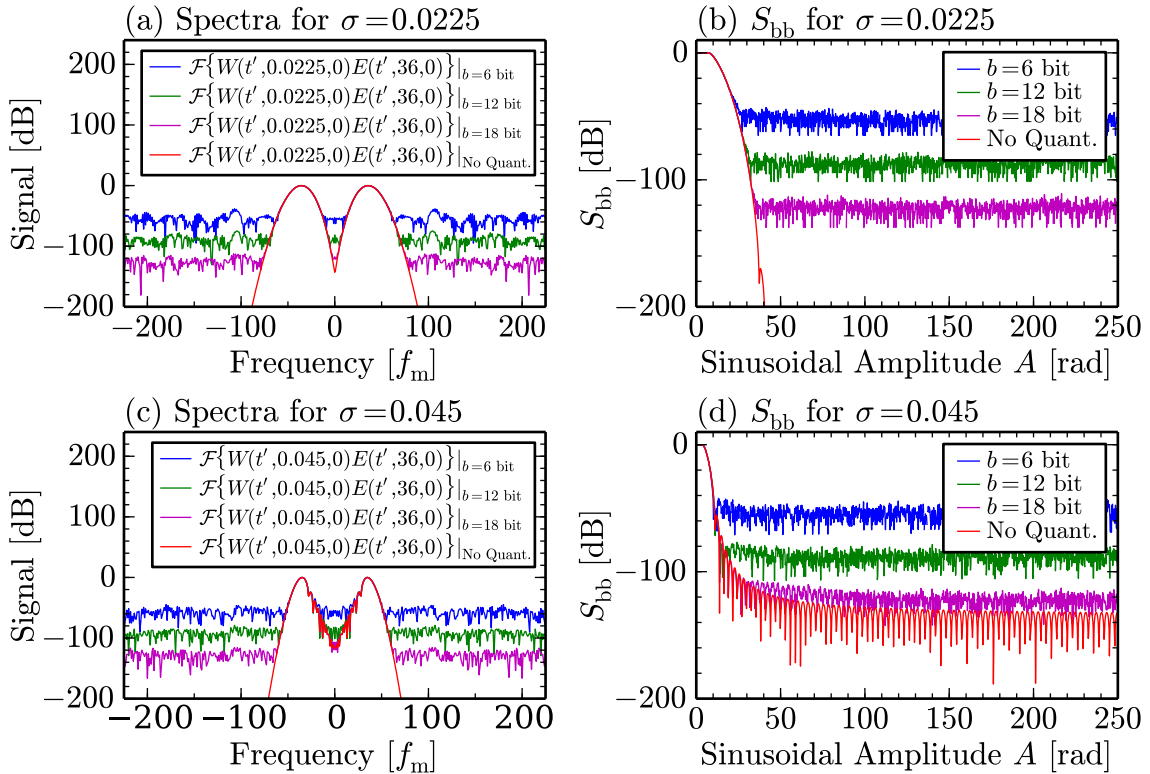


**Figure 6.5.:** Analogous to Fig. 6.2(b), the spectra of the windowed complex exponential term  $W(t', \sigma, 0)E(t', 36, 0)$  are plotted in (a) for  $\sigma = 0.0225$  and in (c) for  $\sigma = 0.045$  for various values of the processing bitwidth  $b$  and without any quantisation. The corresponding baseband suppression graphs, analogous to Fig. 6.3, are then plotted in (b) for  $\sigma = 0.0225$  and in (d) for  $\sigma = 0.045$ .

for the CDM technique in App. D.3 that non-stationary crosstalk contributions, especially from high-amplitude fast-moving phase signals, can often be neglected in practice, stationary crosstalk contributions, such as those that originate for non-zero  $P_{\text{off}}$  but also from other constituent interferometers with stable phase signals, can offset the quadrature signal circle/ellipse in Fig. 3.6 and therefore cause one-cycle non-linearities, as discussed in Sec. 3.1.4.

Apart from resulting in crosstalk between different complex exponential terms in the complete demodulation process (see also Fig. 6.4), quantisation errors can also cause imperfect sideband suppression  $S_{\text{sb}}$  between the two sidebands of the same complex exponential term. As detailed in Sec. 3.1.4, this leads to two-cycle non-linearities. In order to model non-linearities introduced by imperfect sideband suppression, the offset power  $P_{\text{off}}$  was set to zero to exclude one-cycle non-linearities caused by the complex exponential term  $RP_{\text{off}}E(t', A_d, 0)$  in Eq. (6.10). This was then simulated for a single interferometer at phase carrier amplitude  $A_1$  and typical results are illustrated in Fig. 6.6(a) for demodulation parameters  $A_d = A_1 = 36$  rad,  $\sigma = 0.0225$  and for a processing bitwidth of  $b = 6$  bit. In this calculation, an ideal test signal  $\varphi_1(t')$  with phase values increasing linearly from 0 to  $2\pi$  is introduced. Then the phase

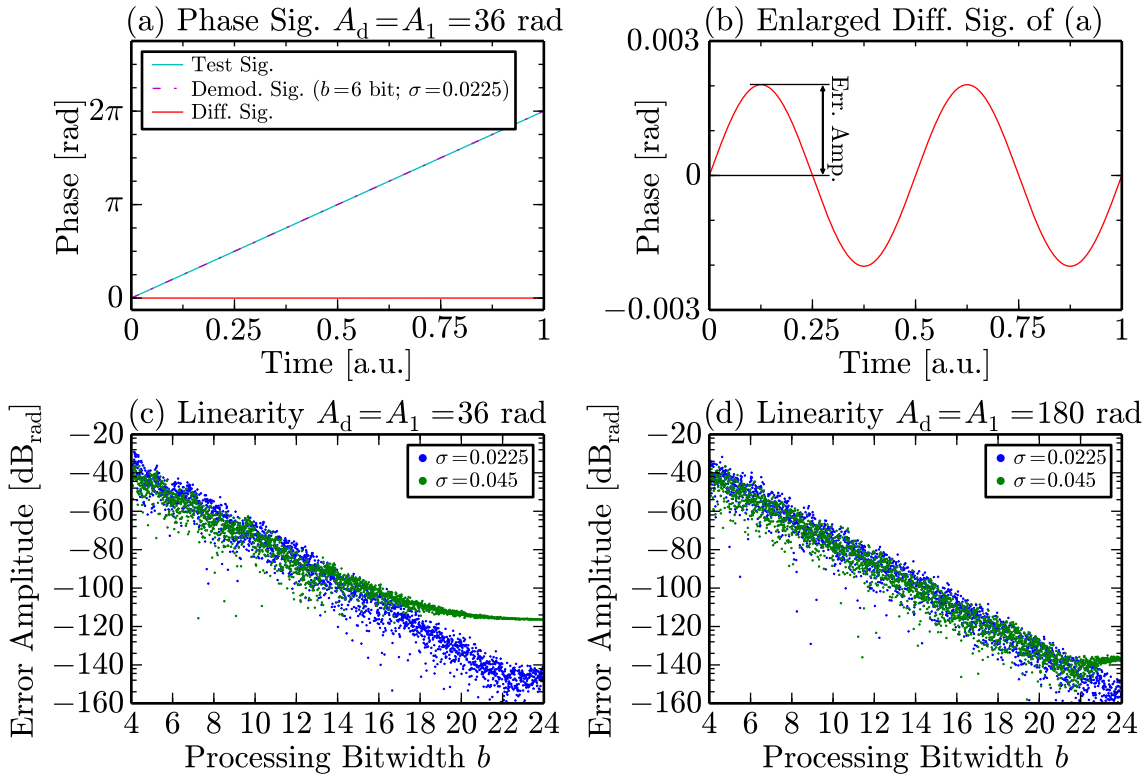


**Figure 6.6.:** An illustration of a typical result from the numerical linearity modelling is shown in (a), where the demodulation for a single interferometer at  $A_d = A_1 = 36$  rad for  $\sigma = 0.0225$  in a quantised system at processing bitwidth  $b = 6$  bit is shown for an ideally linear test signal with phase values ranging from 0 to  $2\pi$ . Here, (b) plots an enlarged version of the difference signal of (a), with the two-cycle error amplitude also marked. For both  $\sigma = 0.0225$  and  $\sigma = 0.045$ , scatter plots of the two-cycle error amplitude values obtained in this way are drawn as a function of  $b$  on a double-logarithmic scale, where for a phase value  $\varphi$  in units of rad, the value in units of dB<sub>rad</sub> is given by  $20 \cdot \log_{10}[\varphi]$ . Here, (c) shows the case for a single interferometer at  $A_d = A_1 = 36$  rad and (d) for a single interferometer at  $A_d = A_1 = 180$  rad.



signal resulting from demodulation under the described conditions is subtracted, with the difference signal displaying the resulting cyclic errors. In Fig. 6.6(a), the input and demodulated signals cannot be distinguished and the difference signal is flat on the scale used, therefore the difference signal is enlarged in Fig. 6.6(b). Here, the resulting two-cycle error amplitude is also marked, corresponding to a value of 2.0 mrad in this example.

Double-logarithmic scatter plots of the dependence of the two-cycle error amplitude on the processing bitwidth  $b$  that were obtained in the way described above are then shown in Fig. 6.6(c) for the previous example of  $A_d = A_1 = 36$  rad and in Fig. 6.6(d) for the case of a large phase carrier amplitude at  $A_d = A_1 = 180$  rad. Both Figs. 6.6(c) and (d) also compare the cases for  $\sigma = 0.0225$  and  $\sigma = 0.045$ . In general, because the effects arising from quantisation errors are very sensitive on the exact number of quantisation levels, the values in Figs. 6.6(c) and (d) are scattered widely. However, for not too large values of  $b$ , a clearly linear dependence of the error amplitudes can be observed, with the phase error amplitude again dropping by approximately a factor of 2 or 6 dB<sub>rad</sub> for every increase in  $b$  of 1, i.e. for every doubling of the available quantisation levels. However, apart from the data for  $\sigma = 0.0225$  in Fig. 6.6(d), the initially linear decline in the error amplitude asymptotically reaches a limiting value. For example, the scatter plot for  $\sigma = 0.045$  in Fig. 6.6(c) asymptotically reaches the value of  $-116$  dB<sub>rad</sub> or  $1.5$   $\mu$ rad for large processing bitwidths  $b$ . This is numerically equal to the baseband suppression value of  $S_{bb} = -116$  dB that can be extracted from Fig. 6.3 for the same demodulation parameters  $A_d = 36$  rad and  $\sigma = 0.045$ . Similar equivalences can be found in the remaining asymptotic cases, indicating that the calculated values for the baseband suppression values  $S_{bb}$  are equal to the sideband suppression ratio  $S_{sb}$ , although the theoretical description incorporating this is still outstanding.

In summary, the modelling results presented here show that both the baseband suppression values  $S_{bb}$ , measuring crosstalk from other complex exponential terms in the demodulation process that can cause one-cycle non-linearities, and sideband suppression values  $S_{sb}$ , measuring imperfect sideband suppression that causes two-cycle non-linearities, approximately halve for every 1 bit increase in signal processing bitwidth. Therefore, for large signal processing bitwidths and sufficient separation between the OPDs of the constituent interferometers, very low non-linearity errors can theoretically be expected using this technique.

### 6.2.5. Correction of Non-Ideal Modulation Characteristics

So far, this theoretical treatment has neglected any intensity modulation that is normally associated with laser injection current modulation, or any deviation from a purely sinusoidal optical frequency modulation waveform. As shown by the later experiments in Sec. 6.3, these effects may be present but their influence is limited and can be corrected to improve performance. Therefore, in this section the previous equations of Sec. 6.2.1 are extended to describe these corrections theoretically.

As a result of the non-ideal current-to-frequency modulation characteristic of laser diodes (see also App. B.1), even ideal sinusoidal laser injection current modulation



can result in non-linear optical frequency modulation. This non-ideal sinusoidal optical frequency modulation waveform may contain harmonic terms of sinusoidal modulation frequency  $n f_m$  at positive integer harmonic index  $n$  for  $n \geq 2$ , which may, in general, also show a phase shift  $\delta_n$  relative to the fundamental component. The relative contribution of each harmonic term compared to the fundamental component can be expressed by the fractional harmonic amplitude  $\beta_n$ . Because the derivation detailed in App. E can readily be extended for multiple sinusoidal optical frequency modulation terms, these non-linearities are proportionally represented in the phase modulation function  $\theta_k(t)$  of Eq. (6.2), which can then be extended to:

$$\theta_{k,\text{ext}}(t) = A_k \left( 1 \cdot \sin[2\pi f_m(t - 0.5\tau_k)] + \sum_{n=2}^{\infty} \beta_n \sin[2\pi n f_m(t - 0.5\tau_k) - \delta_n] \right) \quad (6.12)$$

Also, the laser diode may show sinusoidal optical intensity modulation at frequency  $f_m$ , which, due to the very linear injection current-to-laser power relation (see also App. B.1) typical for laser diodes can be assumed to be purely sinusoidal without harmonics. However, it is well-known [250] that laser diodes undergoing rapid injection current modulation exhibit a delay  $\tau_1$  between intensity modulation and optical frequency modulation. In this work, in order to comply with the previous notation, where the time origin is set relative to the optical frequency modulation waveform, the intensity modulation delay is incorporated by employing a negative delay  $-\tau_1$ . Using the relative amplitude  $\xi$  of the sinusoidal intensity modulation, the intensity modulation function  $I(t')$  is given by:

$$I(t') = \left( 1 + \xi \sin[2\pi f_m t' + \tau_1] \right) \quad (6.13)$$

The physically measured photo detector signal  $U_{\text{pd}}(t')$  of Eq. (6.5), incorporating intensity and non-linear optical frequency modulation, can then be described by:

$$U_{\text{pd}}(t') = I(t') \cdot \left( RP_{\text{off}} + \sum_{k=1}^{k_{\text{max}}} \left( RP_{\text{eff},k} \cdot \cos[\theta_{k,\text{ext}}(t') + \varphi_k(t')] \right) \right) \quad (6.14)$$

In this work, both intensity modulation and non-linear optical frequency modulation can be corrected by modifying the demodulation carrier function  $C(t', A_d, \tau_d)$  of Eq. (6.7). Here, the additional sinusoidal terms in Eq. (6.12) are incorporated, where, for demodulation similar to the previous derivation in Sec. 6.2.1,  $A_d$  is set equal to  $A_k$  and  $\tau_d$  is set equal to  $0.5\tau_k$ . To correct intensity modulation,  $I(t')$  of Eq. (6.13) is then inverted, yielding the corrected demodulation carrier function  $C_{\text{corr}}(t', A_d, \tau_d)$ :

$$C_{\text{corr}}(t', A_d, \tau_d) = I(t')^{-1} \cdot \exp \left[ j \cdot A_d \left( 1 \cdot \sin[2\pi f_m(t' - \tau_d)] + \sum_{n=2}^{\infty} \beta_n \sin[2\pi n f_m(t' - \tau_d) + \delta_n] \right) \right] \quad (6.15)$$

It is straightforward to see that for the correct intensity modulation parameters  $\xi$  and  $\tau_1$ , the multiplicative application of  $C_{\text{corr}}(t', A_d, \tau_d)$  to  $U_{\text{pd}}(t')$  completely corrects the intensity modulation in the photo detector signal  $U_{\text{pd}}(t')$  of Eq. (6.14). Furthermore, the demodulation process of Sec. 6.2.1 and Sec. 6.2.2 remains principally as described

when the non-linear optical frequency modulation parameters  $\beta_n$  and  $\delta_n$  are included in the corrected carrier function  $C_{\text{corr}}(t', A_d, \tau_d)$ . In the remainder of this work, when the corrected carrier function  $C_{\text{corr}}(t', A_d, \tau_d)$  of Eq. (6.15) is used instead of non-corrected carrier function  $C(t', A_d, \tau_d)$  of Eq. (6.7), the resulting demodulated signal and the resulting complex quadrature signal of Eq. (6.10) are denoted by  $U_{\text{dem,corr}}(t', \sigma, A_d)$  and  $U_{Q,\text{corr}}(t', \sigma, A_d)$ , respectively.

## 6.3. Nested Mach-Zehnder Experiment

### 6.3.1. Implementation

**Setup and Processing** A suitable setup to test the proposed signal processing technique is the nested MZ interferometric configuration shown in Fig. 6.7, which is constructed using regular SMF28e+ fibre and standard directional couplers and where test signals can be introduced using Piezo-electric transducers (PZT). Because, unlike an FSI configuration, the MZ interferometer (see also Sec. 3.1.3) works in transmission, the signal powers involved are generally very high, permitting the investigation of the proposed SFM technique in favourable conditions. The nested MZ configuration includes an inner interferometer, consisting of arms A and B, subsequently referred to as interferometer 1 (I1), while the extra outer arm C gives rise to two additional interferometers, referred to as interferometer 2 (I2) for the interference of arms B&C and interferometer 3 (I3) for the interference of arms A&C. Test signals can be introduced by PZT A into arm A and PZT C into arm C. The physical path lengths were designed to increase by at least 0.16 m, corresponding to an OPD difference of 0.23 m per constituent interferometer, i.e. the spatial resolution calculated in Sec. 6.2.3 for  $S_{\text{bb,accept}} = -200$  dB. When measured with a Luna OBR 4400 Reflectometer, the actual OPDs were found to be 0.21 m, 0.51 m and 0.73 m for I1, I2 and I3, respectively. These OPD values also allow to prove that, in contrast to prior work (see Sec. 4.4), the technique can be made to work for constituent interferometers that do not form a simple integer OPD relationship with each other. The nested MZ setup was also chosen because it highlights novel measurement

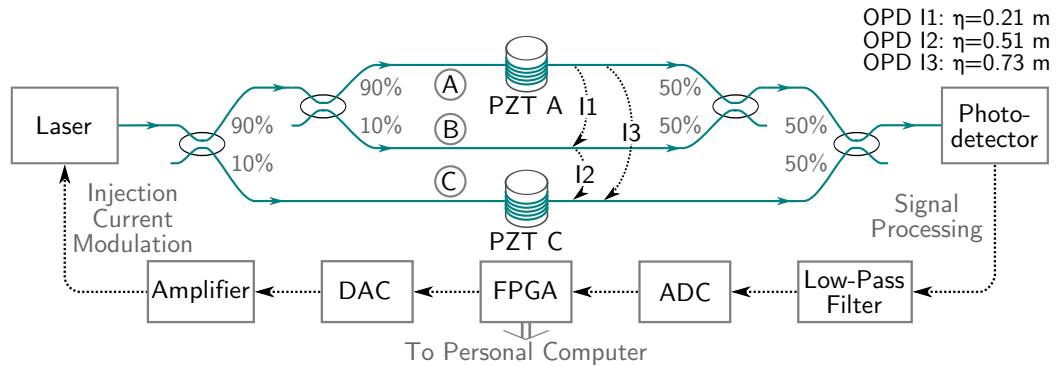


**Figure 6.7.:** Setup for the nested MZ experiment with arms A, B and C, where the three constituent interferometers I1, I2 and I3 correspond to the interference between arms A&B, B&C and A&C, respectively. PZTs are integrated in arms A and C to induce test signals. Both modulation and signal processing are controlled by the FPGA, which controls the ADC and DAC, and performs time-critical demodulation steps, with the data sent to a personal computer for final processing.

possibilities that range-resolved interferometry can offer, allowing the differential signal induced by PZT A as well as the common-mode offset signal induced by PZT C to be measured simultaneously with a single laser and photo detector. It is also important to note that both the differential and the offset signal can be derived in two ways, either measured directly from I1 or I2, respectively, or by subtracting the signals of the other two interferometers, allowing a straightforward method to assess the performance of the technique.

In the experimental setup shown in Fig. 6.7, the laser diode (Eblana Photonics EP1550-NLW-B on Profile LDC200 driver; centre wavelength: 1552 nm, temperature controlled to 25° C, output power: 6 mW at bias current  $I_{LD} = 125$  mA, see App. B for full characterisation) was modulated by a sinusoidal injection current modulation of amplitude  $\Delta I_{LD} = 45$  mA at a modulation frequency  $f_m = 98$  kHz. The measurements shown in App. B.3 then yield a value for the optical frequency modulation amplitude  $\Delta f_{opt}$  of 8.4 GHz. All modulation and signal processing functions are controlled by a field programmable gate array (FPGA) (see also App. C) to ensure precisely synchronized modulation and demodulation, which is essential for the working of the technique. The FPGA (Altera Cyclone IV on Terasic DE2-115 board) is connected to a data acquisition daughter board that runs at a sample frequency  $f_s$  of 100 MHz at  $\pm 13$  bits resolution for both ADC and digital-to-analogue converter (DAC). Here, the sinusoidal laser diode injection current modulation is driven, using an additional amplifier and low-pass filter with cut-off at 1.9 MHz, by the DAC. The ADC then samples the resulting interferometric signals from the photo detector (New Focus 1592; Passband: 10 kHz to 3.5 GHz), which have been low-pass anti-aliasing filtered (BLP50+ from Mini-Circuits) with a cut-off frequency of 50 MHz.

The signal processing is also illustrated in Fig. 6.8 for three range channels, although

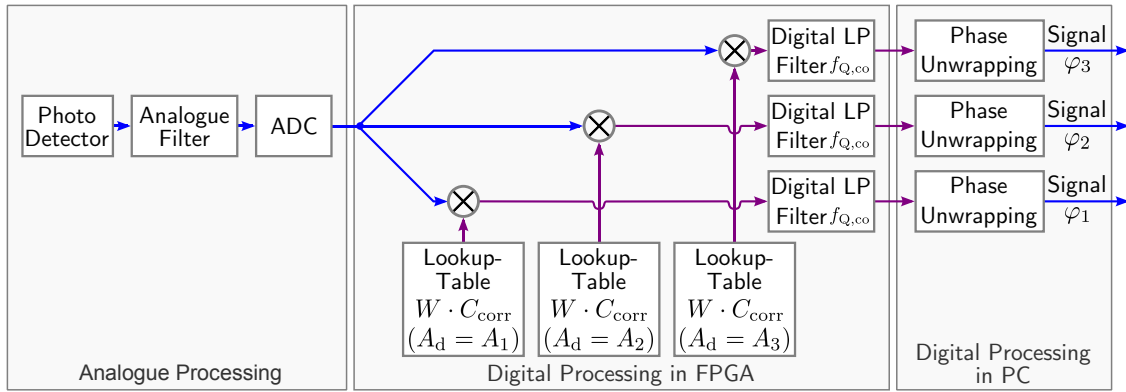


**Figure 6.8.:** Illustration of the signal processing, where real signals are drawn in blue and complex signals are drawn in magenta. After analogue anti-aliasing filtering and digitisation by the ADC, the photo detector signal enters the FPGA. Here, the demodulation of signals is illustrated for three range channels, where the demodulation solely involves the multiplication with a complex lookup-table. These tables incorporate the window function  $W(t', \sigma, 0)$ , the corrected  $C_{corr}(t', A_d, 0)$  or non-corrected  $C(t', A_d, 0)$  carriers with the demodulation carrier amplitude  $A_d$  set to the expected value  $A_k$  of the  $k$ th interferometer and where any signal processing delay  $\tau_{sp}$  is taken into account in the calculation of the lookup-table values. After digital low-pass filtering at quadrature cut-off frequency  $f_{Q,co}$ , the resulting quadrature signals  $U_Q(t', \sigma, A_d)$  of Eq. (6.10) are transmitted from the FPGA to a PC, where phase unwrapping is performed, yielding the desired phase signals  $\varphi_k(t')$ .

in the implementation used for this work eight range channels can be demodulated simultaneously by the FPGA. For each range channel, the demodulation solely involves multiplication with a lookup-table of a length equal to one modulation period  $T_m$  and containing the complex product of the window function  $W(t', \sigma, 0)$  of Eq. (6.6) and the non-corrected carrier function of  $C(t', A_d, 0)$  of Eq. (6.7) or the corrected carrier  $C_{\text{corr}}(t', A_d, 0)$  of Eq. (6.15). Here, the demodulation carrier amplitude  $A_d$  is set to the approximate value of  $A_k$  expected for the desired  $k$ th interferometer. Also, for the calculation of these lookup-tables, the signal processing delay  $\tau_{\text{sp}}$ , with its value determined as described in the next section, is taken into account to allow compensation of  $\tau_{\text{sp}}$ . After the multiplication with the complex lookup-table the resultant demodulated signal for each channel is low-pass filtered with a cut-off frequency of  $f_{Q,\text{co}} = 43 \text{ kHz}$ , slightly below the maximally possible value of  $f_{Q,\text{co,max}} = 0.5f_m = 48 \text{ kHz}$  to allow the practical implementation of the low-pass filter in the FPGA. This then results in the complex quadrature signal  $U_Q(t', \sigma, A_d)$  of Eq. (6.10). Following this, the complex quadrature data is then sent to a personal computer (PC). The PC initially calculates the look-up tables for the FPGA and then performs phase unwrapping for the complex quadrature data of each range channel, yielding the desired phase signals  $\varphi_k(t')$ . The phase unwrapping could, however, also be performed in the FPGA in later implementations.

**Signal and Modulation Properties** Fig. 6.9(a) shows a typical photo detector signal,  $U_{\text{pd}}(t)$ , over one modulation period,  $T_m = f_m^{-1} = 10.24 \mu\text{s}$ , arising from the three constituent interferometers present in the setup of Fig. 6.7. When the symmetry centre of  $U_{\text{pd}}(t)$  in Fig. 6.9(a) is compared to Fig. 6.1(c), a signal processing delay  $\tau_{\text{sp}}$  of approximately a quarter of  $T_m$  can be observed. The Fourier transform of  $U_{\text{pd}}(t)$  is shown in Fig. 6.9(b). The largest phase carrier amplitude that is present in the configuration of Fig. 6.7 is  $A_3$  for interferometer 3 (I3). The value of  $A_3$  is found to be  $A_3 = 146.5 \text{ rad}$  using the method that will be discussed in the next section. It can be seen in Fig. 6.9(b) that the spectral width of the photo detector signal is  $15 \text{ MHz}$ , approximately numerically equal to the product of the modulation frequency  $f_m$  and the phase carrier amplitude  $A_3$  of the constituent interferometer with the largest OPD. In this technique, this product thus determines the bandwidth requirements for the ADC and for the remaining processing hardware.

Analogous to Fig. 6.4(f), the complete demodulation process in the frequency domain is illustrated in Fig. 6.9(b). This is done at a demodulation phase carrier amplitude of  $A_d = A_3 = 146.5 \text{ rad}$  and using the previous simplification of  $\tau_d = 0$ . To enable demodulation, the signal processing delay has been compensated using the exact value of  $\tau_{\text{sp}} = 2.775 \mu\text{s}$  as determined later. Similar to Fig. 6.4(f), the effect of the separation of the spectra of the complex exponential terms into distinct peak regions can be observed in Fig. 6.9(b) when the window function  $W(t', 0.0225, 0)$  of Eq. (6.6) with  $\sigma = 0.0225$  is applied. Seven complex exponential peak pairs are expected for the case of three constituent interferometers and can be clearly identified in Fig. 6.9(b), where the baseband peak at frequency 0 corresponds to the desired complex exponential term and the expected comb spectrum is clearly visible.

In Fig. 6.9(a), a strong intensity modulation envelope of the photo detector signal  $U_{\text{pd}}(t)$  is visible. As discussed in Sec. 6.2.5, this intensity modulation, described by

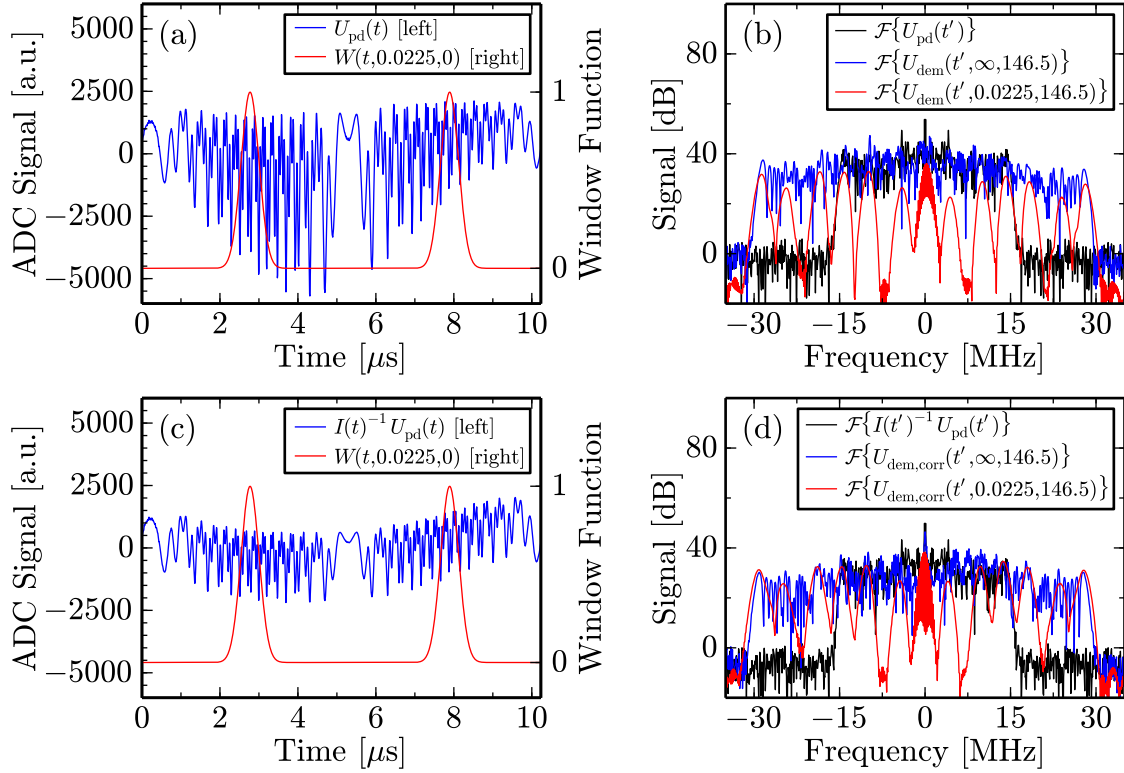


**Figure 6.9.:** (a) directly plots an instance of the photo detector signal  $U_{pd}(t)$  from the ADC over one modulation period, along with the window function  $W(t, 0.0225, 0)$ . Here, the signal processing delay  $\tau_{sp}$  has not yet been compensated. (b) plots the Fourier transform of  $U_{pd}(t)$ , and, similar to Fig. 6.4(f), (b) then shows the Fourier spectrum after demodulation at  $A_d = 146.5$  rad with ( $\sigma = 0.0225$ ) and without ( $\sigma \rightarrow \infty$ ) application of the window function, where  $\tau_{sp}$  has now been compensated to enable demodulation. Analogously, (c) and (d) plot the corresponding corrected signals, where in (c) the intensity modulation  $I(t)$ , and, in (d), both intensity modulation and non-linear optical frequency modulation have been corrected according to Sec. 6.2.5.

the function  $I(t')$  in Eq. (6.13), can be corrected with knowledge of the parameters  $\tau_1$  and  $\xi$ . Here, App. B.3 describes a simple method used in this work to measure these parameters, where, for the previously described injection current modulation parameters, values of  $\tau_1 = 5.92 \mu\text{s}$  and  $\xi = 0.45$  were found. The value of  $\tau_1$  corresponds to an equivalent phase shift of  $208^\circ$  relative to the sinusoidal injection current modulation waveform, which is comparable to the literature [250], where a phase shift of  $225^\circ$  at 100 kHz was found for a typical DFB laser diode. Using these correction parameters to invert the intensity modulation, the corrected photo detector signal  $I(t)^{-1} U_{pd}(t)$ , plotted in Fig. 6.9(c), can be obtained. Here, it can be seen that the correction works well and ensures a constant envelope of the interferometric signals. However, it can also be seen in Fig. 6.9(c) that the correction introduces an artefact that resembles a distorted sinusoid of fundamental frequency  $f_m$ . This is because in this implementation, the photo detector signals are AC-coupled and there is no transmission of the DC signal levels that are assumed to be there in the correction procedure. In this experiment this is of no particular concern because the frequencies of the distorted sinusoid are well away from the frequencies evaluated by the windowed carrier function. Furthermore, in order to complete the correction procedure, the non-linear optical frequency modulation parameters  $\beta_n$  and  $\delta_n$  of

Eq. (6.12) have to be determined. The experiment used to measure these parameters is described in App. B.3. Here, fractional amplitudes of  $\beta_2 = 4.1\%$  for the first harmonic and  $\beta_3 = 0.3\%$  for the second harmonic were found and it was also verified that all higher harmonics are negligible. Corresponding phase shifts of  $\delta_2 = 12^\circ$  and  $\delta_3 = 121^\circ$  have also been extracted. In this work, due to the small value of  $\beta_3$  and negligible higher harmonics, the correction procedure was only implemented for the first harmonic term using parameters  $\beta_2$  and  $\delta_2$ .

As described in Sec. 6.2.5, all described corrections can be included in the corrected carrier function  $C_{\text{corr}}(t', A_d, \tau_d)$  of Eq. (6.15) and are easily incorporated into the FPGA demodulation look-up tables. Fig. 6.9(d) then shows the spectrum of the demodulated signals with corrections applied. It can be seen that, compared to the case without corrections in Fig. 6.9(b), the comb of the baseband signal is larger and more symmetric. In general, one of the aims of this work is to show the robustness of the proposed technique and prove that high-quality measurements can be made even without performing any corrections. Therefore, throughout the remainder of this section, there will be a comparison between corrected and uncorrected results.

**Determination of Demodulation Parameters** For the practical operation of the proposed technique, the correct demodulation parameters, i.e. the signal processing delay,  $\tau_{\text{sp}}$ , as well as the approximate phase carrier amplitudes,  $A_k$ , for each constituent interferometer of index  $k$  have to be identified without any prior knowledge. Both  $\tau_{\text{sp}}$  and the values for  $A_k$  can be found by plotting a map of baseband signal amplitude of the low-pass filtered complex quadrature signal  $|U_Q(t - \tau_{\text{sp}}, \sigma, A_d, \tau_d = 0)|$  of Eq. (6.8) as a function of the demodulation phase carrier amplitude  $A_d$  and the signal processing delay  $\tau_{\text{sp}}$ . Here, the compensated time variable  $t'$  has been replaced with  $t - \tau_{\text{sp}}$  according to Eq. (6.4) and the demodulation delay  $\tau_d$  is set to zero. These calculations were performed on a PC, where it is stressed that the maps shown in Fig. 6.10, despite their smooth appearance, were calculated from the raw photo detector signal, using the same dataset over a single modulation period  $T_m = 10.24 \mu\text{s}$  already plotted in Fig. 6.9(a).

These maps are shown in Figs. 6.10(a), (c) and (e) on the left without any of the corrections of Sec. 6.2.5, while in Figs. 6.10(b), (d) and (f) on the right these corrections were used. Also three values of the window width parameter  $\sigma$  are compared in Fig. 6.10, where the upper plots in Figs. 6.10(a) and (b) are calculated for  $\sigma = 0.0225$ , the value use in the discussion so far, the middle plots in Figs. 6.10(c) and (d) for  $\sigma = 0.045$  and the lower plots in Figs. 6.10(e) and (f) for  $\sigma = 0.0675$ . In the resulting maps in Fig. 6.10, patterns consisting of sets of nodes spread horizontally for each of the three constituent interferometers can be seen. The horizontal distance between these nodes decreases proportionally with the phase carrier amplitude  $A_k$  of the  $k$ th constituent interferometer. The horizontal patterning seen in the maps can only be explained using the unapproximated equation for the complex quadrature signal that is given by Eq. (6.8), where the delays  $\tau_d$  and  $\tau_k$  are taken into account. However, in all maps a set of nodes that overlap vertically can be found and a line, shown in white on the maps, can be drawn connecting the centres of these nodes. This line marks the correct signal processing delay,  $\tau_{\text{sp}}$ , and the assumptions of negligible time-of-flight delays of the constituent interferometers  $\tau_k \approx 0$ , used to obtain the

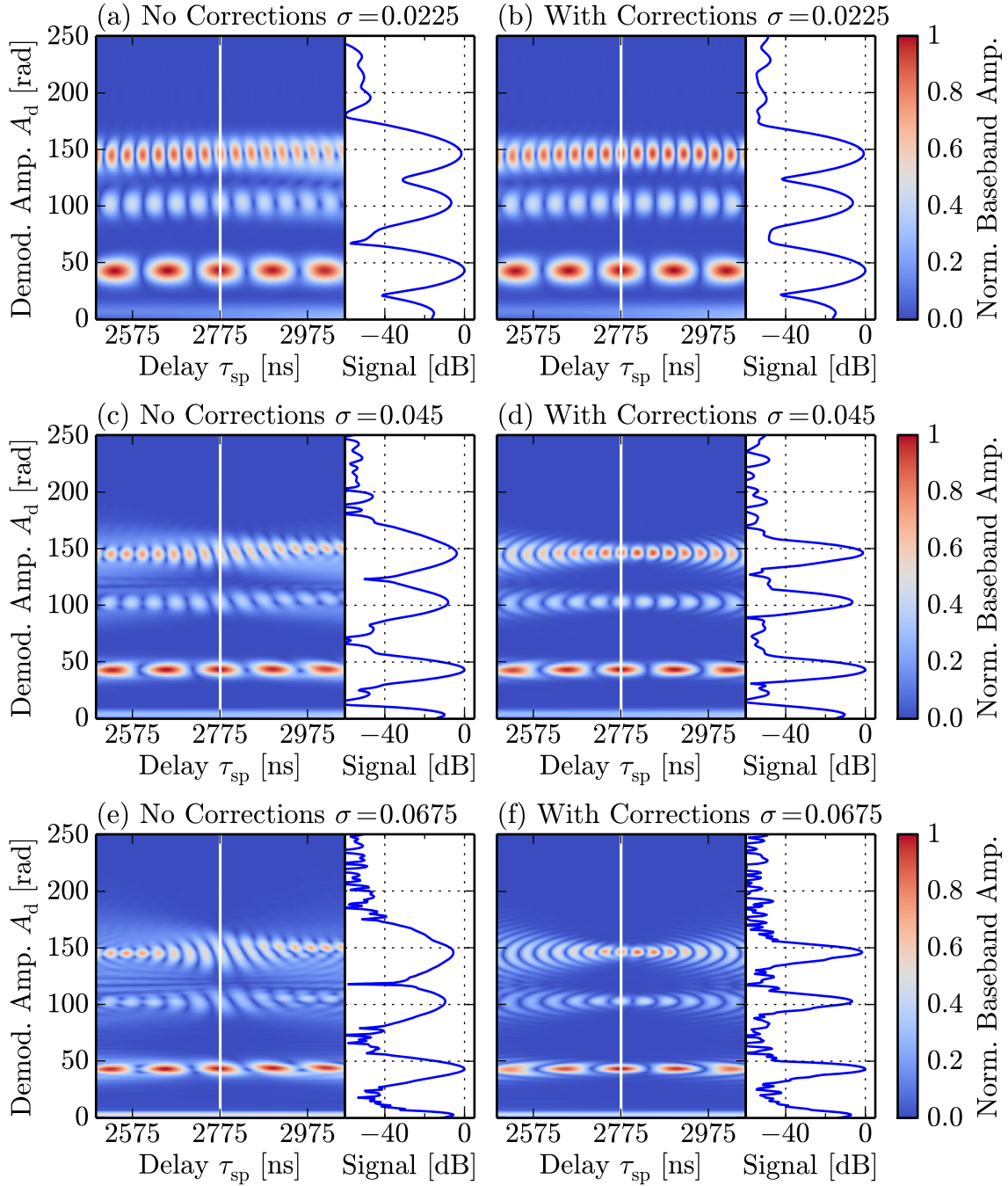


**Figure 6.10.:** Determination of the demodulation parameters using demodulation phase carrier amplitude  $A_d$  versus signal processing delay  $\tau_{sp}$  maps. Here, the cases without the corrections of Sec. 6.2.5 are shown on the left in (a), (c) and (e), while the cases with these corrections applied are shown on the right in (b), (d) and (f). The window width parameter  $\sigma$  increases from 0.0225 in (a) and (b), to  $\sigma = 0.045$  in (c) and (d) and  $\sigma = 0.0675$  in (e) and (f). These maps plot the baseband signal amplitude of the complex quadrature signal normalised to the overall maximum value as a function of  $A_d$  and  $\tau_{sp}$  with a common colour-bar shown on the right. The white, vertical lines mark the chosen evaluation locations and the signals along this line are also plotted on the panel next to each map on a logarithmic scale.



approximated version of the complex quadrature signal given by Eq. (6.10), are valid here. In this work, all signal processing was carried out on this line by digitally compensating  $\tau_{sp}$  in the demodulation look-up tables on the FPGA, where a value of  $\tau_{sp} = 2775$  ns can be extracted from all maps in Fig. 6.10. Furthermore, the panels on the right of each map in Fig. 6.10 plot the baseband signal amplitude along the white evaluation line on a logarithmic scale. These plots allow the phase carrier amplitudes  $A_k$  of the constituent interferometers to be found, where extracted values of  $A_1 = 43.5$  rad,  $A_2 = 103.0$  rad and  $A_3 = 146.5$  rad were subsequently used to demodulate the signals of I1, I2 and I3, respectively. In all plots in Fig. 6.10, the peaks near  $A_d = 0$  are due to the DC-offset and/or the discussed artefacts due to the correction procedure in the photo detector signals shown in Figs. 6.9(a) and (c).

In Fig. 6.10, when comparing the maps on the right, where the corrections of Sec. 6.2.5 have been applied, to the maps on the left without corrections, it can be seen that the corrections make the map patterns appear much more regular. These maps can therefore also serve as a visual diagnostic tool to verify the parameters of the correction procedure, especially for higher values of  $\sigma$ , where, for  $\sigma = 0.0675$ , the corrected and uncorrected map pattern can be seen in Figs. 6.10(e) and (f) to differ strongly. Also, when comparing the maps on the top where  $\sigma = 0.0225$  to the maps at the bottom where  $\sigma = 0.0675$ , it can be seen that the  $A_d$  resolution, and therefore the range resolution, increases and that very regular, symmetric peaks shapes can be obtained, which are particularly narrow in the right panel in Fig. 6.10(f). When a suitable range calibration is performed, this information can also be used to plot the return signal amplitude of the constituent interferometers as a function of range.

### 6.3.2. Results for Nested Mach-Zehnder Experiment

**Quadrature Signals:** Using the operating conditions and demodulation parameters described in Sec. 6.3.1, for a window width parameter  $\sigma = 0.0225$ , measurements employing the nested MZ interferometer shown in Fig. 6.7 have been performed. Here, a sinusoidal test signal of frequency 10 Hz at peak-to-peak phase amplitude 7.2 rad was induced by PZT A, and a test signal of frequency 180 Hz at peak-to-peak phase amplitude 6.8 rad was induced by PZT C and both signals were generated asynchronously by separate function generators. For these excitations, a typical time trace of the corrected low-pass filtered, complex quadrature signal  $U_{Q,corr}(t', 0.0225, A_1)$  for interferometer I1 is pictured in Fig. 6.11(a). Figure 6.11(b) then shows the polar plots for I1, I2 and I3, tracing the complex phasor tip coordinates of the corrected complex quadrature signal for every data point over a period of 5 s without any averaging. On visual inspection, the polar plots are found to be both concentric and highly circular, where both concentricity and circular shape are requirements for linear measurements in the absence of cyclic errors (see also Sec. 3.1.4). Compared to the polar plots for the CDM technique in Fig. 5.24(a), the polar plots in this technique exhibit considerably less amplitude noise, presumably because the OPDs involved in the experimental setup of Fig. 6.7 are two orders of magnitude lower. In this context, a detailed noise analysis of the proposed SFM technique will be carried out in Sec. 6.4 using a single MZ experimental setup.



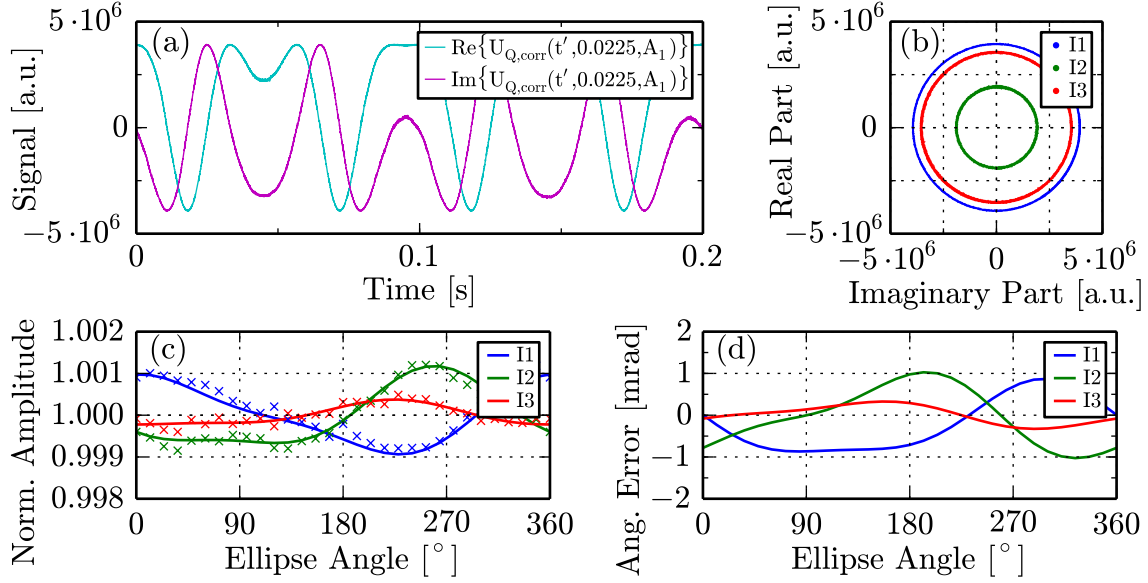


**Figure 6.11.:** The corrected low-pass filtered complex quadrature signal  $U_{Q,\text{corr}}(t', 0.0225, A_1)$  is shown in (a) as a time series over 0.2s for I1, while (b) shows the polar plots of all three constituent interferometers I1, I2 and I3 in the complex plane without any averaging. Analogous to Fig. 5.24, (c) plots the normalized quadrature amplitudes, averaged into 30 angular sectors, for I1, I2 and I3 as a function of phasor angle of the complex quadrature signal using crosses, while the fit of this data with the ellipse model of Eq. (3.8) is drawn using continuous lines of the same colour. Finally, in (d) the angular errors calculated using this model are shown.

**Linearity:** Analogous to Fig. 5.15 and Fig. 5.24, the cyclic error model of Eq. (3.8) is applied to the complex quadrature amplitude data, averaged into 30 angular sections. This is shown in Fig. 6.11(c) for the case where the corrections of Sec. 6.2.5 have been applied. Here, the crosses mark the averaged amplitude data and the continuous lines of the same colour represent the fit according to Eq. (3.8). A very good agreement between the fit and the measured data can be observed for all three constituent interferometers. When compared to the CDM technique, the maximum amplitude variations are reduced by more than an order of magnitude, from  $\approx 2\%$  in Fig. 5.24(b) down to  $0.12\%$  in Fig. 6.11(c). The angular errors resulting from these fits are then shown in Fig. 6.11(d), with extracted error values equal to  $[\pm 0.8 \text{ mrad}, \pm 1.0 \text{ mrad}, \pm 0.3 \text{ mrad}]$  for [I1, I2, I3]. The corresponding angular error values for non-corrected data are  $[\pm 1.0 \text{ mrad}, \pm 1.3 \text{ mrad}, \pm 1.4 \text{ mrad}]$  for [I1, I2, I3] and thus slightly higher. It can furthermore be seen in Fig. 6.11(d) that one-cycle non-linearities are stronger than two-cycle non-linearities, with a numerically determined amplitude ratio of  $\approx 3$  between them for all three interferometers. The signal envelope of the corrected photo detector signal can be seen in Fig. 6.9(c) to be approximately  $\pm 1200$  ADC quantisation levels wide. Therefore, using the amplitude ratios evident in Fig. 6.9(b), this results in an approximate processing bitwidth  $b$  (see also Sec. 6.2.4) of  $b = 9$  bit for I1 and I3, and  $b = 8$  bit for I2. For two-cycle non-linearities, Figs. 6.6(c) and (d) estimate two-cycle error amplitudes between  $0.1 \text{ mrad}$  and  $2 \text{ mrad}$  for these bitwidths, with a wide scattering of error amplitude values expected. A similar magnitude of one-cycle non-linearities due to crosstalk from other complex exponential terms can also be expected as discussed in Sec. 6.2.4. However, in general, crosstalk levels are more difficult to quantify as they are dependent on

the effective powers and temporal variation of the phase signals  $\varphi_k(t')$  of the other interferometers (see also App. D.3) and on any remaining offset value in the ADC signal causing a non-zero offset power term  $P_{\text{off}}$ . Nevertheless, the observed angular errors of  $\pm 1$  mrad or  $-60$  dB<sub>rad</sub> in Fig. 6.11 are on the same order of magnitude and thus entirely consistent with the quantisation error modelling in Sec. 6.2.4.

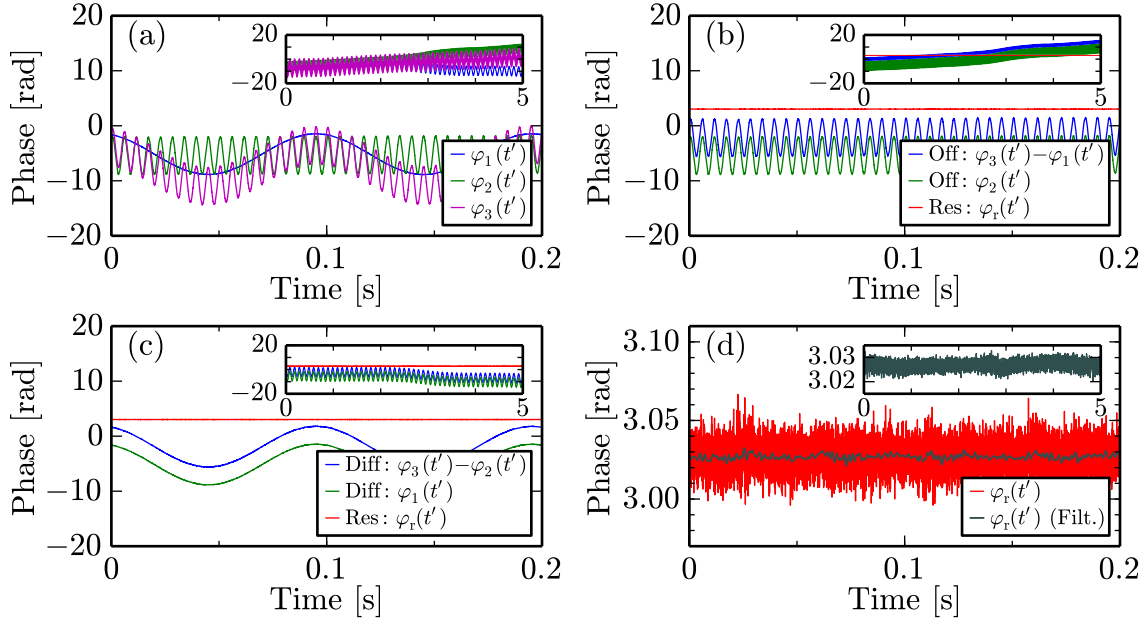
**Phase Signals:** Fig. 6.12 then shows the time traces of the unwrapped phase signals from the experiment and for the test signals described previously. The data in Fig. 6.12 is shown without any corrections of Sec. 6.2.5 applied. This is to demonstrate that high-quality measurements can be achieved even in the simple case without corrections, while the corresponding plots with corrections applied appear virtually indistinguishable. Fig. 6.12(a) plots the signals from the three constituent interferometers over 0.2 s, while the inset shows the same signals over an extended time period of 5 s. As discussed previously, the nested MZ interferometer configuration of Fig. 6.7 permits the common-mode offset phase signal, induced by PZT C, to be recovered in two ways: directly from I2 or indirectly by subtracting the signals from I3 and I1. Both these signals are compared in Fig. 6.12(b), again with an inset over 5 s, along with their difference signal, referred to as residual signal in the following. Analogously, the differential phase signal, induced by PZT A, can be recovered directly from I1 or indirectly by subtracting the signals from I3 and I2, which is shown in Fig. 6.12(c) along with their residual signal.

It is found that both residual phase signals  $\varphi_r(t')$  of Figs. 6.12(b) and 6.12(c) are mathematically equal and given by the same equation:

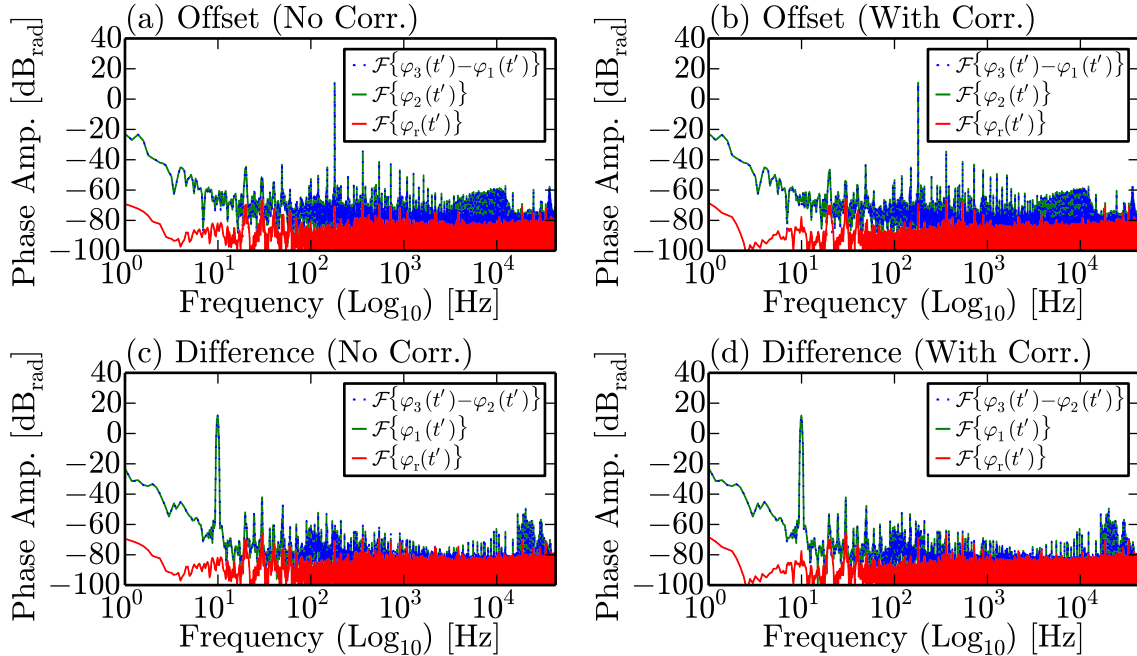
$$\varphi_r(t') = \varphi_3(t') - \varphi_2(t') - \varphi_1(t') \quad (6.16)$$

Fig. 6.12(d) then plots the residual signal  $\varphi_r(t')$  in detail, along with a low-pass filtered version of  $\varphi_r(t')$  at a cut-off frequency of 600 Hz. The inset in Fig. 6.12(d) shows that the filtered residual signal stays remarkably constant, even in the presence of large overall phase changes visible in the other insets in Fig. 6.12. This highlights the high quality of the measurements that can be achieved with the presented technique. Nevertheless, the residual signal should theoretically be zero-valued, even in the presence of laser wavelength drift or laser frequency noise, because the OPDs corresponding to the direct and indirect signals mathematically cancel. However, in Fig. 6.12(d) it can be seen to have a mean value of 3.03 rad, where it was also observed that long-term changes of the residual signal phase can occur. It is thought that this is a manifestation of the, in general, unrelated polarization states of the light within the fibre arms, leading to OPD values of the constituent interferometers that are minutely different from those expected when polarization dependence is neglected. This could explain the observed non-zero phase values in the residual signal as well as any associated slow drifts.

Finally, Figs. 6.13(a) and (b) show the Fourier spectra of the directly and indirectly obtained offset phase signals, induced by PZT A, along with the residual signal, while Figs. 6.13(c) and (d) show the Fourier spectra of the directly and indirectly obtained difference phase signals, induced by PZT C, again together with the residual signal. Here, Figs. 6.13(a) and (c) on the left show the case without any corrections of



**Figure 6.12.:** Time traces of the phase signals over 0.2s in the main plots and over 5s in the insets are shown without any corrections of Sec. 6.2.5. (a) directly plots the phase signals  $\varphi_1(t')$ ,  $\varphi_2(t')$  and  $\varphi_3(t')$  from the three constituent interferometers I1, I2 and I3, exhibiting excitations at 10Hz from PZT A (in I1 and I3) and at 180Hz from PZT C (in I2 and I3). (b) plots the offset phase signals (induced by PZT C) obtained directly  $\varphi_2(t')$  or indirectly  $\varphi_3(t') - \varphi_1(t')$  along with their difference, the residual signal  $\varphi_r(t')$ . (c) shows the differential signal (induced by PZT A) obtained directly  $\varphi_1(t')$  or indirectly  $\varphi_3(t') - \varphi_2(t')$ , again with the residual signal  $\varphi_r(t')$  as their difference. (d) plots only the residual signal  $\varphi_r(t') = \varphi_3(t') - \varphi_2(t') - \varphi_1(t')$ , given by Eq. (6.16) and mathematically identical for both (b) and (c). Here a low-pass filtered version of  $\varphi_r(t')$  with a cut-off at 600Hz is also plotted and the inset over 5s only shows the filtered signal.



**Figure 6.13.:** The Fourier spectra (computed over 5 s) of the direct and indirect versions of the offset signal from PZT C as well as the residual signal  $\varphi_r(t')$  are shown in (a) without any corrections and in (b) with corrections according to Sec. 6.2.5. Analogously, (c) and (d) plot the spectra of the direct and indirect versions of the differential signal from PZT A along with  $\varphi_r(t')$ . All plots are shown on a double logarithmic scale up to the quadrature bandwidth of 43 kHz used.

Sec. 6.2.5 applied, while Figs. 6.13(b) and (d) on the right show the case incorporating these corrections. In all plots, the respective directly obtained and indirectly obtained signal spectra appear virtually indistinguishable. Furthermore, there is no discernible difference between the non-corrected spectra on the left and the respective corrected spectra on the right, except for small differences in the residual signal spectra. In all spectra in Fig. 6.13, the residual signal is free from most noise frequency components that are present in the differential or offset signals, exhibiting a mostly flat noise floor of  $\approx -80 \text{ dB}_{\text{rad}} = 0.1 \text{ mrad}$ . For the recording time of the Fourier spectra of 5 s, this corresponds to a noise level of  $\approx 0.2 \text{ mrad} \cdot \text{Hz}^{-0.5}$ . In all cases the spectra of the residual signal contains harmonics of the original phase signals at 10 Hz and 180 Hz, which are thought to be caused by cyclic errors and that can reach levels up to  $\approx -66 \text{ dB}_{\text{rad}} = 0.5 \text{ mrad}$ , the same order of magnitude as the cyclic error levels determined previously in Fig. 6.11(d).

**Crosstalk** Fig. 6.14 plots the Fourier transformed spectra of the complex quadrature signals in Fig. 6.14(a) and phase signals in Fig. 6.14(b) for interferometers I1 and I2, subject to the previously discussed sinusoidal test phase signals of 10 Hz and 180 Hz, respectively, on a double logarithmic scale. These plots are shown here without any of the corrections of Sec. 6.2.5 applied, with comparable plots resulting for the case where these corrections have been applied. According to Eq. (3.9), the quadrature signals subject to the sinusoidal test signals from PZT A and PZT C carry a series of Bessel terms at harmonics of the test signal frequencies. To improve clarity, the signals for interferometer I3, which contains contributions at both test signal frequencies and thus cannot be used to evaluate crosstalk, are not shown in

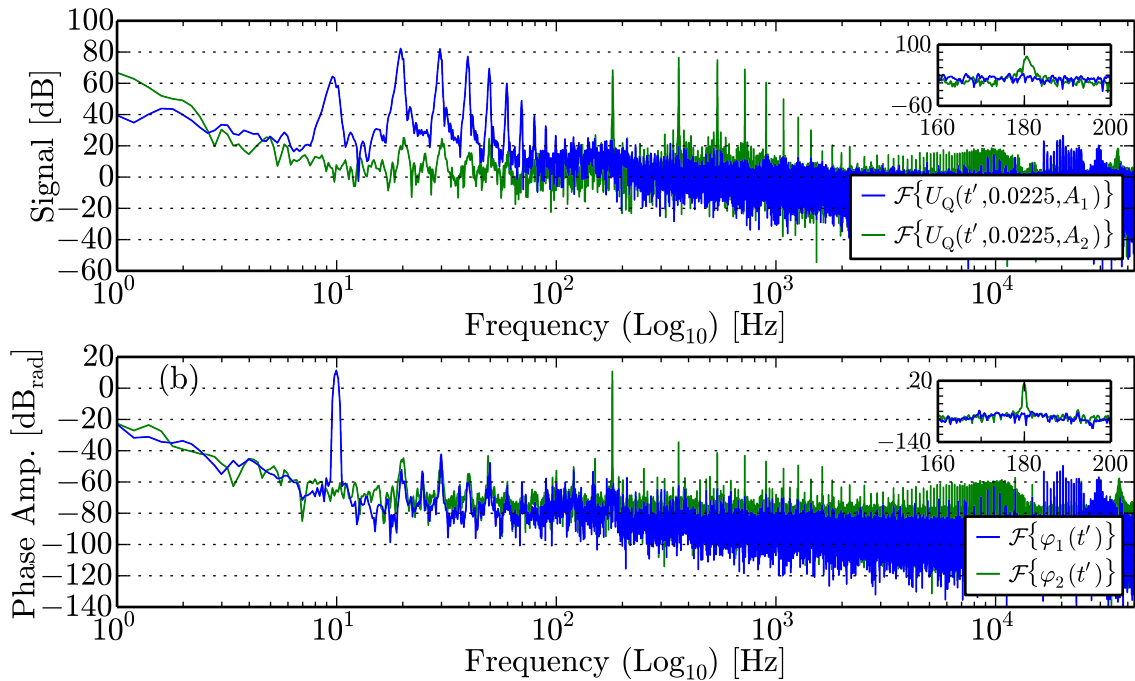


**Figure 6.14.:** Comparison of the Fourier transformed spectra (computed over 5s) of the complex quadrature signal of interferometer I1 and I2 in (a) and the resulting phase signals in (b). None of the corrections detailed in Sec. 6.2.5 were used and the spectra are drawn on a double logarithmic scale. In each plot the inset enlarges the peak at 180 Hz on a non-logarithmic frequency scale.

Fig. 6.14. It can be seen in Fig. 6.14(a) that the peaks at 20 Hz, 30 Hz and 40 Hz of the quadrature signal of interferometer I1 are also present in the quadrature signal of interferometer I2 with a reduction of the peak heights of approximately  $-60$  dB. It can furthermore be seen in the Fourier spectrum of the phase signals in Fig. 6.14(b) and in the inset there that no phase signal crosstalk at the fundamental frequencies 10 Hz and 180 Hz rises above the noise floor, yielding a phase signal crosstalk suppression of at least  $-70$  dB. Nevertheless, it can be seen in Fig. 6.14(b) that harmonic peaks of the 10 Hz test signal appear in the phase signals at frequencies of 20 Hz, 30 Hz and 40 Hz at approximately equal peak heights for both I1 and I2.

Using the data available, the origin of the harmonic peaks at 20 Hz, 30 Hz and 40 Hz in the phase signal Fig. 6.14(b) cannot be deduced. These could result from quadrature signal crosstalk or could genuinely be present due to physical crosstalk. Thus, it is not clear whether the harmonic peaks in the quadrature signal for I2, visible in Fig. 6.14(a), are solely caused by direct quadrature crosstalk or are also the result of a genuine phase signal change. Nevertheless, the available data is sufficient to conclude that the quadrature signal crosstalk suppression  $S_{\text{cr}}$  does not exceed  $-60$  dB. This limit value for the upper quadrature crosstalk suppression  $S_{\text{cr}}$  is entirely consistent with the predictions for the baseband suppression  $S_{\text{bb}} = S_{\text{cr}} \approx -55$  dB to  $S_{\text{bb}} = S_{\text{cr}} \approx -85$  dB due to the presence of quantisation errors that result from the discussion in Sec. 6.2.4 for the processing bitwidths  $b$  between 8 and 9 bit that were determined earlier. In general, the values for  $S_{\text{cr}}$  achieved here are at least an order of magnitude better than the quadrature signal crosstalk suppression determined for the CDM technique in Fig. 5.22. For phase signal crosstalk, as detailed in App. D.3, the magnitude of crosstalk is also dependent on the effective power levels of the individual interferometers involved and, importantly, the resulting crosstalk levels in the phase signals are highly dependent on the temporal variations of the phase signals involved. Particularly due to the latter point it comes as no surprise that no direct crosstalk in the phase signals can be observed to rise above the respective noise floor in Fig. 6.14(b) for the 10 Hz peak and for the 180 Hz peak in the inset, confirming that direct phase signal crosstalk stays  $\leq -70$  dB.

**Residual Measurements** Often in prior work on the assessment of cyclic errors in precision interferometry, such as McRae *et al.* [142], a very linear movement is induced experimentally and cyclic errors are determined by subtraction of the measured phase signal from the assumed linear phase change. Furthermore, the amplitude of the complex quadrature signal can be employed to detect cyclic errors [251], as was also used in this work in Fig. 6.11, where the complex quadrature signal amplitude was averaged into angular sectors. However, the former approach is based on the assumption of linear movement, while the latter approach assumes that the quadrature amplitudes remain constant, apart from the variations induced by the cyclic errors themselves, requiring constant effective powers. In the nested MZ setup, as discussed in the previous section, the possibility of measuring signals in two ways and subtracting them to obtain the residual signal permits a further method of assessing the linearity of the measurements that does not rely on any assumptions of linear movement or constant amplitudes. This measurement can thus serve as an independent verification of the cyclic errors determined in Fig. 6.11(d) and will also

be used here to investigate the effect of changing the window width parameter  $\sigma$  and the influence of the corrections described in Sec. 6.2.5.

In this approach, the residual phase signal  $\varphi_r(t')$  of Eq. (6.16), with its mean removed, is averaged over time and plotted on a two dimensional map as a function of the phases of PZT A (taken from I1) and PZT C (taken from I2). As can be seen in the setup in Fig. 6.7, the signal from PZT C provides the offset phase to the inner, differential interferometer excited by PZT A and thus all possible phase combinations that can occur in the nested MZ interferometer are covered if both PZT A and C have peak-to-peak phase excitations  $> 2\pi$  and are not synchronous to each other. The maximum absolute residual values occurring in these maps yields an upper limit on the cyclic errors occurring in the combined system of the three constituent interferometers. This value corresponds to the sum of the maximum cyclic error amplitudes over all three constituent interferometers. This method assumes that the previously discussed slow polarization drifts can be neglected, which is deemed acceptable as the measurements are taken in quick succession.

The results of these measurements are shown in Fig. 6.15, where the residual measurements described above, recorded over 25s, are binned and averaged into  $20 \times 20$  phase sectors. Figs. 6.15(a) and (b) show these maps for  $\sigma = 0.0075$  and  $\sigma = 0.0225$ , respectively, in each case both with and without using the corrections of Sec. 6.2.5. The residuals in Fig. 6.15(a) for  $\sigma = 0.0075$  are shown as an example of the occurrence of strong cyclic errors, with maximum residual absolute values up to 0.38 rad. In contrast, Fig. 6.15(b) shows the maps corresponding to the optimal choice of  $\sigma$  of approximately 0.0225. Here the maximum residual absolute values are 3.1 mrad and 4.4 mrad for the cases with and without corrections, respectively, and the maps exhibit complex patterns that cannot be straightforwardly interpreted but are repeatable. Finally, Fig. 6.15(c) compares the maximum residual absolute values obtained in this way over a wide range of the window width parameter  $\sigma$ . It can be seen that the best choice of  $\sigma$  for the present interferometric configuration is approximately  $\sigma = 0.0225$  for both corrected and non-corrected data. Both data

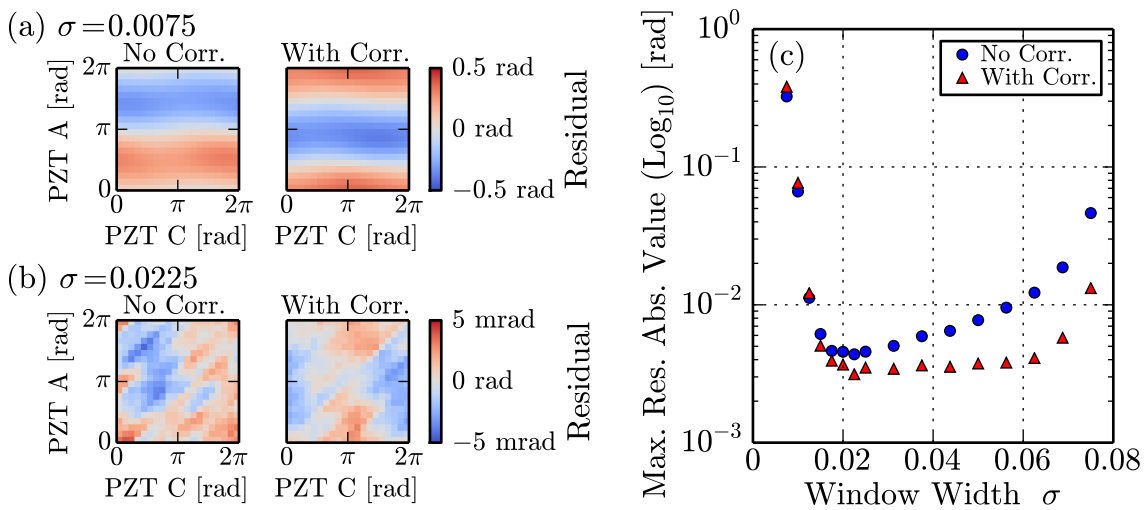


**Figure 6.15.:** Residual maps for the cases of (a)  $\sigma = 0.0075$  and (b)  $\sigma = 0.0225$ , note the different colourbar scaling, are shown both with and without corrections according to Sec. 6.2.5. (c) plots the maximum residual absolute values of these maps over a wide range of the width parameter  $\sigma$ .



sets show a strong increase in non-linear behaviour for  $\sigma < 0.015$ , which can be explained by the strong widening of the baseband suppression peaks in Fig. 6.3 for very small  $\sigma$ . For the case with corrections, a remarkably flat behaviour of the maximum residual absolute values exists up to  $\sigma = 0.06$ , confirming the quality of the applied corrections. Above  $\sigma = 0.06$  the cyclic error amplitudes rise in both cases due to the increase in baseline power also evident in Fig. 6.3. Nevertheless, for a value of  $\sigma = 0.0225$  it can be seen that even in the case without any corrections, very linear measurements with a sum of all cyclic error amplitudes of  $\pm 4.4$  mrad, dropping to  $\pm 3.1$  mrad with corrections applied, can be performed. For the case with corrections, the sum of the maximum cyclic error amplitudes of the three constituent interferometers can be determined to be  $\pm 2.4$  mrad from Fig. 6.11(d). This is less than the value of  $\pm 3.1$  mrad extracted from Fig. 6.15 from the residual maps. This discrepancy could be due to insufficient noise averaging, increasing the apparent maximum residual values in the residual maps, or due to an inadvertent change or drift in the experimental conditions, as this experiment was performed on a separate occasion. However, these values are still on the same order of magnitude and therefore these residual measurements independently confirm the high linearity values that can be obtained with the presented SFM technique as well as the wide range of the width parameter  $\sigma$  for which the technique can be made to work.

**Detuning Tolerance** In the final experiment for the nested MZ configuration, the robustness of the obtainable linearity behaviour is tested against detuning of the demodulation parameters. Here, the demodulation phase carrier amplitude,  $A_d$ , and the signal processing delay,  $\tau_{sp}$ , were detuned from their optimal positions, for all three constituent interferometers simultaneously, and the resulting maximum residual absolute values were determined using the same method employed to obtain Fig. 6.15. For each interferometer,  $A_d$  was altered by values of  $[-2, 0, 2]$  rad and  $\tau_{sp}$  was altered by values of  $[-10, 0, 10]$  ns, resulting in nine detuning parameter combinations [a,...,i] at locations that are illustrated in the inset of Fig. 6.16(a). The window width parameter  $\sigma = 0.0225$  was kept constant throughout. As this

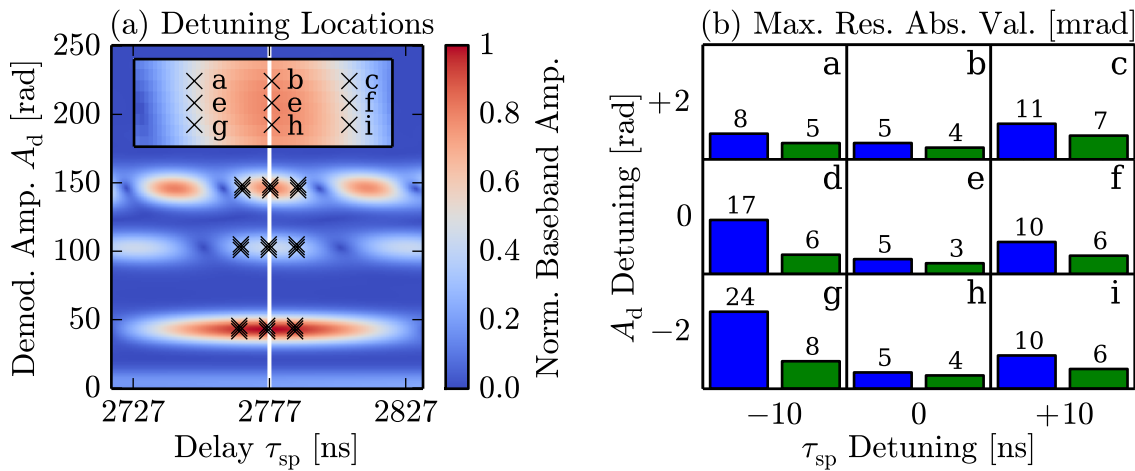


**Figure 6.16.:** The locations of the 9 parameter combinations [a,...,i] are shown on the demodulation parameter map in (a), drawn analogous to Fig. 6.10(a). The resultant maximum residual absolute values are compared in (b), where uncorrected and corrected results according to Sec. 6.2.5 are represented by the blue and green bars, respectively, with values in units of mrad also given.

experiment was performed on a separate occasion from the previous determination of the demodulation parameter map, the signal processing delay  $\tau_{sp}$  had changed by 2 ns compared to Fig. 6.10(a). This is a typical example of instrumental drift observed in  $\tau_{sp}$  and is significantly smaller than the chosen maximum variation of  $\tau_{sp}$  of  $\pm 10$  ns used for this experiment. Also no significant drifts of the phase carrier amplitudes  $A_k$  were ever observed in practice, therefore this experiment can be considered a worst-case scenario. The resulting maximum residual absolute values are illustrated in Fig. 6.16(b) for the nine detuning parameter combinations used. It is evident that the signals where the corrections of Sec. 6.2.5 have been applied are generally more robust against detuning of the signal processing parameters than those measurements without corrections. Nevertheless, while there is a considerable increase in the magnitude of cyclic errors, up to 24 mrad in parameter combination g, there is never a complete breakdown of linearity and the scheme can thus be considered reasonably robust against detuning, especially when the corrections discussed are applied.

## 6.4. Single Interferometer Noise Investigation

Analogous to the single reflector noise measurements performed in Sec. 5.5.1 for the CDM technique, the quadrature noise and phase noise behaviour of the SFM technique presented in this chapter is investigated for the case where only a single interferometric signal source is present. Again, this is done for a variation of effective power at constant OPD and for a variation of OPD at constant effective power. The setup used for this investigation is the single MZ interferometer illustrated in Fig. 6.17. Here, various fibre sections of physical length 38 cm and 89 cm can be inserted between the two FC/PC connectors to alter the OPD of the interferometer. Also, the effective power of the measurement can be attenuated, while keeping the LO power stable, by using the in-fibre attenuator within one arm of the interferometer. In this section, only data corrected according to Sec. 6.2.5 is used and all noise standard deviation values were computed for noise frequencies between 1 kHz and the quadrature cut-off frequency  $f_{Q,co} = 43$  kHz, removing the influence of low-frequency  $1/f$  noise. In all other aspects, the experimental parameters and processing implementation are similar to the previous nested MZ setup experiment of Sec. 6.3, except for the use

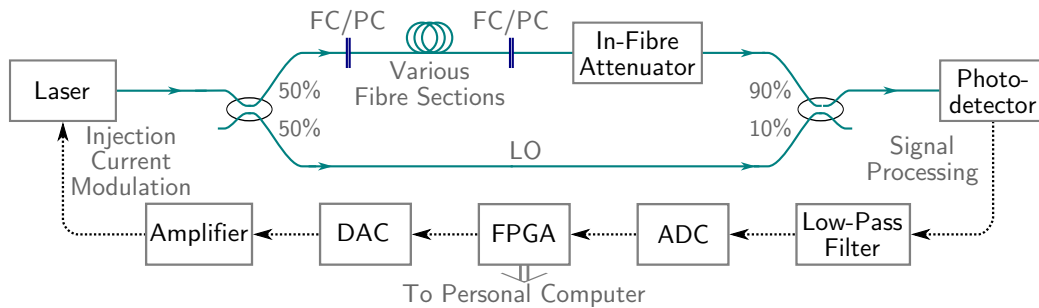


**Figure 6.17.:** The experimental setup for the noise investigation using a single MZ interferometer, allowing changes to the OPD by inserting fibre sections between the two FC/PC connectors and permitting attenuation of the effective power using an in-fibre attenuator within the interferometer path, where the signal processing is similar to the previous nested MZ experiment of Fig. 6.7.



of the window width parameter  $\sigma = 0.025$  instead of  $\sigma = 0.0225$ . This was done for reasons of conceptual simplicity, because it was shown in Fig. 6.15(c) that for corrected data this leads to no significant change in linearity performance.

**Effective Power Dependence** In Chap. 5, the measurement of the power dependence of the noise shown in Fig. 5.19 relied on external power measurements using a power meter. This is only approximate as the simple measurement of the return and LO power neglects any variations in visibility, whilst direct visibility measurements of the interferometric signals are difficult to obtain for low power signals. Instead, in this chapter, the effective power, which is directly obtainable from the signal processing output but in an a priori unknown unit, is calibrated to obtain physical power units. This calibration requires a dedicated setup, with the method and results detailed in App. F. This was then used in the following to determine the effective power  $P_{\text{eff},1}$  of the single MZ interferometer illustrated in Fig. 6.17 for a constant OPD  $\eta_1 = 0.92$  m under various levels of power attenuation.

The results of this procedure are shown in Fig. 6.18(a), where the dependence of the normalised amplitude noise standard deviation  $\sigma_{\text{amp,norm}}$  and the apparent phase noise standard deviation  $\sigma_{\text{phase}}$  are plotted as a function of the effective power  $P_{\text{eff},1}$  on a double logarithmic scale. Fig. 6.18(a) also plots the direct phase noise standard deviation  $\sigma_{\text{phase,direct}}$ , representing phase noise caused by laser frequency noise which was corrected for excess phase noise caused by quadrature noise as described in App. D.1. On the secondary x-axis of Fig. 6.18(a), the processing bitwidth  $b$ , corresponding to  $\pm 2^b$  quantisation levels, is also shown. Because the processing bitwidth for small effective power levels is difficult to determine, the direct proportionality between  $b$  and effective power, confirmed for large values of  $P_{\text{eff},1}$  is

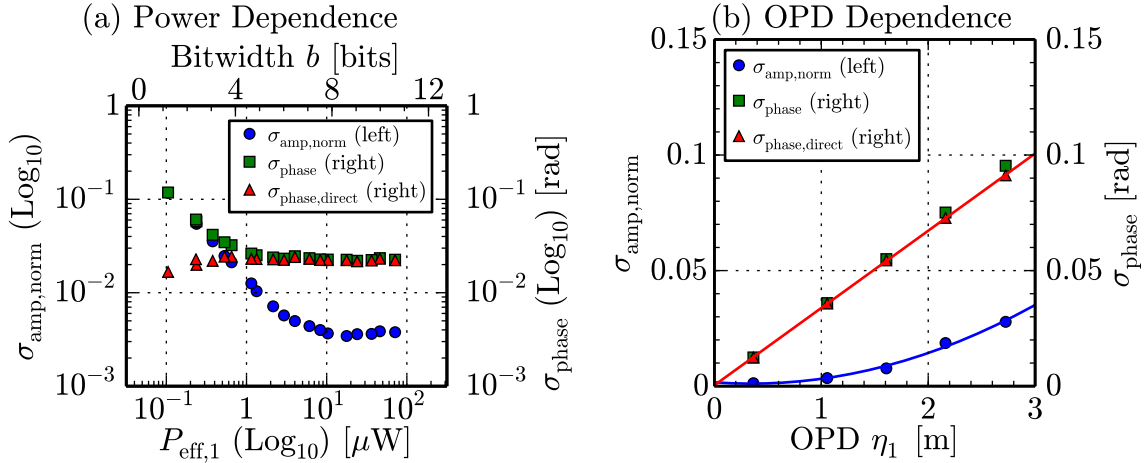


**Figure 6.18.:** For the single interferometer setup of Fig. 6.17, the measurement of the noise dependence on effective power at a constant OPD of  $\eta_1 = 0.92$  m is shown in (a), while (b) shows the noise dependence on the OPD at a constant effective power of  $P_{\text{eff},1} = 40 \mu\text{W}$ . In both (a) and (b), the normalised amplitude noise standard deviation  $\sigma_{\text{amp,norm}}$  is drawn on the primary y-axis and the apparent phase noise standard deviation  $\sigma_{\text{phase}}$  as well as the direct phase noise standard deviation  $\sigma_{\text{phase,direct}}$ , corrected for the excess phase noise according to App. D.1, are plotted on the secondary y-axis. In (a), all axis are on a logarithmic scale and the secondary x-axis additionally shows the estimated processing bitwidth  $b$ . In (b), fits of  $\sigma_{\text{amp,norm}}$  and  $\sigma_{\text{phase,direct}}$  according to Eq. (5.22) are drawn using continuous lines of the respective colour. In both plots, the noise standard deviation values were computed for frequencies between 1 kHz and 43 kHz.

extrapolated for small values of  $P_{\text{eff},1}$  to obtain this axis scaling. This extrapolation, however, does introduce some uncertainties and the processing bitwidth at small values of  $b$  can only be considered an approximation.

It can be seen in Fig. 6.18(a) that for large effective powers, a phase noise dominated region exists, because both the apparent phase noise  $\sigma_{\text{phase}}$  and the direct phase noise  $\sigma_{\text{phase,direct}}$  standard deviation levels are flat and show no dependence on the effective power there. In Fig. 6.18(a), the amplitude noise  $\sigma_{\text{amp,norm}}$  initially shows a flat baseline for large  $P_{\text{eff},1}$  and then starts to rise from its baseline value at effective powers of  $\approx 10 \mu\text{W}$ . Similar to previous discussions for the CDM technique in Sec. 5.5.1, it is thought that for large effective powers, amplitude noise is dominated by aliased high-frequency laser phase noise [244], because, as also discussed below,  $\sigma_{\text{amp,norm}}$  shows a clear OPD dependence in Fig. 6.18(b). It is, however, unknown whether the observed rise in  $\sigma_{\text{amp,norm}}$  below  $\approx 10 \mu\text{W}$  is solely caused by the onset of other physical noise sources, such as shot, electronic or laser intensity noise or whether signal processing effects, such as quantisation, also play a role.

In Fig. 6.18(a), for low effective powers, the amplitude noise  $\sigma_{\text{amp,norm}}$  can be seen to rise proportionally with the decrease in  $P_{\text{eff},1}$ . Similar to the results for the CDM technique in Fig. 5.19(c), it can be seen that  $\sigma_{\text{phase,direct}}$  stays virtually constant, regardless of a rise in  $\sigma_{\text{amp,norm}}$ . Thus any apparent increase in laser phase noise can be entirely attributed to excess phase noise caused by quadrature noise, as detailed in App. D.1. The reason for the very slight curvature in  $\sigma_{\text{phase,direct}}$  at very low values of  $P_{\text{eff},1}$  is unclear but could be due to shortcomings of the validity of the assumptions for the model of App. D.1. It was also verified that spurious phase unwrappings, as discussed in App. D.2, are not present even for the lowest values of  $P_{\text{eff},1}$ , confirming that quality phase measurements can still be obtained even for effective powers as low as  $0.1 \mu\text{W}$ . In summary, it can be seen from Fig. 6.18(a) that the SFM technique can be used for measurements at very low effective powers and that for large effective powers measurements are dominated by laser phase noise.

**OPD Dependence** The results for the OPD dependence of the single interferometer setup in Fig. 6.17 at a constant effective power of  $P_{\text{eff},1} = 40 \mu\text{W}$  are then shown in Fig. 6.18(b). This value for  $P_{\text{eff},1}$  is well within the phase noise dominated region, as established in Fig. 6.18(a). Again,  $\sigma_{\text{amp,norm}}$  is plotted on the primary y-axis and  $\sigma_{\text{phase}}$  and  $\sigma_{\text{phase,direct}}$  are plotted on the secondary y-axis. A linear least square fit of  $\sigma_{\text{phase,direct}}$  and a quadratic least square fit of  $\sigma_{\text{amp,norm}}$  against the OPD  $\eta_1$ , both according to Eq. (5.22), are also shown in Fig. 6.18(b). This is in analogy to the plots of the single reflector experiment for the CDM technique shown in Fig. 5.18(c). It can be seen in Fig. 6.18(b) that the linear fit of  $\sigma_{\text{phase,direct}}$  is in excellent agreement with the expected proportional OPD dependency of  $\sigma_{\text{phase,direct}}$ , with an offset value  $Y_0$  in Eq. (5.22) of only  $Y_0 = 0.39 \text{ mrad}$ . The slope factor  $Y_1$  for this fit is  $Y_1 = 0.033 \text{ rad m}^{-1}$  for phase noise frequencies between 1 kHz and 43 kHz, which corresponds to a phase noise slope value of  $0.16 \text{ mrad} \cdot \text{Hz}^{-0.5} \cdot \text{m}^{-1}$ . This slope value is more than a factor of 7 higher than the value of  $0.022 \text{ mrad} \cdot \text{Hz}^{-0.5} \cdot \text{m}^{-1}$  extracted from Fig. 5.18(c) for the CDM technique. It is thought that this significant increase in direct phase noise is due to the strong injection current modulation used in the SFM technique. One plausible explanation is that the laser driver that was used simply cannot control

rapidly changing injection currents as well as the stationary injection currents that were used in the CDM technique, therefore increasing current noise and thus laser phase noise. Furthermore, it was also observed that the laser phase noise slope can vary for different measurements. For instance, the value of  $\sigma_{\text{phase,direct}}$  extracted from Fig. 6.18(a) at  $P_{\text{eff},1} = 40 \mu\text{W}$  is  $\sigma_{\text{phase,direct}} = 0.023 \text{ rad}$ , where the OPD for that measurement was  $\eta_1 = 92 \text{ cm}$ . For the same OPD value, Fig. 6.18(b) would yield a phase noise value of  $\sigma_{\text{phase,direct}} = 0.031 \text{ rad}$ . These measurements were conducted over the space of several days with otherwise identical parameters but show an increase in phase noise of 35%. Again a plausible explanation is that it is caused by the laser driver, but to confirm this will require further investigation.

The clear OPD dependence of amplitude noise visible in Fig. 6.18(b), which echoes the finding for the CDM technique in Fig. 5.18(c), indicates that the origin of the quadrature noise causing the amplitude noise is fundamentally related to laser phase noise, with aliased high-frequency laser phase noise [244] the most likely origin, as was discussed previously in Sec. 5.5.1. The particular reasons for a quadratic OPD dependence of the quadrature noise, clearly displayed in both Fig. 5.18(c) for the CDM and in Fig. 6.18(b) for the SFM technique, rather than a linear dependence is unknown. One possible explanation for the SFM technique is that, as the OPD increases, both the laser phase noise itself and, due to the proportional increase in the phase carrier amplitude, the number of the evaluated Bessel terms of Eq. (3.9) increases. Therefore, when aliased high-frequency phase noise is assumed as the cause of the quadrature noise, both the number of carriers evaluated that can introduce aliased high-frequency phase noise and the magnitude of the phase noise itself increases, which would lead to a quadratic OPD dependence of the quadrature noise. However, it is not obvious how to extend this theory to explain the quadratic OPD dependence in the CDM technique. Therefore, an investigation of the exact origins of the observed quadrature noise is a high priority for future work and a dedicated experiment will be discussed in Sec. 6.6.1. In summary, the results of Fig. 6.18(b) show that the OPD dependence of direct phase noise in a single interferometer appears reasonably well understood, however, the origins of the quadrature noise, in particular its quadratic OPD dependence will require further in-depth analysis.

## 6.5. Fibre Segment Interferometry Experiment

In this section, the SFM technique that was described and characterised in the previous sections is applied to the FSI approach that forms the main theme of this thesis, demonstrating the interrogation of six fibre segments spanned by seven FBG-based in-fibre partial reflectors.

### 6.5.1. Implementation

**Setup** When used for FSI, the SFM technique permits down-lead insensitive interrogation in a self-referencing configuration (see also Sec. 3.1.3). This effectively combines the simplicity and the physical down-lead insensitivity of the direct inter-

ferometric FSI configuration of Fig. 4.1(a) with the practical advantages arising from heterodyne gain for the choice of in-fibre reflector and the avoidance of undesired path combinations of the common LO configuration of Fig. 4.1(c). This is illustrated by the setup in Fig. 6.19(a), where the common LO is provided by the Fresnel reflection of the cleaved fibre tip at the end of the FSI sensing fibre and where the fibre lead between the interrogation unit and the sensing fibre can be of arbitrary length. The fibre lead is thus completely down-lead insensitive, which was also verified in practice by introducing manual fibre movements.

In the setup of Fig. 6.19(a), the sinusoidally modulated light leaving the laser diode is guided by a fibre-optic circulator to the FSI sensing fibre and the return signals from the seven FBG-based partial in-fibre reflectors and the fibre tip reflection providing the common LO are directed by the circulator to the photo detector. In this setup, the laser emission wavelength is also temperature tuned, with the temperature-wavelength tuning characteristic of the laser detailed in App. B.1. Again, all experimental parameters and the FPGA processing implementation were similar to the previous nested MZ setup experiment of Sec. 6.3, except for the use of the window width parameter  $\sigma = 0.025$ . The details of the signal processing equipment are not drawn in Fig. 6.19(a) but are similar to Fig. 6.7, with the corrections of Sec. 6.2.5 used throughout. Analogous to Fig. 6.9(c), a typical photo detector signal, with the intensity modulation corrected according to Sec. 6.2.5, is shown in Fig. 6.20(a), along with the window function used. Here the recorded signal can be seen to extend over approximately  $\pm 200$  quantisation levels, which, assuming equal distribution over all seven reflectors, corresponds to a processing bitwidth  $b$  of  $b \approx 5$  bit or  $\approx \pm 2^5$  quantisation levels per reflector. In Fig. 6.19(a), the FSI sensing fibre is attached to a solid steel rod (type 316 stainless steel, length: 78.2 cm, diameter: 1.9 cm) using an epoxy adhesive. It can be seen in the photograph in Fig. 6.19(b) that the rod is freely suspended at the side of an optical table and that, as illustrated in Fig. 6.19(a), a hammer can be used to excite the rod.

In this setup, the FBG-based in-fibre partial reflectors were separated by physical distances of 12.5 cm, setting the segment length  $l_s$  also equal to  $l_s = 12.5$  cm. Additionally, an offset distance of  $1.5l_s = 18.75$  cm between the LO and the first

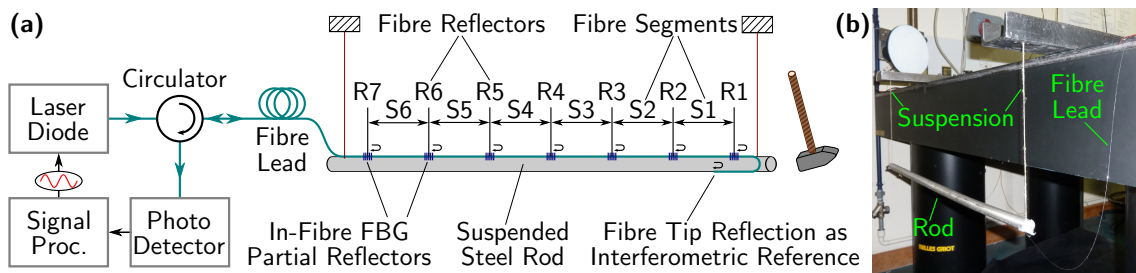


**Figure 6.19.:** The experimental setup used for the FSI experiment is illustrated in (a). Sinusoidally optical frequency modulated light leaving the laser diode is guided by a fibre-optic circulator and a fibre lead to the FSI sensing fibre, where seven FBG-based in-fibre partial reflectors span six fibre segments and the interferometric reference is taken from the cleaved fibre tip. The return light is then guided to the photo detector and the resulting signals processed. The sensing fibre is attached to a freely suspended stainless steel rod, which can be excited using a hammer stroke at the end of the rod, with a photograph of the suspended rod also shown in (b).

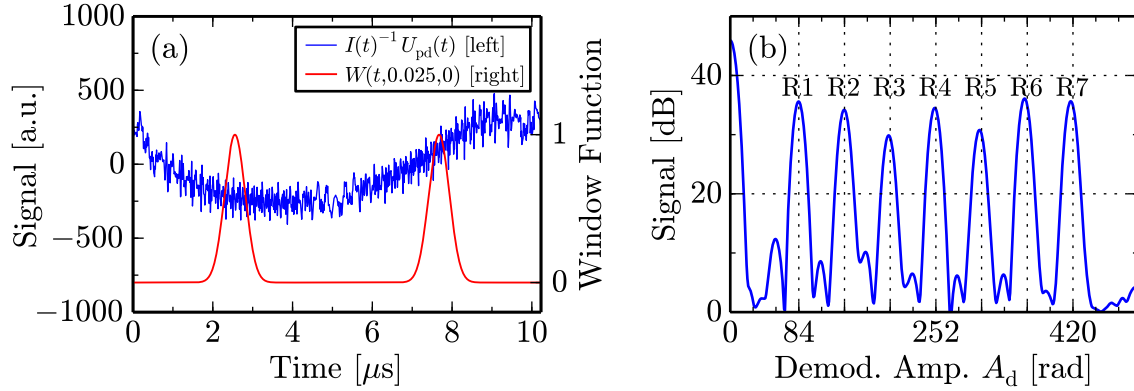


**Figure 6.20.:** Analogous to Fig. 6.9(c), (a) shows a plot of the photo detector signal corrected for intensity modulation according to Sec. 6.2.5 along with the window function used. (b) then shows the OPD dependence of the return signals as a function of demodulation carrier amplitude  $A_d$  analogous to the right panels in Fig. 6.10, with the seven signals R1 to R7 clearly identifiable.

reflector R1 was used. The segment length  $l_s = 12.5$  cm results in a phase carrier amplitude separation  $A_{k+1} - A_k$  of 56 rad between the return signals from adjacent reflectors. This is approximately a factor two more than the value of  $A_{\min}$  required according to the spatial resolution calculation in Sec. 6.2.3 for a specified baseband suppression values of  $S_{\text{bb,max}} = -50$  dB at  $\sigma = 0.025$ . While the common LO configuration is generally tolerant to undesired path combinations, as discussed in Sec. 4.1, the additional offset of  $1.5l_s$  was introduced to interleave any remaining undesired signals due to direct interference between reflectors with the desired signals due to interference with the common LO. Analogous to the right panels in Fig. 6.10, Fig. 6.20(b) plots the OPD dependence of the quadrature signal amplitude as a function of the demodulation carrier amplitude  $A_d$ . Here, it can be seen how undesired peaks due to direct interference between reflectors appear at integer multiples of 56 rad, while the first desired reflector peaks, arising from interference with the common LO, appears at  $1.5 \cdot 56$  rad = 84 rad, with the remaining desired reflector peaks then appearing at subsequent increments of 56 rad at 140 rad, 196 rad, etc. In Fig. 6.20(b), the amplitude of the highest undesired peak at 56 rad is  $\approx 13$  dB, while the amplitude of the lowest desired peak at R3 is  $\approx 30$  dB. While some successful phase measurements could still be carried out with this level of crosstalk, the simple avoidance of any crosstalk from direct interference between reflectors by spatially offsetting the desired and undesired interferences in this way could prove to be valuable for applications where high linearity is needed. However, this procedure comes at the price of an increase in the minimally permissible spatial separation between reflectors by a factor of two. A further option to increase suppression of signals from undesired path combinations and also to improve general signal strengths would be to increase the reflectivity of the fibre tip from its current level of 3.5%, due to Fresnel reflection, by using a fibre-end mirror or reflective coating.

**FBG Inscription** In general, as discussed in Sec. 4.1, FBGs used as in-fibre partial reflectors in FSI need to be sufficiently broadband to return signals under all conceivable strain and temperature conditions, typically requiring a spectral width of at least 1 to 2 nm. Here, chirped gratings offer a very broad return spectrum, however,

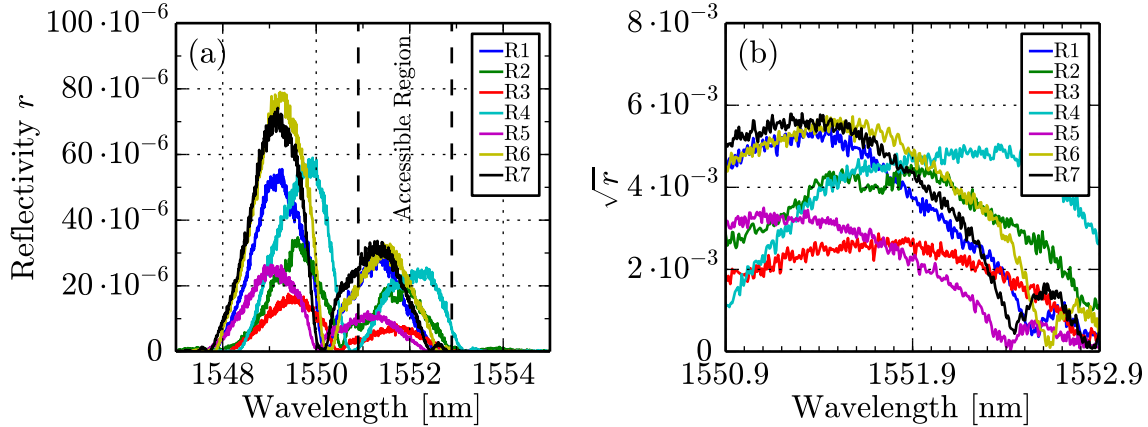


**Figure 6.21.:** The reflectivity spectra of the seven FBGs R1 to R7, measured by the Luna OBR 4400 Reflectometer, are shown in (a). Here, a region of spectral width 2 nm that is accessible to wavelength tuning of the laser diode is marked. (b) then shows the spectra of the square root of the reflectivity  $\sqrt{r}$  over this region.

the point of reflection moves with changes in strain or temperature in a chirped grating [65], which would introduce an additional OPD change into the segment phase signals, making chirped gratings unsuitable for FSI. For non-chirped FBGs, the spectral width generally broadens with decreasing gauge length. The production of non-chirped broadband FBGs of suitable quality for FSI, with a gauge length of  $16 \mu\text{m}$ , a full-width half maximum spectral width of 50 nm and a reflectivity of  $r = 10^{-4}$  has also been demonstrated using hydrogenated standard SMF-28 fibre [94], where hydrogenation yielded the necessary high index modulation of  $1.2 \cdot 10^{-4}$  to achieve relatively high reflectivity over a large spectral width.

The non-chirped FBGs used here were inscribed<sup>1</sup> using a frequency-quadrupled ND-YAG laser emitting at a wavelength of 266 nm on non-hydrogenated SMF-28 fibre. A slit of width of 1.5 mm was placed 24 cm from the phase mask with the fibre 2 mm behind the phase mask. During FBG inscription peak growth was monitored live using the current SFM implementation. The final FBG spectra for reflectors R1 to R7 were then measured using a Luna OBR 4400 Reflectometer and are shown in Fig. 6.21(a). These spectra reach peak reflectivities  $r$  of up to 0.008% and show two distinct regions of  $\approx 2$  nm spectral width each, separated by a region where  $r$  almost drops to zero. Generally, the maximum reflectivities for the spectra of reflectors R1 to R7 vary by a factor of 5 and the reflectivity in the upper spectral region at wavelengths above 1550 nm is reduced by more than a factor of 2 compared to the lower spectral region. Nevertheless, a region of 2 nm width, marked in Fig. 6.21(a), in the upper spectral region is accessible to the experiment through temperature tuning of the laser emission wavelength. The spectrum of the square root of the reflectivity  $\sqrt{r}$  over this region is also plotted in Fig. 6.21(b), where  $\sqrt{r}$  is proportional to the effective powers  $P_{\text{eff},k}$  measured by the SFM technique for the seven reflectors.

<sup>1</sup>The inscription of the FBG-based in-fibre partial reflectors was not considered part of this thesis on signal processing and the reflectors used in this experiment were manufactured by Dr. Ricardo Correia and Prof. Steve James



### 6.5.2. Linearity and Noise Measurements

**Linearity** The quadrature phasor traces resulting from an acoustic excitation of the steel rod, computed over 20 ms for the seven reflectors R1 to R7, are shown in Fig. 6.22(a) in the complex plane. Here, the quadrature amplitudes for the different reflectors vary by up to a factor of three and the resulting quadrature signals can be seen to be both circular and concentric (see also Sec. 3.1.4). In order to quantify the magnitude of any resulting cyclic errors, for each reflector, the angular average over 30 angular sectors is computed analogous to the previous treatment in Fig. 6.11. The results are shown in Fig. 6.22(b), where the fits of the angular averaged data for the seven reflectors with the model of Eq. (3.8) are shown using continuous lines. The data points for the measured angular averages, drawn using crosses, are only shown for reflector R7 to improve clarity, however, the spread of the data points displayed there is representative for the data spread of the other reflectors. It can be seen in Fig. 6.22(b) that the quadrature amplitude can vary by up to 0.8%, with both one-cycle and two-cycle non-linearities occurring. The angular errors calculated using Eq. (3.8) from the fitted quadrature amplitude data are then shown in Fig. 6.22(c), where angular error amplitudes of up to  $\pm 6.4$  mrad are reached. Compared to the previous nested MZ experiment in Fig. 6.11, this is an increase in the non-linearity error of approximately a factor of  $\approx 6$ . However, as was established in Sec. 6.5.1, the processing bitwidth  $b$  in this FSI experiment is only  $b \approx 5$  bits per reflector, a decrease of 3 bits relative to the case for the nested MZ experiment. Therefore, an increase in the cyclic error amplitudes of a factor of  $2^3 = 8$  is expected following the discussion in Sec. 6.2.4 due to the decrease in the number of available quantisation levels. This is close to the observed increase of a factor of  $\approx 6$  and therefore these results are entirely consistent with the order of magnitude calculations of Sec. 6.2.4.

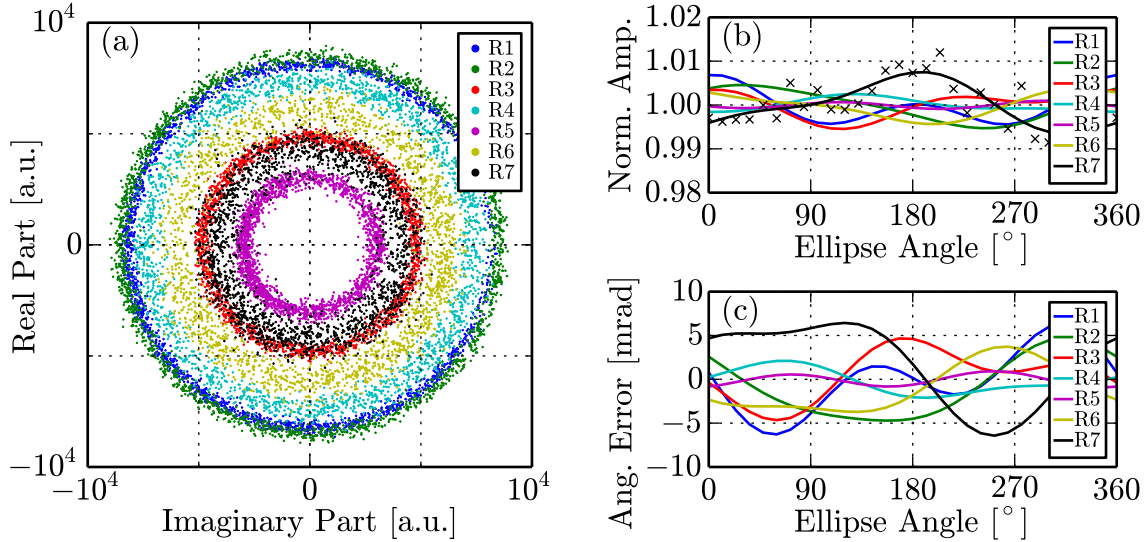


**Figure 6.22.:** The time traces of the complex quadrature signal for the seven reflectors R1 to R7 are shown in (a), recorded over a period of 20 ms during acoustic excitation of the steel rod. Analogous to Fig. 6.11(b) and (c), for each reflector R1 to R7, (b) plots the fits of the normalized quadrature amplitudes, averaged into 30 angular sectors, as a function of phasor angle of the complex quadrature signal according to the model of Eq. (3.8). Here, the measured angular averaged data is plotted using crosses, however, only for R7 to improve clarity. The non-linearity errors resulting from these fits are then drawn in (c).

**Noise Dependency on Interrogation Wavelength** It can be seen in Fig. 6.21(b) that the reflectivities of the FBGs vary considerably with wavelength. Therefore the noise behaviour is investigated as a function of the interrogation wavelength by tuning the laser diode temperature  $T_{LD}$ . The effective power  $P_{eff,k}$ , plotted as a function of  $T_{LD}$ , is shown in Fig. 6.23(a) for all seven reflectors R1 to R7. Here, the secondary x-axis is shown in wavelength units, where the values of  $T_{LD}$  is converted using the calibration measurement of App. B.1. When comparing the plot of the square root of the reflectivity in Fig. 6.21(b) with Fig. 6.23(a), a very strong similarity between the spectra measured using the Luna OBR 4400 Reflectometer and the spectra measured using the SFM technique can be observed, also indicating that the technique could, in principle, be used for wavelength-based FBG interrogation (see also Sec. 2.3) or for other intensity-based sensor concepts. However, due to a lack of cross-calibration the absolute wavelength scales differ by approximately 0.5 nm between Fig. 6.21 and Fig. 6.23(a). In this context, it is also interesting to note that the sinusoidal optical frequency modulation amplitude  $\Delta f_{opt} = 8.4$  GHz corresponds to a swept wavelength region about  $\pm 0.067$  nm, as shown in App. B.3. However, especially for small values of the window width parameter  $\sigma$  of Eq. (6.6), the effective location of most of the evaluated signal is near the optical frequency modulation centre frequency  $f_{opt,c}$  of Eq. (6.1) as visible in Fig. 6.1, therefore the effect of wavelength averaging of the spectra in the SFM technique is expected to be small relative to the wavelength sweep of  $\pm 0.067$  nm.

In Fig. 6.23(a), a working region of spectral width 1.3 nm has been defined and is marked using dashed lines, within which the effective power of every reflector stays above  $0.5 \mu\text{W}$ . When comparing Fig. 6.23(a) with Fig. 6.21(b), this value can be seen to correspond to a reflectivity of about  $r = 10^{-6}$  in the current experimental configuration. The value of  $P_{eff,k} > 0.5 \mu\text{W}$  was chosen as it can be seen in Fig. 6.18(a) to be at the transition between phase noise dominated and amplitude noise dominated

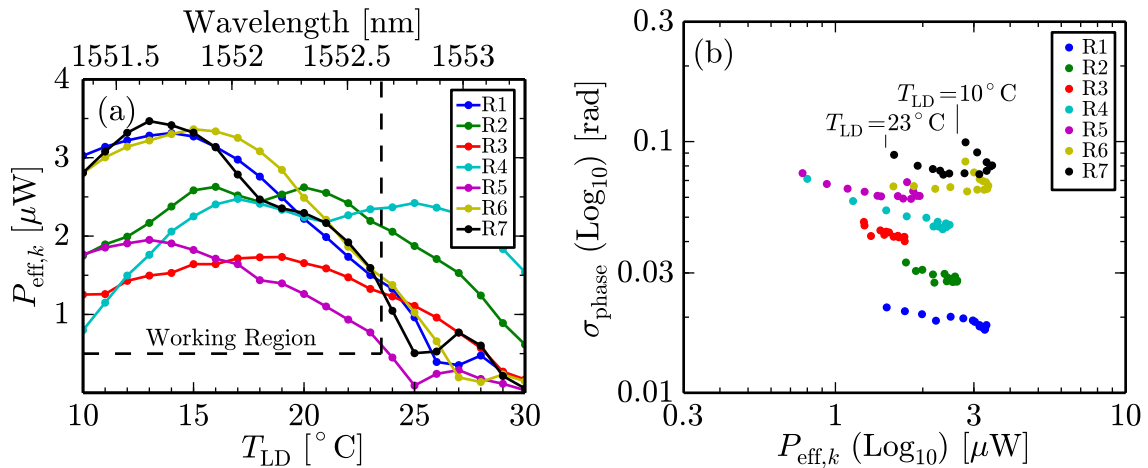


**Figure 6.23.:** The effective powers  $P_{eff,k}$  of the return signals as a result of wavelength tuning are plotted as a function of laser diode temperature  $T_{LD}$  in (a) for all seven reflectors R1 to R7, where the secondary x-axis was converted to wavelength units using the calibration measurement of App. B.1. In (a), a working region can be defined, marked using the dashed lines, where the effective power of all reflectors stays above  $0.5 \mu\text{W}$ . (b) then plots the apparent phase noise standard deviation  $\sigma_{\text{phase}}$  values, computed for noise frequencies for between 1 kHz and 43 kHz, for all data points within the working region of (a) on a double logarithmic scale.



behaviour for a single reflector. Fig. 6.23(b) then shows a scatter plot of the phase noise standard deviation  $\sigma_{\text{phase}}$  for every measurement within the working region in Fig. 6.23(a), again calculated for noise frequencies between 1 kHz and 43 kHz. It can be seen in Fig. 6.23(b) that while, overall, the apparent phase noise levels are approximately proportional to the OPD, with reflector R1 having the lowest phase noise levels and reflector R7 the largest, the  $\sigma_{\text{phase}}$  values also exhibit a U-shaped variation with the interrogation wavelength. This variation is larger in magnitude for the reflectors with larger OPDs. For reflector R7, data points at the borders of the working region are also marked in Fig. 6.23(b), where a sweep pattern is visible that is also echoed by the data points for the other reflectors. Interestingly, reflectors R1 and R7, which strongly differ in OPD but can be seen in Fig. 6.23(a) to have a very similar spectrum, exhibit very different levels of this additional U-shaped noise dependence on the interrogation wavelength in Fig. 6.23(b). This confirms the OPD-related origin of the U-shaped noise dependence and it can be concluded that reflectors at large OPDs generally appear to exhibit a more complex noise behaviour.

In order to further investigate the noise behaviour, the amplitude and phase noise standard deviation at specific interrogation wavelengths within the working region defined in Fig. 6.23(a) are analysed in line with the previous investigation for a single interferometer in Sec. 6.4. Plots of the OPD dependence of the noise are then shown in Figs. 6.24(a),(b), (c) and (d) for measurements where  $T_{\text{LD}}$  was set to  $[10^\circ\text{C}, 16^\circ\text{C}, 18^\circ\text{C}, 23^\circ\text{C}]$ , respectively. Figs. 6.24(a) to (c) additionally plot the linear least-square fits of  $\sigma_{\text{phase,direct}}$  according to Eq. (5.22) using a continuous line. The fits of  $\sigma_{\text{phase,direct}}$  can be seen in Figs. 6.24(a) and (b) to be in very good agreement with the expected proportionality of  $\sigma_{\text{phase,direct}}$  on the OPD  $\eta$ , however, an offset value to this fit emerges in Fig. 6.24(c) and in Fig. 6.24(d) the fit has deteriorated to such an extent that it is not drawn. In general, it has been verified that the deterioration of the fit of  $\sigma_{\text{phase,direct}}$  is of a gradual nature, where fits of  $\sigma_{\text{phase,direct}}$

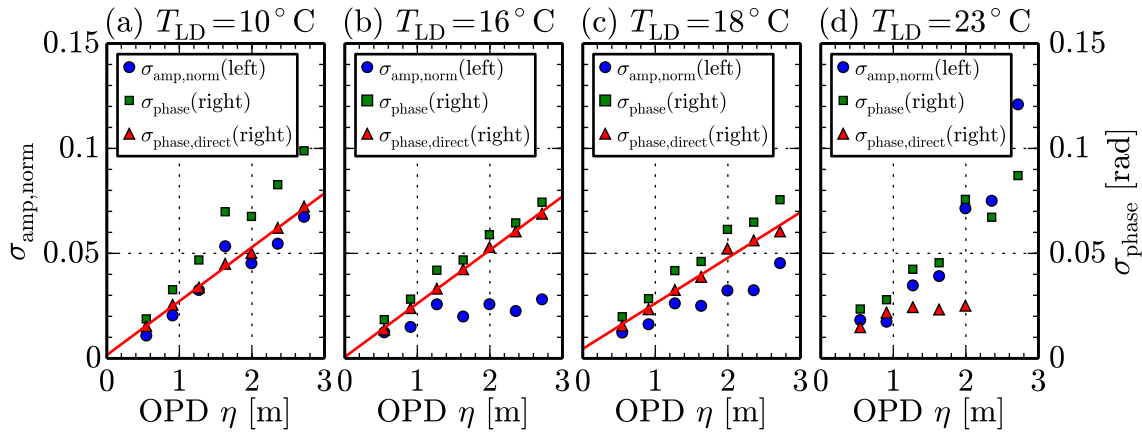


**Figure 6.24.:** Analogous to Fig. 6.18(b), the OPD dependence of the amplitude and phase noise is investigated for various interrogation wavelengths within the working region defined in Fig. 6.23(a). Here, again the normalised amplitude noise standard deviation  $\sigma_{\text{amp,norm}}$  is drawn on the primary y-axis and the apparent phase noise standard deviation  $\sigma_{\text{phase}}$ , as well as the direct phase noise standard deviation  $\sigma_{\text{phase,direct}}$ , corrected for the excess phase noise according to App. D.1, are plotted on the secondary y-axis. Also fits of  $\sigma_{\text{phase,direct}}$  according to Eq. (5.22) are drawn in (a), (b) and (c) using continuous lines. In all plots, the noise standard deviation values were computed for frequencies between 1 kHz and 43 kHz.

that are in good agreement with the expected proportionality on  $\eta$  can be found for all values between  $T_{LD} = 10^\circ\text{C}$  to  $T_{LD} = 17^\circ\text{C}$  and where the fit quality is successively getting worse for values above  $T_{LD} = 17^\circ\text{C}$ . It is also found that, overall, the amplitude noise standard deviations  $\sigma_{\text{amp,norm}}$  are at a minimum at  $T_{LD} = 16^\circ\text{C}$  and increase for other interrogation wavelengths in both directions, therefore the remaining experiments were carried out at this temperature setting. Here, a value of the slope factor  $Y_1 = 0.025\text{ rad} \cdot \text{m}^{-1}$  can be extracted from Fig. 6.24(b) for the OPD dependence of the reflector phase noise  $\sigma_{\text{phase,direct}}$ , which is comparable to the value of  $Y_1 = 0.033\text{ rad} \cdot \text{m}^{-1}$  for a single interferometer found in Sec. 6.4 when the level of variation of this value discussed there is considered.

It was noted before for the CDM technique in Sec. 5.5.2 that for multiple reflectors the noise behaviour is considerably more complex than for the case where only a single reflector is present and that quadrature noise can leak from reflectors, particularly for originating reflectors with large OPDs. A strong OPD dependency was also found in the previous discussion of Fig. 6.23(b), where the observed phase noise variation with interrogation wavelength increases with the OPD. Therefore, this complicated noise behaviour warrants further theoretical and experimental investigation because quadrature noise may ultimately determine the permissible reflector tolerances and may also limit the maximum number of FSI segments that can be multiplexed. A thorough understanding of this behaviour will therefore be very important for any practical application of the proposed FSI technique. Nevertheless, the results shown in Fig. 6.23(b) demonstrate that successful measurements for all seven reflectors over the entire working region of 1.3 nm spectral width can be conducted, with phase noise standard deviations in the individual reflectors signals below 0.1 rad for noise frequencies between 1 kHz and 43 kHz.

**Noise Dependency on Effective Power** The phase noise standard deviations  $\sigma_{\text{phase}}$ , again computed for noise frequencies between 1 kHz and 43 kHz, are shown in Fig. 6.25(a) for reflectors R1 to R7 as a function of the effective power  $P_{\text{eff},k}$ . Here, the necessary attenuation is introduced experimentally through fibre-bend loss in the fibre lead in Fig. 6.19 and, similar to Fig. 6.18(a), the effective power was calibrated according to the method detailed in App. F. This data was recorded for the laser diode temperature set to  $T_{LD} = 16^\circ$ . It can be seen in Fig. 6.25(a) that for each reflector R1 to R7, a unique plateau value exists, where, following the discussion in Sec. 6.4, it is thought that the signals on this plateau are phase noise limited. Plateau values for  $\sigma_{\text{phase}}$  range from 0.018 rad for R1 to 0.075 rad for R7. For small effective powers, the plateaus for all reflectors then asymptotically merge into a common line, where the phase noise standard deviation, similar to the behaviour shown in Fig. 6.18(a), increases proportionally with decreasing effective powers.

In Fig. 6.25(b), the  $\sigma_{\text{phase}}$  data is calculated for the six segment phase signals S1 to S6, obtained by subtracting the respective adjacent reflector signals. Here, the assigned effective powers  $P_{\text{eff,seg}}$  for the segment data points are the arithmetic mean of the effective powers of the participating reflectors. Similar to the discussion in Sec. 5.5.2 for the CDM technique, it can be seen in Fig. 6.25(b) that the calculation of the segment data goes some way in reducing the phase noise present in the reflector signals in Fig. 6.25(a) and that, similar to reflector data, the segment phase noise data

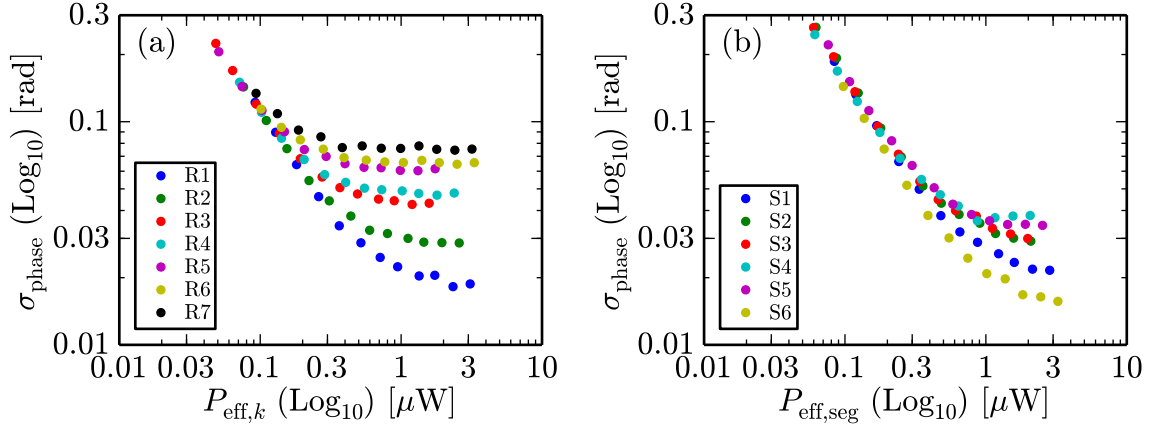


**Figure 6.25.:** A measurement at  $T_{LD} = 16^\circ$  of the dependence of the phase noise standard deviation  $\sigma_{\text{phase}}$  of the seven reflectors R1 to R7 on the effective power is shown in (a). (b) then plots the dependence of  $\sigma_{\text{phase}}$  on segment effective power  $P_{\text{eff,seg}}$  for segments S1 to S6. Here, the effective power is attenuated by introducing bend loss in the fibre lead in Fig. 6.19. In both plots the noise standard deviation values were computed for frequencies between 1 kHz and 43 kHz.

points asymptotically merge into a common line. However, because all segments have the same OPD, they should theoretically show equal phase noise standard deviations. Here, the expected value of  $\sigma_{\text{phase,direct}}$  can be determined from the slope factor of the reflector phase signals  $Y_1 = 0.025 \text{ rad m}^{-1}$  that has been extracted from Fig. 6.24(b). In this setup, the OPD of each segment is  $\eta = 2n_g l_s = 0.365 \text{ m}$  for a group index of refraction  $n_g = 1.46$  and a segment length  $l_s = 0.125 \text{ m}$ . Therefore, the intrinsic phase noise standard deviation for every segment phase signal, assuming the absence of other noise sources, should be as low as 0.0093 rad, while in Fig. 6.25(b), at maximum effective powers, segments S3 and S4 show  $\sigma_{\text{phase}}$  values up to 0.038 rad, four times the theoretical value. No straightforward explanation for this behaviour was found and imperfect suppression of the phase noise in the segment signals should be investigated as part of the previously mentioned investigation into the noise behaviour for multiple reflectors. Nevertheless, it was confirmed by this measurement that at  $T_{LD} = 16^\circ\text{C}$  and without attenuation, the noise behaviour is phase noise limited. Also, for the measurement at maximum effective power,  $\sigma_{\text{phase}}$  values in the segment data do not exceed values of 0.038 rad for noise frequencies between 1 kHz and 43 kHz, resulting in equivalent segment phase noise levels below  $0.19 \text{ mrad} \cdot \text{Hz}^{-0.5}$ .

### 6.5.3. Speed-of-Sound Measurements

In the final experimental section of this chapter, demonstration measurements are presented that confirm the usefulness of the SFM technique for high-speed FSI strain measurements. Here, a hammer is used to acoustically excite the freely suspended stainless steel rod, as illustrated in Fig. 6.19, and the FSI system is then used to determine the speed-of-sound  $v_s$  in the rod employing two independent methods:

- Evaluation of the delays in the transient response of the different segments as the hammer impact event propagates through the rod.
- Measurement of the vibration spectrum, where the fundamental longitudinal mode frequency allows determination of  $v_s$ .

The results of the speed-of-sound measurements are shown in Fig. 6.26. Here, Fig. 6.26(a) shows the phase signals for the six segments S1 to S6 over a period of 2 ms around the time of the hammer impact. Here, equivalent strain units, calculated using Eq. (5.23) for a sensor gauge length  $l_g$  equal to  $l_s = 12.5$  cm, are shown on the secondary y-axis. This also allows quantification of the noise in the strain data, where in Fig. 6.26(a), for the 1 ms period before the hammer stroke, instantaneous noise standard deviations, over the whole quadrature bandwidth of 43 kHz, with values between 17 mrad and 32 mrad are extracted. Using Eq. (5.23), this equates to instantaneous strain noise standard deviation values between  $14 \text{ n}\epsilon$  and  $27 \text{ n}\epsilon$ .

The inset in Fig. 6.26(a) then enlarges the period of the initial signal rise after the hammer impact, where the propagation delays for the different segments are clearly visible. The segment phase data between measurement points was then linearly interpolated to determine the propagation delays between adjacent segments at the chosen threshold level of 0.5 rad, with the threshold level also marked in the inset in Fig. 6.26(a). By evaluating the propagation delay between neighbouring segments over 10 repeats of this experiment, where only the central segments S2 to S5 were used to exclude edge effects, the speed-of-sound  $v_s$  in the rod was determined as  $4.96 \pm 0.34 \text{ km} \cdot \text{s}^{-1}$ . These results are plotted in Fig. 6.26(b), where the dashed line marks the mean and the dotted lines mark the interval corresponding to one standard deviation. The value of  $v_s = 4.96 \pm 0.34 \text{ km} \cdot \text{s}^{-1}$  determined from Fig. 6.26(b) is well

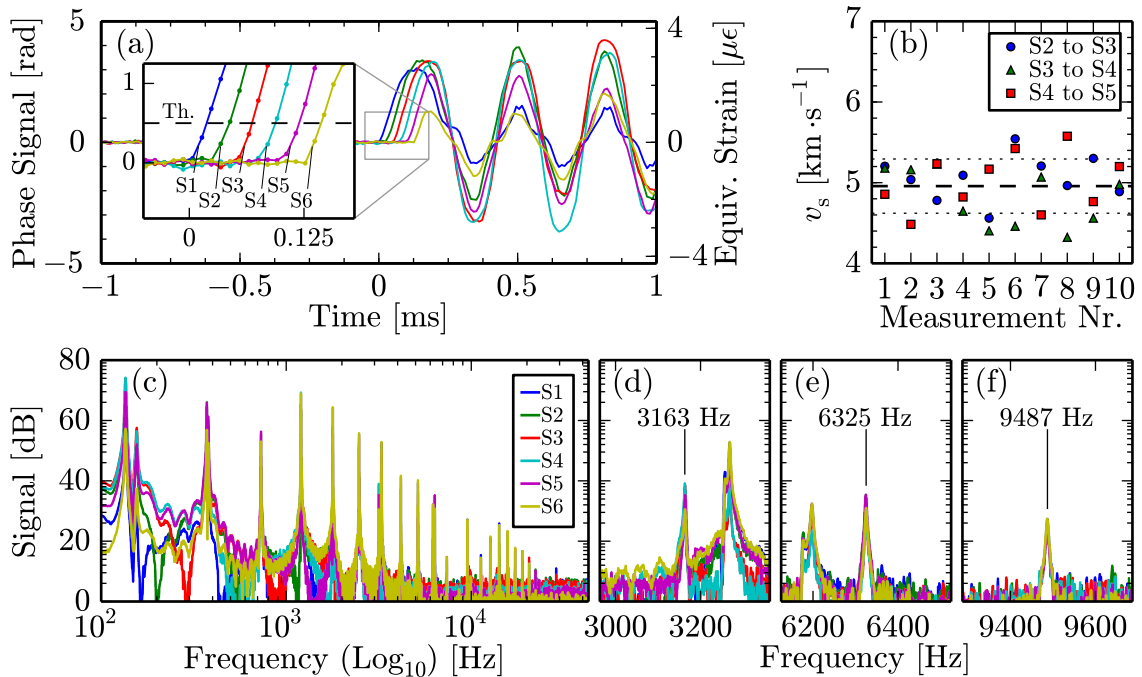


**Figure 6.26.:** Results of the speed-of-sound measurement for the stainless steel rod of Fig. 6.19. (a) shows the phase signals for the six segments S1 to S6 at the time of the hammer impact, with the secondary y-axis in equivalent strain units for a segment length  $l_s = 12.5$  cm, calculated using Eq. (5.23). In (a), the inset also enlarges the initial rise period and the threshold level at 0.5 rad, where the delay times were determined, is marked. (b) then plots the results of 10 delay measurements, excluding data from the outer segments S1 and S6, with the mean and standard deviation marked using the dashed and dotted lines, respectively. (c) shows the complete vibration spectra for segments S1 to S6 on a double logarithmic scale, while (d), (e) and (f) enlarge the peaks corresponding to the fundamental longitudinal mode and its harmonics on a linear frequency scale.

within the error limits of the calculated theoretical value [252] of  $4.91 \text{ km} \cdot \text{s}^{-1}$  for a longitudinal acoustic wave in a type 316 stainless steel [253] thin rod.

The vibration spectra for the phase signals of the six segments are shown in Fig. 6.26(c) on a double logarithmic scale. Here, a range of vibration peaks can be seen, with the fundamental transverse mode occupying a frequency of 137 Hz, and where most of the peaks visible in Fig. 6.26(c) can be identified as direct, integer harmonics of this peak. However, at a frequency of 3163 Hz, as visible in Fig. 6.26(d), a further set of peaks, with harmonics at 6325 Hz and 9487 Hz as plotted in Figs. 6.26(e) and (f), start to appear. These peaks are thought to be longitudinal vibration modes and the speed-of-sound  $v_s$  can be calculated [254] using the formula  $v_s = 2lf$ , where  $l = 0.782 \text{ m}$  is the length of the rod and  $f = 3163 \pm 1 \text{ Hz}$  is the fundamental longitudinal mode frequency used. This yields a value for the speed-of-sound of  $v_s = 4.946 \pm 0.002 \text{ km} \cdot \text{s}^{-1}$ , which agrees to within less than 1% with both the theoretical and the experimental values determined above, further confirming the physical validity of the measurements. Therefore, it can be concluded that the SFM technique can be used for high-speed measurements of transient strain events. Here simultaneous strain measurements of six fibre segments of length  $l_s = 12.5 \text{ cm}$ , with a worst-case instantaneous strain noise standard deviation value of  $27 \text{ n}\epsilon$  over the entire 43 kHz quadrature bandwidth, have been demonstrated.

Finally, Fig. 6.27 shows a measurement over 0.1 s of the six segment phase signals S1 to S6 several seconds after the hammer impact, where all transient excitations have subsided and only the fundamental transverse mode at 137 Hz remains, with this mode also illustrated in the inset. The secondary y-axis in Fig. 6.27 is also shown in equivalent strain units for a segment length  $l_s = 12.5 \text{ cm}$ , calculated using Eq. (5.23). It can be seen in Fig. 6.27 that the signals for the outer segments S1 and S6, the signals for S2 and S5 and the signals for the inner segments S3 and S4 overlap, with the amplitude highest for the inner segments and lowest for the outer segments. This measurement therefore agrees very well with the expected behaviour for the fundamental transverse mode, with the highest vibration amplitudes in the centre and the lowest amplitudes at the edges, and where symmetry with respect to the centre of the rod is given. Thus, this measurement qualitatively confirms that strain transfer onto the sensing fibre is well established, or at least comparable for all segments, and that physically plausible strain signals can be picked up.

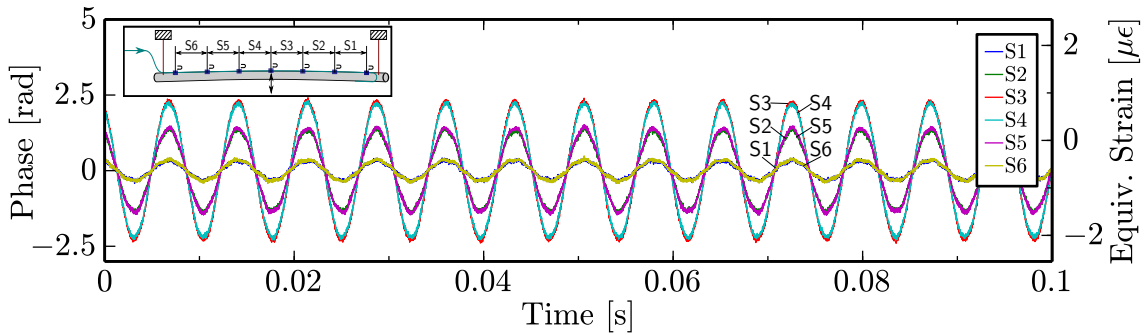


**Figure 6.27.:** Measurement over 0.1 s of the segment phase signals S1 to S6 after all transient events have subsided and only the fundamental transverse mode at 137 Hz, also illustrated in the inset, remains. Here, the secondary y-axis also shows equivalent strain units for a segment length  $l_s = 12.5 \text{ cm}$ , calculated using Eq. (5.23).

## 6.6. Discussion and Future Work

### 6.6.1. Discussion and Improvements to Current Work

**Polarisation Sensitivity:** Similar to the CDM technique, polarisation sensitivity of the FSI sensing fibre has not yet been addressed. However, in the FSI experiments shown, polarisation sensitivity is thought to be less critical for the SFM experiment than for the CDM experiment of Sec. 5.5.3 because the OPDs involved are two orders of magnitude lower, thus polarisation-induced signal fading (see also Sec. 2.4) is less likely to occur. Also, compared to the common LO FSI configuration of Fig. 4.1(c) used in the CDM technique, the physically down-lead insensitive FSI configuration of Fig. 6.19 for the SFM technique eliminates any potential polarisation mismatch originating from the fibre lead, further improving polarisation stability. Nevertheless, there is still no guarantee for the absence of polarisation-induced signal fading and further steps, such as the use of polarisation-maintaining fibre or polarisation-diversity detection [101], may have to be employed. In general, because fibre-optic circulators made from polarisation-maintaining fibre are nearly at the same cost as regular fibre-optic circulators, the setup of Fig. 6.19 for the proposed SFM technique could cost-effectively be adapted to the use of polarisation-maintaining fibre. This is in contrast to the setup of the CDM technique in Fig. 5.11 where several fibre couplers, which are very costly in their polarisation-maintaining versions, would be needed.

**In-Fibre Partial Reflectors:** The FSI experiment of Sec. 6.5 confirms the principle compatibility of the use of FBG-based in-fibre partial reflectors with the SFM technique, demonstrating successful measurements even for reflectivities of individual reflectors as low as  $10^{-6}$ . This is also a major improvement, particularly in terms of stability, to the connector-based approach used in Chap. 5. As also discussed in Sec. 4.1, FBG-based, in-fibre partial reflectors offer many practical advantages compared to other in-fibre reflector techniques, such as the ability to be inscribed through the coating [209] or by a draw-tower process [75], and are therefore thought to have the highest potential for future use in FSI applications. In this work, successful measurements have been demonstrated even though the FBG in-fibre reflectors do not yet display the favourable properties, such as returning a broadband spectrum while also showing comparatively large reflectivities, that were demonstrated in prior work [94] and discussed in Sec. 6.5.1. Nevertheless, this allows to conclude that the SFM technique is very tolerant to the reflector properties and that with some improvements in FBG-inscription, the FBG spectra should be sufficiently broadband and strong to allow interrogation in all practical temperature and strain conditions.

**Spatial Resolution and Reflector Placement:** A major advantage of the SFM technique, compared to other interferometric multiplexing techniques, such as time-division or code-division multiplexing (see also Chap. 4), including the CDM technique of Chap. 5, is that in the SFM approach, spatial resolution is a property of the laser optical frequency modulation amplitude  $\Delta f_{\text{opt}}$  and not of the signal processing hardware. Therefore, spatial resolution and signal processing bandwidth are decoupled and the many GHz of optical frequency modulation amplitude  $\Delta f_{\text{opt}}$  that

can be obtained by, for example, laser diode injection current modulation (see also App. B.3), effectively determine the spatial resolution, as discussed in Sec. 6.2.3. In this work, this allowed an improvement by more than two orders of magnitude in the minimum segment length, decreasing from 16.5 m for the CDM technique to 0.125 m for the SFM technique. Furthermore, as also discussed in Sec. 6.2.3, some improvement in the spatial resolution may also be obtained from the optimisation of the window width parameters. In general, because the spatial resolution in the SFM technique has no fundamental limits other than  $\Delta f_{\text{opt}}$ , replacement of the diode laser used, by, for example, a widely tunable, micro-electromechanical system based external cavity (MEMS-ECL) laser, such as the one used by Baumann *et al.* [255], could be considered. This laser was shown to exhibit a sinusoidal optical frequency modulation amplitude  $\Delta f_{\text{opt}} = 1$  THz at 1 kHz modulation frequency, thus an increase in spatial resolution of a factor of 56 should be achievable compared to the present laser diode. Therefore, in such a system, using a configuration similar to Fig. 6.19(a), fibre segments of segment length  $l_s = 2$  mm could be resolved and interrogated, albeit at lower quadrature bandwidths.

Furthermore, the continuously variable reflector placement that the SFM technique permits, as demonstrated in Sec. 6.3 for the nested MZ experiment where the OPDs are not simple multiples of each other, also relaxes the spatial reflector placement tolerances in FSI. Additionally, the property of continuously variable reflector placement also means that the optical frequency modulation amplitude  $\Delta f_{\text{opt}}$  and thus the laser modulation waveform does not need to be adjusted or controlled, which was the case in prior work, as discussed in Sec. 4.4.

**Quadrature Bandwidth and Dynamic Range:** For a given quadrature bandwidth  $B_Q$ , the permissible amplitudes of the phase signals are approximated by Carson's rule of Eq. (3.4). For the SFM technique, where a quadrature cut-off frequency value of  $f_{Q,\text{co}} = 43$  kHz was used, the usable quadrature bandwidth  $B_Q$  equals 37 kHz, including the previously discussed safety margin of 15%, with the permissible amplitudes for a sinusoidal phase signal in this case also plotted in Fig. 3.5. In general, in the common LO FSI configuration of Fig. 6.19(a), any measured reflector signal carries contributions from all segments on the way to the LO, therefore the highest quadrature bandwidth is required for reflector R7 in this case.

In order to increase the dynamic range, the modulation frequency  $f_m$  has to be increased so that the quadrature LP filter cut-off frequency  $f_{Q,\text{co}}$  can be increased accordingly. In Sec. 6.3.1, the required digital signal processing bandwidth of the ADC and the FPGA-based processing was found to be the product of the modulation frequency  $f_m = 98$  kHz and the highest occurring phase carrier amplitude  $A_k$ . For the FSI experiment demonstrated in Sec. 6.5, the highest value of  $A_k$  can be seen in Fig. 6.20(b) to be  $A_7 \approx 420$  rad. The bandwidth of the raw signal is then expected to be  $\approx 41$  MHz, which is about 80% of the available ADC bandwidth defined by the analogue anti-aliasing filter used in conjunction with the ADC. Therefore increasing the quadrature bandwidth while still multiplexing seven reflector signals will require a corresponding increase in the digital signal processing bandwidth, as will an increase in the number of multiplexed reflectors. Note, however, that the required digital signal processing bandwidth is independent of the segment length  $l_s$  used, because, if



the segment length in an FSI array is increased, a lower optical frequency modulation amplitude  $\Delta f_{\text{opt}}$  can be used, resulting in the same values for the phase carrier amplitudes  $A_k$ . In this context, in the vibrometry experiment shown in the next chapter, the modulation frequency  $f_m$  is increased by a factor of four, proving that increases in  $f_m$  are technically straightforward as long as the laser driver supports the modulation bandwidth. However, for diode lasers, the optical frequency modulation efficiency for injection current modulation generally reduces with increasing  $f_m$ , in turn reducing  $\Delta f_{\text{opt}}$  and thus the spatial resolution achievable.

**Phase Noise and Dynamic Strain Sensitivity:** Following the corresponding discussion for the CDM technique in Sec. 5.6.1, a reference segment could be used to remove  $1/f$  laser phase noise, leading to a flat noise floor, which is a requirement for the statement of phase noise levels in units of  $\text{rad} \cdot \text{Hz}^{-0.5}$  over the whole quadrature bandwidth. In the absence of a measurement with a reference segment, the phase noise levels for the SFM technique can only be stated for phase noise frequencies between 1 kHz and 43 kHz, where such a flat noise floor exists. Here, segment phase noise levels up to  $0.19 \text{ mrad} \cdot \text{Hz}^{-0.5}$  were found in Fig. 6.25(b), four times the value expected for the segment OPD from the measured reflector OPD dependence. Therefore, segment phase noise is insufficiently suppressed and this phenomenon requires further investigation. For the CDM technique, segment phase noise levels of  $2.2 \text{ mrad} \cdot \text{Hz}^{-0.5}$  were found between 1 kHz and 20 kHz in Fig. 5.28(b). The phase segment noise levels stated above for the SFM FSI experiment are only 12 times less than for the CDM FSI experiment, while the OPDs are 132 times less, therefore the OPD specific phase noise levels in the SFM technique are greatly increased. These findings are echoed by the single MZ interferometer experiment of Sec. 6.4, and, as discussed there, it is thought that the ability of the control circuit in the laser driver to suppress injection current noise, which is directly converted into laser frequency/phase noise, is reduced in the presence of the strong injection current modulation required in the SFM technique. Here, a different laser driver concept, where the sinusoidal frequency modulation is supplied directly to the laser diode via a Bias-T adapter, without influencing the control circuit of the driver, is proposed in order to reduce laser phase noise in future implementations.

It was confirmed by plotting the power dependence of the signals for both the single MZ experiment in Fig. 6.18(a), as well as for multiple reflectors in the FSI experiment in Fig. 6.25(a), that, without artificial attenuation, the interrogation is laser phase noise limited. Therefore, the noise performance is not dominated by OPD-independent noise sources such as shot, intensity or electronic noise. However, it is also recognized that the application of a window function reduces the effective sampling time while maintaining the noise bandwidth of the measurement, which would increase the detrimental effect of shot, intensity or electronic noise outside phase noise limited operation. As shown in Fig. 6.18(b) for the single MZ interferometer experiment, the direct proportionality of the laser phase noise on the OPD can be confirmed as soon as excess phase noise caused by quadrature noise is corrected according to the model in App. D.1. Also, in Fig. 6.18(b), the amplitude noise resulting from quadrature noise is in very good agreement with the assumption of a quadratic OPD dependence. The reasons for the quadratic OPD dependence are not



clear, but also echo similar finding for the CDM technique. As discussed in Sec. 6.4, a quadratic dependence could possibly be explained by aliased high-frequency laser phase noise [244], with its influence proportional to both the OPD itself and the number of Bessel carriers (see also Eq.(3.9)) in the photo detector signal. Both quantities are proportional to the OPD and together could explain a quadratic OPD dependence of the quadrature noise. In order to investigate this phenomenon, an experiment where the OPD and the optical frequency modulation amplitude  $\Delta f_{\text{opt}}$  can be varied independently is proposed and where the same phase carrier amplitude  $A_k$  can thus be achieved at different OPDs. This should help find the origins of the quadrature noise, which is particularly important as a quadratic OPD dependence of the quadrature noise would mean that excess phase noise will exceed direct laser phase noise at a given OPD value and may therefore limit the practical application of this technique. This investigation should also include research into the phenomenon of imperfect segment phase noise suppression that can be seen in Fig. 6.25(b) and into the reasons for the more complex noise behaviour when multiple reflectors are present that can be seen in Fig. 6.24.

For the SFM technique, the phase noise levels of  $0.19 \text{ mrad} \cdot \text{Hz}^{-0.5}$  for frequencies between 1 kHz and 43 kHz stated above translate into dynamic strain sensitivities of  $0.16 \text{ n}\epsilon \cdot \text{Hz}^{-0.5}$  using Eq. (5.23) for a gauge length  $l_g$  equal to the segment length  $l_s = 12.5 \text{ cm}$ . Because the FSI experiment for the CDM technique used a reduced sensor gauge length of  $l_g = 2 \text{ m}$ , the dynamic strain sensitivity values achieved here are comparable to the levels achieved for the CDM technique even though the OPD specific phase noise levels are increased in the SFM technique. Following the previous discussion in Sec. 5.6.1, these dynamic strain sensitivity values are not at the performance levels of high-end applications, such as optical hydrophones, but do compare well with other commonly-used strain sensing techniques, such as FBG-based strain sensing and could be improved by employing lasers with lower intrinsic frequency noise levels. This is especially true for the SFM technique, having a very simple and cost-effective setup and, compared to the CDM technique, offering low gauge lengths of  $l_g = l_s = 12.5 \text{ cm}$  that are more akin to the gauge lengths found for FBG or LPG-based sensing concepts (see also Sec. 2.3). Furthermore, the presented SFM interferometric technique inherently permits very high measurement bandwidths. However, as an interferometric technique, FSI does not have the ability for absolute measurements that most grating sensor concepts offer and may also suffer from polarisation-induced fading. Furthermore, similar to the previous discussion in Sec. 5.6.1, the inherent temperature sensitivity of fibre sensors has not yet been addressed here and temperature compensation schemes may be required in practice.

**Linearity and Crosstalk:** Numerical simulations concerning the impact of quantisation errors were shown in Sec. 6.2.4 and it was experimentally confirmed for both the nested MZ and the FSI experiments that the scale of the measured non-linearities is dependent on the processing bitwidth of the photo detector signal at the point of digitisation. It is, however, stressed that non-linear behaviour due to quantisation is very sensitive to the exact number of quantisation levels and that experiments and simulations can only yield or confirm the order of magnitude of error levels. Here, in Fig. 6.11(d), for the nested MZ experiment, using the corrections of Sec. 6.2.5,

angular errors in individual interferometers of maximally  $\pm 1.0$  mrad were found, while for the FSI experiment, non-linearities in the reflector data of up to  $\pm 6.4$  mrad were found due to the reduced processing bitwidth. This equates to worst-case systematic errors in the FSI segment data of  $\pm 13$  mrad. Additionally, the residual measurements for the nested MZ experiment allow a further method to quantify non-linearity errors, measuring the sum of the maximum cyclic error amplitudes of all three interferometers. Here, Fig. 6.15(c) shows that, even for the case without the corrections of Sec. 6.2.5, measurements with total cyclic error amplitudes as low as 4.4 mrad can be obtained. This value drops to 3.1 mrad when these corrections are applied and this value stays constant over a wide range of the window width parameter  $\sigma$ . While not strictly comparable, it is interesting to note that typical cyclic error amplitudes in precision free-space interferometry, using sophisticated polarization isolation equipment for remote interrogation (see also Fig. 3.3), range from  $0.8^\circ$  to  $0.05^\circ$  [142], and are thus on the same order of magnitude as the values of  $1.0$  mrad  $= 0.063^\circ$  achieved here. This clearly shows the potential for range-resolved signal processing to enable highly linear interferometry, especially considering the findings of the numerical calculations of Sec. 6.2.4, indicating that linearity could be improved simply by increasing the processing bitwidth.

Quadrature signal crosstalk suppression values  $S_{cr}$  of  $\leq -60$  dB have been found for the nested MZ experiment in Fig. 6.14. This is at least 20 dB better than the corresponding values for the CDM technique shown in Fig. 5.22. In general, the resulting crosstalk levels in the phase signals are highly dependent on the temporal variations of the phase signals involved, as detailed in App. D.3. For this reason, the crosstalk in the phase signals for the CDM technique did not exceed the noise floor and this is also found for the nested MZ experiment, where crosstalk levels in the phase signals are found to be  $\leq -70$  dB. In practice, crosstalk on these levels is not deemed problematic for most applications and, following the findings in Sec. 6.2.4, increasing the processing bitwidth may further reduce any remaining crosstalk.

**Choice of Window Function:** In this work, the dual Gaussian window function of Eq. (6.6) was used because of its conceptual simplicity and because the parameter  $\sigma$  can be used to scale the window width. This allowed measurements such as that shown in Fig. 6.15(c), where for data corrected according to Sec. 6.2.5, the SFM technique can be seen to operate with almost constant linearity performance over a wide range of  $\sigma$ . It can also be seen in the demodulation maps in Fig. 6.10 that the choice of  $\sigma$  significantly alters the appearance of these maps and that for large values of  $\sigma$ , the range resolution, evident in the right-hand panels in Fig. 6.10 improves considerably. However, because the window function of Eq. (6.6) is only an initial choice, future implementation could specifically investigate the effects of using different types of window functions. Research options include:

- Window functions based on non-Gaussian functions.
- Singular window functions, where the window is only applied once per sinusoidal modulation waveform.
- Multiple window functions, where the window is applied more than twice per sinusoidal modulation waveform.

- Asymmetric window functions, where the window function is not symmetric to the optical frequency modulation centre frequency  $f_{\text{opt,c}}$  of Eq. (6.1).

Improving spatial resolution and easing the process of finding the correct demodulation and correction parameters are thought to be the main motivation for investigating different window functions. Also, a further reduction in the susceptibility to instrumental drift and, using multiple, asymmetric windows, schemes that evaluate phase differences resulting from changes of the effective optical frequency evaluation locations for different window positions on the sinusoidal optical frequency modulation waveform could be investigated. In general, as mentioned before, the application of a window function reduces the effective sampling time while maintaining the noise bandwidth of the processing hardware, increasing the relative influence of shot, intensity or electronic noise. This becomes relevant when very weak signals are evaluated, where operation is no longer phase noise limited.

**Signal Processing:** It was shown in Fig. 6.16(b) that some detuning of the demodulation parameters can be tolerated, especially when corrected data is used. In practice, changes in the signal processing delay  $\tau_{\text{sp}}$  on the order of nanoseconds were found to occur, and variations in  $\tau_{\text{sp}}$  will become more critical for larger values of the photo detector bandwidth, i.e. the product of the phase carrier amplitude  $A_k$  of the constituent interferometer with the largest OPD and the modulation frequency  $f_m$ . This may require an online compensation algorithm or more careful system design in order to avoid variations in  $\tau_{\text{sp}}$  occurring at all. Furthermore, in the current implementation of the SFM technique, the impulse response of the analogue anti-aliasing filter has not yet been compensated, because it was not yet found to be critical to the overall performance. However, in future implementations, it might be necessary to include a digital anti-aliasing correction filter at the ADC input of the FPGA in Fig. 6.8 in order to correct the analogue filter impulse response, similar to the proposal put forward in the previous chapter for the CDM technique.

In this work, the optical frequency modulation waveform was deliberately kept simple, using only a pure sinusoidal laser injection current modulation and applying any corrections in post-processing only. Another approach that could be explored would be to correct the deviations due to the non-linear injection current to optical frequency modulation characteristic described in Sec. 6.3.1 by applying a pre-shaped injection current waveform that would then result in a purely sinusoidal optical frequency modulation. However, intensity modulation associated with laser injection current modulation cannot be corrected in this way and would still require post-processing corrections as described. In addition to the techniques used in App. B.3 to measure the calibration parameters required for the corrections of Sec. 6.2.5, it could also be fruitful to investigate new approaches to obtain this data. Here, it might be possible to extract all necessary correction parameters using only raw measurement data of a test system consisting of several constituent interferometers of known OPDs and using an optimisation algorithm on the appearance of the demodulation maps of Fig. 6.10. This would avoid the use of a dedicated optical setup, as was used in App. B.3, to obtain the correction parameters and would permit laser diodes to be exchanged more readily.

## 6.6.2. Future Research Directions

**FSI Applications** A number of future FSI configurations using direct reflector interference have been proposed in Fig. 5.33 for the CDM technique. The main practical advantage of direct reflector interference, especially for strain sensing on large engineering structures, is that the dynamic range for each sensor is not shared over the sensing fibre, as is the case with the common LO configuration. However, this option is not possible for the SFM technique in the current stage of development, because range-resolved signal processing using the SFM technique is only possible for constituent interferometers differing in OPDs, whereas the CDM technique can distinguish signals based on their offset time-of-flight delays alone. Nevertheless, the much higher spatial resolution possible with the SFM technique, as well as the potential for simple and cost-effective interrogation units, opens up a number of applications for FSI in structural health monitoring. Using a diode laser similar to the one used in this work permits a spatial resolution on the order of 0.1 m. Here, the quasi-distributed long-gauge length sensing (see also Fig. 2.1(c)) that FSI offers could be of benefit for some applications that specifically require strain measurements along the fibre without sensing gaps, guaranteeing that a structural disturbance occurring along the sensing fibre is not missed. Additionally, FSI could be applied to dynamic structural health monitoring techniques of engineering structures, such as vibration-based condition monitoring [256], which could benefit from cost-effective fibre-optic strain measurements [14].

Another potential application for FSI-based sensing for both the CDM and SFM techniques is fibre optic shape sensing [26, 27, 76, 81], where differential strain measurements in laterally offset fibres are used to infer lateral displacements. Because shape is a very important property for aerodynamic structures, this could have applications in areas such as aerospace or wind power. For the simple example case of a cantilever structure, the radius of curvature increases approximately with the square of the cantilever length, therefore the differential strain that amounts to the same tip displacement reduces with the square of the cantilever length, posing a difficult measurement problem. For localised strain sensors, such as FBGs, this leads to a reduction in tip displacement sensitivity with the square of the cantilever length. However, because interferometric curvature sensors can integrate strain along the whole cantilever length, the tip displacement sensitivity only reduces linearly with the cantilever length [26], as also expressed in Eq. (5.24), giving long-gauge length interferometric measurements a principal advantage for shape sensing on large engineering structures. Because of the differential nature of this measurement, relevant low-frequency phase noise is automatically suppressed in a manner similar to the use of the reference segment measurement that was demonstrated in Sec. 5.5.2.

A third potential research direction for the SFM technique is high spatial resolution FSI. In this context, the gauge length of regular FBG sensors is typically 5 to 10 mm (see also Sec. 2.3), while short-gauge length interferometric Fabry-Perot sensors (see also Sec. 2.4) offer much smaller gauge lengths but are difficult to multiplex. In contrast, using a widely tunable laser, very short gauge lengths are possible in FSI, whilst also allowing simple sensor multiplexing. Here, if the MEMS-ECL laser [255] discussed in the previous section would be used, a sensor gauge length of 2 mm would

be possible. Because, as discussed in Sec. 6.5.1, FBG-based partial in-fibre reflectors with gauge lengths as low as  $16\text{ }\mu\text{m}$  can be inscribed, further significant reductions in the sensor gauge lengths, using even more widely tunable lasers, are not limited by the physical length of the in-fibre partial reflectors.

For FSI, a further area where using the SFM technique could be advantageous is two or three wavelength interferometry, allowing absolute strain or temperature measurements by extending the dynamic range of an interferometric measurement beyond  $2\pi$  [108, 257]. Also, as discussed in Sec. 2.1, multiple-wavelength approaches allow temperature/strain discrimination [20, 21]. In all cases, the SFM technique could be used favourably because multi-wavelength approaches require very high linearities and because it would allow the cost-effective use of several diode lasers.

**Non-FSI Applications** In this context, an application of the SFM technique to range-resolved multi-surface vibrometry is presented in the next chapter. A further interesting direction of research to which the SFM technique could be applied is absolute distance sensing. Here, the peak positions in the range data that can be seen in the right-hand panels of the demodulation maps in Fig. 6.10 are evaluated for absolute measurements of the OPD, and therefore the distance of an object from the LO. This approach is related to the widely-used optical coherence tomography (OCT) technique [258, 259], with a spatial resolution proportional to the optical frequency modulation amplitude  $\Delta f_{\text{opt}}$ , however, unlike regular OCT, it uses sinusoidal optical frequency modulation. In any practical application for absolute distance sensing, an additional measurement of a reference segment of known length for online distance calibration would also be required. One potential application of this is thought to be an interferometric displacement sensor where high-quality relative displacement, velocity and acceleration data, useful for control applications, is obtained using interferometric phase evaluation and where the desired absolute distance measurement serves as an additional proximity sensor with coarser spatial resolution.

It has already been demonstrated that the SFM technique allows very linear interferometric measurements, with non-linearity errors as low as  $\pm 1.0\text{ mrad}$ . Using a reflective interferometric configuration (see also Sec. 3.1.3), for a free-space displacement measurement at a wavelength of  $\lambda_0 = 1552\text{ nm}$ , the achieved level of linearity would correspond to a maximum systematic displacement error of  $0.12\text{ nm}$  when laser wavelength drifts are neglected. It has long been noted that “metrological systems nowadays still suffer remarkably from nonlinearity errors” [260] and recently, in 2012, several national metrology institutes set the target to bring systematic interferometric errors down to  $10\text{ pm}$  [261]. The simulation presented in Sec. 6.2.4 indicate that it is feasible, even using the current laser diode, to reduce non-linearity errors down to  $-82\text{ dB}_{\text{rad}}$ , corresponding to the  $10\text{ pm}$  target, simply by increasing the processing bitwidth  $b$  of the signals to values above  $13\text{ bit}$ . It is thought that the simple explanation for the good linearity performance of the SFM technique is that it is range-based and does not rely on polarisation properties of optical components to achieve polarisation-based path isolation (see also Sec. 3.1.3). Important applications for highly linear interferometric measurements are scanning probe microscopy [260] and wafer positioning for lithography [261], and the validity of the calculations of Sec. 6.2.4 should be tested experimentally with high priority.

## 6.7. Summary

In this work, a novel range-resolved interferometric signal processing technique has been presented that uses sinusoidal optical frequency modulation of a laser diode by injection current modulation. The theory has been described and explained extensively. Here, using an appropriate time-variant carrier and a smooth window function to suppress contributions from undesired signal components in the demodulation process, highly linear phase signals can be obtained. Due to the proportionality of the phase carrier amplitude to the OPD in optical frequency modulation, constituent interferometers can be multiplexed based on their range. The OPDs of the constituent interferometers are continuously and independently variable, subject to a minimum OPD separation. Furthermore, a simulation regarding the expected linearity performance resulted in quantisation errors being identified as the main source of the remaining non-linearities, without any fixed theoretical limit.

In a nested MZ experiment, three constituent interferometers with a minimum OPD separation of 21 cm have been multiplexed and maximum cyclic error amplitudes of 1.0 mrad were found. Crosstalk suppression in the quadrature signals was  $-60$  dB and measurements were taken over a quadrature bandwidth of 43 kHz. It has been shown that non-ideal effects that arise due to injection current modulation, such as intensity modulation and deviations from the ideal sinusoidal optical frequency modulation waveform, can straightforwardly be compensated in post-processing and that the technique can operate over a wide parameter range when these corrections are applied. However, even without corrections, highly linear measurements can still be obtained. It was further shown that the technique is reasonably robust against detuning by instrumental drift. In a dedicated single interferometer setup, the system was confirmed to be laser phase noise limited under typical operation conditions. Furthermore, it was found that quadrature noise, which can cause excess phase noise, displays a quadratic OPD dependence.

Finally, an application of the technique to FSI demonstrated the multiplexing of six fibre segments of physical length 12.5 cm each, separated using FBG-based in-fibre partial reflectors, where measurements could be obtained even for FBG reflectivities as low as  $10^{-6}$ . Maximum segment phase noise levels of  $0.19 \text{ mrad} \cdot \text{Hz}^{-0.5}$  for noise frequencies between 1 kHz and 43 kHz were found. The physical plausibility of the FSI measurements was confirmed by measurements of the speed-of-sound in a stainless steel rod using two independent evaluation methods, with results agreeing within 1% of each other and the theoretical value.

The noise behaviour when multiple reflectors are present, as well as the origins of the quadratic quadrature noise OPD dependency, are not well understood and further analysis is required. Key technical considerations and options for future improvement have been discussed and a range of potential applications, both within FSI, but also outside FSI, have been proposed. It can be concluded that, considering that a very simple optical setup with components totalling less than £3k was used, a very linear, robust and cost-effective range-resolved interferometric signal processing technique has been demonstrated.

# 7. Application of the Sinusoidal Frequency Modulation Technique to Multi-Surface Vibrometry

## 7.1. Introduction

In this chapter, the SFM technique presented in Chap. 6 is applied to free-space, multi-surface vibrometry. Laser Doppler vibrometry [161] (LDV) is a widely-used technique enabling non-contact interferometric displacement measurements of vibrating targets. Commercial LDV systems [37, 138, 262, 263] appear to be mainly based on heterodyne signal processing (see also Sec. 3.3.1), using Bragg cells as direct frequency modulators (see also Sec. 3.1.2), and employing a setup similar to Fig. 3.10, where heterodyne signal processing offers high interferometric quadrature bandwidths of many MHz [138, 163]. The delivery of the laser light to and from the measurement object can be free-space or fibre-coupled, where in fibre-coupled heterodyne measurements [32, 33, 37], polarisation-based path isolation (see Fig. 3.3(a)), using polarisation-maintaining fibres, is used to make the fibre down-lead insensitive.

In addition to heterodyne vibrometers, there are several instances in prior work of fibre-coupled vibrometers that use self-referencing signal processing techniques (see Fig. 3.3(c)). Here regular single-mode optical fibre can be used for laser light delivery and the measurements are referenced against the LO provided by the fibre tip reflection, yielding complete down-lead insensitivity. In these systems, signal processing techniques based on optical illuminating frequency modulation (see also Sec. 4.4) can be used, allowing a simple interferometric setup without an external modulator. A particular advantage of self-referencing configurations is that very compact sensing heads, consisting only of a fibre collimator, can be designed [35]. Prior work [34–36] in this area used various dual carrier Bessel signal processing techniques (see also Sec. 3.4) in conjunction with laser diode injection current modulation to obtain sinusoidal optical frequency modulation, typically enabling quadrature bandwidths of several hundred kHz, which is, however, considerably lower than heterodyne vibrometry. A major disadvantage of the use of dual carrier Bessel signal processing techniques is that the sinusoidal optical frequency modulation amplitude has to be maintained at a precise working point (see also Fig. 3.14(a)), making these techniques susceptible to changes in the laser modulation efficiency and requiring retuning for any change in the vibrometer working distance.

The vibrometry techniques reviewed so far only allow the measurement of a single reflective surface. In addition to this, so-called differential vibrometers [263] are also commercially available [37], that allow differential vibration measurements by letting two separate and spatially offset return beams interfere with each other. Applications for differential vibrometers include the measurement of small differential vibrations in the presence of large common-mode vibrations. However, a disadvantage of these systems is that they can only yield differential vibration data whilst the common-mode vibration information is lost. In contrast, in the self-referencing multi-surface vibrometry system that is presented here, only a single delivery beam is employed and range-resolved interferometric signal processing is then used to separate the return signals based on their range. When multiple surface reflections are present in the return beam, this allows the individual measurement of the movement of each surface and both differential and common-mode vibration signals can then be calculated. However, range-resolved techniques can have advantages even when only a single surface is to be interrogated, as the influence of undesired signals, such as window reflections [264], can be suppressed. In general, a very important practical advantage of the presented SFM technique is the property of continuously variable OPD placement of the constituent interferometers, subject to a minimum OPD separation, that was previously discussed in Chap. 6. This allows measurements to be taken anywhere along the beam path without retuning the laser modulation parameters, which is of particular importance for multi-surface vibrometry because there is normally no control over the geometry of the objects under test. In addition to the approach proposed here, range-resolved vibrometry [265] has also recently been demonstrated using an optical frequency comb technique. However, this demonstration uses a complex optical setup and only allows the selection of the range of a single location along the optical beam, thus, unlike the technique presented here, it is not capable of simultaneous multi-surface vibrometry. Conversely, a vibrometry technique with an even simpler optical setup than the proposed technique is self-mixing vibrometry [263, 266, 267], where the signal returned from the target object is used as feedback to a laser diode. However, while this technique is very simple and cost-effective, it only allows the measurement of a single surface.

In the specific application presented in this chapter, the multi-surface vibrometry system is applied, both during the development phases and for final product characterization, to the measurement of the vibration characteristics of a commercial table-top cryostat system [268] (OptistatDry), developed by Oxford Instruments plc, and also depicted later in Fig. 7.4(a). Here, the first signal is provided by the window of the outer vacuum chamber (OVC), while the second signal is reflected off the solid metal sample holder inside the chamber. The sample holder is directly connected to the piston-driven coldhead of the cryostat in order to cool the sample. The coldhead introduces vibrations into the cryostat, in particular to the sample holder through its direct link with the coldhead. In this application, independent measurements of the movements of the OVC and of the sample holder relative to the optical table are required to characterise the expected vibration levels of the final product. Additionally, the ability to distinguish between common-mode vibrations of the whole cryostat and differential vibrations between the OVC window and the sample holder was used during the development phases of the cryostat to identify



the origin of vibrations. These measurements provided an ideal test facility to demonstrate the usefulness of the SFM technique outside fibre sensing, with the implementation details and selected results shown and discussed in this brief chapter that is an addition to the main FSI theme of this thesis.

## 7.2. Setup and Implementation

In Fig. 7.1(a), a picture of the portable signal processing implementation on a breadboard is shown. Fig. 7.1(b) then details the optical setup. Here, sinusoidally modulated light leaving the laser diode is guided by the circulator, using a regular single-mode optical fibre lead that can be of arbitrary length, to the packaged collimator, where it exits the fibre and is collimated by the lens. In general, a collimated beam allows the reception of signals from multiple surfaces that are sufficiently aligned, where, in this case, a fraction of the beam is reflected by the Fresnel reflections of the OVC window, with the remainder reflected by the sample holder surface. The return light collected by the collimator, together with the fibre tip Fresnel reflection providing the interferometric reference, is then guided to the photo detector and the resulting interference signals are subsequently processed.

The details of the signal processing equipment are not drawn in Fig. 6.19(a) but the equipment used is similar to Fig. 6.7. However, for the vibrometry experiment, the FPGA implementation was modified, with the sinusoidal optical frequency modulation frequency  $f_m$  increased by a factor of four to  $f_m = 391$  kHz compared to the previous implementation described in Fig. 6.3.1. The quadrature signal low-pass filter cut-off frequency could then be set as high as  $f_{Q,co} = 180$  kHz. However, because long-term measurements also needed to be performed for this application, the transmission data rate from the FPGA to the PC had to be reduced to enable continuous transfer. Since the application only required the capture of mechanical vibrations up to 1 kHz and no higher vibration frequencies were expected in the phase signals, it was possible to reduce the transmission data rate by performing the phase unwrapping on the FPGA and then downsampling the phase signals by a factor of 192. In this case, an interferometric quadrature bandwidth of  $f_{Q,co} = 180$  kHz could

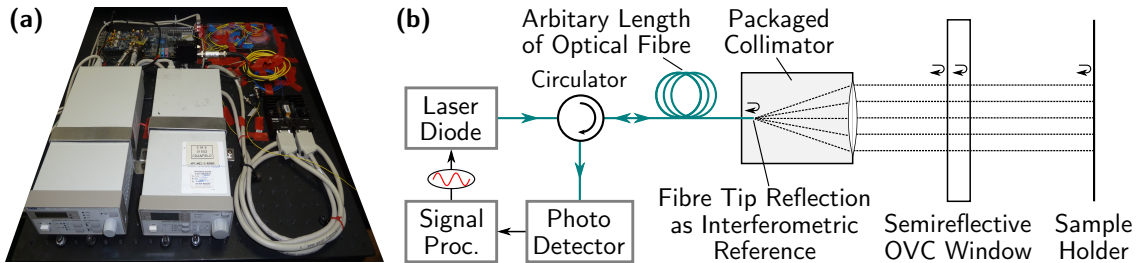


**Figure 7.1.:** (a) shows a picture of the portable signal processing implementation on a breadboard. (b) then illustrates the multi-surface vibrometry setup, where sinusoidally optical frequency modulated light leaves the laser diode and is guided by a circulator, via the fibre lead, to a packaged collimator. Reflections of the collimated beam from the OVC window and the sample holder are returned into the fibre and are guided, together with the fibre tip reflection that forms the interferometric reference, to the photo detector and processed by the signal processing hardware.

still be resolved to capture low frequency phase signals of large amplitude, but the transmission data rate could be reduced to 2.03 kHz. Note, however, that in this case the phase noise bandwidth still remains at 180 kHz.

Also, the corrections according to Sec. 6.2.5 were used throughout, however, the correction parameters for the increase in the modulation frequency of a factor of four were only estimated by manually optimising the appearance of the demodulation maps shown in Fig. 6.10 and not directly measured as described in App. B.3. Analogous to Fig. 6.20 for the SFM FSI experiment, Fig. 7.2(a) shows the photo detector signal corrected for intensity modulation, along with the window function used. It can be seen that the intensity modulation correction works well in keeping the envelope of the interferometric signals constant. In this implementation, a broader window with increased window width parameter of  $\sigma = 0.05$  was used, which, as discussed in Sec. 6.2.3, can provide higher spatial resolution if the baseband suppression expectations are lowered. In Sec. 6.2.3, a spatial resolution on the order of  $\Delta\eta_{\min} = 0.06$  m was calculated for  $\sigma = 0.045$  and  $S_{\text{bb,accept}} = -50$  dB, and similar values could theoretically be expected here for the previous modulation frequency of  $f_m = 98$  kHz. However, because the modulation frequency  $f_m$  was increased by a factor of four, the optical frequency modulation efficiency of the laser diode is reduced. No detailed characterisation measurements were performed, however, it can be estimated from the range dependency of the return signal that the optical frequency modulation amplitude  $\Delta f_{\text{opt}}$  is reduced by approximately a factor of two, increasing the minimum permissible OPD separation to values  $\Delta\eta_{\min} \approx 0.12$  m. Fig. 7.2(b) then shows the range dependency of the return signal, with the initial peak at  $A_d \approx 5$  rad due to the artefact arising from the intensity modulation correction, that is caused by the underlying distorted sinusoid of frequency  $f_m$  that can be seen in Fig. 7.2(a), as previously discussed in Sec. 6.3.1. In Fig. 7.2(b), the range dependency of the returned signals is plotted analogously to the right panels in Fig. 6.10 and the signals are labelled according to their source, with the bounce number  $m$  that is explained in the paragraph below also marked. The slight asymmetry in the range dependency of the signals seen in Fig. 7.2(b) is thought to be because the parameters

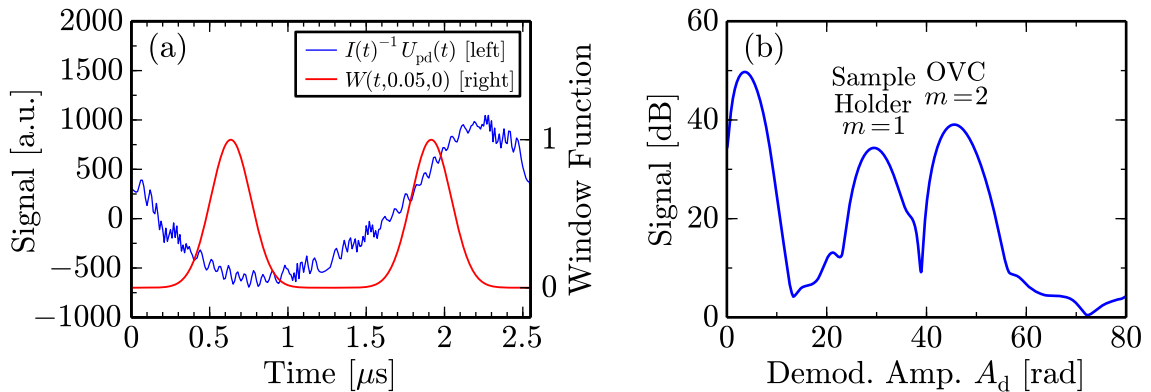


**Figure 7.2.:** Analogous to Fig. 6.9(c), (a) shows a plot of the photo detector signal corrected for intensity modulation according to Sec. 6.2.5 along with the window function used, now at  $\sigma = 0.05$  and over a reduced modulation period  $T_m = 2.56 \mu\text{s}$ . (b) then shows the OPD dependence of the return signals as a function of demodulation carrier amplitude  $A_d$  analogous to the right panels in Fig. 6.10, with the two evaluated reflections and their bounce number  $m$  marked.

for the corrections of Sec. 6.2.5 were only approximated. This does not appear to affect the measurements significantly, which is in line with the discussion in Sec. 6.3.2, where reasonable measurements were possible even without any corrections.

The spatial resolution  $\Delta\eta_{\min} \approx 0.12\text{m}$  calculated above is up to one order of magnitude higher than the minimum return distances between the OVC window and the sample holder for the cryostat. Therefore, the signals of the OVC and the sample holder had to be separated by other means. In general, it was observed that under certain alignment conditions, only the signal corresponding to the second bounce of the OVC window is present, while the regular, first bounce reflection is missing. Here, the light from the second bounce reflection of one of the OVC window surfaces, upon returning from the initial reflection by the OVC window, appears to be reflected by the collimator rim, then travels to the OVC window for a second time, where it is again reflected and then coupled back into the fibre. This is also illustrated in Fig. 7.3 for one of the OVC window surfaces using rays 1 to 4, where the final ray 4 has been reflected twice by the OVC window surface. With the fibre collimator (Thorlabs F280FC-1550) used, it was remarkably simple to align for the second bounce signal and it is thought that concentric, machined grooves on the collimator rim act in a similar manner to a retro-reflector [269], returning light into its original direction for all angles of incidence. Another indication that this phenomenon is based on retro-reflection is that this procedure was only possible for the highly specular window reflections and not for light returned by the metal sample holder, which has a rougher surface leading to more diffuse reflections.

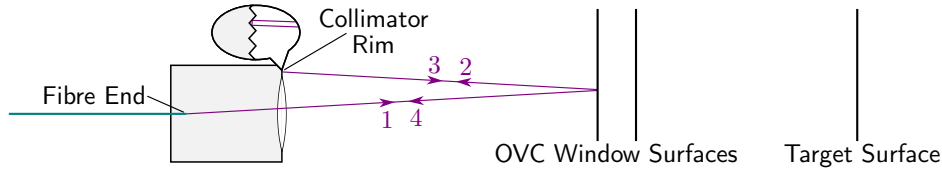


**Figure 7.3.:** Explanation of dual bounce alignment, where the rim of the packaged collimator is thought to act like a retro-reflector by directing ray 3 in the reverse direction of ray 2, so that ray 4, which ultimately reaches the fibre end, has been reflected twice by the OVC window surface.

The occurrence of retro-reflection in the collimator rim could explain the phenomenon observed, however, this conjecture still has to be confirmed by other means. Nevertheless, using this it was possible to consistently align the measurements in such a way that only the second bounce of the OVC window and the first bounce of the metal sample holder were exclusively present in the return signal. In this case the OPDs of the two signals differ widely, allowing their straightforward separation and the range dependence for such a case is shown in Fig. 7.2(b). This procedure was possible for a range of working distances between collimator and cryostat for all three Cartesian coordinate directions X,Y and Z where measurements were performed. However, care had to be taken, using suitable plausibility checks and additional single-surface measurements, using reflective tape on the OVC and thus exclusively receiving this signal, to always correctly identify all peaks and the corresponding bounce numbers  $m$ . A further point to note is that, in this work, the thickness of the window of the OVC is much smaller than the minimum resolvable spatial separation between sources. Therefore the phasor sum of the Fresnel reflections of both window

surfaces is effectively taken as the OVC signal, which does not pose any problems as long as the window thickness remains constant, which can generally be assumed for the short vibrometry measurements shown here.

In general, neglecting small angular differences due to slightly non-normal incidence in a multi-bounce alignment, using the bounce index  $m$ , for a phase signal  $\Delta\varphi(t) = \varphi(t) - \varphi(t_0)$  that was captured from time  $t_0$  onwards, the displacement  $\Delta l(t) = l(t) - l(t_0)$  of the surface in question can be given by:

$$\Delta l(t) = \frac{\lambda_0 \cdot \Delta\varphi(t)}{2m \cdot 2\pi} \quad (7.1)$$

For the cut-off frequency  $f_{Q,co} = 180$  kHz used in this implementation, employing a safety margin of 15% similar to the discussion in Sec. 5.5.2, the quadrature bandwidth  $B_Q$  that the vibration signals are allowed to take up is  $B_Q = 153$  kHz. Plots of permissible signal amplitudes for this case are also shown in Fig. 3.5. For a sinusoidal test signal of frequency  $f_{sig} = 1$  Hz, inserting Eq. 3.5 into Eq. (7.1), this corresponds to a displacement amplitude of 19 mm for  $m = 1$  and 8.9 mm for  $m = 2$ , however, for a test signal of 100 Hz, this is reduced to 0.19 mm for  $m = 1$  and 0.089 mm for  $m = 2$ . Similar to common usage in LDV [138], in an approximation for low frequency phase signals, this can also be described by the maximally resolvable target velocity of  $119 \text{ mm} \cdot \text{s}^{-1}$  for  $m = 1$  and  $59 \text{ mm} \cdot \text{s}^{-1}$  for  $m = 2$ .

A picture of the whole cryostat, without the compressor located at the side of the optical table, is shown in Fig. 7.4(a), where the optical windows of the cryostat can be set to different working heights and where the working height differs between Figs. 7.4(a) and (b). A typical measurement arrangement is then shown in Fig. 7.4(b), illustrating a measurement in the X-direction, with the other Cartesian directions Y and Z also marked. In all cases, a kinematic mount is used to align the optical axis and both the window of the OVC and the sample holder inside the cryostat were

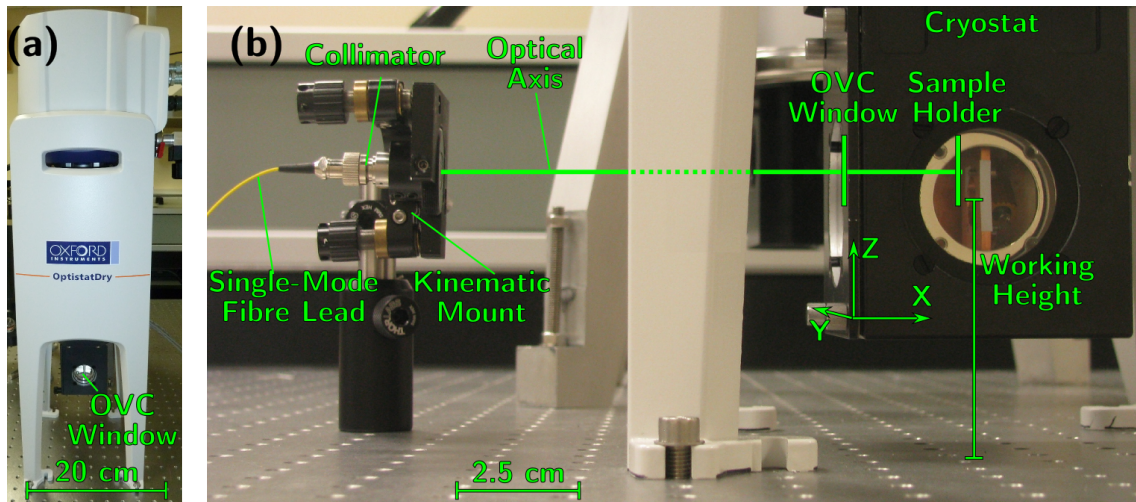


**Figure 7.4.:** A picture of the whole cryostat is shown in (a), while (b) shows an annotated picture of a typical physical measurement arrangement in the X-direction, where the cryostat was set to different working heights in (a) and (b). In (b), light leaving the single-mode fibre lead and packaged collimator is directed to the OVC window and the sample holder inside the cryostat, with correct alignment achieved using the kinematic mount.

measured using the previously described technique of dual-bounce alignment. For the measurement in the Z-direction, the kinematic mount was lowered close to the surface of the optical table and a  $45^\circ$  reflector prism was inserted under the cryostat to direct light upwards through the bottom window. The measurements shown later were obtained using reflective tape on the sample holder to increase signal strength, but successful measurements on other occasions have also been obtained from the unpolished copper surface of the sample holder.

### 7.3. Experimental Results

Using the described multi-surface vibrometry system, a large body of data has been collected for different vertical working heights and operating temperatures of the cryostat and during different stages of the development of the product. Fig. 7.5 shows measurements for the final product at a cryostat temperature of 4 K and at a working height of the optical windows of 172 mm. These measurements, which were recorded sequentially for each Cartesian direction, are representative for the system, although changes in the operating conditions, such as different cryostat temperatures and working heights, result in somewhat different vibration signatures and amplitudes. In Figs. 7.5(a), (c) and (e) on the top, the two displacement signals, determined using Eq. (7.1), corresponding to the OVC and the sample holder, are plotted directly for each of the three Cartesian measurement directions, respectively. Figs. 7.5(b), (d) and (f) then plot the numerically computed difference signals between the OVC and the sample holder. Here, the insets enlarge a section of the difference signal, with a displacement scale that increases going from Fig. 7.5(b) to Fig. 7.5(f).

For final product characterization of the cryostat, the root mean square (RMS) values of the individual surface measurements are required. Here, for the results shown in Figs. 7.5(a), (c) and (e), RMS values of  $[6.5 \mu\text{m}, 1.3 \mu\text{m}, 4.1 \mu\text{m}]$  for the  $[X, Y, Z]$  vibrations of the OVC, and of  $[5.8 \mu\text{m}, 1.0 \mu\text{m}, 8.4 \mu\text{m}]$  for the  $[X, Y, Z]$  vibrations of the sample holder were determined. Therefore it was confirmed that the RMS values are within the product specification limit of  $10 \mu\text{m}$ . However, during the product development phases, the diagnosis of the origin of the vibrations and their quantification was of particular importance. In all the cases plotted in Fig. 7.5, there is a dominant vibration at 1 Hz due to the movement of the coldhead piston. Also, the OVC and the sample holder show considerable common-mode vibrations, for instance at  $\approx 6$  Hz for the X-direction as visible in Fig. 7.5(a) with a peak-to-peak amplitude of  $20 \mu\text{m}$ , with these vibrations completely absent in the corresponding difference signal in Fig. 7.5(b). In the difference signal in the X-direction shown in Fig. 7.5(b), a vibration at  $\approx 95$  Hz can be seen, also enlarged in the inset in Fig. 7.5(b). This is further investigated in Fig. 7.6(a), which plots the two measured signals together with the difference signals in a single plot, over a time span that is the same as in the inset in Fig. 7.5(b). In Fig. 7.6(a) it can be seen that the amplitude of the 95 Hz difference signal is larger than that of both the OVC and the sample holder 95 Hz signals and that the phases of the OVC and the sample holder 95 Hz signals are nearly  $180^\circ$  apart. Therefore a mechanical resonance, where the OVC and the sample holder vibrate anti-phase can clearly be identified in Fig. 7.6(b).



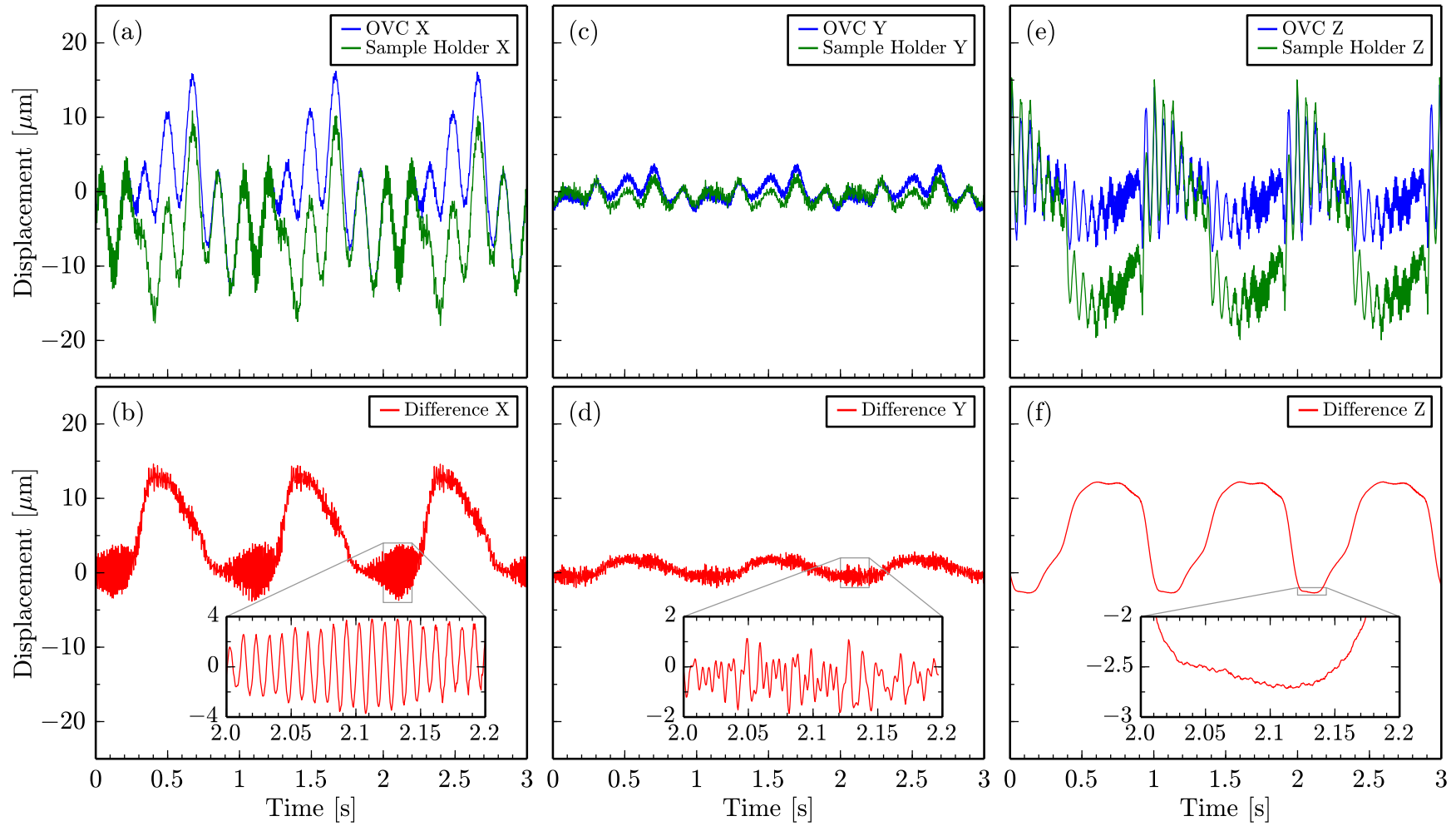


**Figure 7.5.:** Plot of typical vibration signatures recorded over three seconds for the three Cartesian measurement directions. Here, the upper panels (a), (c) and (e) directly plot the measured OVC and sample holder displacement signals for directions X, Y and Z, respectively, while the lower panels (b), (d) and (f) show the corresponding numerically computed difference signals. In each of the lower panels, an inset that plots an enlarged section of the differential vibration signal between 2.0 s and 2.2 s is drawn, where the displacement scale in the insets increases from  $\pm 4 \mu\text{m}$  in (b) to  $\pm 0.5 \mu\text{m}$  in (f).

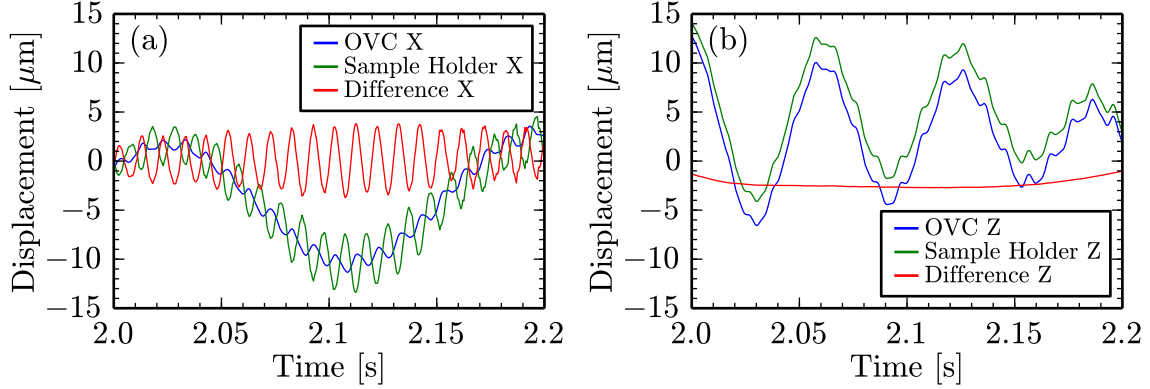


**Figure 7.6.:** Enlarged versions over 0.2 s of the signals of Fig. 7.5 in the X-direction are shown in (a), while (b) shows the signals in the Z-direction. Here, the two directly measured signals are plotted together with their numerical difference signals in order to enable their comparison.

The most striking result presented here is the difference signal in Fig. 7.5(f), which shows that in the Z-direction there is a complete absence of any high-frequency differential vibration signals, even though the 1 Hz coldhead piston movement is clearly present. Again, this is further investigated in Fig. 7.6(b), which plots the directly measured signals and their difference signal in a single plot over an enlarged time-scale of 0.2 s. Here, the complete absence of common-mode vibrations, in particular the  $\approx 15$  Hz vibration visible in the signals of both the OVC and the sample holder, is evident in the difference signal. Therefore, it can be concluded from both Figs. 7.5(e) and (f) and from Fig. 7.6(b) that in the Z direction, the system is very stiff without any resonance, and that both the OVC and the sample holder move practically as one unit, except for the differential coldhead piston movement.

Noise levels were determined from the difference signal in the Z-direction, recorded when the cryostat cooling system was switched off, because the structure is very stiff in the Z-direction and no mechanical resonances appear to exist. The differential signal in the Z-direction can be expected to be mostly free from environmental noise sources, because environmental noise is likely to be common to both measurement surfaces. The resulting instantaneous noise standard deviation for the difference signal in the Z-direction is 3.4 nm. Due to the downsampling of the signals in the FPGA that was described in Sec. 7.2, the phase noise over the whole quadrature bandwidth of 180 kHz is aliased into the signal band below 1 kHz, resulting in a high but very flat noise floor. Therefore it is possible to calculate a displacement noise level, which for the difference signal in Z-direction corresponds to  $8 \text{ pm} \cdot \text{Hz}^{-0.5}$ . From further measurements it is known that the noise shows a clear range dependency, which indicates that the measurements are laser phase noise dominated, as would be expected from the discussions in Chap. 6.

## 7.4. Discussion

The results shown in Fig. 7.5 and Fig. 7.6 clearly highlight the high measurement quality that can be obtained when the SFM technique is applied to vibrometry. Because multiple surfaces are measured simultaneously and along the same optical

beam, valuable insight into the origin of vibrations, allowing, for example, the identification of mechanical resonances, can be gained using the described approach. Regular commercial vibrometers use low-noise helium-neon lasers and can be operated in an OPD-balanced setup. Noise levels in commercial vibrometers [262] of  $0.05 \text{ pm} \cdot \text{Hz}^{-0.5}$  can thus be achieved, which are considerably lower than the value of  $8 \text{ pm} \cdot \text{Hz}^{-0.5}$  typical for the this system. However, it is thought that there are many applications where the instrumental displacement noise is not the limiting factor. Instead, the possibility of suppressing environmental noise [270] by local referencing of the measurement could be a much more important practical advantage. The ability of this approach to perform common-mode vibration suppression was clearly demonstrated by the example measurements in this chapter, where common-mode movements of the cryostat are suppressed to a high degree in the differential signal, as particularly evident in Fig. 7.6(b).

Furthermore, the technique allows the suppression of spurious reflections based on their range and also permits the verification of the range of the return signals, which can be useful in practical operation in order to exclude reflections from surfaces, such as windows [264], that are not of interest. Also, the technique is in principle extendable to more than two measurement surfaces. In general, in a collimated measurement configuration, return signal powers are lower than for a focused configuration. Also, a collimated beam will result in a higher angular sensitivity than the focused beam configurations typically used in LDV [138, 262, 263], requiring tighter angular alignment tolerances of the surfaces. The optical configuration, however, is of no relevance to the signal processing, as long as sufficient return power is received, therefore a focused configuration could equally be used with the SFM technique if only a single surface is of interest. It is thought that, due to the cost-effective implementation and the simplicity of the fibre-coupled setup, the system could have applications for permanently installed displacement or vibration sensors for multi-surface interrogation, even if only a single surface is to be evaluated.

## 7.5. Summary

The range-resolved interferometric signal processing technique based on sinusoidal optical frequency modulation presented in Chap. 6 has been applied to multi-surface vibrometry. Using a very simple fibre-coupled optical setup with complete down-lead insensitivity and with component costs totalling less than £3k, simultaneous measurements of the vacuum window and the sample holder inside an industrial table-top cryostat have been obtained. Vibration measurements with typical displacement noise levels of  $8 \text{ pm} \cdot \text{Hz}^{-0.5}$  have been demonstrated, with an interferometric quadrature bandwidth of 180 kHz. These results highlight the ability of the approach to separate common-mode vibrations of the whole cryostat from differential vibrations between the sample holder and the window. It was demonstrated how this is useful in identifying mechanical resonances. Further applications are envisaged in areas where the cost-effectiveness and robustness of the setup would allow permanently installed vibration or displacement sensors to be used or where local referencing, using a window close to the target, would permit environmental noise suppression.



## 8. Conclusion and Outlook

### 8.1. Conclusion

During the course of this PhD project, two independent, novel, range-resolved optical interferometric signal processing techniques, based on code-division multiplexing (CDM) and sinusoidal optical frequency modulation (SFM), have been proposed and experimentally demonstrated. Both of these techniques were applied to the fibre segment interferometry (FSI) approach that forms the main theme of this thesis, with the SFM technique additionally applied to multi-surface vibrometry.

The main novelty of the first technique is the combination of single-sideband (SSB) signal processing with CDM. This allows both interferometric phase evaluation and range-based signal separation to be performed using only a single, regular electro-optic phase modulator. This is in contrast to prior work in this area, where more complex modulator arrangements were used. A particular achievement of this work is thought to be the realisation and quantification of the significant influence that the anti-aliasing filtering, which is necessary in any digital signal processing system, can have on the linearity and crosstalk performance. This is thought to be a general result that is also applicable to other CDM techniques. In this work, the impact of the anti-aliasing filtering has been included in the theoretical description, albeit only for stationary phase signals in its current state of development. Nevertheless, it was confirmed experimentally that this allows the prediction of the measured linearity performance with good agreement. Therefore this theoretical approach can be used to evaluate different filter design choices and thus accelerate future system design.

The SFM technique was experimentally demonstrated using sinusoidal injection current modulation on a laser diode, leading to a very simple setup without any external modulator. The key innovation in the SFM signal processing technique is the application of a smooth window function to remove sidelobe energy compared to the rectangular window/gating functions that were used in prior work in this area. In addition to this, for the constituent interferometer to be interrogated, a time-variant carrier is used for interferometric phase demodulation that resembles the expected complex version of the interferometric photo detector signal expected. The combination of these improvements then allows the interrogation of constituent interferometers with continuously variable optical path differences (OPD), subject to a minimum OPD separation, without any apparent drop in linearity. This greatly improves the practicality and flexibility of the approach compared to prior work. A detailed theoretical description has been developed for the SFM technique and it was shown through numerical modelling that in practical operation of the SFM technique,

linearity and crosstalk are mainly affected by the number of quantisation levels available to the digitised photo detector signal and that there is no theoretical limit for the achievable linearity. The approximate validity of these modelling predictions was confirmed by two independent experiments. Furthermore, it was experimentally demonstrated that non-idealities arising from injection current modulation in real laser diodes can be reliably corrected in post-processing, however, even without any correction, measurements at reduced performance are still possible.

The linearity, crosstalk and noise performance for both the CDM and the SFM techniques was experimentally characterised using mostly the same criteria for both techniques, where key performance parameters were also discussed individually for the two techniques in the respective summary sections, Sec. 5.7 and Sec. 6.7. Additionally, the most important performance parameters are also summarised in Table 8.1. When comparing the two techniques, the demonstration experiments showed an order of magnitude improvement in the non-linearity errors for the SFM technique compared to the CDM technique, achieving cyclic error levels down to 1.0 mrad for the SFM technique. Similarly, crosstalk suppression levels in the quadrature signals were improved by an order of magnitude for the SFM technique, reaching typical values of  $\leq -60$  dB. In both cases, it was found that crosstalk levels in the resultant phase signals were lower than in the quadrature signals and phase signal crosstalk at the determined magnitudes  $\leq -60$  dB is thought to be negligible in many applications. It was established for both techniques that at typical power levels they are in laser

**Table 8.1.:** Comparison of key performance parameters of the two proposed techniques.

Parameter	Techn.	Value	Notes
<i>Non-Linearity Errors</i>	CDM	$\pm 0.03$ rad	Fig. 5.24(c)
	SFM	$\pm 0.001$ rad	Fig. 6.11(d) for Nested MZ Exp.
		$\pm 0.006$ rad	Fig. 6.22(c) for FSI Exp.
<i>Quadrature Crosstalk</i>	CDM	$\leq -32$ dB	Fig. 5.22(c)
	SFM	$\leq -60$ dB	Fig. 6.14(a)
<i>Phase Signal Crosstalk</i>	CDM	$\leq -60$ dB	Figs. 5.26(c), (d) and (e)
	SFM	$\leq -70$ dB	Fig. 6.14(b)
<i>Quadrature Bandwidth</i>	CDM	20 kHz (208 kHz)	Dem. (Theo.); see Sec. 5.4.4
	SFM	43 kHz	FSI; see Sec. 6.3.1
		180 kHz	Vibrometry; see Sec. 7.2
<i>Single Interf. Phase Noise</i>	CDM	$0.022 \text{ mrad Hz}^{-0.5} \text{ m}^{-1}$	Fig. 5.18(c) for 1 kHz to 20 kHz
	SFM	$0.16 \text{ mrad Hz}^{-0.5} \text{ m}^{-1}$	Fig. 6.18(b) for 1 kHz to 43 kHz
<i>FSI Segments</i>	CDM	4 @ 16.5 m	see Sec. 5.4.3
	SFM	6 @ 0.125 m	see Sec. 6.5.1
<i>FSI Segment Phase Noise</i>	CDM	$2.2 \text{ mrad Hz}^{-0.5}$	Fig. 5.28(c) for 1 kHz to 20 kHz
	SFM	$0.19 \text{ mrad Hz}^{-0.5}$	Fig. 6.25(b) for 1 kHz to 43 kHz

phase noise limited operation, and thus noise is a property of the quality of the laser diode only. However, observed single interferometer OPD-specific phase noise levels in the SFM technique at  $0.16 \text{ mrad Hz}^{-0.5} \text{ m}^{-1}$  were about seven times higher than corresponding values from the CDM results, presumably due to the detrimental effects of strong injection current modulation on the laser driver.

A further achievement in this work is thought to be the realisation of the significance of quadrature noise caused by aliased high-frequency laser phase noise, which is a phenomenon that has been observed before but does not appear to be widely known. This quadrature noise is OPD dependent and can leak from one constituent interferometer into others and has been observed for both CDM and SFM techniques. Therefore, the number of constituent interferometers that can be multiplexed as well as the permissible OPDs may ultimately be limited by quadrature noise. In this work, for the CDM technique, strong quadrature noise due to the large OPDs involved in the experiments has already led to a significant reduction in the available quadrature bandwidth, reducing this to approximately 10% of the theoretically possible value. It was found for both techniques that when only a single interferometer is present, the quadrature noise has a quadratic OPD dependence. It was also found that the noise behaviour for multiple constituent interferometers is very complex and that a future investigation confirming the exact origin of quadrature noise and its mutual interaction and correlation between multiple constituent interferometers is an important open research question arising from this work.

Both techniques were shown to achieve large quadrature bandwidths of many tens of kHz, with values up to 180 kHz demonstrated for the SFM technique. In this work, low-reflectivity (typically  $10^{-5}$ ), broadband ( $\approx 5 \text{ nm}$ ) fibre Bragg gratings (FBG) have been shown to be a suitable partial in-fibre reflector technique for FSI-based sensing, with measurements possible even for reflectivities as low as  $10^{-6}$ . A key advantage of the SFM technique over the CDM technique, apart from the simpler and more cost-effective optical setup, is the significantly increased spatial resolution possible. Here, using the same digital signal processing hardware, the minimum FSI segment length could be reduced from 16.5 m for the CDM technique to 0.125 m for the SFM technique, where 4 segments were multiplexed for the CDM technique and 6 for the SFM technique. This has been possible because the SFM technique, in contrast to the CDM technique, effectively decouples spatial resolution from the signal processing hardware bandwidth, making it a property of the laser source only. The high spatial resolution possible with the SFM technique also enabled the demonstration of the novel concept of simultaneous, single-beam multi-surface vibrometry in Chap. 7 as part of an industrial measurement. This also highlighted the particular usefulness of the approach for the detection of resonances and for the suppression of environmental noise through local referencing using a window.

Therefore, it can be concluded that in this work, two novel range-resolved optical interferometric signal processing techniques, based on very different physical principles, have been successfully theoretically described and experimentally demonstrated. Their performance has been characterised in detail, the advantages and disadvantage of each technique have been extensively discussed and a multitude of future improvements, research directions and applications have been proposed.

## 8.2. Outlook

**Application Overview** The future usefulness of the two proposed techniques will most likely be decided by their spatial resolution capabilities, their linearity performance and their ease of deployment and cost-effectiveness. Based on these criteria, the SFM technique offers very compelling advantages. Therefore, as discussed in Sec. 6.6.2, the SFM technique could be beneficially used in many applications for both FSI-based sensing as well as outside FSI. Potential future FSI applications for the SFM technique could include structural health monitoring, fibre optic shape sensing, high spatial resolution FSI and multi-wavelength FSI for absolute measurements or temperature/strain discrimination. Also outside FSI, the application to multi-surface vibrometry<sup>1</sup> has already proven its usefulness in an industrial environment and its extension to more surfaces, improving the spatial resolution by using more widely-tunable lasers or increasing the quadrature bandwidth through faster modulation remain further research avenues to be pursued. Furthermore, the potential of replacing polarisation-based path isolation with range-based signal separation in combination with the very high linearity values that the SFM technique is thought to offer for large processing bitwidths could lead to future impact in high-precision displacement interferometry.

However, it is also thought that the CDM technique could be advantageously used for longer range applications, using the direct interference, low-coherence FSI configurations proposed in Sec. 5.6.2, and where the SFM technique cannot operate in a direct interference FSI configuration. In direct segment interference, the dynamic range set by the fixed quadrature bandwidth is not shared by all segments, where the sharing of dynamic range between sensors would pose a particular problem for long sensing fibres. Application areas could include structural health monitoring and fibre optic shape sensing on large structures. Using widely available signal processing hardware, the segment length in CDM FSI could be improved to several metres and, for a direct interference configuration, where all segment data is nearly OPD balanced and quadrature noise levels should thus be low, the multiplexing of many more fibre segments is thought to be possible. Targeting total sensing fibre lengths of several hundreds of metres, the CDM technique could bridge the gap between fully distributed sensing techniques and fully localised sensing techniques. Here, in contrast to other dynamic and relatively cost-effective distributed techniques, such as distributed acoustic sensing, FSI, as an interferometric technique, inherently offers fully quantitative measurements, and compared to localised grating-based approaches, FSI offers continuous measurements without sensing gaps.

**Application to Robotic End-Effector Sensing<sup>2</sup>** A specific application of the SFM technique that is highlighted here is robotic end-effector sensing. It has already been discussed in Sec. 6.6.2 that the range information that is present in the demodulation parameter maps of Fig. 6.10 could be used to measure the absolute distance between

<sup>1</sup>Impact acceleration funding has been awarded to upgrade the breadboard-based setup of Fig. 7.1(a) into an enclosed prototype to showcase the approach to interested parties (see Page 179).

<sup>2</sup>This proposal has won impact acceleration funding to build an initial demonstrator and research council funding has been awarded to pursue this in a three year programme (see Page 179).

the fibre-tip reflection and object when suitably calibrated, with feasibility studies resulting in typical resolutions between 10 to 100  $\mu\text{m}$  for absolute distance measurements using modulation parameters similar to Chap. 6. In the proposed sensor concept, using a system similar to the vibrometry setup illustrated in Fig. 7.1(b), interferometric phase evaluation is used to obtain relative displacement measurements with nm resolution alongside coarser absolute distance measurements as described above. The high displacement resolution that the interferometric approach can offer is particularly useful for obtaining accurate derivative velocity and acceleration information for control purposes. Using at least three spatially offset interferometric sensor beams would then additionally allow the measurement of angular changes at high interferometric resolution and absolute tilt angles at lower resolution. This is illustrated in Fig. 8.1(a) for a four-beam interferometric system, with the forth beam used for redundancy purposes. In the proposed sensor concept this is then combined with laser speckle velocimetry [271–273] to provide in-plane measurements of relative motion and rotation, as illustrated in Fig. 8.1(b), with feasibility studies indicating a spatial resolution in the  $\mu\text{m}$  range. The combined sensor could then be mounted on a robotic end-effector, allowing the measurement of relative position and angular changes between a robotic end-effector and a workpiece in all directions, with absolute measurements of the out-of-plane distance and tilt measurements at lower precision and with both techniques allowing high data rates well beyond 1 kHz.

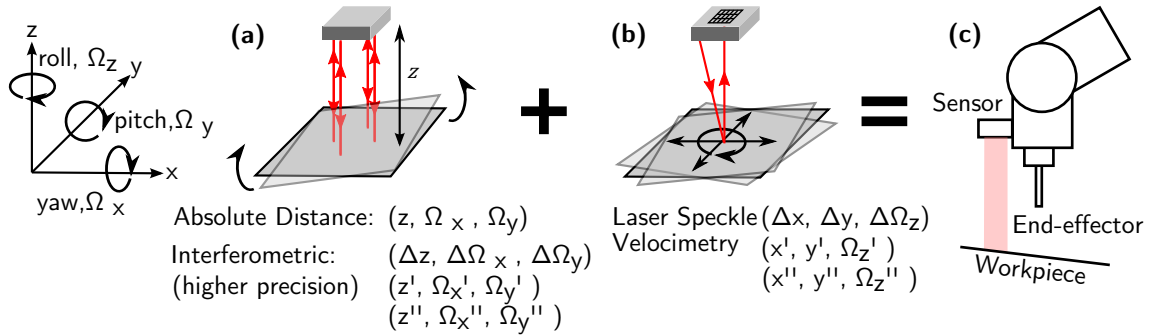


**Figure 8.1.:** Robotic end-effector sensing concept, where (a), using the SFM technique, shows a multi-beam measurement of out-of-plane distance and displacement as well as tilt between robot and the workpiece. (b) then illustrates how laser speckle velocimetry is used to measure in-plane movement and rotation. Finally, (c) shows the combined sensor mounted on the robot end-effector.

The main application area of such an end-effector sensor is thought to be the stabilisation and control of the end-effector relative to the workpiece in order to reduce the negative effects arising from robot end-effector vibrations. Here, it is intended to use the combined sensor to measure linear and angular movements of the robot end-effector relative to the workpiece and use this data to correct the production process. It is thought that this would be particularly beneficial in the area of laser-based processing [274, 275], where the direction and focus of the laser beam used for processing could be adjusted using beam steering and focusing equipment that is often already present in advanced laser processing systems. Further possible applications include motion tracking to lock the robot to a moving assembly line [276] and relative positioning operations, where high relative tolerances between component mounting positions require high-precision relative measurements [277].

**Application to Fibre Optic Shape Sensing<sup>3</sup>** Fibre optic shape sensing [26, 27, 81], often also referred to as bend or curvature sensing, allows the fibre path, and the structure to which the fibre is attached, to be followed through space and any lateral displacements to be inferred. Here, a key advantage is that the measurand, curvature, is directly determined within the sensing fibre and does not rely on strain transfer from the structure. Also, when differential measurements in multi-core fibres (MCF) are used, common-mode influences, such as temperature and longitudinal strain, are automatically compensated. It was discussed in Sec. 6.6.2 that strain resolution increases proportionally with sensor gauge length in interferometric curvature sensing, which is a considerable principle advantage. Here, competing approaches are based on long-period gratings [81] (LPGs) and fibre Bragg gratings [26] (FBGs) (see also Sec. 2.3). However, LPGs are difficult to multiplex and sensitive to the surrounding medium, which affects robustness, whilst FBG-based sensing, as discussed in Secs. 5.6.1 and 6.6.1, offers considerably lower dynamic strain sensitivities.

The fibre-optic shape sensing concept is illustrated in Fig. 8.2 for the SFM technique. Here, using the FSI approach that is detailed in Sec. 6.5 where FBG in-fibre partial reflectors are used, three cores of a commercially available four-core MCF are separately interrogated. This results in curvature sensors for the two Cartesian directions  $x$  and  $y$ , as illustrated in Fig. 8.2. However, in order to mitigate polarisation-induced fading (see Sec. 2.4), polarisation-diversity detection [101] is used, requiring three photo detectors and associated signal processing per interrogated fibre core. In addition to the use of the SFM technique illustrated in Fig. 8.2, a related interrogation approach using the CDM technique could have advantages for longer range applications, where spatial resolution is not critical, as outlined before.

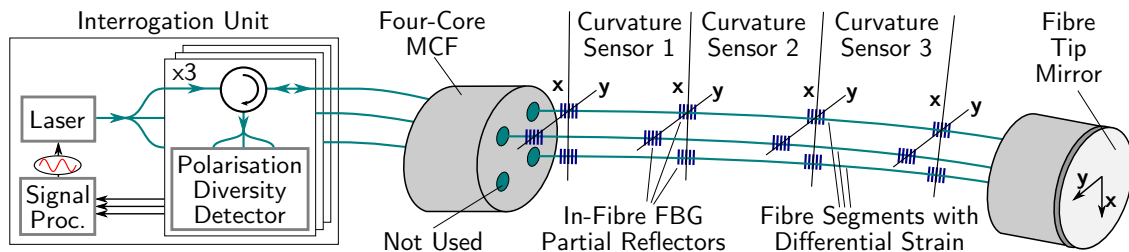


**Figure 8.2.:** Application of the SFM technique to fibre optic shape sensing using MCF. The interrogation setup is similar to the previous FSI setup in Fig. 6.19, except for the use of polarisation-diversity detection, requiring three photo detectors and associated signal processing. Furthermore, three complete detector units for each of the three interrogated MCF cores are required. Within the MCF, the interferometric reference is provided by the fibre tip mirror, and three resulting curvature sensors for both Cartesian directions  $x$  and  $y$  are illustrated.

Key applications of fibre optic shape sensing using the SFM technique are thought to be active control of aerodynamic structures, such as aircraft wings [278, 279] or wind turbine blades [82, 280] to improve efficiency and alleviate loads to increase service life. Further applications include structural health monitoring for engineering structures, in particular dynamic approaches such as vibration-based condition monitoring [256]. Additionally, due to the longer ranges it offers, the CDM technique could be applied advantageously in the monitoring of civil engineering and geotechnical structures.

<sup>3</sup>A research proposal involving this approach is currently in preparation.

# List of Publications and Outcomes

The following publications and other outcomes have resulted from the work presented in this thesis:

## Journal Papers

1. T. Kissinger, T. O. H. Charrett, and R. P. Tatam. Range-resolved interferometric signal processing using sinusoidal optical frequency modulation. *Optics Express*, 24(7):9415-9431 (17pp), 2015.
2. T. Kissinger, T. O. H. Charrett, and R. P. Tatam. Fibre segment interferometry using code-division multiplexed optical signal processing for strain sensing applications. *Measurement Science and Technology*, 24:094011 (13pp), 2013.

## Peer-Reviewed Conference Papers

3. T. Kissinger, R. Correia, T. O. H. Charrett, S. W. James, and R. P. Tatam. Range-resolved signal processing for fibre segment interferometry applied to dynamic long-gauge length strain sensing. *Proceedings of the 24th International Conference on Optical Fiber Sensors (OFS-24), Curitiba, Brazil*, Proc. SPIE 9634:1Q (4pp, Oral presentation), 2015.
4. T. Kissinger, T. O. H. Charrett, and R. P. Tatam. Range-resolved single-sideband optical fibre interferometry for quasi-distributed dynamic strain sensing. *Proceedings of the 22th International Conference on Optical Fiber Sensors (OFS-22), Beijing, China*, Proc. SPIE 8424:8I (4pp, Poster presentation), 2012.

## Further Conference Papers

5. T. Kissinger, T. O. H. Charrett, S. W. James, A. Adams<sup>1</sup>, A. Twin<sup>1</sup>, and R. P. Tatam. Simultaneous laser vibrometry on multiple surfaces with a single beam system using range-resolved interferometry. *Proceedings of SPIE Optical Metrology 2015, Munich, Germany*, Proc. SPIE 9525:20 (7pp, Oral presentation), 2015.

---

<sup>1</sup>Oxford Instruments plc

### **Further Conference Participation**

6. T. Kissinger, T. O. H. Charrett, S. W. James, and R. P. Tatam. Cost-effective vibration and displacement measurement using range-resolved interferometry. *10<sup>th</sup> International Conference on Advances in Experimental Mechanics, Edinburgh, UK*, (Oral presentation), 2015.
7. T. Kissinger, R. Correia, T. O. H. Charrett, S. W. James, and R. P. Tatam. Multiplexing of long-gauge length fibre optic dynamic strain sensors using range-resolved interferometry. *10<sup>th</sup> International Conference on Advances in Experimental Mechanics, Edinburgh, UK*, (Oral presentation), 2015.
8. T. Kissinger, T. O. H. Charrett, and R. P. Tatam. Range-resolved optical fibre interferometry for quasi-distributed dynamic strain sensing. *Photon12, Durham, UK*, (Oral presentation), 2012.

### **Patent Application**

1. T. Kissinger, T. O. H. Charrett, and R. P. Tatam, Range-resolved optical interferometric signal processing using sinusoidal optical frequency modulation, *Patent Application*, GB1416037.8, 2014.

### **Award Nomination**

1. T. Kissinger, T. O. H. Charrett, S. W. James, and R. P. Tatam, Multi-surface optical interferometric vibrometry, Shortlisted for *The IET Innovation Awards 2015: Category Measurement in Action*, 2015.

### **Research Grants**

1. T. Kissinger (Researcher Co-Investigator), T. O. H. Charrett (Co-Investigator), and R. P. Tatam (Principal Investigator). Novel optical instrumentation for robotic manufacturing, *Engineering and Physical Sciences Research Council (EPSRC) UK*, Grant EP/M020401/1, Value: £646880, Duration: 3 years, 2015-2018.
2. T. Kissinger, T. O. H. Charrett, and R. P. Tatam. Novel optical optimisation for robot manufacturing, *Institutional EPSRC Impact Acceleration Account Early Stage Support Funding*, Value: £38400, Duration: 4 months, 2015.
3. T. Kissinger, S. W. James, and R. P. Tatam. Range resolved fibre optic interferometry, *Institutional EPSRC Impact Acceleration Account Early Stage Support Funding*, Value: £39445, Duration: 4 months, 2014-2015.



# A. Derivation of the Single Sideband Equations

The derivation of the single-sideband equations (SSB) is not explained in detail in prior work [164, 165]. Therefore in Appendix A.1, the necessary steps are described for instructive purposes and also include the actual demodulation of the desired phase signal  $\varphi(t)$  not performed in prior work. This is in preparation for the derivation of the extended equations in Appendix A.2, which incorporate multiple signal sources, the influence of the anti-aliasing filter and the decoding function for code-division multiplexing (CDM).

## A.1. Derivation of Single Sideband Equations in Prior Work

Starting by restating Eq. (5.1):

$$U_{\text{pd}}(t) = R(P_{\text{off}} + P_{\text{eff}} \cdot \cos[\varphi(t) + s\tilde{\theta}(t)]) \quad (\text{A.1})$$

Rewriting the cosine using complex exponentials and splitting the phase terms:

$$U_{\text{pd}}(t) = RP_{\text{off}} + 0.5RP_{\text{eff}} \left( \exp[j \cdot \varphi(t)] \cdot \exp[j \cdot s\tilde{\theta}(t)] + \exp[-j \cdot \varphi(t)] \cdot \exp[-j \cdot s\tilde{\theta}(t)] \right) \quad (\text{A.2})$$

Now expanding the phase-modulated exponential terms with  $s\tilde{\theta}(t)$  that are periodic with modulation period  $T_m = f_m^{-1}$  by a complex Fourier series expansion [281] with integer harmonic index  $n$ :

$$U_{\text{pd}}(t) = RP_{\text{off}} + 0.5RP_{\text{eff}} \left( \exp[j \cdot \varphi(t)] \cdot \left( \sum_{n=-\infty}^{\infty} c_n \exp[j \cdot 2\pi n f_m t] \right) + \exp[-j \cdot \varphi(t)] \cdot \left( \sum_{n=-\infty}^{\infty} \hat{c}_n \exp[j \cdot 2\pi n f_m t] \right) \right) \quad (\text{A.3})$$

with

$$c_n = \frac{1}{T_m} \int_{-\frac{T_m}{2}}^{\frac{T_m}{2}} \exp[j \cdot s\tilde{\theta}(t)] \cdot \exp[-j \cdot 2\pi n f_m t] dt \quad (\text{A.4})$$

$$\hat{c}_n = \frac{1}{T_m} \int_{-\frac{T_m}{2}}^{\frac{T_m}{2}} \exp[-j \cdot s\tilde{\theta}(t)] \cdot \exp[-j \cdot 2\pi n f_m t] dt \quad (\text{A.5})$$

Noting that:

$$\hat{c}_n = c_{-n}^* \quad (\text{A.6})$$

Using this to rewrite the last sum term in Eq. (A.3) as:

$$\begin{aligned} \sum_{n=-\infty}^{\infty} \hat{c}_n \exp[j \cdot 2\pi n f_m t] &= \sum_{n=-\infty}^{\infty} \left( c_{-n} \exp[-j \cdot 2\pi n f_m t] \right)^* \\ &= \sum_{n=-\infty}^{\infty} \left( c_n \exp[j \cdot 2\pi n f_m t] \right)^* \end{aligned} \quad (\text{A.7})$$

Here the last operation is just a resorting of the sum terms. Using this allows Eq. (A.3) to be rewritten as:

$$\begin{aligned} U_{\text{pd}}(t) = RP_{\text{off}} + 0.5RP_{\text{eff}} \cdot &\sum_{n=-\infty}^{\infty} \left( c_n \cdot \exp[j \cdot \varphi(t)] \cdot \exp[j \cdot 2\pi n f_m t] \right. \\ &\left. + \left( c_n \cdot \exp[j \cdot \varphi(t)] \cdot \exp[j \cdot 2\pi n f_m t] \right)^* \right) \end{aligned} \quad (\text{A.8})$$

This can be expressed as the real part using the formula  $\text{Re}\{z\} = 0.5z + 0.5z^*$  for any complex number  $z$ , where  $c_n$  is still given by Eq. (A.4), as:

$$U_{\text{pd}}(t) = RP_{\text{off}} + RP_{\text{eff}} \cdot \sum_{n=-\infty}^{\infty} \text{Re} \left\{ c_n \cdot \exp \left[ j \cdot \left( \varphi(t) + 2\pi n f_m t \right) \right] \right\} \quad (\text{A.9})$$

Eq. (A.9) is the analogous version of the SSB equations given in prior work [165]. In this work, however, the demodulation of the phase signal  $\varphi(t)$  is included in the derivation, which is best carried out using the signal of the previous version of the SSB equation of Eq. (A.8). The complex demodulation carrier function  $C_n(t)$  at the chosen carrier harmonic of integer harmonic index  $n$  is given by:

$$C_n(t) = \exp[-j \cdot 2\pi n f_m t] \quad (\text{A.10})$$

For demodulation, the signal  $U_{\text{pd}}(t)$  of Eq. (A.8) is digitally multiplied with the carrier  $C_n(t)$  of Eq. (A.10) and the resultant signal is then low-pass filtered at cut-off frequency  $f_{\text{Q,co}} \leq 0.5f_m$  (see also Sec. 3.1.4). The low-pass filter (LP), in effect, removes the sum sign in Eq. (A.8) and only two exponential terms remain. When the single-sided quadrature bandwidth  $B_{\text{Q,ss}}$  of the phase signal  $\varphi(t)$  is within permitted limits, i.e.  $B_{\text{Q,ss}} \leq f_{\text{Q,co}}$ , only terms at  $+n$  and  $-n$ , for the first and second complex exponential terms in Eq. (A.8) respectively, fall within the output bandwidth of the low-pass filter. Demodulation at  $n = 0$  serves no purpose and therefore, for demodulation with a carrier of harmonic index  $n \neq 0$ , the resultant low-pass filtered complex quadrature signal  $U_{\text{Q},n}(t)$ , with  $c_n$  from Eq. (A.4), is given by:

$$\begin{aligned} U_{\text{Q},n}(t) &= \text{LP} \left\{ C_n(t) \cdot U_{\text{pd}}(t) \right\} \\ &= 0.5RP_{\text{eff}} \cdot \left( c_n \cdot \exp[j \cdot \varphi(t)] + c_{-n}^* \cdot \exp[-j \cdot \varphi(t)] \right) \end{aligned} \quad (\text{A.11})$$

## A.2. Derivation of Extended Single Sideband Equations for Stationary Phase Signals

Starting by inserting  $U_{\text{pd}}(t)$  of Eq. (5.8) into Eq. (5.10) results in:

$$U_{\text{dec}}(t, \tau_d) = d(t - \tau_d) \cdot \left( h_{\text{comb}}(t) * (RP_{\text{off}}) \right) + \sum_{k=1}^{k_{\text{max}}} d(t - \tau_d) \cdot \left( h_{\text{comb}}(t) * \left( RP_{\text{eff},k} \cdot \cos[\varphi_k(t + \tau_k) + s\tilde{\theta}(t + \tau_k)] \right) \right) \quad (\text{A.12})$$

Rewriting the cosine in exponential terms analogous to Eq. (A.2) yields:

$$U_{\text{dec}}(t, \tau_d) = d(t - \tau_d) \cdot \left( h_{\text{comb}}(t) * (RP_{\text{off}}) \right) + \sum_{k=1}^{k_{\text{max}}} d(t - \tau_d) \cdot \left( h_{\text{comb}}(t) * \left( 0.5RP_{\text{eff},k} \cdot \left( \exp[j \cdot \varphi_k(t + \tau_k)] \cdot \exp[j \cdot s\tilde{\theta}(t + \tau_k)] + \exp[-j \cdot \varphi_k(t + \tau_k)] \cdot \exp[-j \cdot s\tilde{\theta}(t + \tau_k)] \right) \right) \right) \quad (\text{A.13})$$

Ideally, in the derivation of the extended SSB equations, the effects of the combined anti-aliasing filter impulse response  $h_{\text{comb}}(t)$  and the CDM decoding function  $d(t - \tau_d)$  would also be included in the Fourier coefficients along with the phase modulation function  $s\tilde{\theta}(t + \tau_k)$ . However, this is not possible because the convolution with respect to time of  $h_{\text{comb}}(t)$  also acts on the time-variable exponential phase terms with  $\varphi_k(t + \tau_k)$ , preventing straightforward disassociation of these terms. If, on the other hand, a stationary phase  $\varphi_k(t + \tau_k) := \varphi_k$  is assumed then the scalar associativity property [282] of the convolution can be used to let  $h_{\text{comb}}(t)$  act only on the exponential terms with  $s\tilde{\theta}(t + \tau_k)$  and all these effects can then be described solely by the Fourier coefficients of the expansion.

This assumption of stationary phase signal is used in the following and appears to hold well in the experiments, apparently because the occurring phase signals  $\varphi_k(t + \tau_k)$  change over time scales much slower than the length  $T_h$  of  $h_{\text{comb}}(t)$ . Using this assumption allows the Fourier expansion of Eq. (A.13) to be carried out analogous to Eq. (A.3) to Eq. (A.8). This is possible because both  $d(t - \tau_d)$  and  $h_{\text{comb}}(t)$  are real functions that do not interfere with the complex conjugations and both  $R$  and  $P_{\text{eff},k}$  are assumed stationary. Note that the common periodic frequency of all terms is now  $f_{\text{code}} = T_{\text{code}}^{-1}$  as given by Eq. (5.7), resulting in:

$$U_{\text{dec}}(t, \tau_d) = d(t - \tau_d) \cdot \left( h_{\text{comb}}(t) * (RP_{\text{off}}) \right) + \sum_{k=1}^{k_{\text{max}}} \sum_{n=-\infty}^{n=\infty} 0.5RP_{\text{eff},k} \cdot \left( c_{n,k}(\tau_d) \cdot \exp[j \cdot \varphi_k] \cdot \exp[j \cdot 2\pi n f_{\text{code}} t] + \left( c_{n,k}(\tau_d) \cdot \exp[j \cdot \varphi_k] \cdot \exp[j \cdot 2\pi n f_{\text{code}} t] \right)^* \right) \quad (\text{A.14})$$

with the Fourier coefficients  $c_{n,k}(\tau_d)$  given by:

$$\begin{aligned}
 c_{n,k}(\tau_d) &= \frac{1}{T_{\text{code}}} \int_{-\frac{T_{\text{code}}}{2}}^{\frac{T_{\text{code}}}{2}} \left( d(t - \tau_d) \cdot \right. \\
 &\quad \left. \left( h_{\text{comb}}(t) * \exp[j \cdot s\tilde{\theta}(t + \tau_k)] \right) \cdot \exp[-j \cdot 2\pi n f_{\text{code}} t] \right) dt \\
 &= \frac{1}{T_{\text{code}}} \int_{-\frac{T_{\text{code}}}{2}}^{\frac{T_{\text{code}}}{2}} \left( d(t - \tau_d) \cdot \right. \\
 &\quad \left. \left( \int_{-\frac{T_{\text{code}}}{2}}^{\frac{T_{\text{code}}}{2}} h_{\text{comb}}(t') \cdot \exp[j \cdot s\tilde{\theta}(t - t' + \tau_k)] dt' \right) \cdot \right. \\
 &\quad \left. \exp[-j \cdot 2\pi n f_{\text{code}} t] \right) dt
 \end{aligned} \tag{A.15}$$

Here, the inner integral is the circular convolution [282] with  $h_{\text{comb}}(t)$ , which unlike the regular convolution is periodic in  $T_{\text{code}}$ . The transition between regular and circular convolution is possible because  $\tilde{\theta}(t + \tau_k)$  is a periodic function and straightforward because  $T_h < T_{\text{code}}$  is assumed.

Analogous to Appendix A.1, demodulation of the phase signal  $\varphi_k$  involves digital multiplication of  $U_{\text{dec}}(t, \tau_d)$  of Eq. (A.14) with the complex carrier  $C_n(t)$  and subsequent low-pass (LP) filtering at quadrature signal cut-off frequency  $f_{Q,\text{co}} \leq 0.5f_{\text{code}}$ . The complex demodulation carrier function  $C_n(t)$  at the chosen carrier of integer harmonic index  $n$  is given by:

$$C_n(t) = \exp[-j \cdot 2\pi n f_{\text{code}} t] \tag{A.16}$$

The absence of any influence from the first term involving  $RP_{\text{off}}$  in Eq. (A.14) can only be guaranteed when the anti-aliasing filter has zero DC transmission on top of the assumption that  $R$  and  $P_{\text{off}}$  are stationary because  $d(t - \tau_d)$  itself is also time-variable. Thus there is an additional requirement for the anti-aliasing filter impulse response  $h_{\text{comb}}(t)$  to adhere to a band-pass characteristic with zero transmission at DC, which can easily be implemented digitally. For the relevant cases with  $n \neq 0$ , where, analogous to App. A.1, the LP-filter selects only two exponential terms for each of the  $k_{\text{max}}$  constituent interferometers and the resultant complex quadrature signal  $U_{Q,n}(t, \tau_d)$ , with  $c_{n,k}(\tau_d)$  as stated in Eq. (A.15), can then be given by:

$$\begin{aligned}
 U_{Q,n}(t, \tau_d) &= \text{LP} \left\{ C_n(t) \cdot U_{\text{dec}}(t, \tau_d) \right\} \\
 &= \sum_{k=1}^{k_{\text{max}}} 0.5 R P_{\text{eff},k} \cdot \left( c_{+n,k}(\tau_d) \cdot \exp[j \cdot \varphi_k] + c_{-n,k}^*(\tau_d) \cdot \exp[-j \cdot \varphi_k] \right)
 \end{aligned} \tag{A.17}$$

### Summary of the mathematical assumptions used in this derivation:

- Stationary phase signals  $\varphi_k$
- An anti-aliasing filter impulse response  $h_{\text{comb}}(t)$  that has zero transmission at DC and a length  $T_h$  shorter than the repetition period of the code  $T_{\text{code}}$
- Stationary power levels  $P_{\text{eff},k}$  and  $P_{\text{off}}$  as well as stationary responsivity  $R$

## B. Laser Diode Characterisation

Throughout this work an Eblana laser diode (EP1550-NLW-B01-200-FA; Serial Nr: YE1363) was used. This diode is packaged in a 14-pin butterfly package, with an optical isolator, a thermo-electric cooler and a thermistor included, and with the laser light leaving the diode through a polarisation-maintaining fibre lead. The laser was connected to a Profile LDC200 current controller and a Profile TED200 temperature controller. The working principle of this diode is known as a discrete mode laser [283] and is based on a regular ridge-waveguide Fabry-Perot cavity. Normally, a Fabry-Perot laser would yield multiple lasing modes, however in the discrete mode technique, the spatial index profile of the ridge is manipulated at several places in such a way that positive gain exists only for a single mode and all other modes are suppressed. In general, the linewidth of a laser is an accepted measure of the expected laser frequency noise and thus of the laser phase noise, with low linewidth corresponding to low frequency noise. Discrete mode laser diodes can reach low linewidths down to 100 kHz, which contrasts with other internal-cavity single-mode laser diode concepts, such as distributed feedback (DFB) lasers that typically reach linewidths between 1 and 5 MHz [283]. The Eblana laser diode used in this work has a specified linewidth of 200 kHz, however, it was found by the linewidth measurement shown in App. B.2 that in practice linewidths on the order of 0.6 MHz can be expected, presumably limited by the injection current noise of the laser driver.

In this Appendix, the laser diode current and temperature characteristics for static operation are first determined in App. B.1, followed by a laser linewidth measurement in App. B.2. Finally, the dynamic laser diode injection current modulation parameters for the SFM technique proposed in Chap. 6 are determined in App. B.3.

### B.1. Current and Temperature Characteristics

The static current and temperature tuning characteristics of the output power of the Eblana laser diode are plotted in Fig. B.1. The power was measured using an Ando AQ-2015 power meter, that was, however, not specifically calibrated. The results are shown as a function of laser injection bias current  $I_{LD}$  in Fig. B.1(a) at a fixed laser diode temperature  $T_{LD} = 25^\circ\text{C}$ , where a linear least square fit according to Eq. (5.22) of the data points above the laser threshold at  $I_{LD} \approx 31\text{ mA}$  is also shown. Fig. B.1(b) then shows the dependence of the output power on  $T_{LD}$  for a fixed value of  $I_{LD} = 100\text{ mA}$ , along with a quadratic least square fit according to

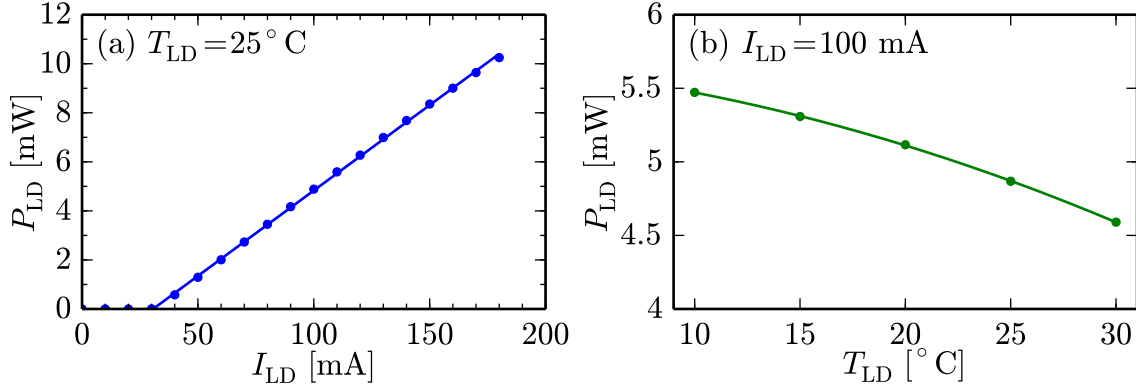


**Figure B.1.:** The output power of the laser diode is shown in (a) as a function of injection bias current  $I_{LD}$  at constant temperature, along with a linear fit above the laser threshold, and in (b), along with a quadratic fit, as a function of the laser diode temperature  $T_{LD}$  at constant current.

Eq. (5.22). Both fits show very good agreement with the measured data points, confirming a linear dependence of the output power on the injection current above the laser threshold and a quadratic dependence on the laser diode temperature.

The current and temperature tuning characteristics of the emission wavelength of the laser diode are then plotted in Fig. B.2. Here, the laser wavelength was measured using an Ando AQ-6310B spectrum analyser, that was, however, not specifically calibrated. The results are shown as a function of injection bias current  $I_{LD}$  in Fig. B.2(a) at a fixed diode temperature  $T_{LD} = 25^\circ\text{C}$ , where a quadratic least square fit of the data points above the laser threshold is also drawn. Fig. B.2(b) then shows the dependence of the output wavelength on  $T_{LD}$  at a fixed value of  $I_{LD} = 100\text{ mA}$ , along with a linear least square fit. Both fits show very good agreement with the measured data points, confirming a quadratic dependence of the emission wavelength on the injection current and a linear dependence of the emission wavelength on the laser diode temperature. The quadratic dependence of the emission wavelength on the injection current is the reason for the observed non-linearities for sinusoidal laser diode injection current modulation that were discussed in Chap. 6 and that are further characterised, as a function of modulation frequency, in App. B.3.

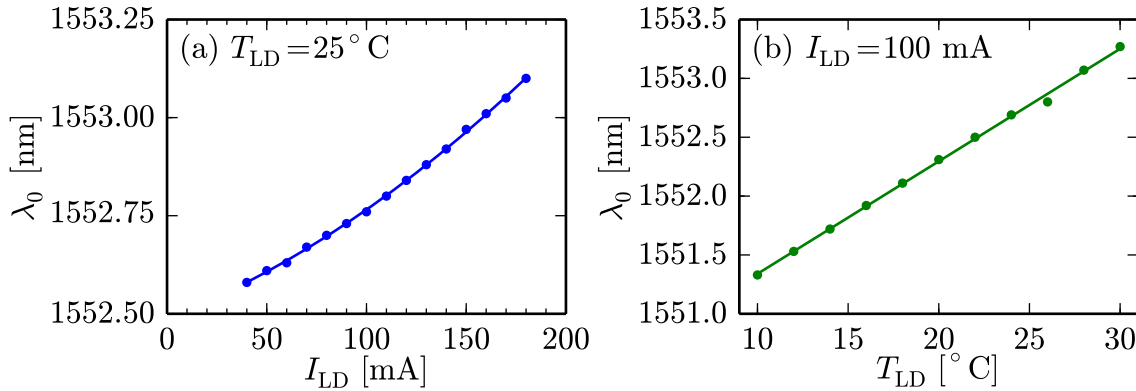


**Figure B.2.:** The emission wavelength of the Eblana laser diode is shown in (a) as a function of injection bias current  $I_{LD}$  at constant temperature, along with a quadratic fit, and in (b), along with a linear fit, as a function of the laser diode temperature  $T_{LD}$  at a constant bias current.

## B.2. Linewidth Measurement

The delayed self-heterodyne/self-homodyne method [284, 285] is widely used in the determination of laser frequency noise of highly coherent lasers, directly measuring the laser linewidth. Here, a self-homodyne approach adapted from Ludvigsen *et al.* [285] is used, with the setup illustrated in Fig. B.3 employing mostly the same equipment as the setup for the CDM technique of Fig. 5.11. In Fig. B.3, a sinusoidal phase modulation waveform of 30 MHz is introduced and the spectrum around this frequency, which is then free from electronic  $1/f$  noise, is evaluated. In this setup, the light leaving the laser diode has to be attenuated using an in-fibre attenuator in order not to saturate the photo detector. Part of the light is then guided via a polarisation controller, which optimises the polarisation modulation efficiency of the phase modulator that introduces the 30 MHz carrier. In order to remove any remaining dependence on the interferometric phase [285], the phase of the interferometer is then scrambled by a PZT modulator, driven using a randomised signal with phase excursions  $\approx 2\pi$ . In the other arm of the interferometer, a long fibre reel of regular SMF-28e+ fibre introduces a delay that is assumed to be much larger than the coherence time of the laser diode. After the two arms of the interferometer are recombined, the FPGA records the raw ADC data, which is then transferred to a PC, where the Fourier transforms are calculated and averaged. The length of the fibre reel was determined as  $1.86 \pm 0.02$  km using 6 repeats of a separate delay measurement. For this delay measurement, the phase of the sinusoidal intensity modulation waveform of the laser was determined using an oscilloscope with and without the fibre reel directly connected between the laser and photo detector.

The resultant laser linewidth measurements, with the spectral region around the carrier evaluated, are then shown in Fig. B.4 for three laser diode bias current settings of  $I_{LD} = [50, 100, 150]$  mA. Because the signal powers for each current setting are different, the number of averages was varied, with [20000, 5000, 2000] averages used for the three current settings, respectively. Here, Fig. B.4(a) shows the spectra for the three laser current settings over a frequency range of  $\pm 10$  MHz, while Fig. B.4(b) shows an enlarged version over a frequency range of  $\pm 2$  MHz. In both graphs, the spectra for  $I_{LD} = 100$  mA and 150 mA lie practically on top of each other while the spectrum for 50 mA is broader. A straightforward interpretation is that

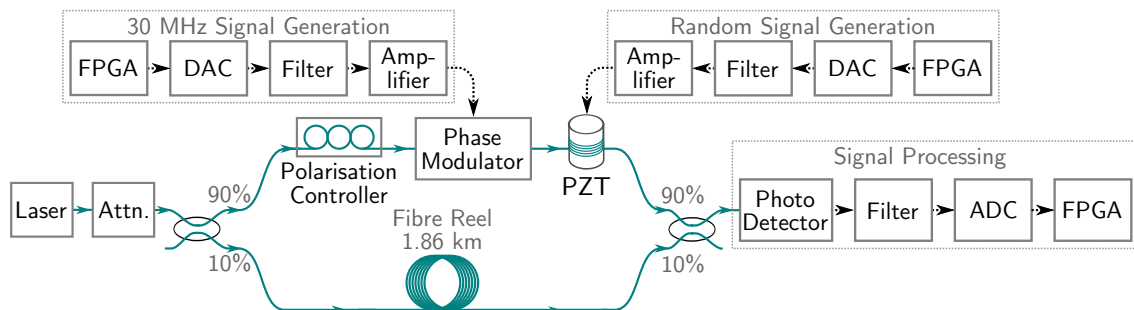


**Figure B.3.:** MZ interferometer setup for the homodyne linewidth measurement incorporating a 1.86 km long fibre reel, a phase modulator and PZT. Here, the FPGA generates both a 30 MHz carrier signal for the phase modulator and a signal that drives the PZT to randomise the interferometric phase, with the FPGA then also used to record the photo detector signal.

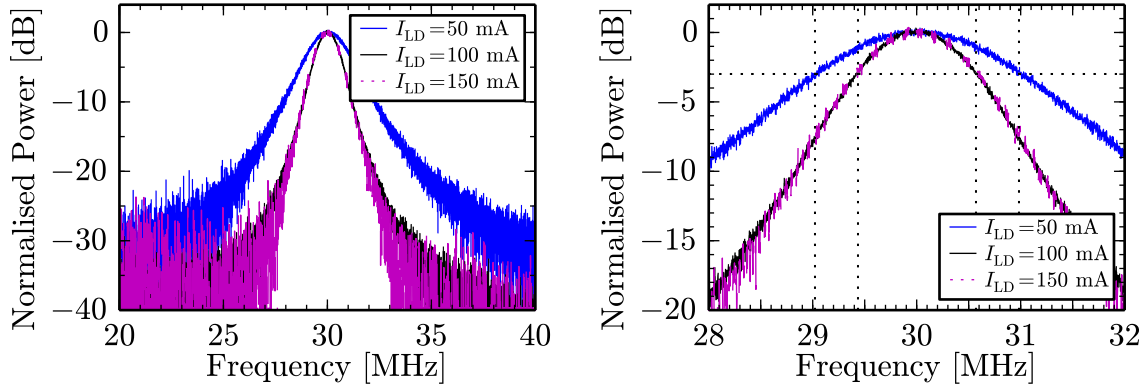


**Figure B.4.:** The results of the linewidth measurements for three laser diode bias current settings are shown over  $\pm 10$  MHz in (a) and over  $\pm 2$  MHz in (b) around the 30 MHz carrier. Guide lines for the determination of the linewidth values at a power level of  $-3$  dB are also shown in (b).

the spectrum at  $I_{LD} = 50$  mA is still broadened by the inverse power dependence of semiconductor laser diodes [283, 286], with any such linewidth narrowing then saturated for  $I_{LD} = 100$  mA and  $150$  mA. It can also be seen in Fig. B.4(a) that the previous assumption of a delay well beyond the coherence time of the laser is justified, because there are no side lobes visible in the spectra [285]. In order to determine the laser linewidth, dashed guide lines are drawn in Fig. B.4(b), marking the full-width half maximum (FWHM) of the spectral peaks, where the FWHM values equal half the linewidth of the laser [285]. The linewidths determined from Fig. B.4(b) are  $0.98$  MHz for  $I_{LD} = 50$  mA and  $0.57$  MHz for  $I_{LD} = 100$  mA and  $150$  mA, where in this work the laser is mainly operated at currents exceeding  $I_{LD} = 100$  mA. These measured laser linewidth values are well above the manufacturer specification of  $200$  kHz for  $I_{LD} \geq 150$  mA. However, it is thought that this could be due to laser injection current noise induced by the laser driver and does not necessarily originate from the laser diode. The injection current noise RMS value of the Profile LDC200 laser driver that is used is specified as up to  $1.5 \mu\text{A}$  for noise frequencies between  $10$  Hz and  $10$  MHz. From Fig. B.2(a), an approximate optical frequency change coefficient of  $0.5$  GHz per mA static injection current modulation can be obtained, where a rough approximation of the linewidth due to current noise of  $0.75$  MHz results from the multiplication of the two values. Therefore, linewidth values on the order of magnitude of the measured values could result from the injection current noise alone. This conjecture would also explain the observed saturation in the linewidth narrowing with laser power. Therefore higher laser driver current noise requirements are likely to be needed in order to improve the laser linewidth and thus reduce laser phase noise in future implementations.

### B.3. Frequency Modulation Characteristics

The characterisation of the sinusoidal frequency modulation parameters, in particular the intensity modulation and non-linear optical frequency parameters, is very important for the SFM technique presented in Chap. 6. In this Appendix, all necessary modulation parameters are determined and, additionally, the influence of changes in the diode bias current or temperature conditions investigated.



### B.3.1. Characterisation Methods

The single-sideband processing (SSB) technique used in Chap. 5, employing an external electro-optic phase modulator, is used here to resolve the phase modulation waveform introduced by the sinusoidal optical frequency modulation of the laser diode at the modulation parameters of interest. In order to capture this phase waveform, a very fast signal processing implementation is required. This is achieved by using the same SSB waveform template  $\hat{\theta}_{\text{wf}}(t_i)$  described by Eq. (5.18) and visible in Fig. 5.3(a), however, without any CDM encoding, i.e.  $x = y = 1$ , on a single interferometer. The resulting quadrature bandwidth can then be as high as  $f_{\text{Q,co,max}} = 0.5 \cdot T_{\text{wf}}^{-1} = 9.38 \text{ MHz}$  as discussed in Sec. 5.4.2 and Table 5.1, where in this measurement the actual quadrature signal bandwidth is limited to  $f_{\text{Q,co}} = 4.69 \text{ MHz}$  to reduce noise.

The optical setup used for this measurement, shown in Fig. B.5, is very similar to the previous setup for the linewidth measurement in Fig. B.3. However, in Fig. B.5, the OPD of the MZ interferometer is nearly balanced, with an OPD of only 3.8 cm remaining, as determined using a Luna OBR 4400 Reflectometer. Here, the small OPD of the interferometer ensures that the induced sinusoidal phase waveform can be entirely resolved by the quadrature bandwidth available from the SSB signal processing. Additionally, the PZT introduces a randomised phase signal with phase excursions  $\approx 2\pi$  in order to suppress, after sufficient averaging, any remaining cyclic errors introduced by the signal processing, easing the requirements for the tuning of the input polarisation of the phase modulator (see also Sec. 5.4.1). After SSB demodulation, the resulting unwrapped phase signal is proportional to the sinusoidal optical frequency modulation waveform, allowing its amplitude  $\Delta f_{\text{opt}}$  to be quantified together with the measured OPD value, as well as the non-linearity parameters  $\beta_n$  and  $\delta_n$  (see also Sec. 6.2.5). In this implementation, because final processing was carried out on a PC, the raw ADC data had to be transferred from the FPGA. Due to the low transmission data rate, the effective averaging time was only 27 ms for each point in the modulation parameter space. The resulting measurement quality

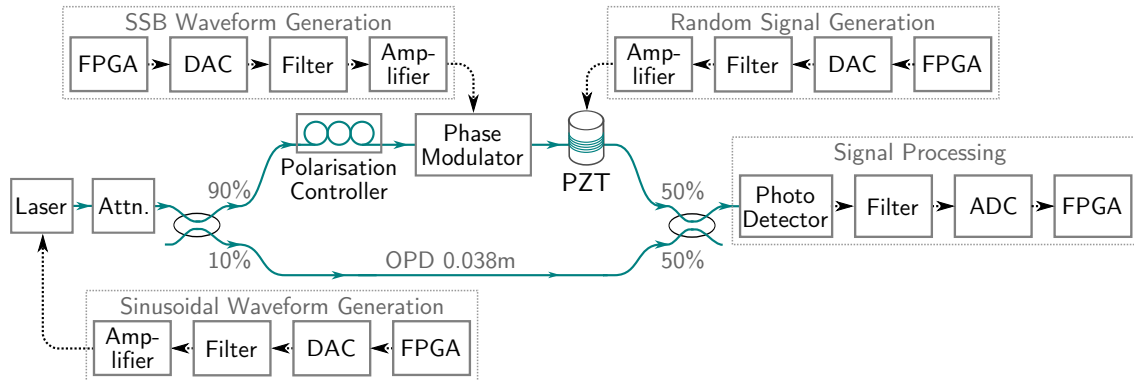


**Figure B.5.:** MZ interferometer setup for the measurement of the sinusoidal optical frequency modulation parameters, mostly similar to the setup of Fig. B.3, except for the near OPD balance of the interferometer. Here, the FPGA generates the sinusoidal laser injection current modulation waveform, the single-sideband waveform for the phase modulator and a signal that drives the PZT to randomise the interferometric phase, with the photo detector signal then recorded by the FPGA.

is sufficient in most cases, but could be improved in future implementations.

In addition to the determination of the optical frequency modulation parameters discussed above, the intensity modulation parameters  $\xi$  and  $\tau_I$  (see also Sec. 6.2.5), resulting from sinusoidal injection current modulation also need to be found. The relative amplitude  $\xi$  of the intensity modulation can be directly measured using a DC-capable photo detector (New Focus 1817) and an oscilloscope. Here, the laser diode, via an attenuator, is directly connected to the photo detector and the resultant intensity modulation signal displayed on the oscilloscope.  $\xi$  can then straightforwardly be determined by dividing the amplitude of the sinusoidal signal by the mean DC power.

Additionally, inserting a widely unbalanced MZ interferometer between the laser attenuator and the photo detector then allows the determination of the intensity modulation delay  $\tau_I$ . The principle behind this measurement is explained by the oscilloscope trace shown in Fig. B.6. Here, due to the large OPD of  $\approx 25$  m, when sinusoidal optical frequency modulation is applied, the bulk of the interference fringes change so fast that they are low-pass filtered by the photo detector bandwidth of 80 MHz. This allows the clean determination of the zero-crossing of the intensity modulation waveform. However, the slow fringes near the peaks of the optical frequency modulation waveform, as seen in Fig. B.6, remain visible in the photo detector signal and their symmetry centre marks this peak. This allows the direct measurement of the delay between the intensity modulation zero-crossing and the peak of the frequency modulation waveform. For instructive purposes, the assumed frequency modulation waveform is also drawn in Fig. B.6 using a dotted line. The desired delay  $\tau_I$  between the intensity modulation and frequency modulation waveform is also shown and is given by the measured delay plus the equivalent of the  $90^\circ$  phase shift between peak and zero-crossing. The reason for not selecting the possible solution due to the other symmetry centre is in line with the treatment of Li *et al.* [250], where the phase shift is always assumed to be  $180^\circ$ .

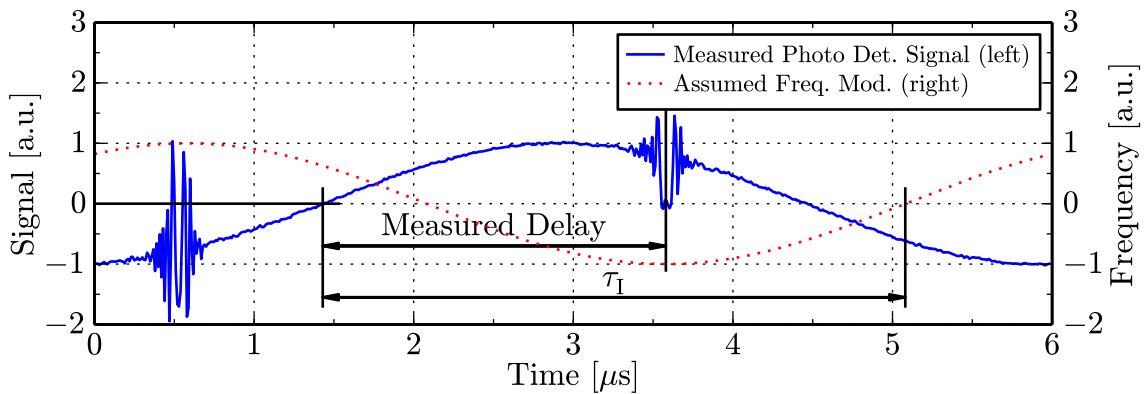


**Figure B.6.:** Determination of the delay  $\tau_I$  between intensity modulation and frequency modulation. Here, the time span between the intensity modulation zero-crossing and the peak of the optical frequency modulation waveform, marked by symmetry centre of the interferometric signal, is evaluated. To illustrate the working principle, the desired delay  $\tau_I$  is also marked and the assumed frequency modulation waveform is drawn using dotted lines.

### B.3.2. Characterisation Results

Using the experimental methods described in the previous section, the relevant modulation parameters were determined as a function of the modulation frequency  $f_m$ . Because the measurement campaign shown below was conducted before the final FPGA implementation of the SFM technique was programmed, the selected frequencies do not match the chosen modulation frequency of  $f_m = 98$  kHz used in the experiments in Chap. 6, however, it is straightforward to linearly interpolate the data to find the applicable parameters. The results are shown in Fig. B.7 for three values of the injection current modulation amplitude  $\Delta I_{LD}$ , where in Chap. 6 a value of  $\Delta I_{LD} = 45$  mA was used throughout. All measurements were recorded for a fixed laser diode bias current  $I_{LD} = 125$  mA and diode temperature of  $T_{LD} = 25^\circ\text{C}$ .

Fig. B.7(a) shows that the optical frequency modulation efficiency reduces for increasing modulation frequency, where the interpolated value at  $f_m = 98$  kHz for  $\Delta I_{LD} = 45$  mA that is applicable to Chap. 6 is  $\Delta f_{\text{opt}} = 8.4$  GHz. In general, the optical frequency modulation efficiency in injection current modulation is a complex interplay of thermal effects in various parts of the laser diode and refractive index changes due to variations in carrier density [123]. Here, thermal effects are generally slower than refractive index effects, however, in some cases thermal effects can still be observed even at frequencies on the order of 10 MHz [123]. Fig. B.7(b) then shows that the relative intensity modulation parameter  $\xi$  stays practically constant with  $f_m$ , with the relevant value for  $\xi$  at  $\Delta I_{LD} = 45$  mA extracted as  $\xi = 0.45$ . In Fig. B.7(c), the equivalent phase shift between intensity modulation and optical frequency modulation is shown, from which the intensity modulation delay  $\tau_I$  can be determined for each value of the modulation frequency  $f_m$ . Here, at  $f_m = 98$  kHz, a phase shift value of  $208^\circ$  can be determined, corresponding to  $\tau_I = 5.92$   $\mu\text{s}$ . In general, the measurements in Fig. B.7(c) correspond well to literature values, where phase shift values were found to rise from near  $180^\circ$  at low modulation frequencies to  $225^\circ$  at a modulation frequency of 100 kHz for the diode laser used by Li *et al.* [250].

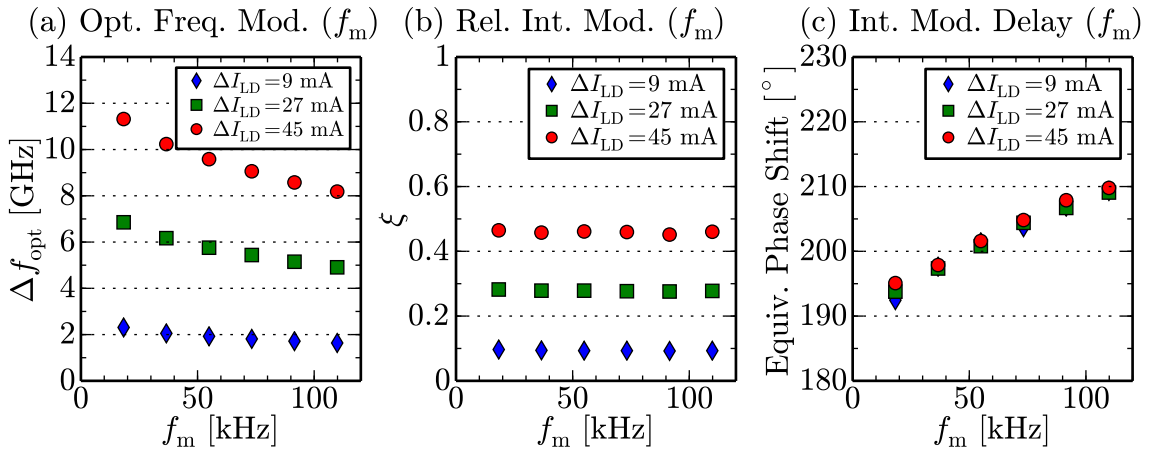


**Figure B.7.:** Measurement of the optical frequency modulation amplitude  $\Delta f_{\text{opt}}$ , the relative intensity modulation amplitude  $\xi$  and of the equivalent phase shift corresponding to the intensity modulation delay  $\tau_I$ , in (a), (b) and (c), respectively, as a function of the modulation frequency  $f_m$  and for three values of the injection current modulation amplitude  $\Delta I_{LD}$ . All measurements were taken at a laser diode bias current of  $I_{LD} = 125$  mA and for a diode temperature of  $T_{LD} = 25^\circ\text{C}$ .

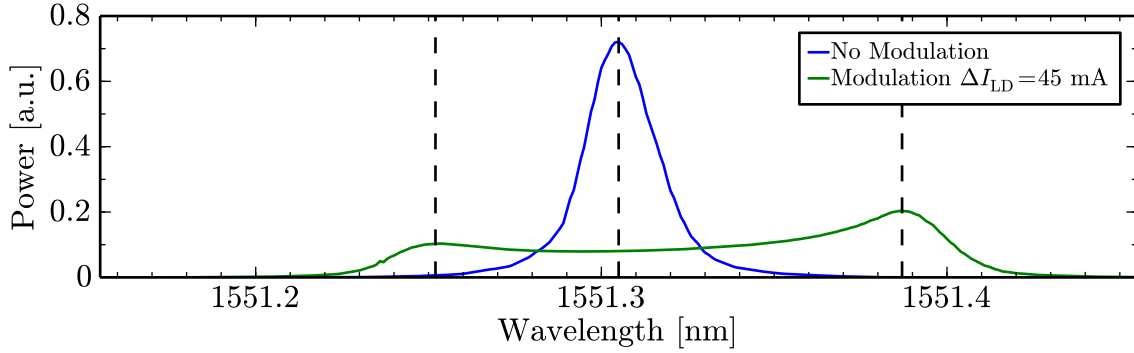


**Figure B.8.:** Measurement of the output spectrum of the laser diode using an optical spectrum analyser, with and without laser injection current modulation at the modulation parameters relevant to Chap. 6 applied, and with the peak values marked using dashed guide lines.

A quick measurement of the optical frequency modulation amplitude  $\Delta f_{\text{opt}}$  can also be obtained using an optical spectrum analyser. The results for the modulation of the laser diode with the exact parameters used in Chap. 6, i.e.  $\Delta I_{\text{LD}} = 45$  mA at  $f_m = 98$  kHz for  $I_{\text{LD}} = 125$  mA and  $T_{\text{LD}} = 25^\circ\text{C}$ , are shown in Fig. B.8. Here, the laser diode output is directly connected, via an attenuator, to a Yokogawa AQ6370 spectrum analyser that was, however, not specifically calibrated. A wavelength excursion of  $\pm 67$  pm can be extracted from Fig. B.8, corresponding to an optical frequency modulation amplitude of  $\Delta f_{\text{opt}} = 8.4$  GHz, independently confirming the values determined from Fig. B.7(a). The broad peak for the case without modulation is due to the 20 pm resolution of the spectrum analyser and it can furthermore be seen that the application of injection current modulation also shifts the optical centre wavelength  $f_{\text{opt,c}}$  by 14 pm compared to the case without modulation.

The results of the investigation into the optical frequency modulation non-linearities are then shown in Fig. B.9. Here, Figs. B.9(a) and (b) plot the fractional harmonic amplitude  $\beta_2$  and the corresponding phase angle  $\delta_2$  of the first harmonic of the sinusoidal optical frequency modulation waveform (see also Sec. 6.2.5). It can be seen in Fig. B.9(a) that  $\beta_2$  shows a small reduction with increasing modulation frequency  $f_m$  and, in Fig. B.9(b), that  $\delta_2$  shows a slight increase with increasing  $f_m$ . The parameters extracted from Figs. B.9(a) and (b) at  $f_m = 98$  kHz and  $\Delta I_{\text{LD}} = 45$  mA that are used in the corrections in this work are  $\beta_2 = 4.1\%$  and  $\delta_2 = 12^\circ$ . Figs. B.9(c) and (d) then plot the corresponding values  $\beta_3$  and  $\delta_3$  for the second harmonic, where it was also confirmed that all higher harmonics are negligible. In Figs. B.9(c) and (d), for some values, especially at low modulation injection current modulation amplitudes  $\Delta I_{\text{LD}}$ , the measured values appear to be strongly influenced by noise and these values should be disregarded. However, it is thought that the values for  $\Delta I_{\text{LD}} = 45$  mA are sufficiently reliable to deduce that the fractional amplitude of the second harmonic non-linearity  $\beta_3$  is  $\approx 0.3\%$  at the relevant frequency  $f_m = 98$  kHz. Therefore, due to its small value the second harmonic and all higher harmonics are neglected in this work and the corrections of Sec. 6.2.5 were only carried out for the first harmonic using parameters  $\beta_2$  and  $\delta_2$ .

While the previous measurements in this section have been obtained at fixed values of the laser diode bias current of  $I_{\text{LD}} = 125$  mA and the diode temperature of  $T_{\text{LD}} = 25^\circ\text{C}$ , which are the values that were used throughout Chap. 6, the

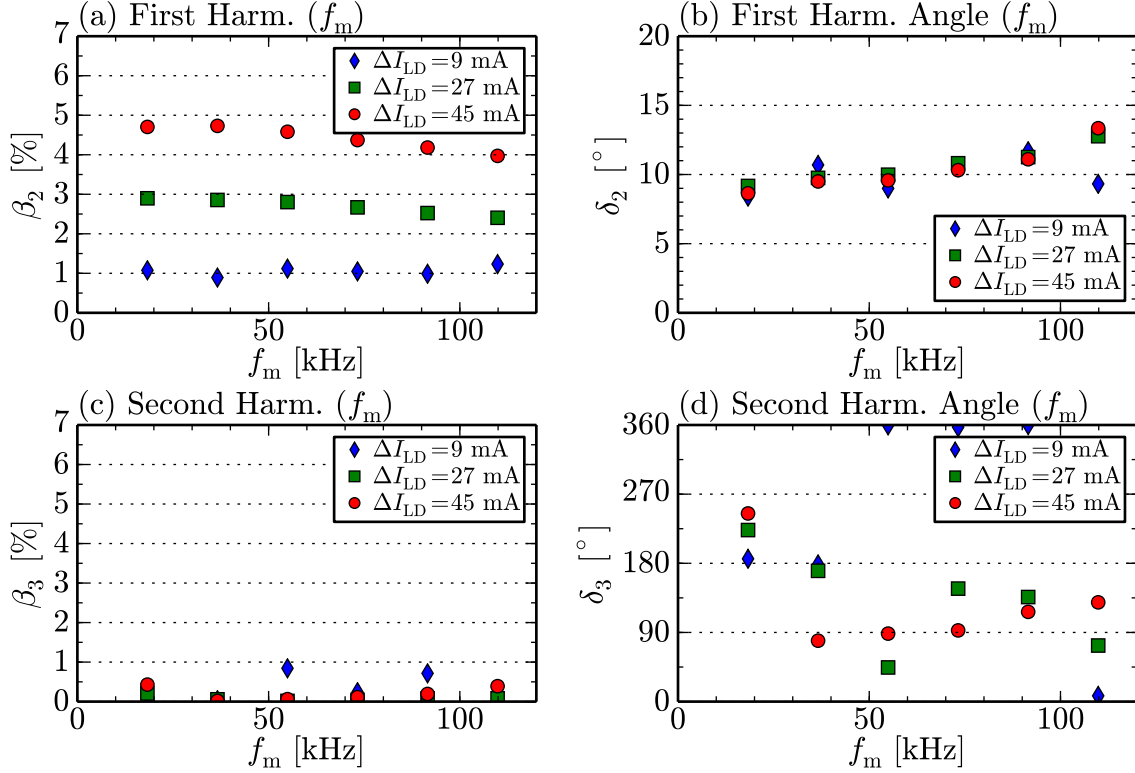


**Figure B.9.:** Measurement of the harmonic content of the optical frequency modulation as a function of the modulation frequency  $f_m$  and for three values of the injection current modulation amplitude  $\Delta I_{LD}$ . Here, (a) and (b) plot the fractional harmonic amplitude  $\beta_2$  and the corresponding phase angle  $\delta_2$  for the first harmonic, while (c) and (d) plot  $\beta_3$  and  $\delta_3$  for the second harmonic, with all measurements taken at  $I_{LD} = 125$  mA and  $T_{LD} = 25^\circ\text{C}$ .

general dependency of the correction parameters on  $I_{LD}$  and  $T_{LD}$  is also of interest. Measurement results for variations in  $I_{LD}$  and  $T_{LD}$  are shown in Fig. B.10. These measurements were recorded at a fixed modulation frequency of  $f_m = 110$  kHz, which is thought to be sufficiently close to the used value of  $f_m = 98$  kHz that similar conclusions can be reached. Here, Figs. B.10(a),(b),(c) and (d) plot the changes of parameters  $\Delta f_{opt}$ ,  $\xi$ ,  $\tau_1$  and  $\beta_2$  as a result of a variation of the bias current  $I_{LD}$  for various values of the modulation amplitude  $\Delta I_{LD}$ . It can be seen in Fig. B.10(a) that the frequency modulation efficiency increases with increasing bias current, a fact that could be used beneficially in future work. The change in the relative intensity modulation  $\xi$  visible in Fig. B.10(b) can straightforwardly be explained using the static intensity modulation characteristic shown in Fig. B.1(a). It can furthermore be seen in Figs. B.10(c) and (d) that the equivalent phase for the intensity modulation delay  $\tau_1$  is independent on the bias current and that the harmonic content  $\beta_2$  shows a small reduction with increasing bias current. In contrast to changes in the bias current, changes in the laser diode temperature do not appear to significantly affect the parameters  $\Delta f_{opt}$ ,  $\xi$ ,  $\tau_1$  and  $\beta_2$ , as can be seen in Figs. B.10(e),(f),(g) and (h). This is an important result as it shows that the laser emission wavelength can be tuned by changing the laser diode temperature without significantly affecting the modulation parameters, which may become relevant for future use of the SFM technique in applications where the laser emission centre wavelength has to be controlled through temperature tuning, such as precision displacement measurements.

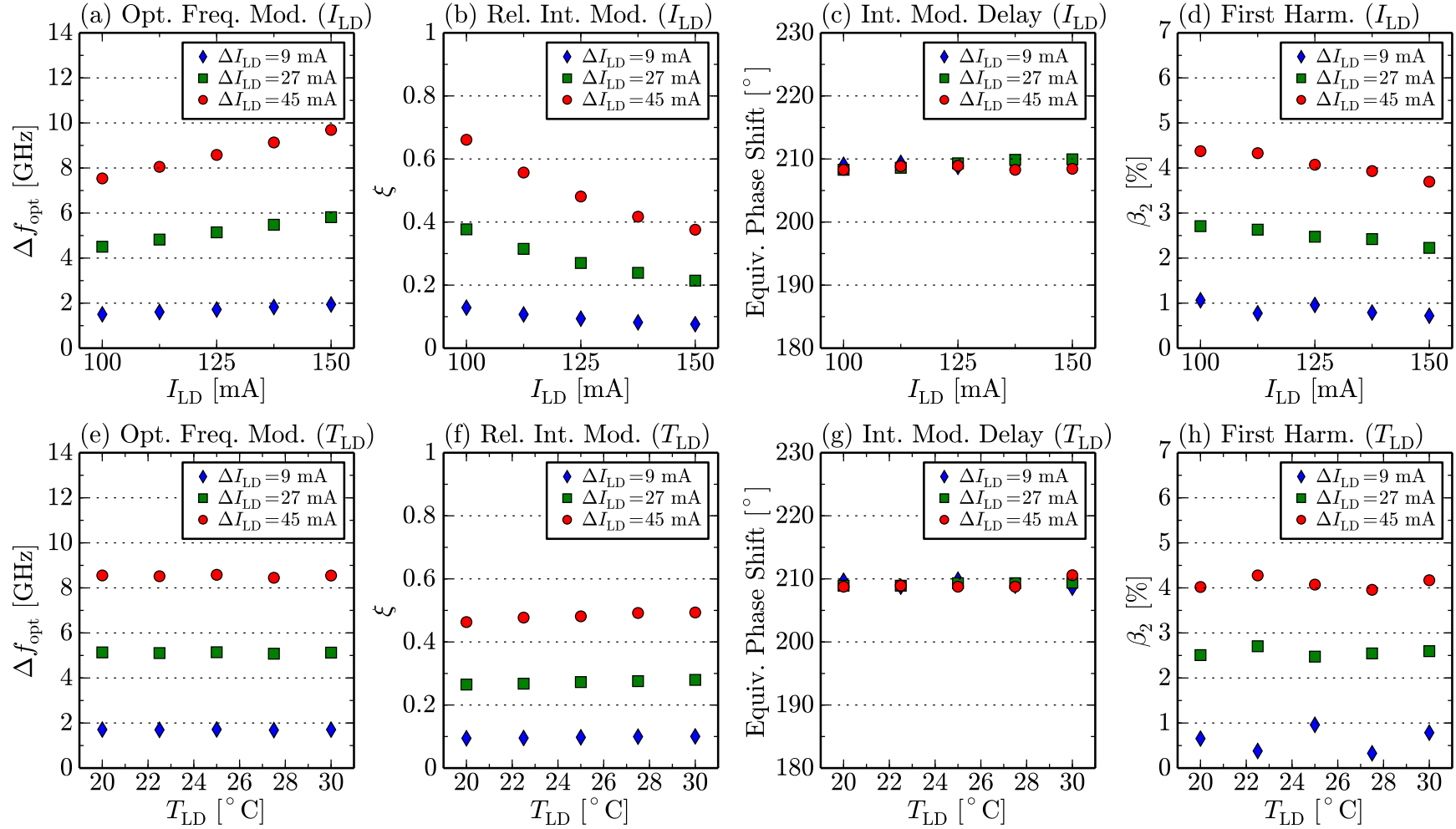


**Figure B.10.:** Dependency of the optical frequency modulation amplitude  $\Delta f_{opt}$ , the relative intensity modulation  $\xi$ , the phase shift corresponding to the intensity modulation to frequency modulation delay  $\tau_1$  and the fractional harmonic amplitude  $\beta_2$  on the laser diode bias current  $I_{LD}$  in (a),(b),(c) and (d), respectively, and on the laser diode temperature  $T_{LD}$  in (e), (f), (g) and (h), respectively. These measurements were taken at a fixed modulation frequency of  $f_m = 110$  kHz and for three values of the injection current modulation amplitude  $\Delta I_{LD}$ .



## C. FPGA Based Processing

Field programmable gate arrays (FPGA) [288, 289] are widely used across digital signal processing and also more generally for real-time processing. The reason for this is that FPGAs inherently allow complete parallelisation of tasks, permitting multiple jobs to be carried out with complete independence. This is in contrast to central processing unit (CPU) architectures, such as those used in regular personal computers (PC), where multiple tasks can share the same processing unit and are processed sequentially. Whereas CPU-type architectures employ high-complexity logic that implements a set of highly specialised instructions, FPGAs consist of a large number of identical low-complexity logic blocks that each perform a basic set of logic functions, as also illustrated in Fig. C.1. In FPGAs, programmable interconnects link these logic blocks, implementing the desired functionality. This is also complemented by a range of speciality function blocks, such as input-output gates or further proprietary logic blocks. Therefore, in essence, an FPGA can be seen as a programmable set of logic gates that can be customised to the desired task and where multiple function blocks can work with complete autonomy.

The inherent parallelisation of FPGAs also requires a completely different style of programming than for regular CPU-based processors, where FPGAs are generally programmed using hardware description languages such as VHDL. Whereas in CPU-based processing, instructions are kept in the working memory, can be changed if required and are executed sequentially, in FPGAs, interconnects are fixed at the time of programming and implement the desired logic permanently until reset. Therefore, in FPGA programming, there is no overall time line and all events can happen at every clock cycle, requiring the use of special programme state registers to implement sequential functionality. A further point to note is that in FPGAs, concurrent

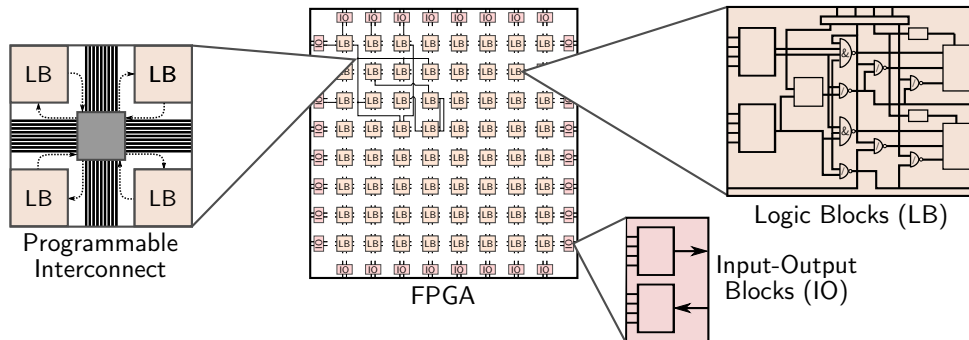


**Figure C.1.:** Illustration (adapted from [287]) of the key building blocks of an FPGA. Here, a matrix of identical logic blocks (LB) that perform a limited set of basic logic functions are linked by programmable interconnects that define the FPGA program. Additionally, a range of speciality functions, such as input-output (IO) gates, complement the basic functionality of the LBs.

execution of multiple function blocks does not decrease the processing speed as it would in CPU-based processing, but rather increases the number of logic blocks used. As an example relevant to this thesis, implementing the demodulation of 16 range channels rather than 8 range channels would not lead to lower execution speed but would use double the amount of FPGA logic blocks. Therefore the number of range channels is ultimately limited by the number of available logic blocks and FPGA capacity is generally measured by the percentage of logic blocks or chip area used.

In the context of this thesis, FPGA-based processing allowed the complete and reliable synchronisation of the modulation and demodulation functions of the implementations at a clock frequency of 150 MHz. This is an absolute necessity for the real-time implementation of both the techniques presented in this thesis and FPGA-based processing is also used by other groups in the area of range-resolved interferometric signal processing [203, 204]. However, because FPGA programming is more generally complex than programming regular CPU-based processors, in this thesis, the use of FPGA-based processing was minimised and post-processing was preferably carried out on a PC to reduce programming effort and permit higher flexibility during development. Nevertheless, if desired, most post-processing functions in this thesis could eventually be carried out on the FPGA if the necessary programming effort is invested. The FPGA development system that is used in this work is shown in Fig. C.2, where the total cost of the complete system is well below £1k. The system consists of a Terasic DE-115 development board in conjunction with a data acquisition daughter board that carries the analogue/digital data converters. In most cases, because of the high data rates of the quadrature signals, the bottleneck in the processing implementations in this thesis was the data transfer to the PC. Initially a low-overhead serial interface was used, however, at a later stage, to improve data transfer rates, a more sophisticated USB-based solution using a separate FPGA communication board was implemented.

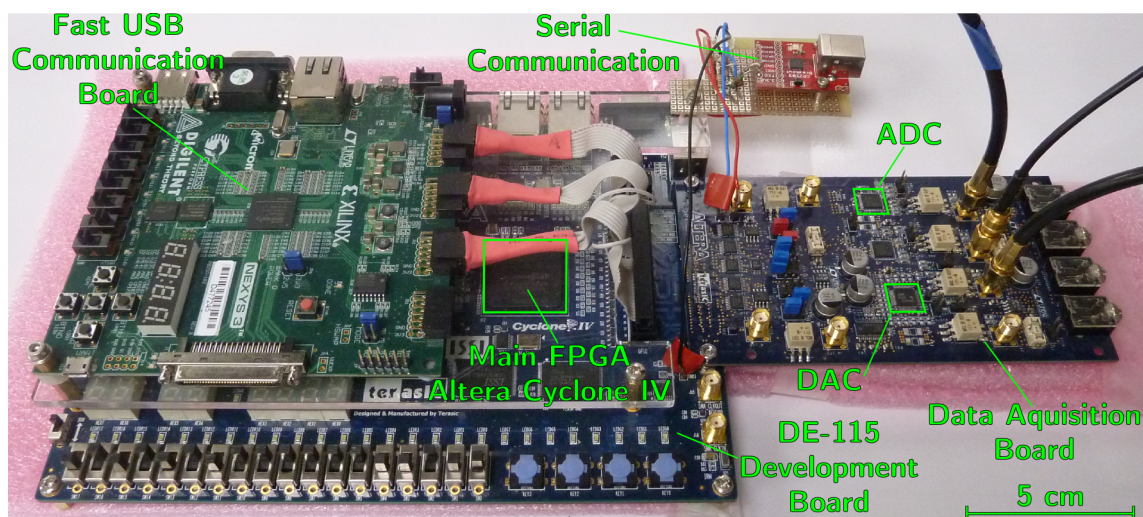


**Figure C.2.:** Picture of the FPGA system used in this work, which is based on a Terasic DE-115 development board that uses an Altera Cyclone IV FPGA. A data acquisition daughter board, accommodating the ADC and the DAC, is connected to this board. Data can be transferred from the FPGA to a PC using a slow, low overhead serial connection or a fast USB interface that uses a separate FPGA communication board, affixed on top of the main FPGA board.



# D. Noise and Crosstalk in the Complex Quadrature Signals

## D.1. Quadrature Noise

In this appendix, a phasor-based model, developed in this thesis, of how quadrature noise can cause both amplitude noise and excess phase noise is presented. This allows, under certain conditions, the inference of the standard deviation of the excess phase noise  $\sigma_{\text{phase,ex}}$  from the normalised amplitude noise standard deviation  $\sigma_{\text{amp,norm}}$ , which is a quantity that can be directly measured. In general, quadrature noise can be caused by any noise source that affects both the real and imaginary parts of the quadrature signal independently. Here, a simplified model of quadrature noise represented by the quadrature noise phasor  $\mathbf{n}$  with a random complex phase is developed. In this model, the quadrature noise phasor  $\mathbf{n}$  is then added to the ideal signal phasor  $\mathbf{i}$ , whose tip is situated on the quadrature circle/ellipse (see also Sec. 3.1.4). This is illustrated in Fig. D.1(a) with example quadrature noise phasors  $\mathbf{n}_1$  to  $\mathbf{n}_4$  of equal amplitude  $|\mathbf{n}|$ . Typical noise sources that can cause quadrature noise include shot noise, laser intensity noise in the stationary offset power term  $P_{\text{off}}$  in Eq. 3.3, electronic noise as well as aliased high-frequency laser phase noise [212, 244]. In contrast, intensity noise in the effective power term  $P_{\text{eff}}$  only affects the amplitude of the ideal signal phasor  $\mathbf{i}$ , while direct laser phase noise that is caused by laser frequency noise is indistinguishable from the desired phase signals and is thus effectively incorporated into the phase of  $\mathbf{i}$ .

For cases where laser intensity noise in  $P_{\text{eff}}$  can be neglected, the projection of the quadrature noise in the direction of the ideal signal phasor  $\mathbf{i}$  leads to amplitude noise of standard deviation  $\sigma_{\text{amp}}$ , as illustrated in Fig. D.1(b) for quadrature noise

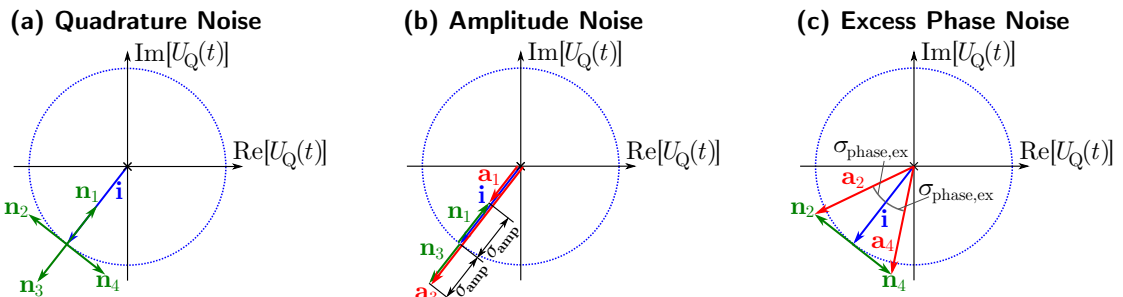


**Figure D.1.:** (a) illustrates four example quadrature noise phasors  $\mathbf{n}_1$  to  $\mathbf{n}_4$  of common amplitude  $|\mathbf{n}|$  added to the tip of the ideal signal phasor  $\mathbf{i}$  that is situated on the quadrature circle/ellipse. (b) then shows how amplitude noise of standard deviation  $\sigma_{\text{amp}}$  is caused by the projection of the quadrature noise phasors in the direction of  $\mathbf{i}$ . Conversely, (c) illustrates that excess phase noise of standard deviation  $\sigma_{\text{phase,ex}}$  is caused by the projection in the direction normal to  $\mathbf{i}$ .

phasors  $\mathbf{n}_1$  and  $\mathbf{n}_3$ , where the amplitude  $|\mathbf{n}|$  of the quadrature noise phasors is taken to be equal to  $\sigma_{\text{amp}}$ . This can be normalised by the amplitude of the ideal signal phasor  $|\mathbf{i}|$ , which is taken to be equal to the mean quadrature signal amplitude  $|\overline{U_Q}|$ , resulting in the normalised amplitude noise standard deviation  $\sigma_{\text{amp,norm}}$ , given by:

$$\sigma_{\text{amp,norm}} = \frac{\sigma_{\text{amp}}}{|\overline{U_Q}|} = \frac{|\mathbf{n}|}{|\mathbf{i}|} \quad (\text{D.1})$$

In general, the time series of any measured quadrature signal allows the determination of the mean quadrature amplitude  $|\overline{U_Q}|$  and the quadrature amplitude noise standard deviation  $\sigma_{\text{amp}}$ , permitting the simple calculation of  $\sigma_{\text{amp,norm}}$ .

Analogously excess phase noise, as illustrated in Fig. D.1(c) for quadrature noise phasors  $\mathbf{n}_2$  and  $\mathbf{n}_4$  of amplitude  $|\mathbf{n}|$ , is caused by the projection of the quadrature noise phasors normal to  $\mathbf{i}$ , with the excess phase noise standard deviation  $\sigma_{\text{phase,ex}}$  given by the tangent of  $|\mathbf{n}|$  and  $|\mathbf{i}|$ . Using the first order approximation of the tangent, i.e.  $\tan(\alpha) \approx \alpha$ ,  $\sigma_{\text{phase,ex}}$  can then be approximated by:

$$\sigma_{\text{phase,ex}} = \frac{|\mathbf{n}|}{|\mathbf{i}|} \quad (\text{D.2})$$

Therefore, from Eq. (D.1) and Eq. (D.2), in the absence of laser intensity noise in  $P_{\text{eff}}$  and using the aforementioned assumption that the quadrature noise has a random complex phase, amplitude noise and excess phase noise share the same statistical properties and  $\sigma_{\text{phase,ex}}$  equals  $\sigma_{\text{amp,norm}}$ , allowing straightforward calculation of  $\sigma_{\text{phase,ex}} = \sigma_{\text{amp}} \cdot |\overline{U_Q}|^{-1}$  from the measurable quantities  $\sigma_{\text{amp}}$  and  $|\overline{U_Q}|$ . However, this conjecture does require the first-order approximation of the tangent and is thus only valid for small quadrature noise amplitudes, with the error in this approximation exceeding 1% for  $\sigma_{\text{amp}} \cdot |\overline{U_Q}|^{-1} > 0.3$ . A more detailed model that does not require the approximations above appears entirely feasible but needs to take into account differences in statistical distributions resulting from the non-linearity of the tangent function and therefore requires further work.

The apparent phase noise standard deviation  $\sigma_{\text{phase}}$  that can be obtained from the measured phase signal can then be expressed by the quadratic addition of the excess phase noise standard deviation  $\sigma_{\text{phase,ex}}$ , caused by quadrature noise, and the direct phase noise standard deviation  $\sigma_{\text{phase,direct}}$  caused by laser frequency noise.

$$\sigma_{\text{phase}}^2 = \sigma_{\text{phase,direct}}^2 + \sigma_{\text{phase,ex}}^2 \quad (\text{D.3})$$

This then allows the relative influence of direct and excess phase noise in the measured phase signals to be conveniently determined.

## D.2. Spurious Unwrappings due to Quadrature Noise

The measured phase signals need to be unwrapped to extend their dynamic range beyond  $\pm\pi$ . In general, for successive samples, the unwrapping algorithm [112], out of the possible phase changes  $[\Delta\varphi, \Delta\varphi - 2\pi]$ , always assumes the one with the

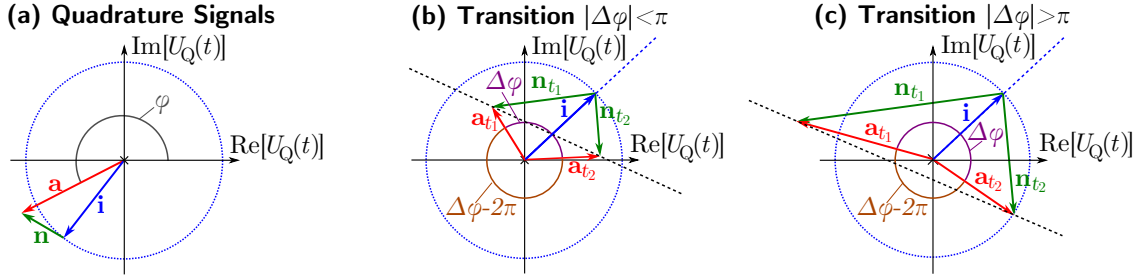


**Figure D.2.:** (a) illustrates that in the presence of the quadrature noise phasor  $\mathbf{n}$ , the measured phase  $\varphi$  is determined by the apparent phasor  $\mathbf{a}$ , the phasor addition of  $\mathbf{n}$  and the ideal signal phasor  $\mathbf{i}$ . (b) then illustrates the case for an unproblematic phase unwrapping, where at two successive samples at times  $t_1$  and  $t_2$ , the correct phase difference  $\Delta\varphi$  is selected by the phase unwrapping algorithm, because the line connecting  $\mathbf{a}_{t_1}$  and  $\mathbf{a}_{t_2}$  (black dashes) intersects  $\mathbf{i}$  or its half-line extension (blue dashes). In contrast, in (c) the phase difference  $\Delta\varphi - 2\pi$  is selected incorrectly, because the line connecting  $\mathbf{a}_{t_1}$  and  $\mathbf{a}_{t_2}$  does not intersect  $\mathbf{i}$  or its half-line extension.

smaller absolute value to be true and integrates the corresponding phase change over time. However, the onset of spurious phase unwrappings due to quadrature noise can put a limit on the achievable quadrature signal bandwidth. A single spurious phase unwrapping will result in a permanent  $\pm 2\pi$  phase error that cannot be unambiguously corrected once it has occurred and may require filtering of the quadrature signals to reduce the likelihood of spurious phase unwrappings occurring. In order to illustrate the conditions where spurious phase unwrappings due to quadrature noise can occur, the following phenomenological phasor model was developed during this thesis. Fig. D.2(a) illustrates a typical phasor diagram for quadrature signals in the presence of the quadrature noise phasor  $\mathbf{n}$ . Here, the phase of  $\mathbf{n}$  is uncorrelated to the phase of the ideal signal phasor  $\mathbf{i}$ , whose endpoint lies on the quadrature circle/ellipse (see also Fig. 3.6), drawn using a dotted blue line. In general, the phase signal  $\varphi$  that is measured by the signal processing is the complex angle of the apparent signal phasor  $\mathbf{a}$ , which results from the phasor addition of  $\mathbf{i}$  with  $\mathbf{n}$ .

An unproblematic case for the phase unwrapping algorithm in the presence of quadrature noise is illustrated in Fig. D.2(b) for the simplified case of a stationary ideal signal phasor  $\mathbf{i}$ . Here, for two successive samples at times  $t_1$  and  $t_2$ , the quadrature noise phasors  $\mathbf{n}_{t_1}$  and  $\mathbf{n}_{t_2}$  lead to a corresponding change in the apparent signal phasor  $\mathbf{a}_{t_1}$  and  $\mathbf{a}_{t_2}$ . The conjecture put forward in this model, developed by observing the conditions in measured quadrature signals where spurious phase unwrappings have occurred, is that this is unproblematic as long as the line connecting the tips of  $\mathbf{a}_{t_1}$  and  $\mathbf{a}_{t_2}$ , drawn using black dashes in Fig. D.2(b), intersects  $\mathbf{i}$  or its half-line extension, drawn using blue dashes. In this case, the phase unwrapping algorithm will correctly integrate the phase difference  $\Delta\varphi$ , with its absolute value smaller than  $\pi$ . In contrast to this, in Fig. D.2(c), where the only change compared to Fig. D.2(b) is the doubling of the amplitudes of  $\mathbf{n}_{t_1}$  and  $\mathbf{n}_{t_2}$ , the line connecting the tips of  $\mathbf{a}_{t_1}$  and  $\mathbf{a}_{t_2}$  does not intersect  $\mathbf{i}$  or its half-line extension. Therefore the phase unwrapping algorithm will incorrectly integrate the phase difference  $\Delta\varphi - 2\pi$ , due to its absolute value being smaller than  $\pi$ , leading to a spurious unwrapping with an error of  $2\pi$  in the resulting phase signal.

A formal proof of this conjecture, as well as its extension to non-stationary ideal signal vectors  $\mathbf{i}$ , is beyond the scope of this work. However, the proposed model is

also backed up by the observation that for phase signals that are free from spurious phase unwrappings, the corresponding quadrature signal scatter plots in the complex plane, such as Fig. 5.15(a) and Fig. 5.24(a), generally exhibit a clearly visible hole in the quadrature circle/ellipse plot. In contrast, for the case where the hole in the quadrature circle/ellipse plot becomes obscured, the quadrature noise phasors  $\mathbf{n}$  in some samples exceeds the ideal signal phasor  $\mathbf{i}$  in amplitude and therefore spurious phase unwrappings, as illustrated in Fig. D.2(c), are likely to occur.

### D.3. Crosstalk in the Phase Signals

In this section, the non-linear transformation of crosstalk in the quadrature signals to crosstalk in the desired phase signals is analysed. While, in general, the crosstalk in the quadrature signals is a measurable quantity, the resulting crosstalk in the phase signals is highly non-linear and strongly depends on the actual phase signal and effective powers of the signal sources. Fig. D.3 illustrates how quadrature signal crosstalk from signal source 1 interacts with the desired phase signal of signal source 2. Here the ideal signal phasor  $\mathbf{i}_1$  is scaled by quadrature signal crosstalk suppression coefficient  $S_{\text{cr}}$  and added to  $\mathbf{i}_2$ . The resulting phase signal  $\varphi_2$  of the desired source 2 is then given by the phase of the apparent signal phasor  $\mathbf{a}_2$ , which is modulated by the crosstalk induced phase signal  $\varphi_{\text{cr}}$  that results from the addition of  $\mathbf{c}_1$  and  $\mathbf{i}_2$ . In general,  $\varphi_{\text{cr}}$  is dependent on the specific angle between  $\mathbf{c}_1$  and  $\mathbf{i}_2$ ,  $\varphi_{\text{cr}}$  will not necessarily resemble the phase signal of source 1. The corresponding Fourier spectrum of  $\varphi_{\text{cr}}$  will be widely dispersed, especially for large phase signal amplitudes  $\gg 2\pi$  of the originating phase signal.

In order to illustrate an example of how crosstalk from the quadrature signal enters the phase signals and also to verify the measured phase signal crosstalk levels in Sec. 5.5.2, the expected crosstalk in the reflector phase signals of reflectors R1 to R4 in Fig. 5.23 for the experimental conditions and test signals described in Sec. 5.5.2 was simulated using the phasor addition model outlined above. Here, the worst-case

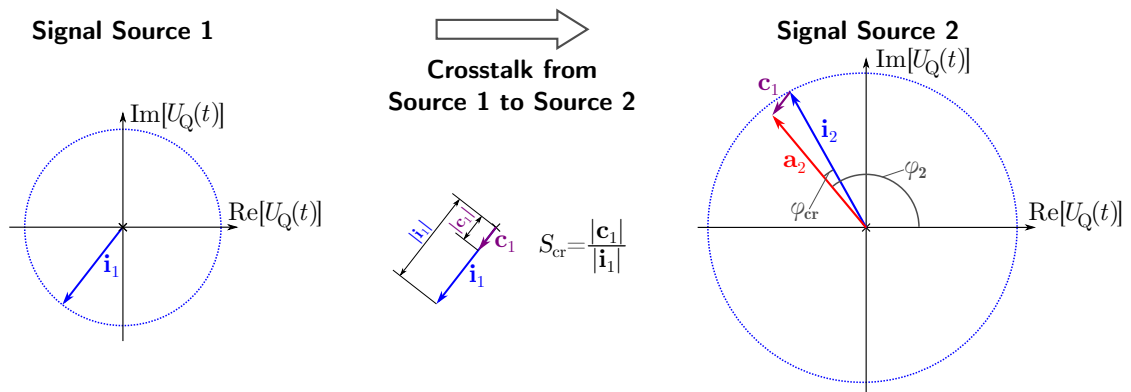


**Figure D.3.:** Illustration of how quadrature signal crosstalk from signal source 1 affects the phase signal of source 2, where reverse crosstalk from source 2 to source 1 is not illustrated. Here, the ideal signal phasor  $\mathbf{i}_1$  of source 1 is scaled by the quadrature signal crosstalk suppression coefficient  $S_{\text{cr}}$  to yield the crosstalk phasor  $\mathbf{c}_1$  that enters the quadrature signal of source 2.  $\mathbf{c}_1$  is then added to the ideal signal phasor  $\mathbf{i}_2$ , which may also differ in amplitude from  $\mathbf{i}_1$ , to yield the apparent signal phasor  $\mathbf{a}_2$ , with corresponding phase signal  $\varphi_2$ .  $\varphi_2$  will be non-linearly modulated by the crosstalk phase signal  $\varphi_{\text{cr}}$ , which, in general, is dependent on the angle between  $\mathbf{i}_1$  and  $\mathbf{i}_2$ .

quadrature signal crosstalk suppression factor  $S_{\text{cr}} = -32$  dB that was determined in Fig. 5.22(c) was used throughout the simulation for the mutual crosstalk between all four signal sources. Additionally, the actual effective power variations evident in Fig. 5.25(a) were taken into account. Typical results of this simulation are plotted in Fig. D.4 and are drawn in analogy to Fig. 5.26. Because the general appearance of the signals and spectra is highly dependent on the initial phase conditions, several iterations of the simulation with random initial phases have been used to verify that the displayed behaviour is indeed representative. Here, in Figs. D.4(a) and (b), two instances of the simulated crosstalk-induced phase variation  $\varphi_{\text{cr}}$  for the signal of reflector R1 are shown, which only differ in the initial phases of the phase signals of the reflectors. The highly irregular appearance in both plots illustrates that crosstalk into phase signals is strongly dependent on the particular initial phase conditions. The Fourier spectra of the simulated phase signals of the four reflectors R1 to R4 are then plotted in Fig. D.4(c) on a logarithmic frequency scale. It can be seen that the spectra resulting from crosstalk under the described conditions are very broad and irregular, and contain strong high-frequency contributions. When compared to Fig. 5.26(c), it can be seen that, except for a few isolated peaks, the calculated crosstalk spectra generally stays well below  $-40$  dB<sub>rad</sub>, which is the noise floor in Fig. 5.26(c). These low crosstalk levels are echoed in the enlarged desired signal peaks at 370 Hz in Fig. D.4(d) and for 570 Hz in Fig. D.4(e). Taken together Figs. D.4(c), (d) and (e) confirm that quadrature signal crosstalk suppression levels of  $S_{\text{cr}} = -32$  dB can indeed lead to crosstalk in the phase signals of levels that are several orders of magnitude lower. Also, it has been shown that the actual crosstalk in the phase signals is highly dependent on the shape of the phase signals itself and on the particular initial phase conditions.

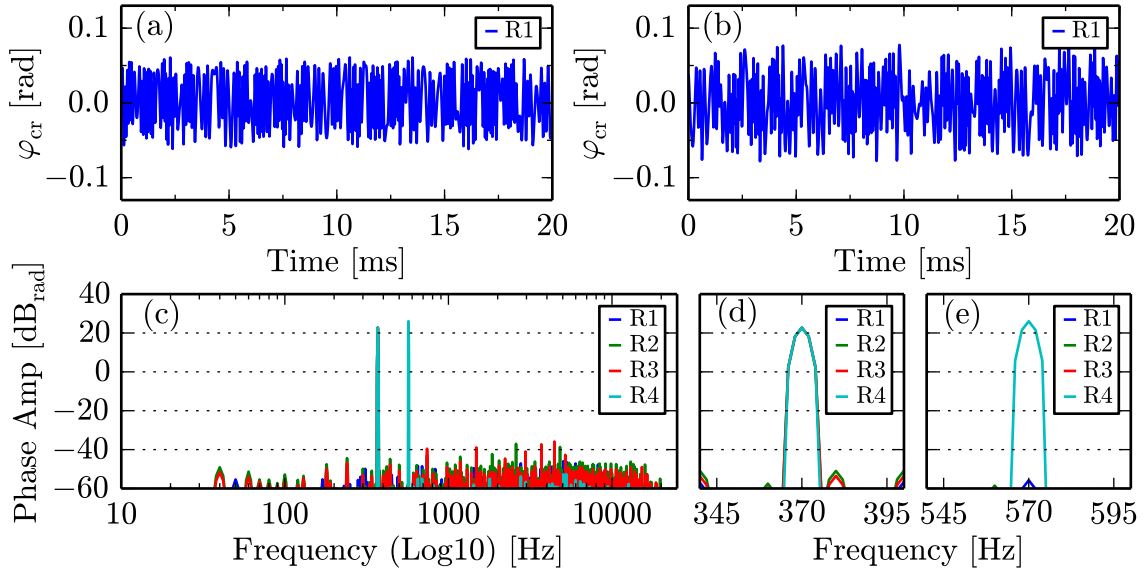


**Figure D.4.:** Results of a simulation of the magnitude of crosstalk in the phase signals for the measurement arm configuration of Fig. 5.23 and test signals described in Sec. 5.5.2, with results drawn analogous to the plot of the reflector signals in Fig. 5.26. Here (a) and (b) show typical instances of crosstalk-induced phase variations  $\varphi_{\text{cr}}$  in the signal of reflector R1 for random initial phase conditions of the phase signals of the other reflectors. (c) shows the spectra of the four phase signals from reflectors R1 to R4 containing the simulated mutual crosstalk between signal sources, while (d) and (e) enlarge the desired signal peaks at 370 Hz and 570 Hz, respectively.

## E. Derivation of Equations for Sinusoidal Optical Frequency Modulation

This appendix repeats the analysis of sinusoidal optical frequency modulation in a single interferometer performed by Zheng [121] for the notation used in this thesis. Additionally, this is derived for a time-variable time-of-flight delay  $\tau(t)$  between the two arms of the interferometer. Starting with the optical frequencies  $f_{\text{opt},1}(t)$  and  $f_{\text{opt},2}(t)$  in the two arms of the interferometer in response to a sinusoidal optical frequency modulation with modulation frequency  $f_m$  and of optical frequency amplitude  $\Delta f_{\text{opt}}$  around optical centre frequency  $f_{\text{opt},c}$ :

$$f_{\text{opt},1}(t) = f_{\text{opt},c} + \Delta f_{\text{opt}} \sin [2\pi f_m t] \quad (\text{E.1})$$

$$f_{\text{opt},2}(t) = f_{\text{opt},c} + \Delta f_{\text{opt}} \sin [2\pi f_m (t - \tau(t))] \quad (\text{E.2})$$

The corresponding phases  $\Phi_1(t)$  and  $\Phi_2(t)$  in the two interferometer arms (see also Sec. 3.1.1) are then given by the integrals of  $2\pi$  times Eq. (E.1) and Eq. (E.2), with the integration constant  $\Phi_0$  equal to the initial phase of the light source:

$$\Phi_1(t) = 2\pi f_{\text{opt},c} t - \frac{\Delta f_{\text{opt}}}{f_m} \cos[2\pi f_m t] + \Phi_0 \quad (\text{E.3})$$

$$\Phi_2(t) = 2\pi f_{\text{opt},c} (t - \tau(t)) - \frac{\Delta f_{\text{opt}}}{f_m} \cos [2\pi f_m (t - \tau(t))] + \Phi_0 \quad (\text{E.4})$$

Inserting this into Eq. (3.1), using the powers  $P_1$  and  $P_2$  of the two interfering arms, the responsivity  $R$  and the time-dependent absolute value of the complex degree of coherence  $|\gamma(\tau(t))|$  defined by Eq. (3.2), then yields the photo detector signal  $U_{\text{pd}}(t)$ :

$$\begin{aligned} U_{\text{pd}}(t) &= RP_1 + RP_2 + 2R|\gamma(\tau(t))|\sqrt{P_1 P_2} \cos [\Phi_1(t) - \Phi_2(t)] \\ &= RP_{\text{off}} + RP_{\text{eff}} \cos [\Phi_1(t) - \Phi_2(t)] \\ &= RP_{\text{off}} + RP_{\text{eff}} \cos \left[ \frac{\Delta f_{\text{opt}}}{f_m} \left( \cos [2\pi f_m (t - \tau(t))] - \cos [2\pi f_m t] \right) + 2\pi f_{\text{opt},c} \tau(t) \right] \end{aligned} \quad (\text{E.5})$$

Similar to Sec. 3.1.1, in Eq. (E.5),  $P_{\text{off}} = P_1 + P_2$  is the stationary offset power and  $P_{\text{eff}} = 2|\gamma(\tau(t))|\sqrt{P_1 P_2}$  is the effective interferometric power, and where any time dependence of  $|\gamma(\tau(t))|$  can subsequently be neglected if a highly coherent source

is used. Employing the following trigonometric identity [179]:  $\{2 \sin[\alpha] \sin[\beta] = \cos[\alpha - \beta] - \cos[\alpha + \beta]\}$ , this results in:

$$\begin{aligned} U_{\text{pd}}(t) &= RP_{\text{off}} + RP_{\text{eff}} \cos \left[ \frac{2\Delta f_{\text{opt}}}{f_m} \sin \left[ 2\pi f_m (t - 0.5\tau(t)) \right] \sin \left[ \pi f_m \tau(t) \right] + 2\pi f_{\text{opt},c} \tau(t) \right] \\ &= RP_{\text{off}} + RP_{\text{eff}} \cos \left[ \theta(t) + \varphi(t) \right] \end{aligned} \quad (\text{E.6})$$

The first line in Eq. (E.6) is the final result of the previous derivation by Zheng [121]. Here, in line with the notation of Eq. (3.3) used throughout this thesis, Eq. (E.6) was then simplified by separating the phase terms into the desired phase signal  $\varphi(t)$  and the phase modulation function  $\theta(t)$ , which are given by:

$$\theta(t) = \frac{2\Delta f_{\text{opt}}}{f_m} \sin \left[ 2\pi f_m (t - 0.5\tau(t)) \right] \sin \left[ \pi f_m \tau(t) \right] \quad (\text{E.7})$$

$$\varphi(t) = 2\pi f_{\text{opt},c} \tau(t) \quad (\text{E.8})$$

Here the time-variant time-of-flight  $\tau(t)$  can be represented by  $\tau(t) = \tau_{\text{avg}} + \tau_{\text{sig}}(t)$ , with the average time-of-flight delay  $\tau_{\text{avg}}$  and the time-variant delay  $\tau_{\text{sig}}(t)$ . This allows Eq. (E.7) and Eq. (E.8) to be restated as:

$$\theta(t) = \frac{2\Delta f_{\text{opt}}}{f_m} \sin \left[ 2\pi f_m (t - 0.5\tau_{\text{avg}} - 0.5\tau_{\text{sig}}(t)) \right] \sin \left[ \pi f_m (\tau_{\text{avg}} + \tau_{\text{sig}}(t)) \right] \quad (\text{E.9})$$

$$\varphi(t) = 2\pi f_{\text{opt},c} \tau_{\text{avg}} + 2\pi f_{\text{opt},c} \tau_{\text{sig}}(t) \quad (\text{E.10})$$

In Eq. (E.10), for standard interferometry applications where  $f_{\text{opt},c}$  does not change,  $\tau_{\text{avg}}$  in  $\varphi(t)$  of Eq. (E.10) can be considered an offset phase value, while the time-variant phase signals that are caused by  $\tau_{\text{sig}}(t)$  are the quantity of interest. This is because the optical centre frequency  $f_{\text{opt},c}$  is very large, typically hundreds of THz, resulting in significant phase changes even for minute changes in  $\tau_{\text{sig}}(t)$ .

In Eq. (E.9), for the case of optical frequency modulation of an interferometer of non-zero OPD, as is the subject of Chap. 6 and of this derivation, the average time-of-flight delay  $\tau_{\text{avg}}$ , corresponding to the OPD  $\eta = \tau_{\text{avg}} c_0$  of the interferometer, is usually much larger than the time-of-flight variations caused by  $\tau_{\text{sig}}(t)$ . Also, in Eq. (E.9), these terms are multiplied by the modulation frequency  $f_m$ , typically kHz to MHz, which is many orders of magnitude lower than optical frequencies. Therefore the phase contribution caused by the term  $\pi f_m \tau_{\text{sig}}(t)$  in Eq. (E.9) is typically  $\ll 1$  and Eq. (E.9) can be rewritten by neglecting  $\tau_{\text{sig}}(t)$ , yielding:

$$\theta(t) = A \sin \left[ 2\pi f_m (t - 0.5\tau_{\text{avg}}) \right] \quad (\text{E.11})$$

with the phase modulation waveform amplitude  $A$  given by:

$$A = \frac{2\Delta f_{\text{opt}}}{f_m} \sin \left[ \pi f_m \tau_{\text{avg}} \right] = \frac{2\Delta f_{\text{opt}}}{f_m} \sin \left[ \frac{\pi f_m \eta}{c_0} \right] \approx \frac{2\pi \Delta f_{\text{opt}} \eta}{c_0} \quad \text{for } \eta \ll \frac{c_0}{\pi f_m} \quad (\text{E.12})$$

Furthermore, in many cases of later usage of these equations discussed in Chap. 6, even the phase change from  $\tau_{\text{avg}}$  in Eq. (E.11) can be neglected. However, this does not entail that  $\tau_{\text{avg}}$  or  $\eta$  can be neglected in Eq. (E.12), as this would result in  $A = 0$ .

## F. Power Calibration for Sinusoidal Optical Frequency Modulation

The measurement of the effective power  $P_{\text{eff}}$  in the SFM technique is required on a number of occasions in Chap. 6. As discussed there, the effective power was determined from signal processing units using a calibrated conversion coefficient. The measurement of this conversion coefficient is not trivial and is detailed here. It is furthermore investigated whether this conversion coefficient changes with the OPD, i.e. with the demodulation amplitude  $A_d$ , as well as with the window width parameter  $\sigma$ . In general, according to Eq. (3.3), the determination of the effective power requires the separate measurement of the powers  $P_1$  and  $P_2$  of both arms of the interferometer as well as the assumption that the polarisation and coherence states are known and do not change during the experiment. Here, because of the small OPDs of several meters, the coherence dependence is neglected and full visibility is assumed. A free-space measurement setup is then used because it allows the OPD to be straightforwardly varied and because, unlike in fibre-coupled propagation, the polarisation state can be expected to be stable during free-space propagation [290].

The setup used in this experiment is illustrated in Fig. F.1 and is similar to the multi-surface vibrometry setup of Fig. 7.1. However, only a single retro-reflector at a variable distance  $l$  is used as a target, where the use of a retro-reflector eases alignment and improves stability as all reflected beams are sent back in the incoming direction by the unique properties of the retro-reflector [269]. In this experiment, it is assumed that the polarisation state of the light after free-space propagation, retro-reflection and re-entering the fibre is the same as the polarisation state of the light reflected from the fibre tip that is used as the interferometric reference. The two light components then travel together towards the photo detector and any polarisation

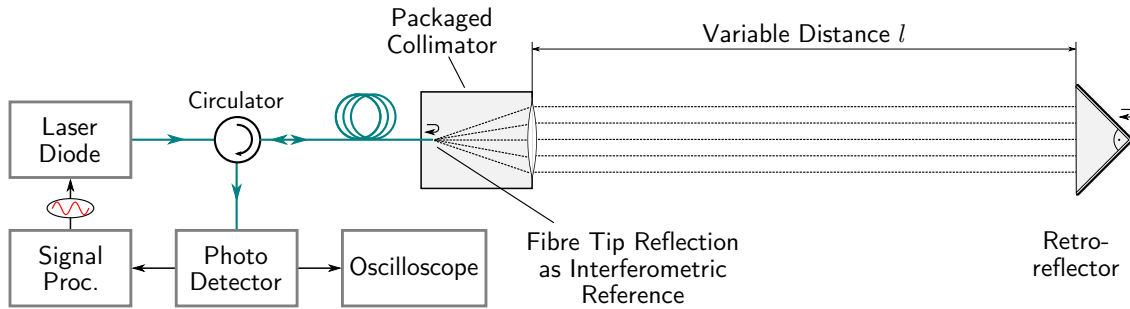


**Figure F.1.:** The setup used for the power calibration is similar to the multi-surface vibrometry setup of Fig. 7.1, except for the use of a single retro-reflector, located at a variable distance  $l$ . Also an oscilloscope is used to additionally determine DC power levels at the photo detector.



change due to fibre birefringence will not affect the measurement as it acts on both components simultaneously. In order to perform the calibration, the regular SFM signal processing, using the implementation detailed in Sec. 6.3.1, is used and the peak return signal values in original signal processing units are registered, while the DC voltage values from the photo detector are simultaneously determined using an oscilloscope. This allows the direct measurement of the mean stationary offset power  $P_{\text{off}} = P_1 + P_2$  of Eq. (3.3), where any influence of the sinusoidal intensity modulation (see also Sec. 6.2.5) will be averaged by the oscilloscope. Blocking the free-space beam then only measures the LO power  $P_1$ , allowing  $P_2$  and the effective power  $P_{\text{eff}}$  to be calculated. In this experiment, the LO power  $P_1$  is kept stable at  $P_1 = 57 \mu\text{W}$  and measurements are taken at three different effective power levels by changing  $P_2$  to values of  $[10, 23, 40] \mu\text{W}$  by misaligning the beam using the kinematic mount of the collimator. This then corresponds to effective powers  $P_{\text{eff}}$  of  $[48, 72, 96] \mu\text{W}$ , respectively, using Eq. (3.3). This is repeated for six values of the distance  $l$ , up to  $l = 1.5 \text{ m}$  corresponding to a maximum demodulation amplitude  $A_d = 465 \text{ rad}$ , and the resulting signal processing units, also for a variation of  $\sigma$  over  $[0.025, 0.05, 0.075]$ , are then recorded for each parameter combination of  $P_{\text{eff}}$ ,  $l$  and  $\sigma$ .

The results of these measurement are shown in Figs. F.2(a), (b) and (c) for the three values of  $\sigma$ , respectively. In each plot it can be seen that the effective power generally increases proportionally with  $P_{\text{eff}}$  and that the power registered by the signal processing increases for large values of  $\sigma$ , as would be expected because a broader window function allows more signal power to be incorporated. However, it can also be seen that the effective power shows an unexpected slope in the dependency on  $A_d$  for large values of  $\sigma$ . The reasons for this slope are unknown and this behaviour requires further investigation. Nevertheless, in this work, the conversion coefficient is only required for  $\sigma = 0.025$  and here the slope in the signal processing power can be neglected. Therefore, the mean over all six values of  $A_d$  in Fig. F.2(a) is computed and lines at the mean values are also drawn there. For each of the three effective power set-points used, the conversion coefficient can be extracted from these mean values with very good proportionality to the effective power. The conversion coefficient can then be given as  $(1.33 \pm 0.06) \cdot 10^3 \text{ Units} \cdot \mu\text{W}^{-1}$  and this value was used in Chap. 6 to determine the effective powers of the return signals.

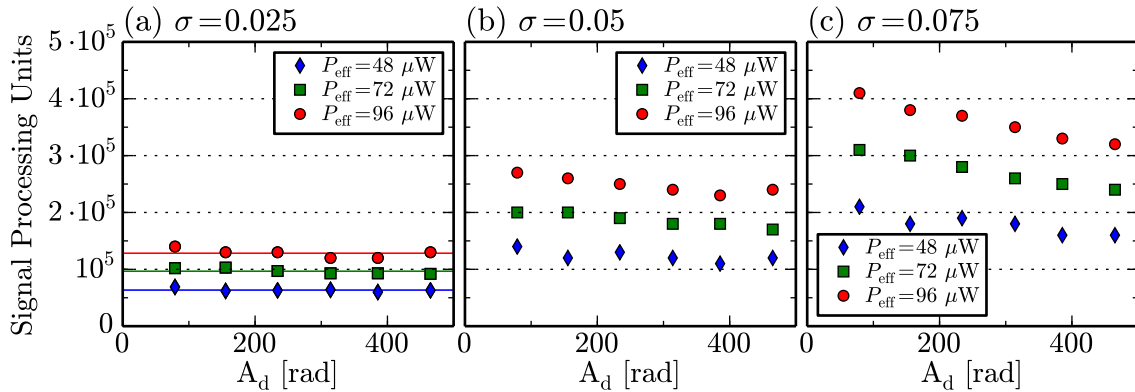


**Figure F.2.:** Measurement results for the determination of the registered signal processing power as a function of the demodulation amplitude  $A_d$  for three values of the effective power  $P_{\text{eff}}$  and for three values of the window width parameter  $\sigma$  in (a), (b) and (c).

# References

- [1] D. A. Shaddock. Digitally enhanced heterodyne interferometry. *Optics Letters*, 32(22):3355–3357, 2007.
- [2] C. J. Karlsson, A. Olsson, D. Letalick, and M. Harris. All-fiber multifunction continuous-wave coherent laser radar at  $1.55\ \mu\text{m}$  for range, speed, vibration, and wind measurements. *Applied Optics*, 39(21):3716–3726, 2000.
- [3] M. Harris, G. N. Pearson, K. D. Ridley, C. J. Karlsson, A. Olsson, and D. Letalick. Single-particle laser Doppler anemometry at  $1.55\ \mu\text{m}$ . *Applied Optics*, 40(6):969–973, 2001.
- [4] B. J. Rask. *Range resolved optical remote sensing using a continuous wave, pseudo-random modulated, CO<sub>2</sub> heterodyne lidar backscattered from aerosols*. PhD thesis, Oregon Graduate Institute of Science and Technology, 1995.
- [5] P. Lindelöw. *Fiber based coherent lidars for remote wind sensing*. PhD thesis, Technical University of Denmark, 2007.
- [6] N. Wang, K. E. Johnson, and A. D. Wright. Lidar-based FX-RLS feedforward control for wind turbine load mitigation. *Proceedings of the 2011 American Control Conference, San Francisco, USA*, pages 1910–1915, 2011.
- [7] T. Mikkelsen, K. H. Hansen, N. Angelou, M. Sjöholm, M. Harris, P. Hadley, R. Scullion, and G. Ellis. Lidar wind speed measurements from a rotating spinner. *Proceedings of the 2010 European Wind Energy Conference, Warsaw, Poland*, 2010.
- [8] P. J. Rodrigo and C. Pedersen. Reduction of phase-induced intensity noise in a fiber-based coherent Doppler lidar using polarization control. *Optics Express*, 18(5):5320–5327, 2010.
- [9] S. Kameyama, T. Ando, K. Asaka, Y. Hirano, and S. Wadaka. Compact all-fiber pulsed coherent Doppler lidar system for wind sensing. *Applied Optics*, 46(11):1938–1962, 2007.
- [10] J. P. Dakin, C. A. Wade, and M. Henning. Novel optical fibre hydrophone array using a single laser source and detector. *Electronics Letters*, 20(1):53–54, 1984.
- [11] G. A. Cranch and P. J. Nash. Large-scale multiplexing of interferometric fiber-optic sensors using TDM and DWDM. *Journal of Lightwave Technology*, 19(5):687–699, 2001.
- [12] G. A. Cranch, P. J. Nash, and C. K. Kirkendall. Large-scale remotely interrogated arrays of fiber-optic interferometric sensors for underwater acoustic applications. *IEEE Sensors Journal*, 3(1):19–30, 2003.
- [13] J. M. López-Higuera, L. Rodriguez Cobo, A. Quintela Incera, and A. Cobo. Fiber

- optic sensors in structural health monitoring. *Journal of Lightwave Technology*, 29(4):587–608, 2011.
- [14] C. C. Ciang, J. R. Lee, and H. J. Bang. Structural health monitoring for a wind turbine system: a review of damage detection methods. *Measurement Science and Technology*, 19(12):122001, 2008.
- [15] D. Kinet, P. Mégret, K. W. Goossen, L. Qiu, D. Heider, and C. Caucheteur. Fiber Bragg grating sensors toward structural health monitoring in composite materials: challenges and solutions. *Sensors*, 14(4):7394–7419, 2014.
- [16] B. Glisic. Influence of the gauge length on the accuracy of long-gauge sensors employed in monitoring of prismatic beams. *Measurement Science and Technology*, 22(3):035206, 2011.
- [17] C. D. Butter and G. B. Hocker. Fiber optics strain gauge. *Applied Optics*, 17(18):2867–2869, 1978.
- [18] G. B. Hocker. Fiber-optic sensing of pressure and temperature. *Applied Optics*, 18(9):1445–1448, 1979.
- [19] D. A. Jackson and J. D. C. Jones. Fibre optic sensors. *Optica Acta*, 33(12):1469–1503, 1986.
- [20] F. Farahi, D. J. Webb, J. D. C. Jones, and D. A. Jackson. Simultaneous measurement of temperature and strain: cross-sensitivity considerations. *Journal of Lightwave Technology*, 8(2):138–142, 1990.
- [21] J. D. C. Jones. Review of fibre sensor techniques for temperature-strain discrimination. *Proceedings of the 12th International Conference on Optical Fiber Sensors (OFS-12)*, Williamsburg, USA, pages 36–39, 1997.
- [22] W. Jin, W. C. Michie, G. Thursby, M. Konstantaki, and B. Culshaw. Simultaneous measurement of strain and temperature: error analysis. *Optical Engineering*, 36(2):598–609, 1997.
- [23] W. W. Morey, G. Meltz, and J. M. Weiss. Evaluation of a fiber Bragg grating hydrostatic pressure sensor. *Proceedings of the 8th International Conference on Optical Fiber Sensors (OFS-8)*, Monterey, USA, page PD 4.4, 1992.
- [24] S. W. James, M. L. Dockney, and R. P. Tatam. Simultaneous independent temperature and strain measurement using in-fibre Bragg grating sensors. *Electronics Letters*, 32(12):1133–1134, 1996.
- [25] M. G. Xu, J. L. Archambault, L. Reekie, and J. P. Dakin. Discrimination between strain and temperature effects using dual-wavelength fibre grating sensors. *Electronics Letters*, 30(13):1085–1087, 1994.
- [26] P. M. Blanchard, J. G. Burnett, G. R. G. Erry, A. H. Greenaway, P. Harrison, B. Mangan, J. C. Knight, P. St J. Russell, M. J. Gander, R. McBride, and J. D. C. Jones. Two-dimensional bend sensing with a single, multi-core optical fibre. *Smart Materials and Structures*, 9(2):132–140, 2000.
- [27] M. J. Gander, W. N. MacPherson, R. McBride, J. D. C. Jones, L. Zhang, I. Bennion, P. M. Blanchard, J. G. Burnett, and A. H. Greenaway. Bend measurement using Bragg gratings in multicore fibre. *Electronics Letters*, 36(2):120–121, 2000.
- [28] H. J. Patrick, C. C. Chang, and S. T. Vohra. Long period fibre gratings for structural bend sensing. *Electronics Letters*, 34(18):1773–1775, 1998.

- [29] C. C. Ye, S. W. James, and R. P. Tatam. Simultaneous temperature and bend sensing with long-period fiber gratings. *Optics Letters*, 25(14):1007–1009, 2000.
- [30] C. K. Kirkendall and A. D. Dandridge. Overview of high performance fibre-optic sensing. *Journal of Physics D: Applied Physics*, 37(18):197–216, 2004.
- [31] A. D. Dandridge, A. B. Tveten, G. H. Sigel, E. J. West, and T. G. Giallorenzi. Optical fibre magnetic field sensors. *Electronics Letters*, 16(11):408–409, 1980.
- [32] D. A. Egan, S. W. James, and R. P. Tatam. A polarization-based optical fibre vibrometer. *Measurement Science and Technology*, 8(3):343–347, 1997.
- [33] D. A. Jackson and J. D. C. Jones. Extrinsic fibre-optic sensors for remote measurement: part two. *Optics and Laser Technology*, 18(6):299–307, 1986.
- [34] R. I. Laming, M. P. Gold, D. N. Payne, and N. A. Halliwell. Fibre-optic vibration probe. *Proceedings of Fiber Optic Sensors I Conference, Cannes, France*, Proc. SPIE 0586:38–44, 1985.
- [35] A. C. Lewin, F. Ritter, and G. Siegmund. Laser-diode-based pseudo-heterodyne interferometer for online process control of wire bonders. *Proceedings of the 4th International Conference on Vibration Measurements by Laser Techniques, Ancona, Italy*, Proc. SPIE 4072:8–18, 2000.
- [36] Q. Lin, L. Chen, S. Li, and X. Wu. A high-resolution fiber optic accelerometer based on intracavity phase-generated carrier (PGC) modulation. *Measurement Science and Technology*, 22(1):015303, 2011.
- [37] A. C. Lewin. Research activities arising from the University of Kent. *Photonic Sensors*, 1(4):351–361, 2011.
- [38] K. Peters. Polymer optical fiber sensors - a review. *Smart Materials and Structures*, 20(1):013002, 2011.
- [39] M. R. Layton and J. A. Bucaro. Optical fiber acoustic sensor utilizing mode-mode interference. *Applied Optics*, 18(5):666–670, 1979.
- [40] G. D. Peng, Z. Xiong, and P. L. Chu. Photosensitivity and gratings in dye-doped polymer optical fibers. *Optical Fiber Technology*, 5(2):242–251, 1999.
- [41] H. Dobb, D. J. Webb, K. Kalli, A. Argyros, M. C. Large, and M. A. Van Eijkelenborg. Continuous wave ultraviolet light-induced fiber Bragg gratings in few-and single-mode microstructured polymer optical fibers. *Optics Letters*, 30(24):3296–3298, 2005.
- [42] S. Liehr, P. Lenke, M. Wendt, K. Krebber, M. Seeger, E. Thiele, H. Metschies, B. Gebreselassie, and J. C. Munich. Polymer optical fiber sensors for distributed strain measurement and application in structural health monitoring. *IEEE Sensors Journal*, 9(11):1330–1338, 2009.
- [43] M. K. Barnoski and S. M. Jensen. Fiber waveguides: a novel technique for investigating attenuation characteristics. *Applied Optics*, 15(9):2112–2115, 1976.
- [44] W. Eickhoff and R. Ulrich. Optical frequency domain reflectometry in single-mode fiber. *Applied Physics Letters*, 39(9):693–695, 1981.
- [45] A. Güemes, A. Fernández-López, and B. J. Soller. Optical fiber distributed sensing-physical principles and applications. *Structural Health Monitoring*, 9(3):233–245, 2010.
- [46] A. J. Rogers. Polarization-optical time domain reflectometry: a technique for the

- measurement of field distributions. *Applied Optics*, 20(6):1060–1074, 1981.
- [47] B. J. Soller, D. K. Gifford, M. S. Wolfe, and M. E. Froggatt. High resolution optical frequency domain reflectometry for characterization of components and assemblies. *Optics Express*, 13(2):666–674, 2005.
  - [48] A. H. Hartog. A distributed temperature sensor based on liquid-core optical fibers. *Journal of Lightwave Technology*, 1(3):498–509, 1983.
  - [49] M. C. Farries, M. E. Fermann, R. I. Laming, S. B. Poole, D. N. Payne, and A. P. Leach. Distributed temperature sensor using Nd<sup>3+</sup> doped optical fibre. *Electronics Letters*, 22(8):418–419, 1986.
  - [50] S. V. Shatalin, V. N. Treschikov, and A. J. Rogers. Interferometric optical time-domain reflectometry for distributed optical-fiber sensing. *Applied Optics*, 37(24):5600–5604, 1998.
  - [51] A. D. Kersey. Fiber optic sensors shine bright: industrial applications where FOS bring differentiated performance/value. *Proceedings of the 22th International Conference on Optical Fiber Sensors (OFS-22), Beijing, China*, Proc. SPIE 8421:0F 1–4, 2012.
  - [52] M. E. Froggatt and J. Moore. High-spatial-resolution distributed strain measurement in optical fiber with Rayleigh scatter. *Applied Optics*, 37(10):1735–1740, 1998.
  - [53] J. P. Dakin, D. J. Pratt, G. W. Bibby, and J. N. Ross. Distributed optical fibre Raman temperature sensor using a semiconductor light source and detector. *Electronics Letters*, 21(13):569–570, 1985.
  - [54] K. T. V. Grattan and T. Sun. Fiber optic sensor technology: an overview. *Sensors and Actuators A: Physical*, 82(1):40–61, 2000.
  - [55] A. H. Hartog. Raman sensors and their applications. *Proceedings of the 22th International Conference on Optical Fiber Sensors (OFS-22), Beijing, China*, Proc. SPIE 8421:0K 1–6, 2012.
  - [56] T. Horiguchi, T. Kurashima, and M. Tateda. Tensile strain dependence of Brillouin frequency shift in silica optical fibers. *IEEE Photonics Technology Letters*, 1(5):107–108, 1989.
  - [57] D. Culverhouse, F. Farahi, C. N. Pannell, and D. A. Jackson. Potential of stimulated Brillouin scattering as sensing mechanism for distributed temperature sensors. *Electronics Letters*, 25(14):913–915, 1989.
  - [58] L. Thévenaz. Brillouin distributed time-domain sensing in optical fibers: state of the art and perspectives. *Frontiers of Optoelectronics in China*, 3(1):13–21, 2010.
  - [59] X. Bao and L. Chen. Recent progress in Brillouin scattering based fiber sensors. *Sensors*, 11(4):4152–4187, 2011.
  - [60] S. M. Maughan, H. H. Kee, and T. P. Newson. 57-km single-ended spontaneous Brillouin-based distributed fiber temperature sensor using microwave coherent detection. *Optics Letters*, 26(6):331–333, 2001.
  - [61] Y. Dong, L. Chen, and X. Bao. Time-division multiplexing-based BOTDA over 100km sensing length. *Optics Letters*, 36(2):277–279, 2011.
  - [62] D. Eloo, Y. Antman, N. Levanon, and A. Zadok. High-resolution long-reach distributed Brillouin sensing based on combined time-domain and correlation-domain analysis. *Optics Express*, 22(6):6453–6463, 2014.

- 
- [63] K. O. Hill, Y. Fujii, D. C. Johnson, and B. S. Kawasaki. Photosensitivity in optical fiber waveguides: application to reflection filter fabrication. *Applied Physics Letters*, 32(10):647–649, 1978.
- [64] G. Meltz, W. W. Morey, and W. H. Glenn. Formation of Bragg gratings in optical fibers by a transverse holographic method. *Optics Letters*, 14(15):823–825, 1989.
- [65] B. Lee. Review of the present status of optical fiber sensors. *Optical Fiber Technology*, 9(2):57–79, 2003.
- [66] M. Ando, M. Yamauchi, K. Nakayama, K. Moriyama, K. Fujita, Y. Masuda, M. Kimura, Y. Mizutani, S. Kimura, and T. Yokouchi. Dependence of fiber Bragg grating characteristics on its length. *Japanese Journal of Applied Physics*, 43(7R):4234, 2004.
- [67] A. D. Kersey, M. A. Davis, H. J. Patrick, M. LeBlanc, K. P. Koo, C. G. Askins, M. A. Putnam, and E. J. Friebele. Fiber grating sensors. *Journal of Lightwave Technology*, 15(8):1442–1463, 1997.
- [68] A. D. Kersey, T. A. Berkoff, and W. W. Morey. High-resolution fibre-grating based strain sensor with interferometric wavelength-shift detection. *Electronics Letters*, 28(3):236–238, 1992.
- [69] A. J. Rogers. Distributed optical-fibre sensing. *Measurement Science and Technology*, 10(8):R75–R99, 1999.
- [70] R. Correia, E. Chehura, S. W. James, and R. P. Tatam. A pressure sensor based upon the transverse loading of a sub-section of an optical fibre Bragg grating. *Measurement Science and Technology*, 18(10):3103, 2007.
- [71] P. Zhang, H. H. Cerecedo-Nunez, B. Qi, G. R. Pickrell, and A. Wang. Optical time-domain reflectometry interrogation of multiplexing low-reflectance Bragg-grating-based sensor system. *Optical Engineering*, 42(6):1597–1603, 2003.
- [72] M. E. Froggatt and J. Moore. Distributed measurement of static strain in an optical fiber with multiple Bragg gratings at nominally equal wavelengths. *Applied Optics*, 37(10):1741–1746, 1998.
- [73] K. Yüksel, V. Moeyaert, P. Mégret, and M. Wuilpart. Complete analysis of multi-reflection and spectral-shadowing crosstalks in a quasi-distributed fiber sensor interrogated by OFDR. *IEEE Sensors Journal*, 12(5):988–995, 2012.
- [74] B. A. Childers, M. E. Froggatt, S. G. Allison, T. C. Moore Sr., D. A. Hare, C. F. Batten, and D. C. Jegley. Use of 3000 Bragg grating strain sensors distributed on four eight-meter optical fibers during static load tests of a composite structure. *Proceedings of the 2001 Smart Structures and Materials Conference, Newport Beach, USA*, Proc. SPIE 4332:133–142, 2001.
- [75] C. G. Askins, M. A. Putnam, G. M. Williams, and E. J. Friebele. Stepped-wavelength optical-fiber Bragg grating arrays fabricated in line on a draw tower. *Optics Letters*, 19(2):147–149, 1994.
- [76] R. G. Duncan, M. E. Froggatt, S. T. Kreger, R. J. Seeley, D. K. Gifford, A. K. Sang, and M. S. Wolfe. High-accuracy fiber-optic shape sensing. *Proceedings of the 2007 Sensor Systems and Networks Conference, San Diego, USA*, Proc. SPIE 6530:1S 1–11, 2007.
- [77] J. P. Moore and M. D. Rogge. Shape sensing using multi-core fiber optic cable and

- parametric curve solutions. *Optics Express*, 20(3):2967–2973, 2012.
- [78] V. Bhatia and A. M. Vengsarkar. Optical fiber long-period grating sensors. *Optics Letters*, 21(9):692–694, 1996.
- [79] S. W. James and R. P. Tatam. Optical fibre long-period grating sensors: characteristics and application. *Measurement Science and Technology*, 14(5):R49–R61, 2003.
- [80] V. Bhatia. Applications of long-period gratings to single and multi-parameter sensing. *Optics Express*, 4(11):457–466, 1999.
- [81] T. Allsop, A. Gillooly, V. Mezentsev, T. Earthgrowl-Gould, R. Neal, D. J. Webb, and I. Bennion. Bending and orientational characteristics of long period gratings written in D-shaped optical fiber [directional bend sensors]. *IEEE Transactions on Instrumentation and Measurement*, 53(1):130–135, 2004.
- [82] L. Glavind, I. S. Olesen, B. F. Skipper, and M. Kristensen. Fiber-optical grating sensors for wind turbine blades: a review. *Optical Engineering*, 52(3):030901 1–9, 2013.
- [83] H. J. Patrick, A. D. Kersey, and F. Bucholtz. Analysis of the response of long period fiber gratings to external index of refraction. *Journal of Lightwave Technology*, 16(9):1606, 1998.
- [84] R. P. Murphy, S. W. James, and R. P. Tatam. Multiplexing of fiber-optic long-period grating-based interferometric sensors. *Journal of Lightwave Technology*, 25(3):825–829, 2007.
- [85] J. D. C. Jones. *Interferometry and polarimetry for optical sensing*, pages 227–245. Handbook of optical fibre sensing technology. Wiley, 2002.
- [86] V. Bhatia, M. E. Jones, J. L. Grace, K. A. Murphy, R. O. Claus, J. A. Greene, and T. A. Tran. Applications of absolute fiber optic sensors to smart materials and structures. *Proceedings of the 10th International Conference on Optical Fibre Sensors (OFS-10), Glasgow, UK*, Proc. SPIE 2360:171–174, 1994.
- [87] A. D. Kersey. A review of recent developments in fiber optic sensor technology. *Optical Fiber Technology*, 2(3):291–317, 1996.
- [88] X. Zhou and Q. Yu. Wide-range displacement sensor based on fiber-optic Fabry-Perot interferometer for subnanometer measurement. *IEEE Sensors Journal*, 11(7):1602–1606, 2011.
- [89] C. Ma and A. Wang. Signal processing of white-light interferometric low-finesse fiber-optic Fabry-Perot sensors. *Applied Optics*, 52(2):127–138, 2013.
- [90] E. Cibula, S. Pevec, B. Lenardic, E. Pinet, and D. Donlagic. Miniature all-glass robust pressure sensor. *Optics Express*, 17(7):5098–5106, 2009.
- [91] C. E. Lee and H. F. Taylor. Interferometric optical fibre sensors using internal mirrors. *Electronics Letters*, 24(4):193–194, 1988.
- [92] K. A. Murphy, M. F. Gunther, A. Wang, R. O. Claus, and A. M. Vengsarkar. Extrinsic Fabry-Perot optical fiber sensor. *Proceedings of the 8th International Conference on Optical Fiber Sensors (OFS-8), Monterey, USA*, pages 193–196, 1992.
- [93] M. Singh, C. J. Tuck, and G. F. Fernando. Multiplexed optical fibre Fabry-Perot sensors for strain metrology. *Smart Materials and Structures*, 8(5):549–553, 1999.

- [94] Z. Wang, F. Shen, L. Song, X. Wang, and A. Wang. Multiplexed fiber Fabry-Perot interferometer sensors based on ultrashort Bragg gratings. *IEEE Photonics Technology Letters*, 19(8):622–624, 2007.
- [95] J. A. Bucaro, H. D. Dardy, and E. F. Carome. Fiber-optic hydrophone. *The Journal of the Acoustical Society of America*, 62(5):1302–1304, 1977.
- [96] F. Bucholtz, C. A. Villarruel, A. R. Davis, C. K. Kirkendall, D. M. Dagenais, J. A. McVicker, S. S. Patrick, K. P. Koo, G. Wang, H. Valo, T. Lund, A. G. Andersen, R. Gjessing, E. J. Eidem, and T. Knudsen. Multichannel fiber-optical magnetometer system for undersea measurements. *Journal of Lightwave Technology*, 13(7):1385–1395, 1995.
- [97] J. Roths and F. Jülich. Determination of strain sensitivity of free fiber Bragg gratings. *Proceedings of the 2008 Optical Sensors Conference, Strasbourg, France*, Proc. SPIE 7003:08 1–8, 2008.
- [98] D. W. Stowe, D. R. Moore, and R. G. Priest. Polarization fading in fiber interferometric sensors. *IEEE Transactions on Microwave Theory and Techniques*, 30(10):1632–1635, 1982.
- [99] M. Tur, Y. S. Boger, and H. J. Shaw. Polarization-induced fading in fiber-optic sensor arrays. *Journal of Lightwave Technology*, 13(7):1269–1276, 1995.
- [100] H. C. Lefèvre. Single-mode fibre fractional wave devices and polarisation controllers. *Electronics Letters*, 16(20):778–780, 1980.
- [101] N. J. Frigo, A. D. Dandridge, and A. B. Tveten. Technique for elimination of polarisation fading in fibre interferometers. *Electronics Letters*, 20(8):319–320, 1984.
- [102] I. Sakai. Frequency-division multiplexing of optical-fibre sensors using a frequency-modulated source. *Optical and Quantum Electronics*, 18(4):279–289, 1986.
- [103] A. D. Kersey, A. D. Dandridge, and A. B. Tveten. Overview of multiplexing techniques for interferometric fiber sensors. *Proceedings of the Fiber Optic and Laser Sensors V Conference, San Diego, USA*, Proc. SPIE 0838:184–193, 1987.
- [104] P. J. Nash. Review of interferometric optical fibre hydrophone technology. *IEE Proceedings-Radar, Sonar and Navigation*, 143(3):204–209, 1996.
- [105] A. D. Kersey and M. J. Marrone. Bragg grating based nested fibre interferometers. *Electronics Letters*, 32(13):1221–1223, 1996.
- [106] D. Inaudi, S. Vurpillot, N. Casanova, and A. Osa-Wyser. Development and field test of deformation sensors for concrete embedding. *Proceedings of the 1996 Smart Structures and Materials Conference, San Diego, USA*, Proc. SPIE 2721:138–148, 1996.
- [107] A. D. Kersey and A. D. Dandridge. Comparative analysis of multiplexing techniques for interferometric fiber sensors. *Proceedings of the Fibre Optics '89 Conference, London, UK*, Proc. SPIE 1120:236–246, 1989.
- [108] C. Polhemus. Two-wavelength interferometry. *Applied Optics*, 12(9):2071–2074, 1973.
- [109] A. D. Kersey, A. D. Dandridge, and W. K. Burns. Two-wavelength fibre gyroscope with wide dynamic range. *Electronics Letters*, 22(18):935–937, 1986.
- [110] H. Kikuta, K. Iwata, and R. Nagata. Distance measurement by the wavelength shift of laser diode light. *Applied Optics*, 25(17):2976–2980, 1986.



- [111] M. Born and E. Wolf. *Principles of optics*. Cambridge University Press, 7th (expanded) edition, 2002.
- [112] K. Itoh. Analysis of the phase unwrapping algorithm. *Applied Optics*, 21(14):2470–2470, 1982.
- [113] K. Creath. Phase-measurement interferometry techniques. *Progress in Optics*, 26(26):349–393, 1988.
- [114] E. L. Wooten, K. M. Kissa, A. Yi-Yan, E. J. Murphy, D. A. Lafaw, P. F. Hallemeier, D. Maack, D. V. Attanasio, D. J. Fritz, and G. J. McBrien. A review of lithium niobate modulators for fiber-optic communications systems. *IEEE Journal of Selected Topics in Quantum Electronics*, 6(1):69–82, 2000.
- [115] D. E. N. Davies and S. A. Kingsley. Method of phase-modulating signals in optical fibres: application to optical-telemetry systems. *Electronics Letters*, 10(2):21–22, 1974.
- [116] D. A. Jackson, R. G. Priest, A. D. Dandridge, and A. B. Tveten. Elimination of drift in a single-mode optical fiber interferometer using a piezoelectrically stretched coiled fiber. *Applied Optics*, 19(17):2926–2929, 1980.
- [117] E. H. Young Jr and S. K. Yao. Design considerations for acousto-optic devices. *Proceedings of the IEEE*, 69(1):54–64, 1981.
- [118] C. J. Duffy and R. P. Tatam. Optical frequency shifter technique based on stimulated Brillouin scattering in birefringent optical fiber. *Applied Optics*, 32(30):5966–5972, 1993.
- [119] O. S. Khan and R. P. Tatam. Optical frequency shifter based on stimulated Brillouin scattering in a birefringent optical fibre ring resonator. *Optics Communications*, 103(1-2):161–168, 1993.
- [120] B. Sheard, G. Heinzl, and K. Danzmann. LISA long-arm interferometry: An alternative frequency pre-stabilization system. *Classical and Quantum Gravity*, 27(8):084011, 2010.
- [121] J. Zheng. Analysis of optical frequency-modulated continuous-wave interference. *Applied Optics*, 43(21):4189–4198, 2004.
- [122] A. D. Dandridge and L. Goldberg. Current-induced frequency modulation in diode lasers. *Electronics Letters*, 18(7):302–304, 1982.
- [123] H. Shalom, A. Zadok, M. Tur, P. J. Legg, W. D. Cornwell, and I. Andonovic. On the various time constants of wavelength changes of a DFB laser under direct modulation. *IEEE Journal of Quantum Electronics*, 34(10):1816–1822, 1998.
- [124] L. A. Coldren. Monolithic tunable diode lasers. *IEEE Journal of Selected Topics in Quantum Electronics*, 6(6):988–999, 2000.
- [125] B. Mroziewicz. External cavity wavelength tunable semiconductor lasers - a review. *Opto-Electronics Review*, 16(4):347–366, 2008.
- [126] A. Q. Liu and X. M. Zhang. A review of MEMS external-cavity tunable lasers. *Journal of Micromechanics and Microengineering*, 17(1):R1–R13, 2007.
- [127] Y. Li, S. Verstuyft, G. Yurtsever, S. Keyvaninia, G. Roelkens, D. Van Thourhout, and R. Baets. Heterodyne laser Doppler vibrometers integrated on silicon-on-insulator based on serrodyne thermo-optic frequency shifters. *Applied Optics*, 52(10):2145–2152, 2013.

2013.

- [128] I. Sakai, R. C. Youngquist, and G. Parry. Multiplexing of optical fiber sensors using a frequency-modulated source and gated output. *Journal of Lightwave Technology*, 5(7):932–940, 1987.
- [129] B. Qi, F. Ye, L. Qian, and H. K. Lo. Reflectometry based on a frequency-shifted interferometer using sideband interference. *Optics Letters*, 38(7):1083–1085, 2013.
- [130] J. L. Santos, A. P. Leite, and D. A. Jackson. Optical fiber sensing with a low-finesse Fabry-Perot cavity. *Applied Optics*, 31(34):7361–7366, 1992.
- [131] M. J. Lawrence, B. Willke, M. E. Husman, E. K. Gustafson, and R. L. Byer. Dynamic response of a Fabry-Perot interferometer. *Journal of the Optical Society of America B*, 16(4):523–532, 1999.
- [132] B. Culshaw. The optical fibre Sagnac interferometer: an overview of its principles and applications. *Measurement Science and Technology*, 17(1):R1–R16, 2006.
- [133] C. Delisle and P. Cielo. Application de la modulation spectrale à la transmission de l’information. *Canadian Journal of Physics*, 53(11):1047–1053, 1975.
- [134] J. L. Brooks, R. H. Wentworth, R. C. Youngquist, M. Tur, B. Y. Kim, and H. J. Shaw. Coherence multiplexing of fiber-optic interferometric sensors. *Journal of Lightwave Technology*, 3(5):1062–1072, 1985.
- [135] A. D. Kersey and A. D. Dandridge. Phase-noise reduction in coherence-multiplexed interferometric fibre sensors. *Electronics Letters*, 22(11):616–618, 1986.
- [136] I. Glover and P. M. Grant. *Digital communications*. Pearson Education, 3rd edition, 2009.
- [137] D. A. Jackson. A prototype digital phase tracker for the fibre interferometer. *Journal of Physics E: Scientific Instruments*, 14(11):1274–1278, 1981.
- [138] M. Bauer, F. Ritter, and G. Siegmund. High-precision laser vibrometers based on digital Doppler signal processing. *Proceedings of the 5th International Conference on Vibration Measurements by Laser Techniques, Ancona, Italy*, Proc. SPIE 4827:50–61, 2002.
- [139] J. R. Carson. Notes on the theory of modulation. *Proceedings of the Institute of Radio Engineers*, 10(1):57–64, 1922.
- [140] H. Taub and D. L. Schilling. *Principles of communication systems*. McGraw-Hill, 1971.
- [141] C. M. Wu and C. S. Su. Nonlinearity in measurements of length by optical interferometry. *Measurement Science and Technology*, 7(1):62–68, 1996.
- [142] T. G. McRae, M. T. L. Hsu, C. H. Freund, D. A. Shaddock, J. Herrmann, and M. B. Gray. Linearization and minimization of cyclic error with heterodyne laser interferometry. *Optics Letters*, 37(13):2448–2450, 2012.
- [143] P. L. M. Heydemann. Determination and correction of quadrature fringe measurement errors in interferometers. *Applied Optics*, 20(19):3382–3384, 1981.
- [144] F. Kullander. A novel algorithm for passive demodulation of optical fiber interferometric signals using a 3x3 coupler. *Proceedings of the 14th International Conference on Optical Fiber Sensors (OFS-14), Venice, Italy*, Proc. SPIE 4185:480–483, 2000.
- [145] K. P. Koo, A. B. Tveten, and A. D. Dandridge. Passive stabilization scheme for

- fiber interferometers using (3x3) fiber directional couplers. *Applied Physics Letters*, 41(7):616–618, 1982.
- [146] G. M. B. Bouricius and S. F. Clifford. An optical interferometer using polarization coding to obtain quadrature phase components. *Review of Scientific Instruments*, 41(12):1800–1803, 1970.
  - [147] J. H. Bruning, D. R. Herriott, J. E. Gallagher, D. P. Rosenfeld, A. D. White, and D. J. Brangaccio. Digital wavefront measuring interferometer for testing optical surfaces and lenses. *Applied Optics*, 13(11):2693–2703, 1974.
  - [148] A. D. Kersey, D. A. Jackson, and M. Corke. Demodulation scheme fibre interferometric sensors employing laser frequency switching. *Electronics Letters*, 19(3):102–103, 1983.
  - [149] M. Milnes, A. Tikhomirov, S. Foster, and S. Goodman. Fast four step digital demodulation for multiplexed fibre laser sensors. *Proceedings of the 19th International Conference on Optical Fibre Sensors (OFS-19)*, Perth, Australia, Proc. SPIE 7004:22 1–5, 2008.
  - [150] P. Carré. Installation et utilisation du comparateur photoélectrique et interférentiel du Bureau International des Poids et Mesures. *Metrologia*, 2(1):13–23, 1966.
  - [151] A. Patil and P. Rastogi. Approaches in generalized phase shifting interferometry. *Optics and Lasers in Engineering*, 43(3-5):475–490, 2005.
  - [152] O. Sasaki, H. Okazaki, and M. Sakai. Sinusoidal phase modulating interferometer using the integrating-bucket method. *Applied Optics*, 26(6):1089–1093, 1987.
  - [153] P. De Groot. Design of error-compensating algorithms for sinusoidal phase shifting interferometry. *Applied Optics*, 48(35):6788–6796, 2009.
  - [154] J. Chen, Y. Ishii, and Kazumi Murata. Heterodyne interferometry with a frequency-modulated laser diode. *Applied Optics*, 27(1):124–128, 1988.
  - [155] H. C. Lefèvre. Fundamentals of the interferometric fiber optic gyroscope. *Proceedings of the Fiber Optic Gyros: 20th Anniversary Conference, Denver, USA*, Proc. SPIE 2837:2–17, 1996.
  - [156] M. N. Armenise, C. Ciminelli, F. Dell’Olio, and V. M. N. Passaro. *Advances in gyroscope technologies*. Springer, 2010.
  - [157] A. D. Dandridge and A. B. Tveten. Phase compensation in interferometric fiber-optic sensors. *Optics Letters*, 7(6):279–281, 1982.
  - [158] A. D. Kersey, M. J. Marrone, K. P. Koo, and A. D. Dandridge. Optically demodulated interferometric sensor system. *Proceedings of the 10th International Conference on Optical Fibre Sensors (OFS-10)*, Glasgow, UK, Proc. SPIE 2360:343–346, 1994.
  - [159] H. A. Deferrari, R. A. Darby, and F. A. Andrews. Vibrational displacement and mode-shape measurement by a laser interferometer. *The Journal of the Acoustical Society of America*, 42(5):982–990, 1967.
  - [160] Y. Ohtsuka. Dynamic measurements of small displacements by laser interferometry. *Transactions of the Institute of Measurement and Control*, 4(3):115–124, 1982.
  - [161] F. J. Eberhardt and F. A. Andrews. Laser heterodyne system for measurement and analysis of vibration. *Journal of the Acoustical Society of America*, 48(3 pt 1):603–609, 1970.
  - [162] A. J. H. Meskers, J. W. Spronck, and R. H. Munnig Schmidt. Heterodyne displacement

- interferometer, insensitive for input polarization. *Optics Letters*, 39(7):1949–1952, 2014.
- [163] A. T. Waz, P. R. Kaczmarek, and K. M. Abramski. Laser-fibre vibrometry at 1550 nm. *Measurement Science and Technology*, 20(10):105301 1–8, 2009.
  - [164] O. Ostwald and B. Schiek. Network analysis by phase-modulated homodyne detection. *IEEE Transactions on Instrumentation and Measurement*, IM-30(2):152–154, 1981.
  - [165] E. Voges, O. Ostwald, B. Schiek, and A. Neyer. Optical phase and amplitude measurement by single sideband homodyne detection. *IEEE Journal of Quantum Electronics*, QE-18(1):124–129, 1982.
  - [166] R. C. Cumming. The serrodyne frequency translator. *Proceedings of the Institute of Radio Engineers*, 45(2):175–186, 1957.
  - [167] M. Izutsu, S. Shikama, and T. Sueta. Integrated optical SSB modulator/frequency shifter. *IEEE Journal of Quantum Electronics*, 17(11):2225–2227, 1981.
  - [168] S. Gao and R. Hui. Frequency-modulated continuous-wave lidar using I/Q modulator for simplified heterodyne detection. *Optics Letters*, 37(11):2022–2024, 2012.
  - [169] D. Eberhard and E. Voges. Fiber gyroscope with phase-modulated single-sideband detection. *Optics Letters*, 9(1):22–24, 1984.
  - [170] C. Laskoskie, H. Hung, T. El-Wailly, and C. C. Chang. Ti-LiNbO<sub>3</sub> waveguide serrodyne modulator with ultrahigh sideband suppression for fiber optic gyroscopes. *Journal of Lightwave Technology*, 7(4):600–606, 1989.
  - [171] J. Zheng. Reflectometric fiber optic frequency-modulated continuous-wave interferometric displacement sensor. *Optical Engineering*, 44(12):124404, 2005.
  - [172] D. A. Jackson, A. D. Kersey, M. Corke, and J. D. C. Jones. Pseudoheterodyne detection scheme for optical interferometers. *Electronics Letters*, 18(25-26):1081–1083, 1982.
  - [173] R. Onodera and Y. Ishii. Effect of beat frequency on the measured phase of laser-diode heterodyne interferometry. *Applied Optics*, 35(22):4355–4360, 1996.
  - [174] R. P. Tatam, J. D. C. Jones, and D. A. Jackson. Opto-electronic processing schemes for the measurement of circular birefringence. *Optica Acta*, 33(12):1519–1528, 1986.
  - [175] A. D. Kersey, A. C. Lewin, and D. A. Jackson. Pseudo-heterodyne detection scheme for the fibre gyroscope. *Electronics Letters*, 20(9):368–370, 1984.
  - [176] A. C. Lewin, A. D. Kersey, and D. A. Jackson. Non-contact surface vibration analysis using a monomode fibre optic interferometer incorporating an open air path. *Journal of Physics E: Scientific Instruments*, 18(7):604–608, 1985.
  - [177] R. P. Tatam and D. A. Jackson. Remote probe configuration for Faraday effect magnetometry. *Optics Communications*, 72(1):60–65, 1989.
  - [178] P. Y. Chien and C. L. Pan. Deep phase-modulation approach to an open-loop fiber optic gyroscope. *IEEE Photonics Technology Letters*, 3(3):284–286, 1991.
  - [179] M. Abramowitz and I. A. Stegun. *Handbook of mathematical functions with formulas, graphs, and mathematical tables*. US Department of Commerce, 10th printing with corrections 1972.
  - [180] A. D. Dandridge, A. B. Tveten, and T. G. Giallorenzi. Homodyne demodulation scheme for fiber optic sensors using phase generated carrier. *IEEE Journal of*

- Quantum Electronics*, 18(10):1647–1653, 1982.
- [181] A. D. Dandridge, A. B. Tveten, A. D. Kersey, and A. M. Yurek. Multiplexing of interferometric sensors using phase carrier techniques. *Journal of Lightwave Technology*, 5(7):947–952, 1987.
- [182] L. Wang, Q. Shi, H. Wang, X. Zeng, Q. Tian, C. Tian, H. Zhang, L. Huang, M. Zhang, and Y. Liao. Performance improvement of phase-generated carrier method by eliminating laser-intensity modulation for optical seismometer. *Optical Engineering*, 49(2):024402, 2010.
- [183] C. C. Chang and J. S. Sirkis. Design of fiber optic sensor systems for low velocity impact detection. *Smart Materials and Structures*, 7(2):166–177, 1998.
- [184] R. Sato and S. Saito. Design of fiber-optic magnetometer utilizing magnetostriction. *Japanese Journal of Applied Physics, Part 1*, 46(2):817–820, 2007.
- [185] S. T. Vohra, B. A. Danver, A. B. Tveten, and A. D. Dandridge. High performance fibre optic accelerometers. *Electronics Letters*, 33(2):155–157, 1997.
- [186] J. He, L. Wang, F. Li, and Y. Liu. An ameliorated phase generated carrier demodulation algorithm with low harmonic distortion and high stability. *Journal of Lightwave Technology*, 28(22):3258–3265, 2010.
- [187] O. Sasaki and H. Okazaki. Sinusoidal phase modulating interferometry for surface profile measurement. *Applied Optics*, 25(18):3137–3140, 1986.
- [188] E. L. Green and P. G. Cable. Passive demodulation of optical interferometric sensors. *IEEE Journal of Quantum Electronics*, 18(10):1639–1644, 1982.
- [189] J. H. Cole, B. A. Danver, and J. A. Bucaro. Synthetic-heterodyne interferometric demodulation. *IEEE Journal of Quantum Electronics*, 18(4):694–697, 1982.
- [190] V. S. Sudarshanam and K. Srinivasan. Linear readout of dynamic phase change in a fiber-optic homodyne interferometer. *Optics Letters*, 14(2):140–142, 1989.
- [191] W. Jin, L. M. Zhang, D. Uttamchandani, and B. Culshaw. Modified J1...J4 method for linear readout of dynamic phase changes in a fiber-optic homodyne interferometer. *Applied Optics*, 30(31):4496–4499, 1991.
- [192] G. Heinzl, F. Guzmán Cervantes, A. F. García Marin, J. Kullmann, W. Feng, and K. Danzmann. Deep phase modulation interferometry. *Optics Express*, 18(18):19076–19086, 2010.
- [193] O. Gerberding. Deep frequency modulation interferometry. *Optics Express*, 23(11):14753–14762, 2015.
- [194] J. P. Dakin. Multiplexed and distributed optical fibre sensor systems. *Journal of Physics E Scientific Instruments*, 20:954–967, 1987.
- [195] A. D. Kersey. Multiplexed fiber optic sensors. *Proceedings of the Distributed and Multiplexed Fiber Optic Sensors II Conference, Boston, USA*, Proc. SPIE 1797:161–185, 1992.
- [196] M. Volanthen, H. Geiger, and J. P. Dakin. Time-division-multiplexed optical fibre strain-sensor using subcarrier interferometry. *Electronics Letters*, 31(22):1943–1944, 1995.
- [197] M. A. Davis, A. D. Kersey, T. A. Berkoff, and D. G. Bellemore. Subcarrier based path-integrating strain sensor array utilising fiber Bragg gratings. *Proceedings of the*

- Distributed and Multiplexed Fiber Optic Sensors IV Conference, San Diego, USA*, Proc. SPIE 2294:93–99, 1994.
- [198] S. Liehr and K. Krebber. Application of quasi-distributed and dynamic length and power change measurement using optical frequency domain reflectometry. *IEEE Sensors Journal*, 12(1):237–245, 2012.
  - [199] C. Okawara and K. Saijyou. Fiber optic interferometric hydrophone using fiber Bragg grating with time division multiplexing. *Acoustical Science and Technology*, 28(1):39–42, 2007.
  - [200] A. D. Kersey, K. L. Dorsey, and A. D. Dandridge. Cross talk in a fiber-optic Fabry-Perot sensor array with ring reflectors. *Optics Letters*, 14(1):93–95, 1989.
  - [201] G. De Vine, D. S. Rabeling, B. J. Slagmolen, T. T. Lam, S. Chua, D. M. R. Wuchenich, D. E. McClelland, and D. A. Shaddock. Picometer level displacement metrology with digitally enhanced heterodyne interferometry. *Optics Express*, 17(2):828–837, 2009.
  - [202] D. M. R. Wuchenich, T. T. Lam, J. H. Chow, D. E. McClelland, and D. A. Shaddock. Laser frequency noise immunity in multiplexed displacement sensing. *Optics Letters*, 36(5):672–674, 2011.
  - [203] K. S. Isleif, O. Gerberding, S. Köhlenbeck, A. J. Sutton, B. Sheard, S. Gößler, D. A. Shaddock, G. Heinzl, and K. Danzmann. Highspeed multiplexed heterodyne interferometry. *Optics Express*, 22(20):24689–24696, 2014.
  - [204] A. J. Sutton, O. Gerberding, G. Heinzl, and D. A. Shaddock. Digitally enhanced homodyne interferometry. *Optics Express*, 20(20):22195–22207, 2012.
  - [205] C. E. Lee, R. A. Atkins, and H. F. Taylor. Reflectively tapped optical fibre transversal filters. *Electronics Letters*, 23(11):596–598, 1987.
  - [206] E. Cibula and D. Donlagic. Low-loss semi-reflective in-fiber mirrors. *Optics Express*, 18(11):12017–12026, 2010.
  - [207] J. Qiu, K. Miura, and K. Hirao. Femtosecond laser-induced microfeatures in glasses and their applications. *Journal of Non-Crystalline Solids*, 354(12):1100–1111, 2008.
  - [208] W. W. Morey. Distributed fiber grating sensors. *Proceedings of the 7th Optical Fibre Sensors Conference, Edgecliff, Australia*, pages 285–288, 1990.
  - [209] S. J. Mihailov, D. Grobnić, and C. W. Smelser. Efficient grating writing through fibre coating with femtosecond IR radiation and phase mask. *Electronics Letters*, 43(8):442–443, 2007.
  - [210] V. V. Protopopov. *Laser heterodyne radars and lidars*, pages 105–190. Laser Heterodyning. Springer, 2009.
  - [211] Y. Liao, E. Austin, P. J. Nash, S. A. Kingsley, and D. J. Richardson. Highly scalable amplified hybrid TDM/DWDM array architecture for interferometric fiber-optic sensor systems. *Journal of Lightwave Technology*, 31(6):882–888, 2013.
  - [212] Y. Liao, E. Austin, P. J. Nash, S. A. Kingsley, and D. J. Richardson. Phase sensitivity characterization in fiber-optic sensor systems using amplifiers and TDM. *Journal of Lightwave Technology*, 31(10):1645–1653, 2013.
  - [213] O. H. Waagaard, E. Rønnekleiv, S. Forbord, and D. Thingbø. Reduction of crosstalk in inline sensor arrays using inverse scattering. *Proceedings of the 19th International Conference on Optical Fibre Sensors (OFS-19), Perth, Australia*, Proc. SPIE 7004:4Z

- 1–4, 2008.
- [214] J. L. Brooks, B. Moslehi, B. Y. Kim, and H. J. Shaw. Time-domain addressing of remote fiber-optic interferometric sensor arrays. *Journal of Lightwave Technology*, 5(7):1014–1023, 1987.
  - [215] A. D. Kersey, A. D. Dandridge, and A. B. Tveten. Time-division multiplexing of interferometric fiber sensors using passive phase-generated carrier interrogation. *Optics Letters*, 12(10):775–777, 1987.
  - [216] F. Farahi, A. S. Gerges, J. D. C. Jones, and D. A. Jackson. Time-division multiplexing of fibre optic interferometric sensors using a frequency modulated laser diode. *Electronics Letters*, 24(1):54–55, 1988.
  - [217] A. M. Street and D. J. Edwards. Bandwidth requirements for bit-sequence codes used in fibre optic multiplexing systems. *IEE Proceedings - Optoelectronics*, 142(4):202–206, 1995.
  - [218] N. Takeuchi, N. Sugimoto, H. Baba, and K. Sakurai. Random modulation CW lidar. *Applied Optics*, 22(9):1382–1386, 1983.
  - [219] J. F. Holmes and B. J. Rask. Coherent, CW, pseudo-random-code-modulated lidar for path-resolved optical remote sensing. *Proceedings of the Atmospheric Propagation and Remote Sensing III Conference, Orlando, USA*, Proc. SPIE 2222:20–28, 1994.
  - [220] M. Bashkansky, H. R. Burris, E. E. Funk, R. Mahon, and C. I. Moore. RF phase-coded random-modulation lidar. *Optics Communications*, 231(1-6):93–98, 2004.
  - [221] H. S. Al-Raweshidy and D. Uttamchandani. Spread spectrum technique for passive multiplexing of interferometric optical fiber sensors. *Optics Communications*, 80(1):18–22, 1990.
  - [222] A. D. Kersey, A. D. Dandridge, and M. A. Davis. Low-crosstalk code-division multiplexed interferometric array. *Electronics Letters*, 28(4):351–352, 1992.
  - [223] F. Kullander, C. Laurent, S. Zyra, and H. Geis. Crosstalk reduction in a code division multiplexed optical fiber sensor system. *Optical Engineering*, 37(7):2104–2107, 1998.
  - [224] P. S. Cho, J. B. Khurgin, and I. Shpanzter. Closed-loop bias control of optical quadrature modulator. *IEEE Photonics Technology Letters*, 18(21):2209–2211, 2006.
  - [225] A. J. Hymans and J. Lait. Analysis of a frequency-modulated continuous-wave ranging system. *Proceedings of the IEE - Part B: Electronic and Communication Engineering*, 107(34):365–372, 1960.
  - [226] I. P. Giles, D. Uttam, B. Culshaw, and D. E. N. Davies. Coherent optical-fibre sensors with modulated laser sources. *Electronics Letters*, 19(1):14–15, 1983.
  - [227] A. Cabral and J. Rebordão. Accuracy of frequency-sweeping interferometry for absolute distance metrology. *Optical Engineering*, 46(7):073602, 2007.
  - [228] A. Davila, J. M. Huntley, C. Pallikarakis, P. D. Ruiz, and J. M. Coupland. Wavelength scanning interferometry using a Ti:Sapphire laser with wide tuning range. *Optics and Lasers in Engineering*, 50(8):1089–1096, 2012.
  - [229] R. Onodera and Y. Ishii. Selective imaging with a frequency-modulated laser-diode interferometer. *Optics Letters*, 20(7):761–763, 1995.
  - [230] A. Olsson and C. L. Tang. Dynamic interferometry techniques for optical path length measurements. *Applied Optics*, 20(20):3503–3507, 1981.

- 
- [231] D. J. Webb, R. M. Taylor, J. D. C. Jones, and D. A. Jackson. Interferometric optical path difference measurement using sinusoidal frequency modulation of a diode laser. *Optics Communications*, 66(5):245–248, 1988.
- [232] I. P. Giles, D. Uttam, B. Culshaw, and D. E. N. Davies. Coherent optical-fibre sensors with modulated laser sources. *Electronics Letters*, 19(1):14–15, 1983.
- [233] I. Sakai, G. Parry, and R. C. Youngquist. Multiplexing fiber-optic sensors by frequency modulation: cross-term considerations. *Optics Letters*, 11(3):183–185, 1986.
- [234] G. Economou, R. C. Youngquist, and D. E. N. Davies. Limitations and noise in interferometric systems using frequency ramped single-mode diode lasers. *Journal of Lightwave Technology*, 4(11):1601–1608, 1986.
- [235] J. Zheng. Triple-sensor multiplexed frequency-modulated continuous-wave interferometric fiber-optic displacement sensor. *Applied Optics*, 46(12):2189–2196, 2007.
- [236] C. J. Karlsson and F. A. Olsson. Linearization of the frequency sweep of a frequency-modulated continuous-wave semiconductor laser radar and the resulting ranging performance. *Applied Optics*, 38(15):3376–3386, 1999.
- [237] S. A. Al-Chalabi, B. Culshaw, D. E. N. Davies, I. P. Giles, and D. Uttam. Multiplexed optical fibre interferometers: an analysis based on radar systems. *IEE Proceedings J (Optoelectronics)*, 132(2):150–156, 1985.
- [238] F. Farahi, J. D. C. Jones, and D. A. Jackson. Multiplexed fibre-optic interferometric sensing system: combined frequency and time division. *Electronics Letters*, 24(7):409–410, 1988.
- [239] P. C. Won, L. K. Seah, and G. Xie. Quasi-distributed frequency-modulated continuous-wave reflectometric optical fiber strain sensor. *Optical Engineering*, 41(4):788–795, 2002.
- [240] R. C. Dixon. *Spread spectrum systems*. Wiley, 2nd edition, 1984.
- [241] D. V. Sarwate and M. B. Pursley. Crosscorrelation properties of pseudorandom and related sequences. *Proceedings of the IEEE*, 68(5):593–619, 1980.
- [242] S. W. Smith. *The scientist and engineer’s guide to digital signal processing*. California Technical Pub., 1997.
- [243] F. J. Harris. On the use of windows for harmonic analysis with the discrete fourier transform. *Proceedings of the IEEE*, 66(1):51–83, 1978.
- [244] C. K. Kirkendall, A. D. Kersey, A. D. Dandridge, M. J. Marrone, and A. R. Davis. Sensitivity limitations due to aliased high frequency phase noise in high channel-count TDM interferometric arrays. *Proceedings of the 11th International Conference on Optical Fibre Sensors (OFS-11)*, Sapporo, Japan, page Fr14, 1996.
- [245] S. Gao, M. O’Sullivan, and R. Hui. Complex-optical-field lidar system for range and vector velocity measurement. *Optics Express*, 20(23):25867–25875, 2012.
- [246] R. E. Bartolo, A. B. Tveten, and C. K. Kirkendall. The quest for inexpensive, compact, low phase noise laser sources for fiber optic sensing applications. *Proceedings of the 20th International Conference on Optical Fibre Sensors (OFS-20)*, Edinburgh, UK, Proc. SPIE 7503:70 1–4, 2009.
- [247] R. Willsch, W. Ecke, and H. Bartelt. Optical fiber grating sensor networks and their application in electric power facilities, aerospace and geotechnical engineering.



- Proceedings of the 15th International Conference on Optical Fibre Sensors (OFS-15), Portland, USA*, pages 49–54, 2002.
- [248] M. A. Davis and A. D. Kersey. Matched-filter interrogation technique for fibre Bragg grating arrays. *Electronics Letters*, 31(10):822–823, 1995.
  - [249] J. He, F. Li, L. Feng, H. Xiao, and Y. Liu. Elimination of environmental noise in interferometric wavelength shift demodulation for dynamic fiber Bragg grating sensor array. *Optics Communications*, 282(14):2836–2840, 2009.
  - [250] H. Li, G. B. Rieker, X. Liu, J. B. Jeffries, and R. K. Hanson. Extension of wavelength-modulation spectroscopy to large modulation depth for diode laser absorption measurements in high-pressure gases. *Applied Optics*, 45(5):1052–1061, 2006.
  - [251] D. Ryan, A. Abramovici, F. Zhao, F. Dekens, X. An, A. Azizi, J. Chapsky, and P. Halverson. Measuring cyclic error in laser heterodyne interferometers. Technical Report NPO-45157, NASA, 2010.
  - [252] K. F. Graff. *Wave motion in elastic solids*. Dover Publications, 2003.
  - [253] 316/316L Stainless Steel Datasheet, <http://www.aksteel.com>. (Accessed 16/02/2015).
  - [254] D. Meschede. *Gerthsen Physik*. Springer, 21. edition, 2001.
  - [255] E. Baumann, F. R. Giorgetta, I. Coddington, L. C. Sinclair, K. Knabe, W. C. Swann, and N. R. Newbury. Comb-calibrated frequency-modulated continuous-wave ladar for absolute distance measurements. *Optics Letters*, 38(12):2026–2028, 2013.
  - [256] E. P. Carden and P. Fanning. Vibration based condition monitoring: a review. *Structural Health Monitoring*, 3(4):355–377, 2004.
  - [257] K. Meiners-Hagen, R. Schödel, F. Pollinger, and A. Abou-Zeid. Multi-wavelength interferometry for length measurements using diode lasers. *Measurement Science Review*, 9(1):16–26, 2009.
  - [258] D. Huang, E. A. Swanson, C. P. Lin, J. S. Schuman, W. G. Stinson, W. Chang, M. R. Hee, T. Flotte, K. Gregory, and C. A. Puliafito. Optical coherence tomography. *Science*, 254(5035):1178–1181, 1991.
  - [259] M. Wojtkowski. High-speed optical coherence tomography: basics and applications. *Applied Optics*, 49(16):D30–D61, 2010.
  - [260] G. Dai, F. Pohlenz, H. U. Danzebrink, K. Hasche, and G. Wilkening. Improving the performance of interferometers in metrological scanning probe microscopes. *Measurement Science and Technology*, 15(2):444–450, 2004.
  - [261] M. Pisani, A. Yacoot, P. Balling, N. Bancone, C. Birlikseven, M. Çelik, J. Flügge, R. Hamid, P. Köchert, and P. Kren. Comparison of the performance of the next generation of optical interferometers. *Metrologia*, 49(4):455, 2012.
  - [262] M. Johansmann, G. Siegmund, and M. Pineda. Targeting the limits of laser Doppler vibrometry. *Proceedings of IDEMA*, pages 1–12, 2005.
  - [263] P. Castellini, M. Martarelli, and E. P. Tomasini. Laser Doppler vibrometry: development of advanced solutions answering to technology’s needs. *Mechanical Systems and Signal Processing*, 20(6):1265–1285, 2006.
  - [264] G. Siegmund. Sources of measurement error in laser Doppler vibrometers and proposal for unified specifications. *Proceedings of the 8th International Conference on Vibration Measurements by Laser Techniques, Ancona, Italy*, Proc. SPIE 7098:0Y

- 1–13, 2008.
- [265] S. Boudreau and J. Genest. Range-resolved vibrometry using a frequency comb in the OSCAT configuration. *Optics Express*, 22(7):8101–8113, 2014.
- [266] M. J. Rudd. A laser Doppler velocimeter employing the laser as a mixer-oscillator. *Journal of Physics E: Scientific Instruments*, 1(7):723–726, 1968.
- [267] L. Scalise, Y. Yu, G. Giuliani, G. Plantier, and T. Bosch. Self-mixing laser diode velocimetry: application to vibration and velocity measurement. *IEEE Transactions on Instrumentation and Measurement*, 53(1):223–232, 2004.
- [268] [www.oxford-instruments.com/optistatdry](http://www.oxford-instruments.com/optistatdry). (Accessed 24/04/2015).
- [269] E. R. Peck. Theory of the corner-cube interferometer. *Journal of the Optical Society of America*, 38(12):1015–1015, 1948.
- [270] C. N. Pannell, J. D. C. Jones, and D. A. Jackson. The effect of environmental acoustic noise on optical fibre based velocity and vibration sensor systems. *Measurement Science and Technology*, 5(4):412–417, 1994.
- [271] I. Yamaguchi. Speckle displacement and decorrelation in the diffraction and image fields for small object deformation. *Optica Acta*, 28(10):1359–1376, 1981.
- [272] D. Francis, T. O. H. Charrett, L. Waugh, and R. P. Tatam. Objective speckle velocimetry for autonomous vehicle odometry. *Applied Optics*, 51(16):3478–3490, 2012.
- [273] T. O. H. Charrett and R. P. Tatam. Objective speckle displacement: an extended theory for the small deformation of shaped objects. *Optics Express*, 22(21):25466–25480, 2014.
- [274] T. Brogårdh. Present and future robot control development - an industrial perspective. *Annual Reviews in Control*, 31(1):69–79, 2007.
- [275] M. F. Zaeh, J. Hatwig, J. Musiol, O. Roesch, and G. Reinhart. Analysis of the accuracy of industrial robots and laser scanners for remote laser beam welding and cutting. *Proceedings of the 41st International Symposium on Robotics, Munich, Germany*, 2010.
- [276] B. Hamner, S. Koterba, J. Shi, R. Simmons, and S. Singh. Mobile robotic dynamic tracking for assembly tasks. *Proceedings of the IEEE/RSJ International Conference on Intelligent Robots and Systems Conference (IROS 2009), St. Louis, USA*, pages 2489–2495, 2009.
- [277] P. G. Maropoulos, J. E. Muelaner, M. D. Summers, and O. C. Martin. A new paradigm in large-scale assembly - research priorities in measurement assisted assembly. *The International Journal of Advanced Manufacturing Technology*, 70(1-4):621–633, 2014.
- [278] B. K. S. Woods, C. S. Kothera, and N. M. Wereley. Wind tunnel testing of a helicopter rotor trailing edge flap actuated via pneumatic artificial muscles. *Journal of Intelligent Material Systems and Structures*, 22(13):1513–1528, 2011.
- [279] C. V. Jutte, W. L. Ko, C. A. Stephens, J. A. Bakalyar, W. L. Richards, and A. R. Parker. Deformed shape calculation of a full-scale wing using fiber optic strain data from a ground loads test. Technical Report TP-2011-215975, NASA, 2011.
- [280] J. K. Rice and M. Verhaegen. Robust and distributed control of a smart blade. *Wind Energy*, 13(2-3):103–116, 2010.

- [281] W. Wasyliwskyj. *Signals and transforms in linear systems analysis*. Springer, 2013.
- [282] J. G. Proakis and D. G. Manolakis. *Digital signal processing: principles, algorithms and applications*. Pearson Education, 3rd edition, 1996.
- [283] B. Kelly, R. Phelan, D. Jones, C. Herbert, J. O’Carroll, M. Rensing, J. Wendelboe, C. B. Watts, A. Kaszubowska-Anandarajah, and P. Perry. Discrete mode laser diodes with very narrow linewidth emission. *Electronics Letters*, 43(23):1282–1284, 2007.
- [284] T. Okoshi, K. Kikuchi, and A. Nakayama. Novel method for high resolution measurement of laser output spectrum. *Electronics Letters*, 16(16):630–631, 1980.
- [285] H. Ludvigsen, M. Tossavainen, and M. Kaivola. Laser linewidth measurements using self-homodyne detection with short delay. *Optics Communications*, 155(1):180–186, 1998.
- [286] C. H. Henry. Theory of the linewidth of semiconductor lasers. *IEEE Journal of Quantum Electronics*, 18(2):259–264, 1982.
- [287] <http://www.rfneulink.com/FPGA-whitepaper.htm>. (Accessed 13/05/2015).
- [288] N. Sulaiman, Z. A. Obaid, M. H. Marhaban, and M. N. Hamidon. Design and implementation of FPGA-based systems - a review. *Australian Journal of Basic and Applied Sciences*, 3(4):3575–3596, 2009.
- [289] U. Meyer-Baese. *Digital signal processing with field programmable gate arrays*. Springer, 3rd edition, 2007.
- [290] A. V. Anufriev, Y. A. Zimin, A. L. Vol’pov, and I. N. Matveev. Change in the polarization of light in a turbulent atmosphere. *Quantum Electronics*, 13(12):1627–1628, 1983.